1 Performance Analysis of a Commodity-Class Linux Cluster for Computational Chemistry Applications

Computational chemistry is the discipline of computing the physical and chemical properties of atoms and molecules using the fundamentals of quantum mechanics. The expense of computational chemistry calculations is significant and limited by available computational capabilities. The use of high-performance computing clusters alleviates such calculations. However, high-performance computing (HPC) clusters have always required a balance between four major factors: raw compute power, memory size, I/O capacity, and communication capacity. In this chapter, we present the results of standard HPC benchmarks in order to help assess the performance characteristics of the various hardware and software components of an own built commodity-class Linux cluster.

1.1 Introduction

Distributed computing is usually used to describe computing that spans multiple machines or multiple locations. Entries in the distributed computing taxonomy include cluster computing, grid computing, peer-to-peer computing, federated clusters and constellations. The primary distinction between cluster computing and other forms of distributed computing is the scope of the interconnecting network and the degree of coupling among the individual machines [1].

Initially, the terms cluster computing and high-performance computing were synonymous. Nowadays, the term cluster computing has expanded beyond high-performance to include high-availability (failover) clusters and load-balancing clusters. In practice, there is great overlap among these [1,2].

Commercial clusters often use proprietary computers and software, while commodity clusters, including Beowulf clusters, are constructed using commodity off-the-shelf computers and hardware, and freely available, open source software.

Unlike commodity clusters, in proprietary clusters, the software is often highly integrated into the system, and the CPU performance and network performance are well matched. The main disadvantage of commercial clusters, however, is their cost [1].

Parallel programming models for such clusters include shared-memory (e.g., POSIX threads (Pthreads) and OpenMP), message-passing (e.g., theoretical chemistry group message-passing (TCGMSG), message-passing interface (MPI), and parallel virtual machine (PVM)), virtual shared-memory (e.g., global arrays (GA) and distributed data interface (DDI)), and remote memory access (RMA) (e.g., aggregate remote memory copy interface (ARMCI)).

Over the past decade, high-performance computing clusters built from low cost computers have been used in diverse fields to help provide a cost-effective solution (i.e., a good price/performance ratio) and to handle large problem sizes beyond the capability of a single computer. Interest in high-performance computing clusters has been driven by the increase performance of commodity off-the-shelf computers, and high-speed, low-latency network technologies.

The high-performance cluster components are generally broken down into multiple categories: the cluster nodes (head node and compute nodes), cluster network, operating system, cluster middleware and cluster parallel applications [2].

Each node may have different characteristics such as single processor or symmetric multiprocessor (SMP) design, and access to various types of storage devices. In determining the performance of a node, the most important factors are processor clock rate, cache size, bus speed, memory capacity, disk access speed, and network latency. The first four are determined by CPU and motherboard [1,2].

The choice of network technology depends on price, performance (bandwidth and latency), compatibility with other cluster hardware and system software, as well as communication characteristics of the application that will use the cluster. There are a number of choices including Ethernet, Myrinet, Infiniband or Quadrics [1,2].

Linux provides the most flexible operating system environment for clusters and is being widely used as cluster's operating system. This is due to its wide hardware support, stability, manageability, flexibility, scalability, openness, availability and low cost [3].

Allocating the resources necessary for a cluster's parallel applications, scheduling the application components, providing the necessary communication paths over the network, and monitoring the performance and health of the cluster is the concern of the cluster's middleware. There are hundreds of choices available, many of which are open source. Examples include the MPICH library that allows parallel application components to communicate with each other, the Ganglia package, which is a very powerful collection and visualization tool for internal system performance parameters, and the Maui scheduler software that manages and schedules parallel MPI jobs over network [1,3]. The installation and configuration of cluster's middleware can be simplified by installing cluster management software [4] such as OSCAR [5] and NPACI Rocks [6-8]. These clustering toolkits simplify cluster deployment, maintenance, and management; and include everything that is likely needed for a dedicated high-performance computing cluster.

Cluster parallel applications fall into three primary categories: compute intensive, data or input/output (I/O) intensive, and transaction intensive. Each of these has its own characteristics, and network and I/O subsystem requirements [2].

The Northwest Chemistry (NWChem) [9] represents a typical cluster parallel application. It is an open source computational chemistry package developed by the Molecular Sciences Software group of the Environmental Molecular Sciences Laboratory (EMSL) at the Pacific Northwest National Laboratory (PNNL). It is designed to run on high-performance parallel computing systems. The package includes: (1) high-performance parallel-programming tools and libraries (known as ParSoft) such as global arrays (GA), aggregate remote memory copy interface (ARMCI), theoretical chemistry group message-passing (TCGMSG), parallel I/O (ParIO), memory allocator (MA), parallel linear algebra (PeIGS), and runtime database (RTDB), (2) chemistry based objects and application programming interfaces (APIs) (e.g., integral API, geometry and basis set objects, symmetry API, property module, and python), and (3) NWChem modules that spans the range of computational chemistry methods such as Hartree-Fock (HF) or self-consistent field (SCF), multiconfiguration SCF (MCSCF), density functional theory (DFT), pseudopotential plane-wave (PSPW), coupled cluster singles and doubles (CCSD), second-order Møller-Plesset (MP2), configuration interaction (CI), molecular mechanics, and molecular dynamics [10].

GAMESS-UK [11] is another computational chemistry package that has the capability to run on parallel machines. It uses a number of the high-performance parallel-programming tools and libraries used by the NWChem package. In contrast to NWChem, both SCF and DFT modules are parallelized in a replicated data fashion, with each node maintaining a copy of all data structures present in the serial version.

Computational chemistry problems have insatiable appetite for computer resources and typically take several days or even weeks on a single processor to produce a final result. Cluster computing solutions from commercial vendors are very expensive and are often beyond the capabilities of small to medium-sized research groups.

In order to achieve better computing speed and performance, we have built a commodity-class cluster of 8 Pentium® PCs already available at our department. In addition, this cluster can act as a prototype system and future implementations of Linux clusters at our department can benefit from the benchmarks and suggestions made in this study. We present performance evaluations of the CPU, memory, disk and network. We also consider the effects of some possible configuration and software choices on the computational performance, communications bandwidth and latency, and I/O performance. We emphasize on the tools that are provided by the NWChem and GAMESS-UK computational chemistry packages as well as on the software packages that can improve the performance of these two programs. It is hoped that the outcome of this study be of assistance to computational chemists willing to design and build a commodity-class cluster.

1.2 Cluster Software and Hardware

Our test system for the measurements is a Linux cluster running the NPACI Rocks 4.1 clustering toolkit (using CentOS 4.2 Linux operating system). It consists of one head node (frontend) and seven compute nodes. The frontend node contains Intel® Pentium® IV 2.6 GHz processor with 800 MHz front side bus (FSB), 512 KB level 2 (L2) cache, 3 GB of PC3200 DDR400 SDRAM (dual-channel architecture), and 80 GB 7200 RPM EIDE hard disk. The compute nodes are Intel® Pentium® IV 2.4 GHz processor with 533 MHz FSB, 512 KB L2 cache, 2 GB of PC3200 DDR400 SDRAM (single-channel architecture), and 40 GB 7200 RPM EIDE hard disk. All nodes have integrated Intel Gigabit Ethernet adapters that are connected by an 8-port

Gigabit Ethernet layer 2 switch using category 6 unshielded twisted pair (UTP) copper cables. The nodes are interconnected using the star topology. The frontend node has one extra fast Ethernet network interface card (NIC) connecting it to the external, public network.

1.3 Benchmark Results and Analysis

The performance of a computer is a function of many interrelated quantities. These include the application, the algorithm, the size of the problem, the high-level language, the implementation, the human level of effort used to optimize the program, the compiler's ability to optimize, the age of the compiler, the operating system, the architecture of the computer, and the hardware characteristics [12].

There are three main reasons to run benchmarks. First, if any changes are made to the cluster, a benchmark will provide with a baseline to see if performance is really any different. Second, benchmarks are useful when comparing systems or cluster configurations and thus can offer a reasonable basis for selecting between alternatives. Finally, benchmarks can be helpful with planning such as making better estimates of the impact of scaling the cluster [1].

In this section, we describe the performance of the various components (hardware and software) of our test system based on the results obtained from available benchmarks. All the software packages used are open source and are thus freely available (except the Intel compilers for Linux that were obtained under the non-commercial license and the GAMESS-UK package that was obtained under the academic parallel license). Compatibility of the various software packages with each other, and with the Linux kernel and hardware were checked prior to installing any package. Scheme 1.1 depicts the layered structure of the components of our cluster which will be discussed in the sections to follow.

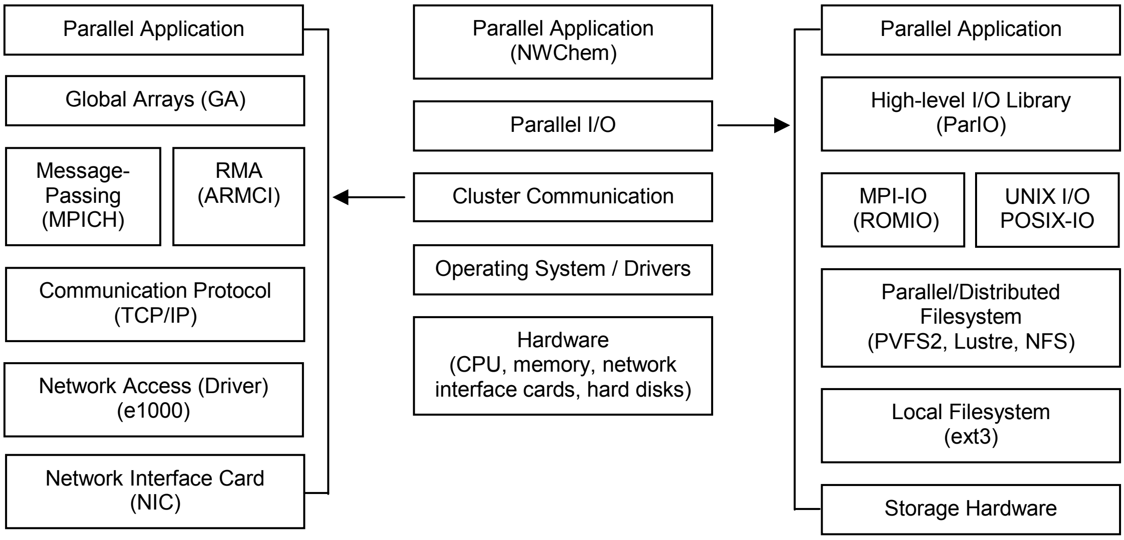

Scheme 1.1: Layered structure of the test cluster.

1.3.1 Compilers, processor, and memory performance

Compilers offer options to optimize the application code by applying several techniques. For example, compilers try to optimize the usage of caches and registers and may significantly reduce the application's demand for memory bandwidth. Using the right set of compiler flags while generating the executable code can affect the performance of the application. We tested the NWChem and GAMESS-UK codes generated by the GNU compiler collection (GCC version 3.4.4) and Intel compilers (version 9.1). The default optimization flags in the makefile were used. Several computational chemistry methods (HF, DFT and MP2) using various basis sets were examined. The Intel compilers generated more optimized code and performance gains of 7-30% with respect to GCC were obtained.

Since scientific applications such as NWChem and GAMESS-UK are floating-point intensive, we will concentrate on the processor's double-precision floating point performance. The performance of a processor is a combination of both clock frequency (GHz) and instructions per clock cycle (IPC). The frequency is a function of both the manufacturing process and the microarchitecture. At a given clock frequency, the IPC is a function of processor microarchitecture and how well the specific application being executed is optimized for the processor microarchitecture. In addition, it is also possible to increase the processor's performance by reducing the number of instructions required to execute the specific task being measured. This can be achieved (as in the case of Pentium® processor) by using the SSE2 (streaming SIMD (single instruction multiple data) extensions 2) instruction set that enables operation on multiple values at once. The use of SSE2 requires the support from both the application and the compiler. Moreover, the speed and size of the processor's L2 and L3 caches can help improve the performance [13].

The High Performance Linpack (HPL) benchmark [14] measures the floating point execution rate for solving a dense system of linear equations in double precision (64-bit) arithmetic on distributed-memory computers. It provides a testing and timing program to quantify the accuracy of the obtained solution as well as the time it took to compute it.

The HPL benchmark depends on the basic linear algebra subprograms (BLAS) library for much of the computation. The BLAS correspond to a collection of subprograms intended for performing basic linear algebra operations (i.e., vector and matrix operations). The Level 1 BLAS perform scalar, vector and vector-vector operations, the Level 2 BLAS perform matrix-vector operations, and the Level 3 BLAS perform matrix-matrix operations. Thus, to get good performance on the HPL benchmark, a high-performance implementation of the BLAS must be available. Optimized BLAS libraries are available for a variety of computer architectures. In the current study, we tested three implementations of the BLAS library, namely, the automatically tuned linear algebra software (ATLAS) (version 3.6-0) [15], Goto BLAS (version 1.07) [16], and Intel math kernel library (Intel MKL) (version

8.1.014) [17]. ATLAS library is installed as part of a standard NPACI Rocks installation. However, both Goto BLAS and Intel MKL libraries need to be manually installed.

We used the HPL benchmark that is distributed with the HPC Challenge benchmark (version 1.0.0) [18]. The executable binary was generated from Intel compilers (version 9.1). Regarding some of the tunable parameters in the HPL input file [19,20], we have chosen a problem size (N) of 34500 in order to fit 80% of the total amount of memory, that is,

$$N = \sqrt{\frac{no.of\ machines \times memory\ per\ node\,(byte)}{8}} \times 0.80, \qquad (1\text{-}1)$$

a block size (NB) of 80, and a process grid P × Q of 1 × 7.

Table 1.1 shows the performance data obtained on our test system using the three optimized BLAS libraries. The data are obtained after the network has been tuned as described in Section 1.3.2. The performance numbers were also given as percentages of the theoretical peak performance in order to determine system efficiency. The Pentium® IV processor can perform two double precision floating-point operations per clock cycle. Hence, the theoretical peak performance of the Pentium® IV processor running at 2.4 GHz is 4.8 Gflop/s. For our test system (7 compute nodes), this would give a theoretical peak performance of 33.6 Gflop/s. It can be seen from the table that Intel MKL has the best performance followed by Goto BLAS and then by ATLAS.

Table 1.1: HPL benchmark results using different BLAS libraries.

BLAS library	No. of processors	Problem size (N)	Block size (NB)	Processor grid	Theoretical performance (Gflop/s)	Performance (Gflop/s)	%
ATLAS	7	34500	80	1×7	33.6	19.2	57
Goto BLAS	7	34500	80	1×7	33.6	23.7	71
Intel MKL	7	34500	80	1×7	33.6	24.1	72

The NWChem and GAMESS-UK programs rely on the BLAS library for performing linear algebra operations. Both programs have their own BLAS. We ran some tests to see how this can be compared to the three BLAS libraries mentioned above. Table 1.2 shows the CPU times (in seconds). As can be seen, all BLAS libraries have comparable performance to the program's own BLAS. The most noticeable observation is the improved performance using the Goto BLAS library when running DFT calculations.

Table 1.2: CPU times (in seconds) for NWChem and GAMESS-UK calculations using different BLAS libraries.

Program/BLAS	Method		
	HF*	DFT§	MP2$
NWChem			
NWChem-BLAS	1445	118	183
ATLAS	1454	132	182
Goto BLAS	1453	80	179
Intel MKL	1452	121	179
GAMESS-UK			
GAMESS-UK-BLAS	1194	1943	455
Goto BLAS	1158	1795	455
Intel MKL	1172	1928	447

* For NWChem: calculation on arecoline using the 6-311G basis set. For GAMESS-UK: calculation on cyclosporin using the 6-31G basis set.

§ For NWChem: calculation on pyrrole using the 6-311G** basis set. For GAMESS-UK: calculation on cyclosporin using the 6-31G basis set.

$ For NWChem: calculation on propane using the 6-311G** basis set. For GAMESS-UK: calculation on C_2H_4S using the cc-pVTZ basis set.

Memory bandwidth is the rate at which data can be read from or written into the memory by the processor. The memory bandwidth might have an influence on the performance of scientific applications, and depends on the memory subsystem design [21,22]. The STREAM benchmark [23] is designed to measure sustainable memory bandwidth (in GB/s) for four simple operations:

Copy: $a(i) = b(i)$
Scale: $a(i) = \text{constant} \times b(i)$
Add: $a(i) = b(i) + c(i)$
Triad: $a(i) = b(i) + \text{constant} \times c(i)$

Each of the four tests adds independent information to the results: Copy measures transfer rates in the absence of arithmetic, Scale adds a simple arithmetic operation, Add adds a third operand to allow multiple load/store, Triad allows chained/overlapped/fused multiply/add operations. By measuring these four simple kernels, the benchmark measures traffic all the way from registers to main memory and vice versa.

We used the MPI version of STREAM that is part of the HPC Challenge benchmark (version 1.0.0) [18]. Each of the above operations is repeated ten times (only the best time is reported) on an array of 56678571 (determined automatically at run time to be large enough not to fit in the processor's caches) double precision numbers. Total memory required was 1.3 GB. The average performance (per node) of the four operations was 1.76 GB/s, 1.13 GB/s, 1.33 GB/s, and 1.33 GB/s, respectively (theoretical memory bandwidth is 3.2 GB/s). As can be observed, the copy test is faster than the other tests implying the cost for floating-point arithmetic operation(s).

1.3.2 Network performance

In any cluster, the network is often the greatest determinant of parallel application speed and cluster efficiency, and should be interoperable with the selected hardware and operating system as well as be capable of efficiently supporting the communication protocols that are necessary for the middleware and applications.

Parallel high-performance computing applications have wide variation in communication patterns and impose diverse requirements on the network subsystem. Some applications' workloads are partitioned such that each compute node can work with limited interaction with other nodes. These application classes are referred to as 'embarrassingly parallel'. Other applications require significant communication between compute nodes. This type of applications can either be sensitive to the network bandwidth (i.e., communicate with larger message sizes) or be sensitive to the network latency (i.e., communicate with high messaging rates). Many applications may fall in between these variations [24,25]. Applications with high computation to communication ratio are referred to as ‘coarse-grained’, whilst those with low ratio are referred to as ‘fine-grained’.

Communication performance is affected by a number of factors including processor speed, I/O speed, PCI and memory bus architecture, network adaptors, device drivers, and protocol stack processing. The two chief characteristics establishing the operational properties of a network are bandwidth and latency. Peak bandwidth is the maximum amount of data that can be transferred in a single unit of time through a single connection and is measured in millions of bits per second (Mbps). Latency is the time it takes for a message to be passed from one processor to another including the latency of the switch and is measured in microseconds (μs) [25]. The communication performance at the application level depends on the collaboration of all components in the communication system, and inefficiencies can occur at many levels between the application and hardware layers [26-28] (cf. Scheme 1.1).

Gigabit Ethernet (GigE) is a popular interconnection technology used to build cluster systems. It is a strong candidate when the cost is considered as an important design requirement. TCP/IP is the most popular low-level communication protocol for GigE. Since TCP/IP was originally engineered to provide a general transport protocol, it is not by default optimized for high-speed communication. Thus, a number of TCP parameters need to be optimized in order to tune the TCP/IP protocol for GigE [29-35].

For optimizing the performance, we have modified several driver (the Linux base driver for the Intel GigE adapter; e1000) and TCP/MPICH parameters:

(1) Allow the driver to buffer more incoming packets and to queue more transmits by increasing the RxDescriptors and TxDescriptors values to 4096, respectively.

(2) Turning off interrupt coalescence (IC) by setting the InterruptThrottleRate value to zero. The InterruptThrottleRate value represents the maximum number of interrupts per second the controller generates. Increasing this value reduces the number of context switches made by the kernel to process the packets, but adds to the latency.

To make the changes in 1 and 2 permanently, one can edit the `/etc/modprobe.conf` file and add the following line:

```
options e1000 InterruptThrottleRate=0 RxDescriptors=4096 \
TxDescriptors=4096
```

(3) Turn on TCP segmentation offload (TSO). This can be done by running '`ethtool -K eth0 tso on`' command. Turning on TSO significantly reduces the work done by the processor.

(4) Enable jumbo frames by increasing the maximum transmission unit (MTU) to 8160-byte. Ethernet has used 1500-byte packets. Jumbo frames extend Ethernet to 9000 bytes. Smaller packets usually mean more CPU interrupts and more processing overhead for a given data transfer size. Thus, jumbo frames provide less CPU load than 1500-byte packets and more bandwidth. An 8160-byte MTU allows an entire packet to fit in a single 8192-byte block [31]. To make the change permanently, the following entry is added to the `/etc/sysconfig/network-scripts/ifcfg-eth0` file:

```
MTU=8160
```

(5) Increase the maximum TCP buffer size (maximum receive/send window size) to 8 MB. To make the changes permanently, one can edit the `/etc/sysctl.conf` file and add the following two lines:

```
net.core.rmem_max = 8388608
net.core.wmem_max = 8388608
```

(6) Increase the socket buffer sizes (memory reserved for TCP receive/send) to 8 MB. To make the changes permanently, one can edit the `/etc/sysctl.conf` file and add the following two lines:

```
net.ipv4.tcp_rmem = 4096 87380 8388608
net.ipv4.tcp_wmem = 4096 16384 8388608
```

A note about 5 and 6 is that when an application does not explicitly request buffer sizes by calling `setsockopt ()`, the kernel uses heuristics to choose system default values based on `net/ipv4/tcp_[rw]mem` kernel variables (the middle values in 6) and current memory consumption. In this case, the 'congestion window' (a TCP technique to determine how many packets can be sent at one time) will start at the default and increase up to the maximum value (the third values in 6). This is called 'Linux TCP autotuning'. The third values must be the same as or less than the values specified in 5. When an application explicitly request buffer sizes by calling `setsockopt ()`, the default values based on `net/ipv4/tcp_[rw]mem` kernel variables are not chosen. However, the maximum sizes for socket buffers declared via the `SO_SNDBUF` and `SO_RCVBUF` mechanisms are limited by the global `net/core/[rw]mem_max` kernel parameters (the values in 5).

(7) Increase the amount of allowed unprocessed packets to 1000 to avoid losing (dropping) packets at the receiver side. This can be done by adding the following line to the `/etc/sysctl.conf` file:

```
net.core.netdev_max_backlog = 1000
```

(8) Clear TCP cache between connections by adding the following line to the `/etc/sysctl.conf` file:

```
net.ipv4.tcp_no_metrics_save = 1
```

(9) Increase the P4_SOCKBUFSIZE to 512 KB. This value must be less than the maximum TCP buffer size. To set it, the following entry can be added to the `~/.bashrc` file:

```
export P4_SOCKBUFSIZE = 512000
```

(10) Stop the IPTables (firewall) by running '`/etc/init.d/iptables stop`' command.

Detailed descriptions about these parameters and their impacts can be found in references 36 – 42. Below we outline the performance results obtained on our test system.

The benchmark used to test the communication performance is NetPIPE (version 3.6.2) [43]. It performs simple ping-pong tests, bouncing messages of increasing sizes (1 to 8 MB) between two processors. It directly tests message-passing libraries and the native communication layers they run upon (e.g., TCP/IP).

Different socket buffer sizes (128 KB to 16 MB) against different sizes of MTU (1500, 3000, 4500, 6000, 7500, 9000 and 8160) have been tested. The best value for socket buffer size was found to be 8 MB. Figure 1.1 shows the obtained throughput (bandwidth) for MTU sizes of 1500, 8160 and 9000 at this socket buffer size. The non-standard 8160-byte MTU yielded the best peak throughput (816 Mbps) compared to 754 Mbps for 9000-byte MTU and 626 Mbps for the conventional 1500-byte MTU. The enhanced throughput in the case of jumbo frames is apparent for messages larger than 128 KB. For messages in the range of 2 KB to 128 KB, the conventional 1500-byte MTU showed better performance, while for messages smaller than 2 KB all MTU sizes exhibited the same performance. Turning on interrupt coalescence (IC) increased the peak throughput for the 1500-byte MTU from 626 Mbps to 796 Mbps but no influence of IC on the 8160-byte MTU is observed. However, turning on interrupt coalescence will increase the latency for shorter messages.

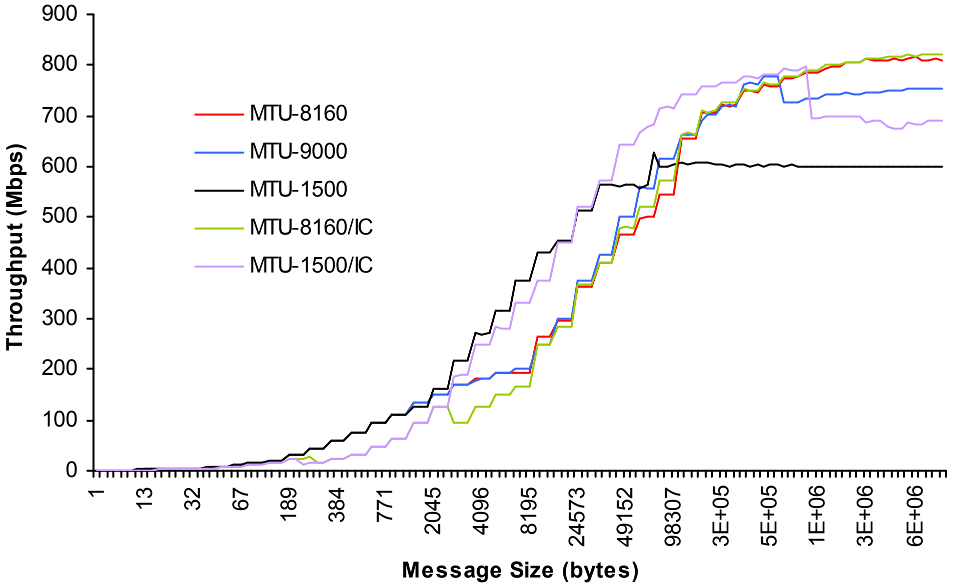

Figure 1.1: Bandwidths for MTU 1500, 8160, and 9000 with and without interrupt coalescence (IC) at 8 MB socket buffer size.

Figures 1.2-1.4 illustrate the latency for different message size ranges. It can be seen that (1) for messages less than 2 KB, all MTU sizes showed comparable latencies, (2) for messages in the range of 2 KB – 128 KB, the 1500-byte MTU had lower latency, and (3) for messages greater than 128 KB, the 8160-byte gave lower latencies. To see the effect of IC on latency, Figures 1.2-1.4 show the case for 8160-byte MTU with and without IC. Disabling interrupt coalescence significantly reduced the latency from 62.5 μs (the latency for 8-byte message) to 46.5 μs. For messages larger than 12 KB, the effect was not apparent and both cases showed comparable latencies.

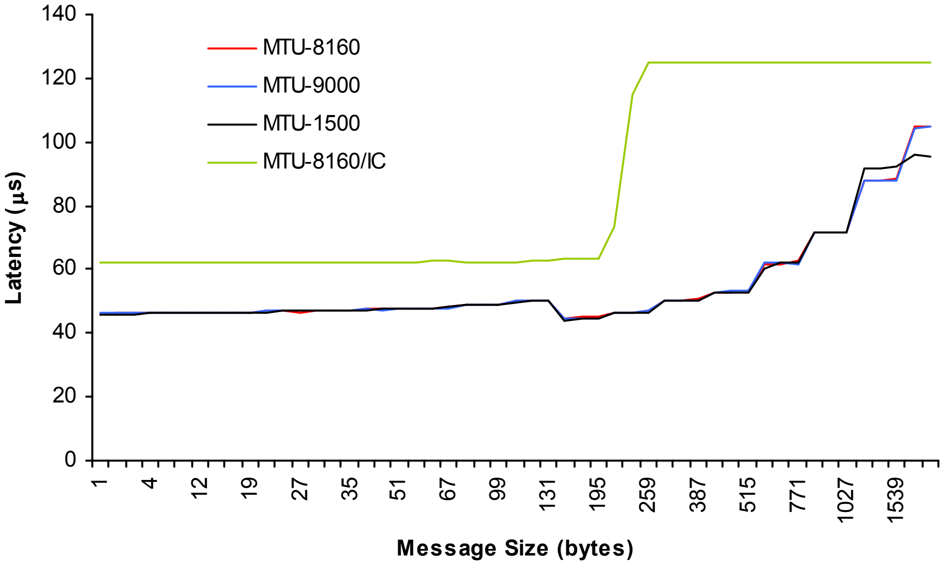

Figure 1.2: Latencies for MTU 1500, 8160, and 9000 for message sizes less than 2 KB.

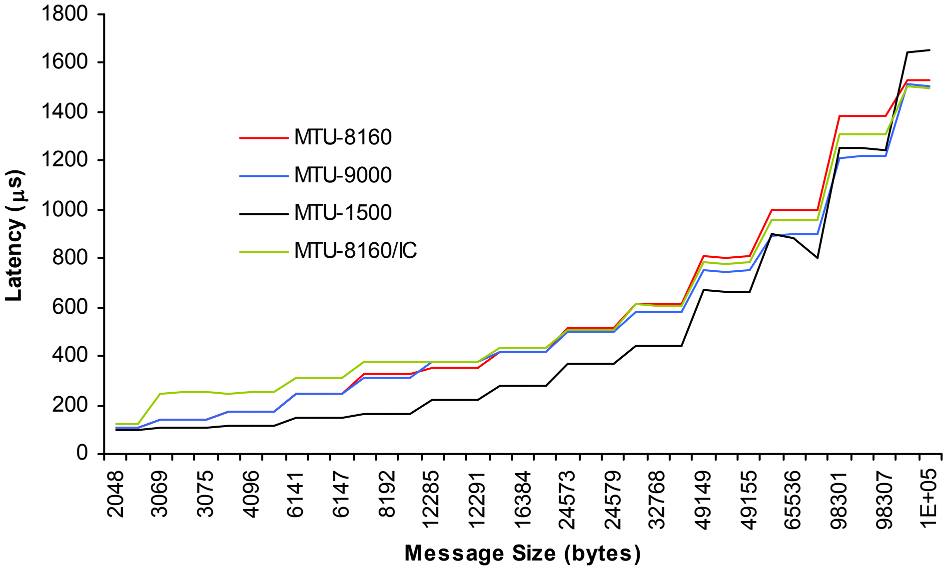

Figure 1.3: Latencies for MTU 1500, 8160, and 9000 for message sizes in the range of 2 KB to 128 KB.

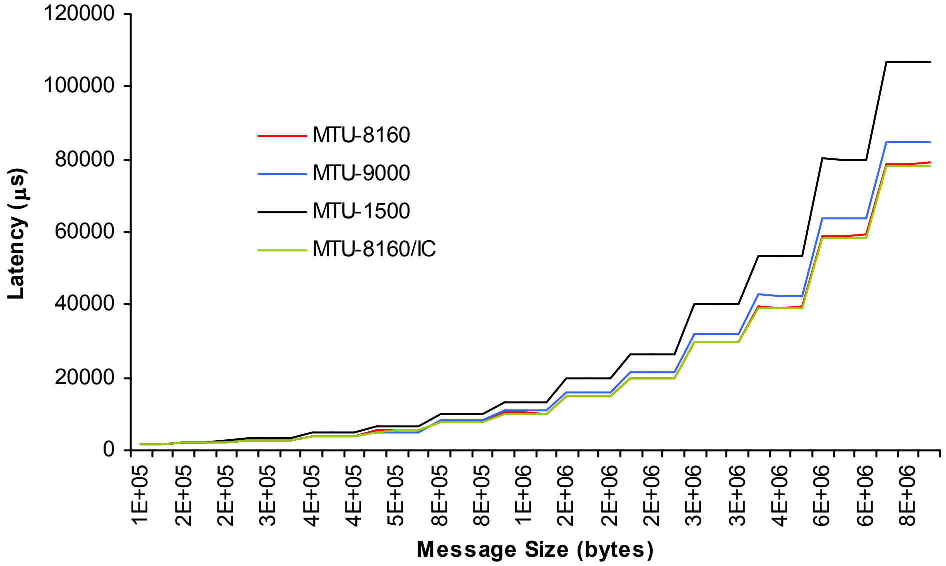

Figure 1.4: Latencies for MTU 1500, 8160, and 9000 for message sizes greater than 128 KB.

To estimate the CPU load, we read the output of '`cat /proc/loadavg`' command before and after each run. At the server side, the load averages for 1500-byte and 8160-byte MTU were 0.27 and 0.16, respectively. At the client side, they were 0.11 and 0.05, respectively. This gives us the conclusion that the use of jumbo frames reduces the load on the system probably through less CPU utilization.

From the above discussion, it can be deduced that if the application communicates with message sizes in the range of 2 KB to 128 KB, the 1500-byte MTU is a better choice since it has better throughput performance and lower latency at that range of message sizes. In general, the 8160-byte MTU gave the best throughput for larger message sizes, and turning off interrupt coalescence reduced the latency of smaller ones. Thus, the 8160-byte MTU in conjunction with disabling interrupt coalescence will be used throughout this study.

The message-passing programming model is based on the concept of distributed address space in which data exchange is achieved through explicit message passing. The message-passing interface MPI-1 is a message-passing standard that allows data to be moved between the cluster's nodes by sending and receiving the data as messages. MPI-1 functions include primitives for point-to-point communications (i.e., communication between two nodes) and collective operations (i.e., global communications between groups of nodes). MPI-2 introduces enhancements to the MPI-1 specifications such as one-sided communication operations and MPI-IO (specification for parallel I/O). MPI over GigE uses TCP as its transport; similarly, MPI-based applications use MPI as their transport [1,44].

Our system uses MPICH1 (version 1.2.7p1), configured with the ch_p4 device, as the MPI implementation [45]. MPICH 1.2.7p1 is installed as part of a standard NPACI Rocks installation. MPICH 1.2.7p1 has some limits that do not fully utilize today's computing power, and thus source modifications, reconfiguration, and recompiling the source code are needed. We followed the modifications recommended by He [46]. These include: (1) changing the upper limit for P4_GLOBMEMSIZE from 256 MB to 1.5 GB, (2) changing the upper limit for P4_SOCKBUFSIZE from 16 KB to 1 MB, and (3) changing the maximum size of single message from 256 MB to 1 GB. Linux kernel 2.6 has a default maximum segment size (SHMMAX) of 32 MB, a default maximum number of segments of 4096, and a default maximum shared memory of 8 GB. Shared memory segments are not only resources for the MPICH implementation, but also resources for the system. In NPACI Rocks, the maximum segment size for a compute node is set by default to ¾ the available physical memory (1.5 GB on our test system). The values of the two environment variables P4_GLOBMEMSIZE and P4_SOCKBUFSIZE can be set during run-time by adding entries to the `~/.bashrc` file but not exceeding the upper limits mentioned above. We used the GNU GCC compilers (version 3.4.4) and Intel compilers (version 9.1) to compile the MPICH library. There was no clear performance difference between the two compilers.

The primary optimization parameter that is important to maximize the performance of MPICH is the P4_SOCKBUFSIZE environment variable. Varying this variable from 64 KB to 1 MB, the best result was obtained at 512 KB with peak throughput performance of 666 Mbps (Figure 1.5). Figure 1.5 shows that MPICH suffers a 5-20% loss as compared to raw TCP performance. The latency increased from 46.5 μs for raw TCP to 52 μs for MPICH. Turning off IPTables reduced the latency for MPICH from 52 μs to 49 μs.

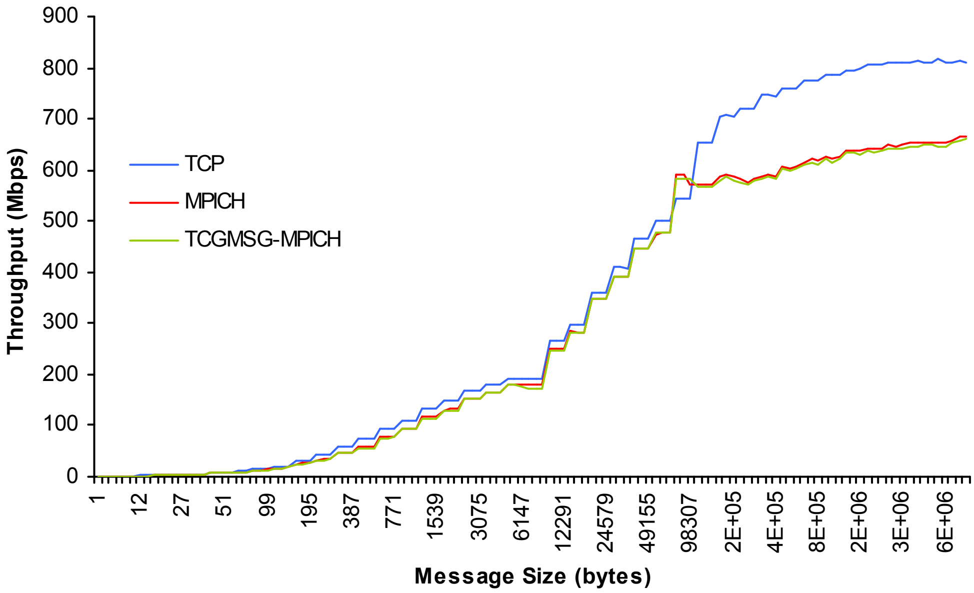

Figure 1.5: Bandwidths for raw TCP, MPICH, and TCGMSG-MPICH.

The theoretical chemistry group message-passing (TCGMSG) is a toolkit for writing portable parallel programs using a message-passing model. It has a small set of functions and provides an interface between applications (e.g., NWChem and GAMESS-UK) and either TCP or an underlying message-passing library like MPI. TCGMSG-MPI is a TCGMSG interface implementation on top of MPI, and the library is distributed with the global arrays package [47]. The overhead introduced by using the TCGMSG layer on top of MPICH is very minor. The TCGMSG-MPICH curve (Figure 1.5) falls to within 1% of the MPICH curve and the latency has increased by less than 1 μs. This is not surprising since TCGMSG is only a thin layer on top of MPICH.

For some parallel applications, the use of remote memory access (RMA) operations (i.e., one-sided communication operations) offers several advantages over message passing in terms of simplicity of use, applicability, and performance. Libraries that implement RMA operations include the MPICH2 library (an implementation of the MPI-2 standard), the aggregate remote memory copy interface (ARMCI) library, and the global arrays (GA) library.

The ARMCI [48-53] is a portable implementation of RMA. The operations that are supported by ARMCI include contiguous and non-contiguous one-sided data transfer operations including put, get and accumulate; synchronization operations; and memory management and error handling. Unlike MPI-2 that uses ‘active target’ operations, ARMCI allows any process of any parallel application to copy data between local and remote memory without the explicit cooperation of the remote process whose memory is accessed. In this sense, the data transfer operations in ARMCI are truly one-sided. This decoupling of synchronization leads to performance improvement.

The GA programming model [54-58] has been implemented in the GA toolkit as a portable virtual shared-memory programming model for distributed memory computers. The GA is used to share arrays between processors as if the memory were physically shared and combines the better features of message-passing and shared-memory models. There are two types of the shared distributed-memory: local and remote. Local distributed-memory is defined as the memory a given process uses to store its portion of the distributed data, whereas remote distributed-memory is the memory reserved by all the remaining parallel processes for their portions of the distributed data. Every process can independently, asynchronously, and efficiently access logical blocks of the physically distributed arrays with no need for explicit cooperation by other processes. The GA model acknowledges that remote data is slower to access than local data. The elimination of processor interactions, as opposed to the message-passing model, makes the GA model simpler for parallel programming. It should be pointed out that the GA model is designed to complement rather than replace message-passing libraries and that the two mechanisms are completely interoperable (i.e., a single program can contain calls to both libraries). In the GA model, the elementary one-sided communication operations (e.g., put and get) are crucial to the overall performance of the application that uses it. All RMA operations in GA are facilitated by the ARMCI library included in the GA package. Unlike ARMCI, GA presents a global view of data. Both programs NWChem and GAMESS-UK make use of the GA library.

Figure 1.6 shows the performance of MPICH, ARMCI and GA. For ARMCI, the curve represents the average of remote put and get operations to transfer both contiguous and non-contiguous (strided) data. For GA, the curve represents the average of remote put and get operations to transfer both 1-D and 2-D array sections.

The MPICH results were obtained using the multi-PingPong benchmark available from the Intel MPI benchmarks (IMB) suite (version 2.3) [59]. In contrast to the NetPIPE benchmark that focuses on a single message transfer between only two processes, in multi-PingPong benchmark, N/2, where N is total number of processes, disjoint groups of 2 processes each will be formed, all and simultaneously running. It is based on `MPI_Send` and `MPI_Recv` routines. The GA (version 4.0.1) and ARMCI (version 1.1) were used in the tests. The benchmarks used to generate the results are available within the GA package.

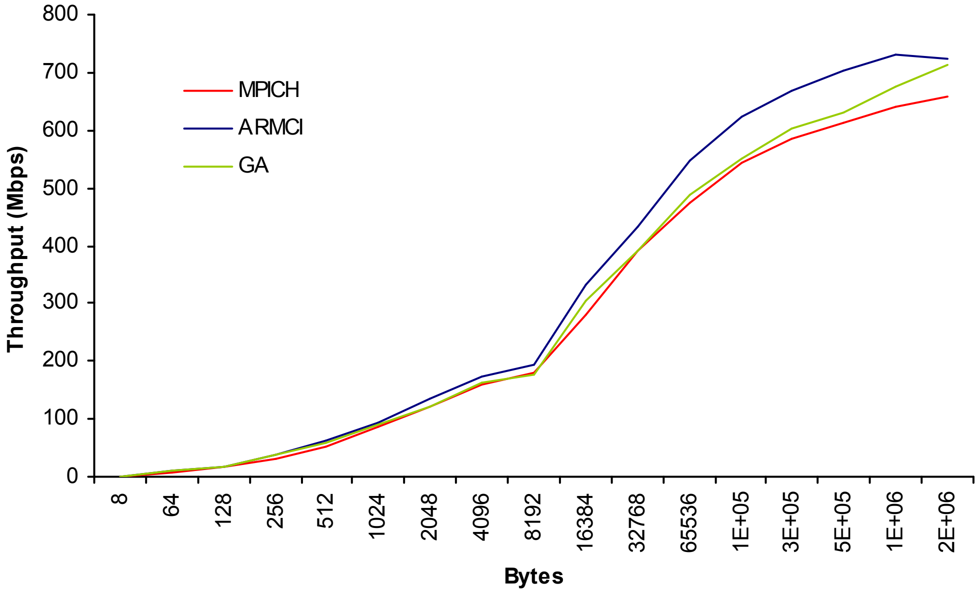

Figure 1.6: Bandwidths for MPICH, ARMCI, and GA libraries.

In the case of both contiguous and non-contiguous (strided) data transfers, the ARMCI put and get operations outperform the corresponding MPI send/receive operations (Figure 1.6). GA's communication interfaces form a thin wrapper around ARMCI interfaces. As can be seen in Figure 1.6, the GA curve falls to within 1-20% of the ARMCI curve. Table 1.3 shows the latency numbers for the MPI send/receive, the ARMCI remote put/get, and the GA remote put/get operations. The wide gap between the put and get operations may be attributed to the fact that the put operation only signals that the data has been copied out of the calling process' local memory and may occur before data is actually transferred to the remote process, while the get operation does not complete until the remote data has been written to the calling process' local memory.

Table 1.3: Latency numbers for MPICH, ARMCI, and GA operations.

Interface	Latency (μs)	
MPI	56.6	
	put	*get*
ARMCI	1.4	50.1
GA	2.1	55.3

1.3.3 Disk storage and parallel I/O performance

In out-of-core parallel computations, disk storage is treated as another level in the memory hierarchy, below CPU registers, caches (level 1, level 2, and level 3), local memory, and remote memories. Each level of this hierarchy owns a larger memory capacity and is slower than the higher levels. The latency of accesses to memory can be minimized by caching frequently used data in higher hierarchy levels thus producing a maximum data supply to the processor. The bandwidth of data transfers between main memory and disk storage is the slowest between all levels.

Most scientific applications need to perform I/O for a number of reasons such as reading initial data, writing the results, checkpointing, out-of-core data sets, and scratch files for temporary storage. Computational chemistry algorithms [60,61] may be generally classified as a combination of in-core, conventional or direct method, and sequential or parallel operation. In-core calculations are fastest but often require prohibitively large amounts of memory. In contrast to direct method, conventional computation stores in disk many of the intermediate results and thus avoids redundant recomputation. Semi-direct calculations are between these extremes with some intermediate results being precomputed and stored (memory or disk) while the remaining being recomputed as necessary. The size of storage space required depends on the computational chemistry method being used, the basis set(s) used, the use of symmetry or not, and the number of atoms in the simulation. Computational speed as well as memory and secondary storage capacities influence the choice between these methods. Either distributed storage or replicated storage can be used in parallel calculations with the latter limiting the size of calculations to the same size that could be achieved on a single node.

The two main requirements for I/O-intensive applications are I/O speed (i.e., the rate at which the program can read or write data) and storage capacity. I/O performance has lagged behind the computation and communication performance of high-performance computing clusters. The use of parallel filesystem can help solve this problem by typically striping files across multiple I/O nodes thus aggregating the moderate I/O capabilities of each node to make up a very fast disk [62]. In small clusters, all nodes can act as I/O nodes and compute nodes, whereas large clusters have a dedicated set of I/O nodes where no compute jobs are run on them [63]. Each I/O node can support a large number of compute nodes, and it is common to deploy 1 GB/s of I/O aggregate throughput per 1 Tflop/s of compute power.

Parallel I/O may have a different meaning for different applications. Types of parallel I/O operations in computational chemistry applications [60] include: (1) collective I/O operations in which multiple processors cooperate in a read or write operation to a shared file (used in checkpoint/restart, and RI-SCF and RI-MP2 methods), (2) noncollective I/O operations in which each processor perform an independent read or write operation to an arbitrary location in a shared file (used in MRCI method), and (3) noncollective I/O operations in which each processor carries out an independent read or write operation to a private file (used in HF, DFT and MP2 methods).

Applications can access files located in (parallel) filesystems by using an interface such as UNIX/POSIX I/O, MPI-IO (e.g., ROMIO), or high-level libraries (e.g., ParIO). The UNIX/POSIX I/O was designed mainly to support filesystems on a local storage device, and for access patterns commonly found in serial applications. However, all parallel filesystems provide a support for such an interface (e.g., [64,65]). ROMIO is a high-performance, portable MPI-IO implementation that can be configured to operate on top of various filesystems using an abstract I/O device (ADIO) layer [66]. It contains features specifically designed for I/O parallelism and performance. ParIO [60] is a high-level I/O library that has been designed to meet the parallel I/O requirements of computational chemistry applications discussed above. It consists of three library modules: (1) disk resident arrays (DRA) library: extends the GA model to support explicit transfer between global memory and secondary storage, and supports the first form of parallel I/O operations mentioned above, (2) shared files (SF) library: supports the second type, and (3) exclusive access files (EAF) library: supports the third type of parallel I/O operations. The three ParIO library modules are fully independent and are layered upon the ELIO (Elementary IO) device library that provides a portable interface to different filesystems. The ELIO can take advantage of any system specific performance libraries available. Both programs NWChem and GAMESS-UK utilize the ParIO library.

There are three issues to consider for hard disks: interface type (EIDE, SATA, or SCSI), disk latency which is a function of rotational speed, and disk capacity. IOZone [67] is a serial filesystem benchmark for the POSIX I/O interface. It tests file I/O performance for a variety of file operations. We ran IOZone in order to determine the baseline for our storage hardware with its local filesystem 'third extended filesystem' (ext3). The hardware performance analysis was done by writing a 4 GB file, that is, twice the amount of the available RAM in order to avoid any caching effects. Disk read and write speeds were 55 MB/s and 49 MB/s, respectively.

The performance of a parallel filesystem depends on the physical network interconnect, the type of storage, the amount of storage, the storage interconnect, the operating system, the parallel filesystem itself, and the application utilizing the filesystem [68]. The performance of three different parallel filesystems (NFS, PVFS2, and Lustre) was examined using the 'common_file' benchmark that is part of the PRIOmark benchmarks collection (version 0.9.1) [69-71]. All performance tests were run after the network had been optimized (Section 1.3.2).

NFS (network file system) was developed to allow machines to mount a disk partition on a remote machine as if it were on a local hard disk and thus provides sharing of files across a network. A central NFS server is used to store the data and hence the server represents a bottleneck and a single point of failure. NFS does not scale well across large clusters. NFS is automatically installed with a standard NPACI Rocks installation where the frontend node is designated as the NFS server. The frontend node exports a directory from a partition to all compute nodes. The partition's local filesystem type is ext3. By default, the NFS is mounted with the `async` option.

PVFS2 (parallel virtual file system 2) [72] is an open source, stable, and scalable parallel filesystem that can be run on Linux clusters and on various computer architectures (e.g., x86, IA-64). PVFS2 is designed as a client-server system. The server is split into I/O and metadata servers that can be running on the same nodes or on different nodes. I/O servers serve data to the rest of the cluster while the metadata servers keep track of information about the data (e.g., file names and permissions). The MPI-IO interface has been implemented on top of PVFS2 by using the ROMIO implementation of MPI-IO. PVFS2 also supports the standard UNIX I/O functions.

PVFS2 is not included with the NPACI Rocks version we run on our system (the recent NPACI Rocks version 4.2.1 includes a PVFS2 roll). We installed PVFS2 version 1.5.1 which was a relatively easy process. One major problem was the incompatibility of this PVFS2 version with the ‘Berkeley DB’ database version 4.2.52 that comes with NPACI Rocks 4.1. This was solved by building PVFS2 against a newly built Berkeley DB (version 4.3.29) [73]. Performance tuning of PVFS2 [68] is done by:

(1) Mounting the ext3 filesystem with the `noatime` and `data=writeback` options in the ‘`/etc/fstab`’ file.

(2) Providing the `--enable-epoll` option to the configure script at compile time in order to provide better performance for TCP/IP sockets.

(3) Providing the `--enable-fast` option to the configure script at compile time in order to disable many of the debugging routines.

(4) Setting `TroveSyncData` option to `no` in the ‘`/etc/pvfs2-fs.conf`’ file in order to disable the server from issuing a sync call after each data update (The sync call forces all unwritten data to be written to disk). This is analogous to

mounting the NFS with the `async` option. We note here that setting this option to no can lead to data loss if an I/O server is terminated unexpectedly.

We partitioned our test cluster so as the first compute node acts as the metadata server while the remaining compute nodes act as I/O nodes. PVFS2 aggregates the storage space created on the servers into one globally accessible namespace that the clients mount. The underlying local filesystem is ext3.

Lustre is an open source, scalable, secure, robust, and highly-available parallel filesystem for Linux clusters [74]. Lustre system consists of four types of subsystems: (1) clients that access the filesystem, (2) object storage target (OST) that handles file data and enforce security for client access, (3) metadata target (MDT) that owns and manages information about the files in the Lustre filesystem (e.g., namespace operations such as file creation, which file is located on which OST, how the blocks of files are striped across the OSTs, date and time the file was modified, etc) but it does not contain any file data, and (4) MGS, which is a management configuration server that compiles configuration information about all Lustre filesystems running at a site. Client nodes mount the Lustre filesystem over the network and access files with POSIX filesystem semantics. Lustre also supports parallel I/O libraries (e.g., MPI-IO) but does not require them. Each client mounts Lustre, uses the MDT to access metadata, and performs file I/O directly through the OSTs. Each OST contributes to the total capacity and the aggregate throughput. Lustre can use any physical device that can be formatted as an ext3 filesystem.

We tested Lustre version 1.5.95. This version of Lustre does not require the Linux kernel of the client node to be patched. However, Lustre kernel patches need to be applied to the source of the kernel running in the server node. This can be facilitated by using the Quilt package (a patch management tool) provided by Cluster

File Systems (CFS). CFS also provides pre-patched, Lustre-enabled Linux kernels as well as Lustre RPMs. These RPMs are only available for SMP machines. Hence, for our test system that comprises only uniprocessor nodes, we had to build the Linux kernel after applying the Lustre kernel patches using Quilt, and then built Lustre from the available source code. We partitioned our test cluster so as the first compute node acts as the MDT/MGS while the remaining compute nodes act as OSTs. A single partition in each compute node was allocated for use by Lustre filesystem.

The Lustre filesystem provides several `/proc` filesystem variables that control aspects of Lustre performance and provide information. Lustre will always attempt to pack an optimal amount of data into each I/O RPC (remote procedure call) and will attempt to keep a consistent number of issued RPCs in progress at a time. Lustre offers several tuning variables to adjust behavior according to network conditions and cluster size [75,76]. The files related to tuning the RPC stream are: (1) `/proc/fs/lustre/osc/<object name>/max_dirty_mb` that controls how many megabytes of dirty data can be written and queued up in the OSC (object storage client), (2) `/proc/fs/lustre/osc/<object name>/cur_dirty_bytes` which is a read-only value that returns the current amount of bytes written and cached on this OSC, (3) `/proc/fs/lustre/osc/<object name>/max_pages_per_rpc` that represents the maximum number of pages that will undergo I/O in a single RPC to the OST, and (4) `/proc/fs/lustre/osc/<object name>/max_rpcs_in_flight` that represents the maximum number of concurrent RPCs that the OSC will issue at a time to its OST. We chose to change the `/proc/fs/lustre/osc/<object name>/max_dirty_mb` value from the default of 32 to 128, and the `/proc/fs/lustre/osc/<object name>/max_rpcs_in_flight` value from the default of 8 to 32. These can be changed while the server is running using the "`lctl`" utility.

The `/proc/sys/portals/debug` can be used to delimit the debugging information written out to the kernel debug logs. Running the command "`echo 0 > /proc/sys/portals/debug`" for all clients and servers turns off the Lustre debugging completely and enhances the performance [77].

Lustre stores files in one or more objects on OSTs. When a file is comprised of more than one object, Lustre will stripe the file data across them in a round-robin fashion. Lustre can be configured with a custom stripe size which determines the amount of data from a particular file that is written to each OST. The number of OSTs to stripe a single file across can also be set to a single OST, all OSTs, or any number in between. The choice depends on the application that utilizes the Lustre filesystem [75]. The changes can be done using the "`lfs`" tool.

Our system uses MPICH version 1.2.7p1 with ROMIO version 2005-06-09. It is compiled with support for NFS, PVFS2, and general support for all UNIX like filesystems (UFS). ROMIO's 'UFS' works fine with Lustre. We ran the 'common_file' benchmark for 7 processes. Each MPI process has its own data block in a common file. The file size is set to 4 GB and the size of the I/O-request is set to 64 KB. The I/O-request size of 64 KB is chosen as to resemble that for the NWChem program [78,79]. Both POSIX I/O and MPI-IO interfaces were tested. Access patterns tested are 'write', 'read/write', and 'random read/write'. All measurements used the collective and noncollective blocking (synchronous) MPI-IO access methods 'individual file pointer' (i.e., allowing every process to work on its own part of the file thus having its own file pointer) and 'explicit offset' (i.e., a process specifies the position of any operation within the file).

As shown in Figure 1.7, Lustre (with striping across all OSTs) outperformed NFS and PVFS2 using the POSIX I/O interface. For the MPI-IO interface, Lustre provided the best bandwidth for noncollective operations, whereas PVFS2 slightly outperformed Lustre for collective operations.

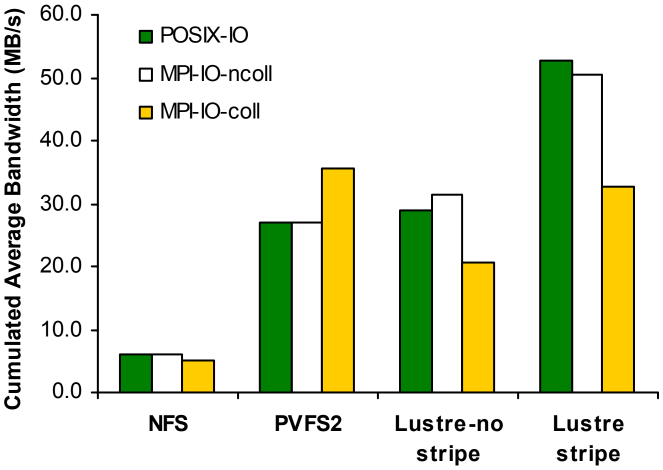

Figure 1.7: Bandwidths for NFS, PVFS2, and Lustre using the POSIX IO and MPI-IO interfaces. Shown is the average of access patterns 'write', 'read/write', and 'random read/write'. In the case of MPI-IO, this includes access methods 'individual file pointer' and 'explicit offset'.

We tested both direct and semi-direct algorithms for the HF and MP2 computational chemistry methods as implemented in the NWChem program using the three parallel filesystems (NFS, PVFS2, and Lustre) as well as the local filesystem (Table 1.4). From Table 1.4 we observe that (1) Lustre with striping the file across all available OSTs outperforms Lustre without striping, (2) the effect of striping size for Lustre is very minimal, (3) Lustre outperforms NFS and PVFS2 at all file size ranges, (4) the best performance for these methods is achieved when writing/reading the integral file to local filesystem (a parallel filesystem is still needed for shared files such as checkpointing files), (5) Lustre achieves a great percentage of the local filesystem (> 90%) and its performance is consistent at all file size ranges, and (6) PVFS2 performance is poor compared to NFS. However, one can see that PVFS2 is matching up with NFS as the file size gets larger and closer to the size of the available memory on the node (Linux allocates all free memory for disk cache). The reason for this is that PVFS2 does not cache file data on the client node and is not affected by any buffering/caching effects since data is always transferred over the network [64]. We note here that NFS is not recommended for writing such large files because of the increased overhead on the frontend node which may affect some running programs (e.g., the Ganglia monitoring tool). For our test cluster, the direct algorithm (i.e., recomputing the integrals for each iteration) outperforms the semi-direct algorithm for runs that involve writing/reading an integral file larger than 100 MB per each compute node (Table 1.4).

Table 1.4: Wall times (in seconds) for NWChem direct and semi-direct algorithms using different filesystems.

Method	Filesystem				
	NFS	PVFS2	Lustre-no stripe	Lustre-stripe	Local$
HF-arecoline-6-311G (100 MB)‡	395 [60]	-	-	243 [97]	235
dHF-arecoline-6-311G (100 MB)	-	-	-	258	-
HF-arecoline-6-311G* (275 MB)	-	-	-	469	-
dHF-arecoline-6-311G* (275 MB)	-	-	-	400	-
HF-arecoline-6-311G** (600 MB)	2570 [26]	4042 [17]	902	716§ [94]	673
dHF-arecoline-6-311G** (600 MB)	-	-	-	571	-
HF-atropine-6-31G* (1.2 GB)	5364 [21]	6655 [17]	-	1216 [91]	1108
dHF-atropine-6-31G* (1.2 GB)	-	-	-	853	-
HF-morphine-6-31G* (1.6 GB)	4509 [19]	4639 [19]	-	936 [93]	872
dHF-morphine-6-31G* (1.6 GB)	-	-	-	653	-
HF-morphine-6-31G** (2.2 GB)	-	-	1666	1200 [93]	1120
dHF-morphine-6-31G** (2.2 GB)	-	-	-	807	799
MP2-propane-6-311G** (8 MB)	427 [83]	-	-	386 [92]	356
dMP2-propane-6-311G**	520	1865	701	460	415

$ Files that need to be shared (e.g., the runtime database file that is similar to the GAMESS-UK dumpfile and is needed for checkpointing) were read from/written to Lustre filesystem. ‡ Integral file size per compute node. § Three stripe sizes were compared: 0.5, 1, and 2 MB (no difference was observed). [ ] Percentage of raw local filesystem. Note: the 'd' before the method name denotes 'direct'.

1.4 Conclusion

A critical issue in the design of computer cluster is the understanding of the applications that it will be supporting. The application's requirements for computing power, memory, I/O and communication must be balanced. Benchmarks, though not real applications, capture essential measurable characteristics that reflect real applications. In the current work, a commodity-class Linux cluster was built and tested in order to achieve better computing speed and performance. The performance analysis of the CPU, memory, disk and network was achieved using open source benchmarks. Various TCP/MPICH parameters were optimized and a maximum bandwidth of 666 Mbps for MPICH was achieved. The GA put/get operations outperformed the corresponding MPICH send/receive operations in terms of both bandwidth and latency. Three different parallel filesystems (NFS, PVFS2, and Lustre) were examined. In most cases, Lustre provided the best performance achieving greater than 90% of the local filesystem read/write bandwidths.

1.5 References

1. J.D. Sloan, High Performance Linux Clusters with OSCAR, Rocks, openMosix, and MPI, O'Reilly, Sebastopol, CA, 2005.
2. Cluster Computing, Cisco Systems Inc., 2004. http://www.cisco.com/-application/pdf/en/us/guest/netsol/ns500/c654/cdccont_0900aecd80281846.pdf
3. R.W. Lucke, Building Clustered Linux Systems, Prentice Hall PTR, Upper Saddle River, NJ, 2005.
4. E. Imamagić, D.D. Žagar, Cluster distributions review, CARNet Users' Conference 2004. http://www.srce.hr/dokumenti/crogrid/radovi/Cluster_Distr-ibutions_Review.pdf
5. http://oscar.openclustergroup.org
6. http://www.rocksclusters.org
7. P.M. Papadopoulos, M.J. Katz, G. Bruno, NPACI Rocks: Tools and techniques for easily deploying manageable Linux clusters, Proceedings of the 2001 IEEE International Conference on Cluster Computing (CLUSTER.01), p. 258-267, IEEE Computer Society Press. http://ieeexplore.ieee.org/iel5/7602/20737/-00959986.pdf?isnumber=&arnumber=959986
8. R. Gupta, Y-C. Fang, M. Hussain, Streamlining Beowulf cluster deployment with NPACI Rocks, Dell Power Solutions, Dell Inc., 2005. http://www.-dell.com/downloads/global/power/ps1q05-20040176-Gupta.pdf

9. Aprà, E.; Windus, T.L.; Straatsma, T.P.; Bylaska, E.J.; de Jong, W.; Hirata, S.; Valiev, M.; Hackler, M.; Pollack, L.; Kowalski, K.; Harrison, R.; Dupuis, M.; Smith, D.M.A; Nieplocha, J.; Tipparaju V.; Krishnan, M.; Auer, A.A.; Brown, E.; Cisneros, G.; Fann, G.; Früchtl, H.; Garza, J.; Hirao, K.; Kendall, R.; Nichols, J.; Tsemekhman, K.; Wolinski, K.; Anchell, J.; Bernholdt, D.; Borowski, P.; Clark, T.; Clerc, D.; Dachsel, H.; Deegan, M.; Dyall, K.; Elwood, D.; Glendening, E.; Gutowski, M.; Hess, A.; Jaffe, J.; Johnson, B.; Ju, J.; Kobayashi, R.; Kutteh, R.; Lin, Z.; Littlefield, R.; Long, X.; Meng, B.; Nakajima, T.; Niu, S.; Rosing, M.; Sandrone, G.; Stave, M.; Taylor, H.; Thomas, G.; van Lenthe, J.; Wong, A.; Zhang, Z.; NWChem, A Computational Chemistry Package for Parallel Computers, Version 4.7 (2005), Pacific Northwest National Laboratory, Richland, Washington 99352-0999, USA.
High Performance Computational Chemistry: an Overview of NWChem a Distributed Parallel Application, Kendall, R.A.; Aprà, E.; Bernholdt, D.E.; Bylaska, E.J.; Dupuis, M.; Fann, G.I.; Harrison, R.J.; Ju, J.; Nichols, J.A.; Nieplocha, J.; Straatsma, T.P.;Windus, T.L.;Wong, A.T. Computer Phys. Comm., 2000, 128, 260–283.
10. R.A. Kendall, E. Aprà, D.E. Bernholdt, E.J. Bylaska, M. Dupuis, G.I. Fann, R.J. Harrison, J. Ju, J.A. Nichols, J. Nieplocha, T.P. Straatsma, T.L. Windus, A.T. Wong, High performance computational chemistry: An overview of NWChem a distributed parallel application, Computer Physics Communications 128 (2000) 260-283.
11. GAMESS-UK is a package of ab initio programs. See: "http://www.cfs.dl.ac.uk/gamess-uk/index.shtml", M.F. Guest, I. J. Bush, H.J.J. van Dam, P. Sherwood, J.M.H. Thomas, J.H. van Lenthe, R.W.A Havenith, J. Kendrick, "The GAMESS-UK electronic structure package: algorithms, developments and applications", Molecular Physics, Vol. 103, No. 6-8, 20 March-20 April 2005, 719-747.
12. J.J. Dongarra , P. Luszczek , A. Petitet, The LINPACK benchmark: Past, present and future, Concurrency and Computation: Practice and Experience 15 (2003) 803-820.
13. M. Hussain, R. Radhakrishnan, K. Chadalavada, Understanding the scalability of NWChem in HPC environments, Dell Power Solutions, Dell Inc., 2005. http-://www.dell.com/downloads/global/power/ps1q05-20040136-Hussain.pdf
14. http://www.netlib.org/benchmark/hpl
15. http://math-atlas.sourceforge.net
16. http://www.tacc.utexas.edu/~kgoto
17. http://www.intel.com/cd/software/products/asmo-na/eng/307757.htm
18. http://icl.cs.utk.edu/hpcc
19. http://www.netlib.org/benchmark/hpl/faqs.html
20. S.N. Kandadai, Tuning tips for HPL on IBM xSeries Linux clusters, IBM Redbooks Paper, IBM Corp., 2003. http://www.redbooks.ibm.com/redpapers/-pdfs/redp3722.pdf
21. P.J. Mucci, Memory bandwidth and the performance of scientific applications: A study of the AMD Opteron™ processor, Advanced Micro Devices. http-://whitepapers.techrepublic.com.com/whitepaper.aspx?docid=117213
22. J. Landman, Performance comparison of AMD multi-core systems and single-core systems on chemistry and informatics applications, Scalable Informatics. http://eugen.leitl.org/Dual_Core_Performance.pdf
23. http://www.cs.virginia.edu/stream

24. J.S. Kim, D.J. Lilja, Characterization of communication patterns in message-passing parallel scientific application programs, Proceedings of the Workshop on Communication, Architecture, and Applications for Network-based Parallel Computing, International Symposium on High Performance Computer Architecture 1998, p. 202-216. http://www.arctic.umn.edu/papers/comm-char.pdf
25. Cluster Computing White Paper, M. Baker (Ed.), 2000. http://arxiv.org/ftp/cs/-papers/0004/0004014.pdf
26. D. Turner, X. Chen, Protocol-dependent message-passing performance on Linux clusters, Proceedings of the IEEE International Conference on Cluster Computing 2002 (CLUSTER'02), p. 187-194, IEEE Computer Society Press. http://ieeexplore.ieee.org/iel5/8231/25385/01137746.pdf?isnumber=&arnumber=1137746
27. K.N. Nguyen, T.T. Le, Evaluation and comparison performance of various MPI implementations on an OSCAR Linux cluster, Proceedings of the International Conference on Information Technology: Computers and Communications 2003 (ITCC.03), p. 310-314, IEEE Computer Society Press. http://ieeexplore.ieee.-org/iel5/8532/26947/01197546.pdf
28. W-c. Feng, J.G. Hurwitz, Analyzing MPI performance over 10-Gigabit Ethernet, Journal of Parallel and Distributed Computing 65 (2005) 1253-1260.
29. P.A. Farrell, H. Ong, Communication performance over a gigabit Ethernet network, Proceedings of the 19th IEEE International Performance, Computing, and Communications Conference 2000 (IPCCC '00), p. 181-189. http://-ieeexplore.ieee.org/iel5/6712/17967/00830317.pdf
30. P.A. Farrell, H. Ong, Factors involved in the performance of computations on Beowulf clusters, Electronic Transactions on Numerical Analysis 15 (2003) 211-224.
31. W-c. Feng, J.G. Hurwitz, H. Newman, S. Ravot, R. Les Cottrell, O. Martin, F. Coccetti, C. Jin, X.D. Wei, S. Low, Optimizing 10-Gigabit Ethernet for networks of workstations, clusters, and grids: A case study, Proceedings of the ACM/IEEE SC2003 Conference 2003 (SC'03). http://ieeexplore.ieee.org/iel5/-10619/33528/01592953.pdf?isnumber=&arnumber=1592953
32. W. Feng, P. Balaji, C. Baron, L.N. Bhuyan, D.K. Panda, Performance characterization of a 10-Gigabit Ethernet TOE, Proceedings of the 13th Symposium on High Performance Interconnects 2005 (HOTI'05), p. 58- 63, IEEE Computer Society Press. http://ieeexplore.ieee.org/iel5/10367/32970/-01544578.pdf?isnumber=&arnumber=1544578
33. J. Hurwitz, W-c. Feng, Initial end-to-end performance evaluation of 10-Gigabit Ethernet, Proceedings of the 11th Symposium on High Performance Interconnects 2003 (HOTI'03), p. 116- 121, IEEE Computer Society Press. http://ieeexplore.ieee.org/iel5/8712/27585/01231487.pdf?isnumber=&arnumber=1231487
34. S. Majumder, S. Rixner, Comparing Ethernet and Myrinet for MPI Communication, Proceedings of the Workshop on Languages, Compilers, and Run-time Support for Scalable Systems 2004 (LCR). http://www.cs.rice.edu/-CS/Architecture/docs/majumder-lcr04.pdf
35. P.J. Sokolowski, D. Grosu, Performance considerations for network switch fabrics on Linux clusters, Proceedings of the 16th IASTED International Conference on Parallel and Distributed Computing and Systems 2004 (PDCS

2004), p. 150-156. https://www.grid.wayne.edu/WSU_Campus_Grid/Publications/papers/IASTED_PDCS_2004_Final.pdf

36. Linux* Base Driver for the Intel® PRO/1000 Family of Adapters, 2005. http://-downloadmirror.intel.com/df-support/4833/ENG/e1000.txt
37. E. Ciliendo, Tuning Red Hat Enterprise Linux on IBM xSeries servers, IBM Redpaper, IBM Corp., 2005. http://www.redbooks.ibm.com/redpapers/pdfs/-redp3861.pdf
38. How to Achieve Gigabit Speeds with Linux, http://datatag.web.cern.ch/-datatag/howto/tcp.html
39. Enabling High Performance Data Transfers, http://ncne.nlanr.net/networking/-projects/tcptune
40. Linux TCP Tuning. http://www-didc.lbl.gov/TCP-tuning/linux.html
41. S. Ubik, P. Cimbal, Achieving reliable high performance in LFNs, Terena Networking Conference 2003 (TNC). http://www.terena.nl/events/archive/-tnc2003/programme/papers/p4b2.pdf
42. M.T. Jones, Boost Socket Performance on Linux, 2006. http://www-128.ibm.com/developerworks/linux/library/l-hisock.html
43. http://www.scl.ameslab.gov/netpipe
44. R. Gupta, M. Kashyap, Y-C. Fang, S. Iqbal, Considering middleware options in high-performance computing clusters, Dell Power Solutions, Dell Inc., 2005. http://www.dell.com/downloads/global/power/ps1q05-20040177-Gupta-OE.pdf
45. http://www-unix.mcs.anl.gov/mpi/mpich
46. X. He, Installing and using MPICH, MPICH-GM, and MPICH-MX on Linux systems, IBM Redbooks Paper, IBM Corp., 2006. http://www.redbooks.ibm.-com/redpapers/pdfs/redp4183.pdf
47. http://www.emsl.pnl.gov/docs/global
48. J. Nieplocha, B. Carpenter, ARMCI: A portable remote memory copy library for distributed array libraries and compiler run-time systems, Proceedings of the 3rd Workshop on Runtime Systems for Parallel Programming 1999 (RTSPP). http://ipdps.cc.gatech.edu/1999/rtspp/nieploch.pdf
49. J. Nieplocha, J. Ju, T. P. Straatsma, A multiprotocol communication support for the global address space programming model on the IBM SP, In A. Bode et al (Eds.): Proceedings of the 6th International Euro-Par Conference on Parallel Processing 2000, Lecture Notes in Computer Science 1900 (2000) 718-728. http://-www.springerlink.com/content/jkyfwjplmwrrmwaj/fulltext.pdf
50. J. Nieplocha, J. Ju, E. Apra, One-sided communication on the Myrinet-based SMP clusters using the GM message-passing library, Proceedings of the 15th International Parallel and Distributed Processing Symposium 2001 (IPDPS'01), p. 1707-1716, IEEE Computer Society Press. http://ieeexplore.ieee.org/iel5/-7373/20001/00925158.pdf
51. J. Nieplocha, V. Tipparaju, A. Saify, D.K. Panda, Protocols and strategies for optimizing performance of remote memory operations on clusters, Proceedings of the 16th International Parallel and Distributed Processing Symposium 2002 (IPDPS'02), p. 164-173, IEEE Computer Society Press. http://ieeexplore.ieee.-org/iel5/7926/21854/01016563.pdf
52. V. Tipparaju, G. Santhanaraman, J. Nieplocha, D.K. Panda, Host-assisted zero-copy remote memory access communication on InfiniBand, Proceedings of the 18th International Parallel and Distributed Processing Symposium 2004

(IPDPS'04), p. 31-40, IEEE Computer Society Press. http://ieeexplore.ieee.org/iel5/9132/28950/01302943.pdf?isnumber=&arnumber=1302943

53. M. Krishnan, J. Nieplocha, Optimizing performance on Linux clusters using advanced communication protocols: How 10+ Teraflops was achieved on a 8.6 Teraflops Linpack-rated Linux cluster, Proceedings of the 6th International Conference on Linux Clusters, The HPC Revolution 2005. http://www.linuxclu-stersinstitute.org/Linux-HPC-Revolution/Archive/PDF05/24-Krishnan_M.pdf
54. J. Nieplocha, R. Harrison, R. Littlefield, Global Arrays: A portable "shared-memory" programming model for distributed memory computers, Proceedings of Supercomputing'94, p. 340–349, IEEE Computer Society Press. http://www.emsl.pnl.gov/docs/global/papers/super94.pdf
55. J. Nieplocha, R. J. Harrison, R. J. Littlefield, Global Arrays: A nonuniform memory access programming model for high-performance computers, The Journal of Supercomputing 10 (1996) 169-189.
56. T. Steinke, Tools for parallel quantum chemistry software, Modern Methods and Algorithms of Quantum Chemistry, Proceedings, Second Edition, J. Grotendorst (Ed.), John von Neumann Institute for Computing, Jülich, NIC Series, Vol. 3, p. 67-96, 2000. http://www.fz-juelich.de/nic-series/Volume3/steinke.pdf
57. J. Nieplocha, R.J. Harrison, M.K. Kumar, B. Palmer, V. Tipparaju, H. Trease, Combining distributed and shared memory models: Approach and evolution of the Global Arrays Toolkit. http://www.emsl.pnl.gov/docs/global/papers/jarek.pdf
58. C. S. Guiang, A. Purkayastha, K. F. Milfeld, Remote memory operations on Linux clusters: Expressiveness and efficiency of current implementations. http://www.tacc.utexas.edu/publications/remotememoryoperations.pdf
59. http://www.intel.com/cd/software/products/asmo-na/eng/219848.htm
60. J. Nieplocha, I. Foster, R.A. Kendall, ChemIO: High performance parallel I/O for computational chemistry applications, International Journal of High Performance Computing Applications 12 (1998) 345-363.
61. K.A. Hawick, D.A. Grove, P.D. Coddington, M.A. Buntine, Commodity cluster computing for computational chemistry, DHPC Technical Report 2000 (DHPC-073). http://www.dhpc.adelaide.edu.au/reports/073/html/
62. R. Thakur, E. Lusk, W. Gropp, I/O in parallel applications: The weakest link, The International Journal of High Performance Computing Applications 12 (1998) 389-395.
63. C. Dumontier, O. Hess, F. Thomas, Building an HPC cluster with Linux, pSeries, Myrinet, and various open source software, IBM Redbooks Paper, IBM Corp., 2004. http://www.redbooks.ibm.com/redpapers/pdfs/redp3756.pdf
64. M. Vilayannur, R.B. Ross, P.H. Carns, R. Thakur, A. Sivasubramaniam, M. Kandemir, On the performance of the POSIX I/O interface to PVFS, Proceedings of the 12th Euromicro Conference on Parallel, Distributed and Network-Based Processing 2004 (EUROMICRO-PDP'04), p. 332-339, IEEE Computer Society Press. http://ieeexplore.ieee.org/iel5/8971/28471/01271463.pdf?isnumber=&arnumber=1271463
65. A. Ching, K. Coloma, J. Li, A. Choudhary, W-k. Liao, High-performance techniques for parallel I/O, In Handbook of Parallel Computing: Models, Algorithms, and Applications, CRC Press, 2007. http://www.ece.northwestern.edu/~aching/paper_download/2007handbook.pdf

66. R. Thakur, W. Gropp, E. Lusk, On implementing MPI-IO portably and with high performance, Proceedings of the 6th Workshop on I/O in Parallel and Distributed Systems 1999, p. 23-32, ACM Press. http://citeseer.ist.psu.edu/-cache/papers/cs/4162/ftp:zSzzSzinfo.mcs.anl.govzSzpubzSztech_reportszSzreportszSzP732.pdf/thakur99implementing.pdf
67. http://www.iozone.org/
68. T. Leggett, R. Latham, R. Ross, TeraGrid PVFS2 best practices, TG-11 Informational Data Working Group 2006. http://www.teragridforum.org/media-wiki/index.php?title=TG-11
69. http://www.ipacs-benchmark.org/index.php?s=download&unterseite=bench
70. M. Krietemeyer, D. Versick, D. Tavangarian, The PRIOmark parallel I/O benchmark, International Conference on Parallel and Distributed Computing and Networks 2005. http://www.ipacs-benchmark.org/download/marketing/-IPACS_PRIOmark_0205.pdf
71. M. Krietemeyer, H. Kopp, D. Versick, D. Tavangarian, Environment for I/O performance measurement of distributed and local secondary storage, Proceedings of the 2005 International Conference on Parallel Processing Workshops (ICPPW'05), p. 501–508, IEEE Computer Society Press. http-://ieeexplore.ieee.org/iel5/9965/32020/01488735.pdf
72. http://www.pvfs.org
73. http://sleepycat2.inetu.net/products/bdb.html
74. http://www.lustre.org
75. Lustre Manual. https://mail.clusterfs.com/wikis/attachments/LustreManual.html
76. https://mail.clusterfs.com/wikis/lustre/MountConf
77. https://mail.clusterfs.com/wikis/lustre/LustreDebugging
78. M.A. Kandaswamy, M.T. Kandemir, A.N. Choudhary, D.E. Bernholdt, Optimization and evaluation of Hartree-Fock application's I/O with PASSION, Proceedings of the ACM/IEEE SC97 Conference 1997 (SC'97), IEEE Computer Society Press. http://ieeexplore.ieee.org/iel5/10614/33523/-01592612.pdf?arnumber=1592612
79. E. Smirni, D.A. Reed, Workload characterization of input/output intensive parallel applications, Proceedings of the 9th International Conference on Modeling Techniques and Tools for Computer Performance Evaluation 1997. http://citeseer.ist.psu.edu/cache/papers/cs/577/http:zSzzSzvibes.cs.uiuc.eduzSzPublicationszSzPaperszSzTools97.pdf/reed97workload.pdf

2

Enantioselective Synthesis and Theoretical Backgrounds

In this chapter, an introduction to enantioselective synthesis is first provided. Quantum mechanical methods including density functional theory are then briefly introduced. Description of the ONIOM method is also provided.

2.1 Enantioselective Synthesis

2.1.1 Stereochemistry and stereoisomerism

Stereochemistry is concerned with the three-dimensional aspects of molecules and provided the basis for understanding the relationship between structure and reactivity. Isomers are molecules having the same molecular formula but with different connectivity between the atoms (constitutional (structural) isomers) or arrangement of atoms in space (stereoisomers) [1].

A chiral molecule is non-superimposable on its mirror image and has the ability to rotate the plane of polarized light while an achiral one does not possess such properties [2]. Another practical but not always accurate method to determine whether a molecule is chiral or achiral is the evaluation of its symmetry elements (axis of symmetry (C_n), plane of symmetry (σ), center of symmetry (i), and axis of rotation-reflection (S_n)). A molecule with an S_n, i or σ symmetry elements is achiral. A molecule, however, can have a symmetry element and be chiral if a C_n axis is present but does not have an S_n axis [3,4].

The most common reason for chirality in organic molecules is the existence of a tetrahedral sp^3-hybridized carbon atom connected to four different substituents (commonly referred to as chiral or asymmetric carbon). The presence of such carbon atom is not a necessary condition for chirality. For example, the biphenyls **1** and **2** are chiral molecules with no tetrahedral carbon bonded to four different groups whereas molecules **3** and **4** are achiral even though they possess tetrahedral carbons having four distinct groups (Figure 2.1) [3,5]. Hence, the term ‘stereogenic carbon’ is introduced to eliminate the confusion and, in a sense, is broader than the term ‘chiral carbon’ since it implies nothing about the chirality of the molecule [1]. An atom is considered to be a ‘stereogenic atom’ if the interchange of two groups connected to it produces a stereoisomer. This new stereoisomer can be an enantiomer or a diastereomer of the original molecule [1,3].

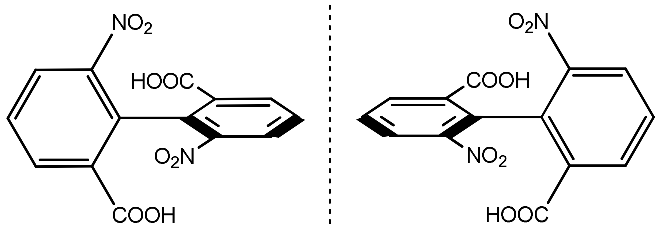

1 **2**

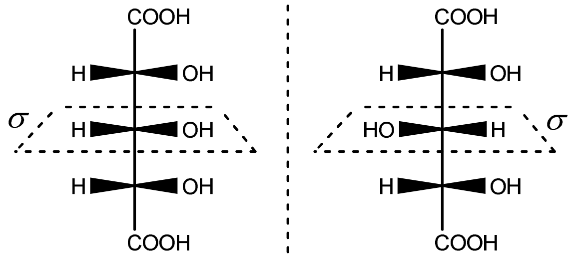

3 **4**

*Figure 2.1: Chiral molecules with no asymmetric carbon atoms (**1** and **2**) vs. achiral molecules with asymmetric carbon atoms (**3** and **4**).*

Conformers are stereoisomers characterized by different spatial orientation of atoms as a result of rotation around single bonds while rotamers are conformers differing by rotation around only one single bond. Enantiomers are non-superimposable mirror image stereoisomers with identical physical and chemical properties except for the direction in which they rotate plane-polarized light. In addition, the rates at which they react with other chiral molecules are different [2,5]. The difference in these rates can be negligible or can be so large that one enantiomer conveniently undergoes a reaction while the other does not react at all. This is one reason why many molecules are biologically active whereas their enantiomers are not [2]. However, enantiomers react at the same rate with achiral molecules except in the presence of optically active catalyst or solvent (i.e. a chiral environment) though in most cases the difference is too small to be measured [2]. Diastereomers, on the other hand, are non-superimposable, non-mirror-image stereoisomers differing in all physical, chemical and spectral properties, and are distinguishable under any environment (chiral or achiral).

The stereochemical configuration of a stereogenic carbon atom can be determined using the Cahn-Ingold-Prelog system in which the four groups bonded to the stereogenic carbon are ranked according to a set of priority rules as follows: (1) the atom(s) with the highest atomic number is (are) given the highest priority, (2) in the case when more than one atom in the different groups are the same, the atomic number of the next atom determines the priority, (3) double and triple bonds are counted as two or three single bonds, respectively, and (4) for isotopes, the one with the highest atomic mass is assigned higher priority. The molecule is then oriented with the lowest priority group pointing away from the viewer and the stereogenic carbon is closer. The three remaining substituents are then ranked from highest to lowest priority. The stereogenic carbon is in the *R* configuration if the path traced from the highest group to the lowest group is clockwise or in the *S* configuration if it is counterclockwise (Figure 2.2). Enantiomers possess opposite configuration at all stereogenic carbons while diastereomers have the same configuration in at least one stereogenic carbon but opposite configurations at the others. A molecule with n stereogenic carbons can have up to 2^n stereoisomers (2^{n-1} pairs of enantiomers). In some cases, the actual number is less than 2^n due to the existence of meso molecules (i.e. molecules having stereogenic carbons but achiral owing to the presence of a plane of symmetry (e.g., **3** and **4**)).

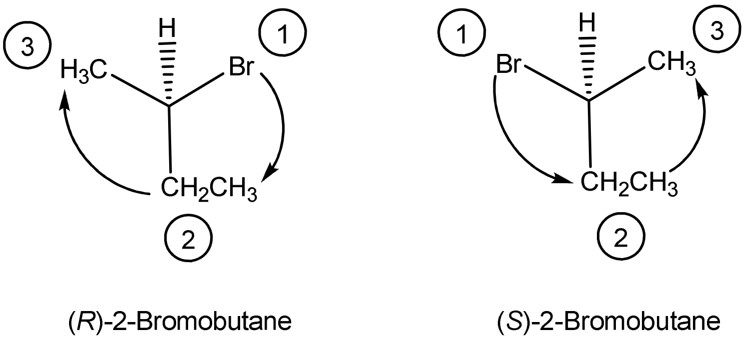

Figure 2.2: R vs. S stereochemical assignments.

2.1.2 Selective synthesis of enantiomers

The two major forms of selectivity in chemistry are substrate selectivity, in which a reagent transforms different substrates under the same conditions to different products at different rates, and product selectivity where one of the reaction products is formed preferentially [6]. When the products are diastereomers or enantiomers the terms diastereoselectivity and enantioselectivity are used, respectively. The most commonly used measure of the extent of enantioselectivity is the enantiomeric excess (*ee*) defined as

$$ee = |F_R - F_S| \tag{2-1}$$

where F_R and F_S are the mole fractions of the R and S enantiomers, respectively and

$$F_R + F_S = 1. \tag{2-2}$$

An *ee* value of one corresponds to an enantiomerically pure molecule and a reaction that has such value is said to be enantiospecific. On the other hand, an *ee* value of zero corresponds to a 50:50 mixture of enantiomers (i.e. a racemic mixture).

The building-blocks of biological systems (carbohydrates, α-amino acids and nucleotides) are chiral and present in enantiomerically pure forms. Thus, molecules synthesized by humankind to interact with biological systems must be produced in enantiomerically pure (or enriched) forms. For instance, (*S*)-propranolol **5** is used to treat heart and circularity conditions whereas the (*R*)-enantiomer **6** acts as a contraceptive [7].

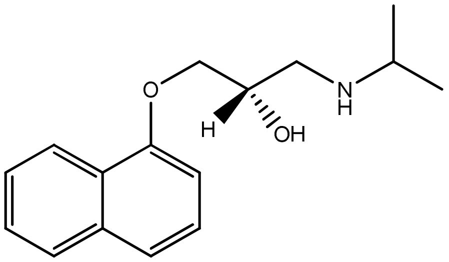

5

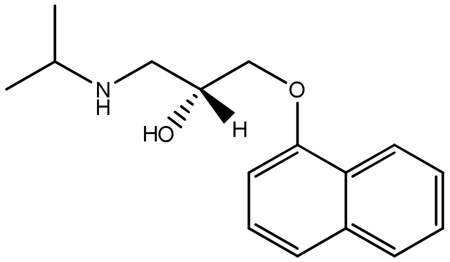

6

The main approaches to enantioselective syntheses include [8,9]: (1) chiral starting materials of natural origin, (2) chiral auxiliaries, (3) chiral reagents, and (4) chiral catalysts. The latter two methods have the advantages that the choice of starting materials are far wider since they need not come from the natural chiral pool as well as the elimination of the extra two steps of attaching and removing the chiral auxiliary [9].

2.1.3 Enantioselective organocatalysis

In general, three main classes of chiral catalysts have been utilized in enantioselective synthesis. They are: (1) transition-metal complexes with chiral ligands, (2) biocatalysts (enzymes), and (3) chiral organocatalysts [10-13]. Organocatalysts are low-molecular-weight organic molecules that do not contain metals. Compared to organometallic and enzymatic catalysts, they have the advantages of being readily available, less expensive, more stable, and, due to their insensitivity towards moisture and oxygen, can be applied in less-demanding reaction conditions [10,11]. The absence of metals in this class of catalysts renders it attractive for the synthesis of pharmaceutical and agrochemical products that do not tolerate metal contamination [10,11]. Moreover, organocatalysts can often be immobilized on solid supports and be reused more easily than organometallic and biocatalysts [10,11]. Consequently, the last few years have seen a substantial and rapid growth in the field of enantioselective organocatalysis. Some typical examples of chiral organocatalysts are shown in Scheme 2.1.

Organocatalysis can be broadly classified into two main groups; covalent and non-covalent organocatalysis. The majority of organocatalytic reactions proceeds through the formation of covalent catalyst–substrate adduct that can take place by single step Lewis-acid–Lewis-base interaction or by multi-step reactions where reactive intermediates such as enamine, iminium, and acyl ammonium among others are formed [10,12]. On the other hand, non-covalent catalysis depends on the formation of hydrogen-bonded adducts between substrate and catalyst or on the protonation/deprotonation processes [10,12]. Phase-transfer catalysis (PTC) by organic phase-transfer catalysts belongs to the non-covalent catalysis category [10].

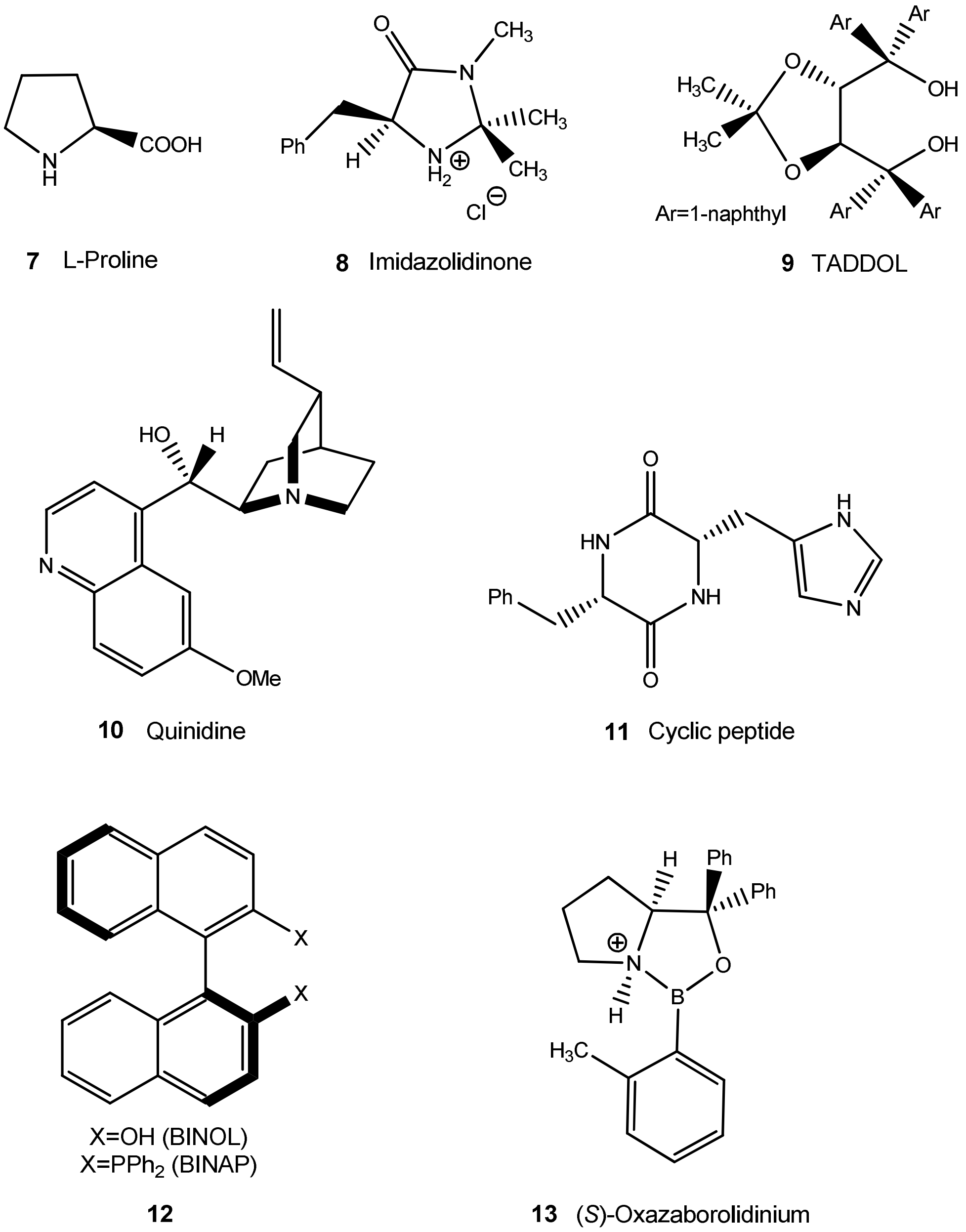

7 L-Proline

8 Imidazolidinone

Ar=1-naphthyl

9 TADDOL

10 Quinidine

11 Cyclic peptide

X=OH (BINOL)
X=PPh_2 (BINAP)

12

13 (*S*)-Oxazaborolidinium

Scheme 2.1: Typical chiral organocatalysts.

2.1.4 Enantioselective organocatalytic Diels-Alder reactions

The Diels-Alder cycloaddition reaction is extremely powerful in organic synthesis as it introduces two carbon-carbon bonds in a single step and is one of few methods for forming cyclic compounds. It had been used, in its original form, as a key step in many important syntheses of complex natural products which converted achiral components to racemic adducts. The conversion of these classical syntheses to the enantioselective versions has been made possible by the introduction of chiral organocatalysts [14-16]. Chiral organocatalysts that have been used in enantioselective Diels-Alder cycloaddition reactions include α-amino acid derivatives such as imidazolidinone **8** [10], C_2-symmetric organocatalysts (e.g., TADDOL **9)** [10], cinchona alkaloids like quinidine **10** [10], and oxazaborolidinium cation **13** [14,16-24].

2.2 Theoretical Backgrounds[1]

2.2.1 The Schrödinger equation and the potential energy surface

Nonrelativistic quantum mechanics in the form of Schrödinger equation has been shown to offer accurate description of the nature of organic molecules in terms of energetics, structures, properties, and reactions. The nonrelativistic time-independent Schrödinger equation for a molecule consisting of N nuclei and n electrons (cf. Figure 2.3) is given by

$$\hat{H}\Psi(\mathbf{R}_1,\mathbf{R}_2,...,\mathbf{R}_N,\mathbf{x}_1,\mathbf{x}_2,...,\mathbf{x}_n) = E\Psi(\mathbf{R}_1,\mathbf{R}_2,...,\mathbf{R}_N,\mathbf{x}_1,\mathbf{x}_2,...,\mathbf{x}_n)\,. \tag{2-3}$$

The $\hat{H}$ is the Hamiltonian operator, Ψ is the wavefunction of all nuclei and electrons, and E is the energy of the molecule. The Hamiltonian operator contains the operations associated with the kinetic and potential energies and can be written in atomic units as

$$\begin{aligned}\hat{H} &= -\frac{1}{2}\sum_{I=1}^{N}\frac{1}{m_I}\nabla_I^2 - \frac{1}{2}\sum_{i=1}^{n}\nabla_i^2 - \sum_{i=1}^{n}\sum_{I=1}^{N}\frac{Z_I}{r_{iI}} + \sum_{I=1}^{N}\sum_{J>I}^{N}\frac{Z_I Z_J}{R_{IJ}} + \sum_{i=1}^{n}\sum_{j>i}^{n}\frac{1}{r_{ij}} \\ &= \hat{T}_\mathrm{n} + \hat{T}_\mathrm{e} + \hat{V}_\mathrm{ne} + \hat{V}_\mathrm{nn} + \hat{V}_\mathrm{ee}\end{aligned} \tag{2-4}$$

Z is the atomic number, m_I is the ratio of the mass of nucleus I to the mass of an electron, and ∇^2 is the Laplacian operator

---

[1] For a detailed description of the theories and methods discussed in this section cf. references 4, 25 – 124.

$$\nabla^2 \equiv \frac{\partial^2}{\partial x^2} + \frac{\partial^2}{\partial y^2} + \frac{\partial^2}{\partial z^2} \,. \tag{2-5}$$

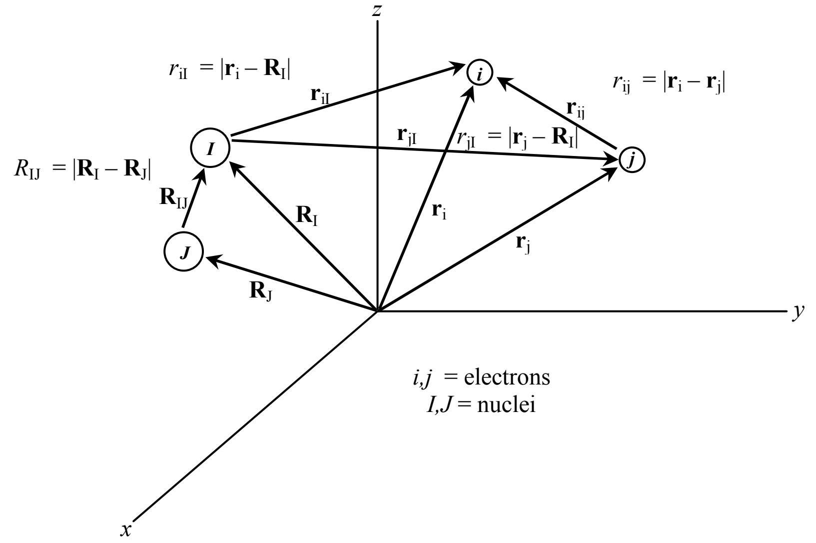

*Figure 2.3: A simple molecular coordinate system showing position vectors (***R** *and* **r***) and their magnitudes (R and r).*

The first and second terms in Eq. 2-4 are the operators for the kinetic energies of the nuclei and the electrons, respectively. The remaining three terms define the potential part of the Hamiltonian and correspond to the electrostatic attraction between nuclei and electrons, and the coulombic repulsions between nuclei and between electrons, respectively. The restriction $J > I$ (or $j > i$) avoids counting the same internuclear (or interelectronic) repulsion twice and avoids terms like $Z_I Z_I / R_{II}$ (or $1/r_{ii}$). The total molecular wavefunction depends on the $3n$ spatial coordinates (**r**) and the n spin coordinates (s) of the electrons (collectively termed as electronic coordinates **x**), and the $3N$ spatial coordinates of the nuclei (**R**).

Because nuclei are much heavier than electrons, and hence move much more slowly, electrons, to a very good approximation, can be considered as moving in the field of fixed nuclei (Born-Oppenheimer approximation). This approximation renders the kinetic energy of the nuclei (the first term in Eq. 2-4) zero (neglected) and causes the potential energy due to internuclear repulsion (the fourth term in Eq. 2-4) to be constant. Thus, the Schrödinger equation (2-3) for a molecule can be decoupled into an electronic and a nuclear equation (Eqs. 2-6 and 2-8, respectively),

$$\hat{H}_{\mathrm{e}}\Psi_{\mathrm{e}}(\mathbf{x};\mathbf{R}) = E_{\mathrm{e}}(\mathbf{R})\Psi_{\mathrm{e}}(\mathbf{x};\mathbf{R}) \tag{2-6}$$

$$(\hat{H}_{\mathrm{e}} + V_{nn})\Psi_{\mathrm{e}}(\mathbf{x};\mathbf{R}) = U(\mathbf{R})\Psi_{\mathrm{e}}(\mathbf{x};\mathbf{R}) \tag{2-7}$$

$$(\hat{T}_{\mathrm{n}} + U(\mathbf{R}))\Psi_{\mathrm{n}}(\mathbf{R}) = E\Psi_{\mathrm{n}}(\mathbf{R})\,. \tag{2-8}$$

$\hat{H}_{\mathrm{e}}$ is the electronic Hamiltonian describing the motion of n electrons in the field of N point charges and is given by

$$\hat{H}_{\mathrm{e}} = -\frac{1}{2}\sum_{i=1}^{n}\nabla_i^2 - \sum_{i=1}^{n}\sum_{I=1}^{N}\frac{Z_I}{r_{iI}} + \sum_{i=1}^{n}\sum_{j>i}^{n}\frac{1}{r_{ij}} \; = \hat{T}_{\mathrm{e}} + \hat{V}_{\mathrm{ne}} + \hat{V}_{\mathrm{ee}}\,. \tag{2-9}$$

The solution of the electronic Schrödinger equation (2-6) involving $\hat{H}_{\mathrm{e}}$ is the electronic wavefunction Ψ_{e} and the electronic energy E_{e}. The electronic wavefunction Ψ_{e} depends explicitly on the electronic coordinates (**x**) and parametrically on the nuclear coordinates (**R**). The energy of the molecule U is then the sum of the electronic energy, E_{e} and the constant due to internuclear repulsion, V_{nn}.

Solving the electronic Schrödinger equation for different sets of fixed nuclear coordinates (**R**) allows the construction of the molecular potential energy surface (PES) [25]. There are $3N$ nuclear coordinates that define the structure of a molecule and the PES is thus a hypersurface with $3N$ dimensionality. Three of these coordinates describe the overall translation of the molecule, and another three (two for linear molecules) describe the overall rotation of the molecule with respect to the three axes. The remaining $3N - 6$ ($3N - 5$ for linear molecules) coordinates describe the internal motion of the nuclei, which for small displacements corresponds to vibrations of the molecule. The PES is important since it helps one understand the structure, properties, reactivities, and spectra of molecules. Points of interest on the PES (cf. Figure 2.4) include minima that correspond to equilibrium structures and first-order saddle points that are often called transition structures (Section 2.2.5).

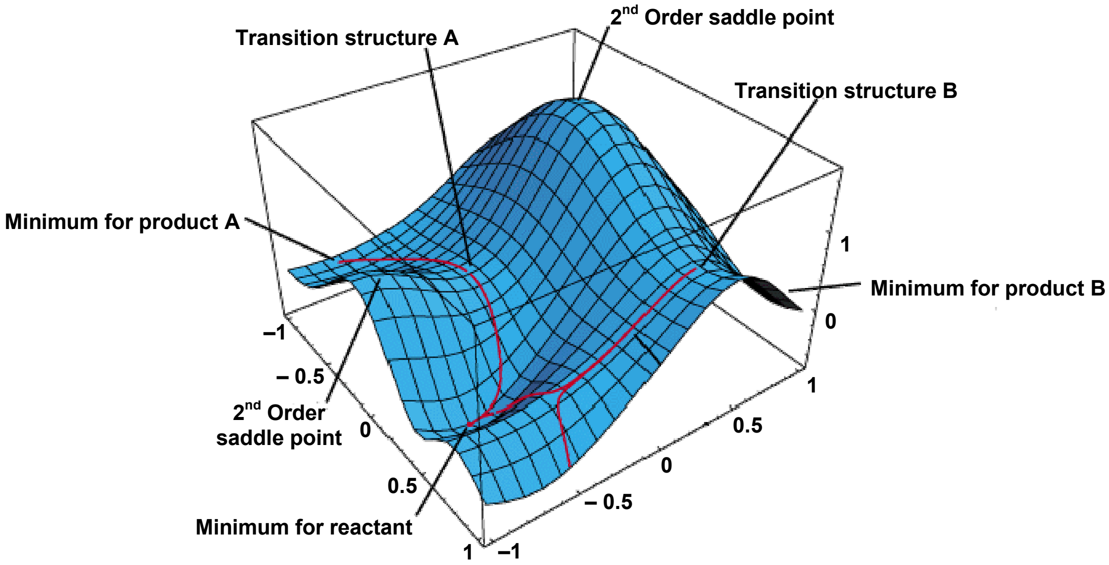

Figure 2.4: A model potential energy surface showing important stationary points. Taken from reference 25.

The solution of the nuclear Schrödinger equation (2-8) describe the translation, rotation and vibration of the molecule where E in Eq. 2-8 is the Born-Oppenheimer approximation to the total energy of (2-3) and is the sum of electronic, translational, rotational and vibrational energies (Section 2.2.5). The related approximation to the total wavefunction of (2-3) is given by

$$\Psi = \Psi_{\mathrm{e}} \Psi_{\mathrm{trans}} \Psi_{\mathrm{rot}} \Psi_{\mathrm{vib}} . \tag{2-10}$$

The main approaches to finding approximate solutions to the electronic Schrödinger equation are *ab initio* (first principles) calculations and semiempirical methods. In contrast to *ab initio* calculations, semiempirical methods use a simplified form for the Hamiltonian and use parameters with values adjusted to fit experimental data. *Ab initio* computational methods include Hartree-Fock (HF) method and post-Hartree-Fock methods such as configuration interaction (CI), coupled cluster (CC), and Møller-Plesset (MP) perturbation theories. The major sources of error in *ab initio* calculations include: (1) the Born-Oppenheimer approximation, (2) the elimination of relativistic effects, (3) the use of incomplete basis set, and (4) the (partial) omission of electron correlation.

2.2.2 The Hartree-Fock method

The presence of the interelectronic potential energy that depends on the electron-electron separations r_{ij} as given by the third term in Eq. 2-9 makes molecular electronic structure calculations extremely complicated.

Hartree introduced the idea that the electronic wavefunction can be written as a product of one-electron wavefunctions (spatial orbitals),

$$\Psi_{\mathrm{HP}}(\mathbf{r}_1,\mathbf{r}_2,\ldots,\mathbf{r}_n) = \psi_1(\mathbf{r}_1)\psi_2(\mathbf{r}_2)\ldots\psi_n(\mathbf{r}_n) \tag{2-11}$$

where Ψ_{HP} is called the 'Hartree-product' wavefunction and

$$\hat{H}\Psi_{\mathrm{HP}} = \left(\sum_{i=1}^{n} \varepsilon_i\right)\Psi_{\mathrm{HP}} \tag{2-12}$$

where ε_{i} is the one-electron orbital energy and the Hamiltonian $\hat{H}$ is the sum of one-electron core Hamiltonians defined by

$$\hat{H}^{\mathrm{core}}(\mathbf{r}_1) = -\frac{1}{2}\nabla_1^2 - \sum_{I=1}^{N} \frac{Z_I}{r_{1I}} . \tag{2-13}$$

The Hamiltonian of Eq. 2-13 does not include interelectronic repulsion term (i.e. the Hamiltonian corresponds to a non-interacting system of electrons). Hartree introduced this term into the Hamiltonian as an expression that describes the average repulsion (V_{eff}) experienced by an electron due to the charge distribution associated with other electrons. Replacing the exact interelectronic repulsion by the effective potential (V_{eff}) completely neglects the ability of the electron to instantaneously respond to the position of other electrons (i.e. there is no electron correlation). The effective one-electron Hamiltonian is then given by

$$\hat{H}^{\text{eff}}(\mathbf{r}_1) = -\frac{1}{2}\nabla_1^2 - \sum_{I=1}^{N}\frac{Z_I}{r_{1I}} + \sum_{j\neq 1}\int \frac{\rho_j}{r_{1j}}\,d\mathbf{r}_j \qquad (2\text{-}14)$$

where the final term is the V_{eff} described above and ρ_j is the charge (probability) density of electron j given by $\left|\psi_j(\mathbf{r}_j)\right|^2$. The integral in the final term is called the Coulomb operator.

The energy of the system is no longer given by the $\sum_{i=1}^{n}\varepsilon_i$ since this double-counts the interelectronic repulsion and is given by

$$\begin{aligned} U &= \sum_{i=1}^{n}\varepsilon_i - \sum_{i=1}^{n}\sum_{j>i}^{n}\iint \psi_i^*(\mathbf{r}_1)\psi_j^*(\mathbf{r}_2)\,\frac{1}{r_{12}}\,\psi_i(\mathbf{r}_1)\psi_j(\mathbf{r}_2)\,d\mathbf{r}_1 d\mathbf{r}_2 \;+\; V_{nn} \\ &= \sum_{i=1}^{n}\varepsilon_i - \sum_{i=1}^{n}\sum_{j>i}^{n}J_{ij} \;+\; V_{nn} \end{aligned} \qquad (2\text{-}15)$$

where ε_i is the energy of spatial orbital i obtained from the solution of the one-electron Schrödinger equation ($\hat{H}^{\text{eff}}(\mathbf{r}_1)\psi_i(\mathbf{r}_1) = \varepsilon_i\psi_i(\mathbf{r}_1)$) using the effective one-electron Hamiltonian of Eq. 2-14 and J_{ij} is the Coulomb integral.

The Hartree product wavefunction does not satisfy the Pauli Exclusion Principle and any approximation to the exact wavefunction must explicitly include spin and must be antisymmetric (change sign) with respect to interchange of any two electron coordinates. To represent the wavefunction, Fock suggested the use of Slater determinant which automatically satisfies the Pauli Exclusion Principle and is always antisymmetric. The molecular Hartree-Fock (HF) wavefunction represented by Slater determinant is given by

$$\Psi_{\mathrm{HF}} = \frac{1}{\sqrt{n!}} \begin{vmatrix} \psi_1(\mathbf{r}_1)\alpha(s_1) & \psi_1(\mathbf{r}_1)\beta(s_1) & \cdots & \psi_{n/2}(\mathbf{r}_1)\beta(s_1) \\ \psi_1(\mathbf{r}_2)\alpha(s_2) & \psi_1(\mathbf{r}_2)\beta(s_2) & \cdots & \psi_{n/2}(\mathbf{r}_2)\beta(s_2) \\ \vdots & \vdots & \ddots & \vdots \\ \psi_1(\mathbf{r}_{\mathrm{n}})\alpha(s_n) & \psi_1(\mathbf{r}_{\mathrm{n}})\beta(s_n) & \cdots & \psi_{n/2}(\mathbf{r}_{\mathrm{n}})\beta(s_n) \end{vmatrix} \tag{2-16}$$

where $\psi_i(\mathbf{r}_i)\alpha(s_i)$ and $\psi_i(\mathbf{r}_i)\beta(s_i)$ are spin-orbitals defined as the product of the spatial orbital (molecular orbital) $\psi_i(\mathbf{r}_i)$ and the spin function $\alpha(s_i)$ or $\beta(s_i)$, and $1/\sqrt{n!}$ is a normalization factor.

The energy of the molecule is then given by

$$U_{\mathrm{HF}} = 2\sum_{i=1}^{n/2} \varepsilon_i - \sum_{i=1}^{n/2}\sum_{j=1}^{n/2} (2J_{ij} - K_{ij}) \; + \; V_{nn} \tag{2-17}$$

where J_{ij} is the same Coulomb integral defined in Eq. 2-15, K_{ij} is the exchange integral defined by

$$K_{ij} = \iint \psi_i^*(\mathbf{r}_1)\psi_j^*(\mathbf{r}_2)\, \frac{1}{r_{12}}\, \psi_i(\mathbf{r}_2)\psi_j(\mathbf{r}_1)\, d\mathbf{r}_1 d\mathbf{r}_2 \, , \tag{2-18}$$

and ε_i is the energy of molecular orbital (Hartree-Fock orbital) i obtained from the solution of the one-electron Hartree-Fock equation given by

$$\hat{F}(\mathbf{r}_1)\psi_i(\mathbf{r}_1) = \varepsilon_i \psi_i(\mathbf{r}_1) \qquad\qquad i = 1, 2, ..., n/2 \tag{2-19}$$

where the Fock operator $\hat{F}$ is defined as

$$\hat{F}(\mathbf{r}_1) = \hat{H}^{\mathrm{core}}(\mathbf{r}_1) + \sum_{j=1}^{n/2} [2\hat{J}_j(\mathbf{r}_1) - \hat{K}_j(\mathbf{r}_1)] \tag{2-20}$$

where $\hat{H}^{\text{core}}(\mathbf{r}_1)$ is the one-electron core Hamiltonian given by Eq. 2-13, and the Coulomb operator $\hat{J}_j$ and the exchange operator $\hat{K}_j$ are defined by

$$\hat{J}_j(\mathbf{r}_1)\psi_i(\mathbf{r}_1) = \psi_i(\mathbf{r}_1)\int \psi_j^*(\mathbf{r}_2)\,\frac{1}{r_{12}}\,\psi_j(\mathbf{r}_2)\,d\mathbf{r}_2 \tag{2-21}$$

$$\hat{K}_j(\mathbf{r}_1)\psi_i(\mathbf{r}_1) = \psi_j(\mathbf{r}_1)\int \psi_j^*(\mathbf{r}_2)\,\frac{1}{r_{12}}\,\psi_i(\mathbf{r}_2)\,d\mathbf{r}_2\,. \tag{2-22}$$

The Coulomb operator is the potential energy due to the repulsion between electron *i* and the charge distribution associated with electron *j*. The exchange operator, on the contrary, has no classical analog and arises from the required antisymmetry of the wavefunction. However, it can be thought of as a correction to the Coulomb operator since it represents the interaction between electrons of the same spin that tend to avoid each other more than electrons of different spin.

Equations 2-16 through 2-22 are for closed-shell molecules having even number of electrons and the method is called the restricted Hartree-Fock (RHF) method in which every spatial orbital is used to accommodate two electrons having opposite spin function (α and β). For open-shell molecular systems, the unrestricted Hartree-Fock (UHF) method is used where the α and β electrons are allowed to occupy two different spatial orbitals. Though the UHF method accounts for spin polarization, the final UHF wavefunction has some degree of contamination from higher spin states (i.e. spin contamination) derived from the flipping of one or more electrons [26].

The Hartree-Fock equation (2-19) corresponds to a set of *n*/2 coupled non-linear integro-differential equations that can be solved by the self-consistent field (SCF) procedure. In this procedure an initial guess for the molecular orbitals is made (usually by using a semiempirical method) and used to calculate an initial set of Fock operators. Solution of Eq. 2-19 is then possible and produces a new set of molecular orbitals that can be used to calculate an improved set of Fock operators which in turn are used to calculate an improved set of molecular orbitals. This iterative procedure is repeated until the molecular orbitals obtained from one cycle are essentially the same as those obtained from the previous cycle to within a numerical convergence threshold (i.e. self-consistent).

2.2.3 Basis sets and the Roothaan-Hall equations

For molecules of interest in chemistry, the solution of the Hartree-Fock equations (2-19) by numerical methods is unfeasible. It is practical to transform these equations into a set of algebraic equations that are independent of the size and geometry of the molecule and provide a more systematic procedure of solution. Roothaan and Hall, independently, introduced the method of using a basis set that converts the Hartree-Fock equations into a matrix equation [27]. In this method, the unknown molecular orbitals are approximated as linear combinations of a set of known one-electron basis functions φ_r

$$\psi_i = \sum_{r=1}^{b} c_{ri}\varphi_r \tag{2-23}$$

where the coefficients c_{ri} are the molecular orbital expansion coefficients to be determined.

To accurately represent the molecular orbital ψ_i, a complete (infinite) set of basis functions φ_r is required though practically a finite number b of basis functions is used. Basis sets used in electronic structure calculations include plane and augmented waves, Slater-type orbitals (STOs), and Gaussian-type orbitals (GTOs). Plane and augmented waves are completely delocalized functions and are thus suitable for solid-state calculations such as studies on metallic crystalline materials. STOs and GTOs, on the other hand, are centered (localized) on the atomic nuclei and hence bear some resemblance to atomic orbitals. Although STOs closely resemble hydrogenic atomic orbitals, the presence of more than four atoms in a molecule causes difficulties since there are no analytical solutions available for the two-electron multi-center integrals when the basis functions are STOs. GTOs instead are more computationally convenient and are therefore being the most widely used basis functions for molecular orbital calculations.

A normalized Cartesian GTO centered on an atom has the general form

$$g = \left(\frac{2\alpha}{\pi}\right)^{3/4} \left[\frac{(8\alpha)^{k+l+m} k!l!m!}{(2k)!(2l)!(2m)!}\right]^{1/2} x^k y^l z^m e^{-\alpha(x^2+y^2+z^2)} \tag{2-24}$$

where α is a positive exponent determining the radial extent of the GTO, and k, l, and m are non-negative integers that establish the nature of the orbital (e.g., when $k + l + m = 2$, the orbital is called a *d-type* Gaussian). There are six *d*-type and ten *f*-type Cartesian Gaussians in contrast to the five 3*d* and seven 4*f* atomic orbitals. However, different Gaussian basis sets adopt different conventions regarding their *d* and *f* functions where some use all the six *d* and ten *f* Cartesian Gaussians and others use linear combinations to have the same angular behavior as the pure five 3*d* and seven 4*f* atomic orbitals [28].

As shown in Figure 2.5, Gaussian functions do not have cusps at the nucleus ($r = 0$) that the Slater functions do and hence they poorly represent an atomic orbital for small values of r. In addition, they decay faster at larger r and thus have less ability to represent diffused electron density distribution. Therefore, a linear combination of GTOs is used to approximate an STO, that is,

$$\varphi_r = \sum_p d_{pr} g_p \tag{2-25}$$

where φ_r is called contracted GTO and the g_p's are called primitive Gaussians having the same k, l, m values as one another but different α's. For a given basis set, the exponents α's and the contraction coefficients d_{pr} have predetermined values and remain constant during the calculation.

The expansion for molecular orbital ψ_i defined by Eq. 2-23 is then given by

$$\psi_i = \sum_{r=1}^{b} c_{ri} \left(\sum_{p} d_{pr} g_p \right). \tag{2-26}$$

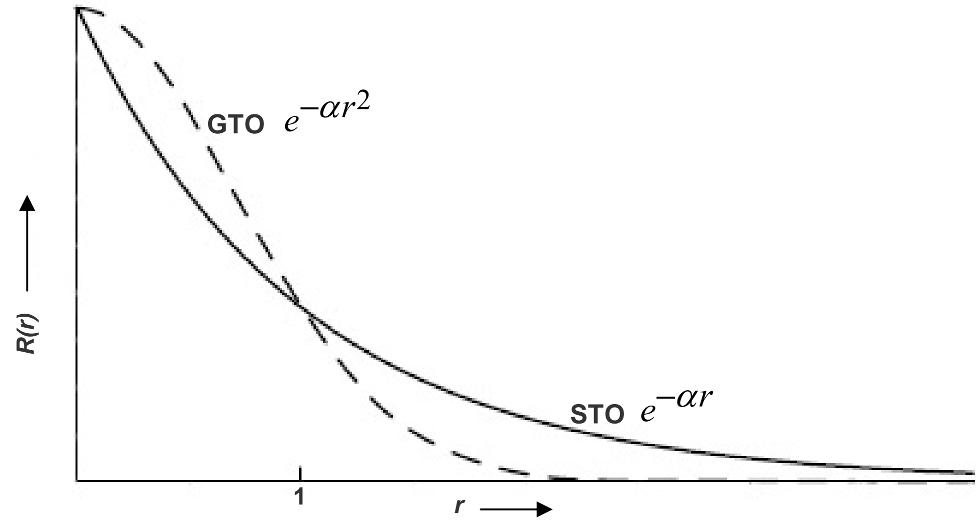

Figure 2.5: Radial behavior of STO and GTO.

A commonly used family of GTO basis sets for calculations on organic molecules is the Pople basis sets. An example of such basis sets is the basis set indicated by the notation 6-31G. This notation means that each core atomic orbital is expanded by a contraction of six primitive Gaussians and each valence shell atomic orbital is represented by two contractions, one with three primitive Gaussians and the other with one primitive Gaussian. Additional polarization functions can be added in order to give the wavefunction more flexibility to change its shape upon molecule formation. For example, the 6-31G(d) adds a set of six *d*-type Cartesian Gaussians on each atom other than hydrogen. Moreover, diffuse functions that describe the shape of the wavefunction far distant from the nucleus can be added for example for anionic systems that have large electron density distribution and for van der Waal complexes to describe long range interactions. The 6-31+G(d) basis set adds diffuse functions to all atoms with the exception of hydrogen.

The method of using basis set proposed by Roothaan and Hall transforms the set of Hartree-Fock equations (2-19) into the matrix form

$$\mathbf{FC} = \mathbf{SC}\boldsymbol{\varepsilon} \tag{2-27}$$

where $\boldsymbol{\varepsilon}$ is a $b \times b$ diagonal matrix of orbital energies with each of its elements ε_i representing the one-electron orbital energy of molecular orbital ψ_i, **C** is the $b \times b$ matrix of the molecular orbital expansion coefficients c_{ri}, **S** is the $b \times b$ overlap matrix indicating the overlap between basis functions the elements of which are given by

$$S_{rs} = \int \varphi_r(\mathbf{r}_1)\varphi_s(\mathbf{r}_1)\,d\mathbf{r}_1\,, \tag{2-28}$$

and **F** is a $b \times b$ matrix called the Fock matrix whose elements are given by

$$F_{rs} = H_{rs}^{core} + J_{rs} - K_{rs} \tag{2-29}$$

where H_{rs}^{core}, J_{rs} and K_{rs} are given by

$$H_{rs}^{\mathrm{core}} = \int \varphi_r(\mathbf{r}_1)\hat{H}^{\mathrm{core}}(\mathbf{r}_1)\,\varphi_s(\mathbf{r}_1)\,d\mathbf{r}_1 \tag{2-30}$$

$$\begin{aligned} J_{rs} &= \sum_{t=1}^{b}\sum_{u=1}^{b}\mathbf{P}_{tu}\iint \varphi_r(\mathbf{r}_1)\varphi_s(\mathbf{r}_1)\,\frac{1}{r_{12}}\,\varphi_t(\mathbf{r}_2)\varphi_u(\mathbf{r}_2)\,d\mathbf{r}_1 d\mathbf{r}_2 \\ &= \sum_{t=1}^{b}\sum_{u=1}^{b}\mathbf{P}_{tu}(rs\,|\,tu) \end{aligned} \tag{2-31}$$

$$\begin{aligned} K_{rs} &= \frac{1}{2}\sum_{t=1}^{b}\sum_{u=1}^{b}\mathbf{P}_{tu}\iint \varphi_r(\mathbf{r}_1)\varphi_u(\mathbf{r}_1)\,\frac{1}{r_{12}}\,\varphi_t(\mathbf{r}_2)\varphi_s(\mathbf{r}_2)\,d\mathbf{r}_1 d\mathbf{r}_2 \\ &= \frac{1}{2}\sum_{t=1}^{b}\sum_{u=1}^{b}\mathbf{P}_{tu}(ru\,|\,ts). \end{aligned} \tag{2-32}$$

In Eqs. 2-28 through 2-32, the basis functions are indexed by *r*,*s*,*t*, and *u* and are real functions. The integral in Eq. 2-30 is called the one-electron integral whereas integrals in Eqs. 2-31 and 2-32 are called the two-electron repulsion integrals (multi-center integrals) whose number can go up to $b^4/8$ different integrals depending on the use of symmetry and integral accuracy cutoffs. The **P** in Eqs.2-31 and 2-32 is called the density matrix whose elements are

$$P_{tu} = 2\sum_{i=1}^{n/2} c_{ti} c_{ui} \tag{2-33}$$

where the summation is over occupied molecular orbitals.

The energy of the molecule can be written in terms of the density matrix elements as

$$\begin{aligned} U_{\mathrm{HF}} &= \sum_{i=1}^{n/2} \varepsilon_i + \frac{1}{2}\sum_{r=1}^{b}\sum_{s=1}^{b} P_{rs} H_{rs}^{core} \ + \ V_{nn} \\ &= \frac{1}{2}\sum_{r=1}^{b}\sum_{s=1}^{b} P_{rs}\left(H_{rs}^{core} + F_{rs}\right) \ + \ V_{nn}\,. \end{aligned} \tag{2-34}$$

Eq. 2-27 is solved iteratively by the self-consistent field (SCF) method as illustrated in Scheme 2.2.

2.2.4 Density functional theory and the Kohn-Sham equations

The performance of density functional theory (DFT) in terms of energetics, molecular structures, vibrational frequencies, and other chemical and physical properties is comparable and competitive with post-HF methods such as MP2 and CC methods. Meanwhile, DFT is less computationally intensive than these methods and as a result DFT is one of the most popular methods for electronic structure calculations in chemistry and materials science.

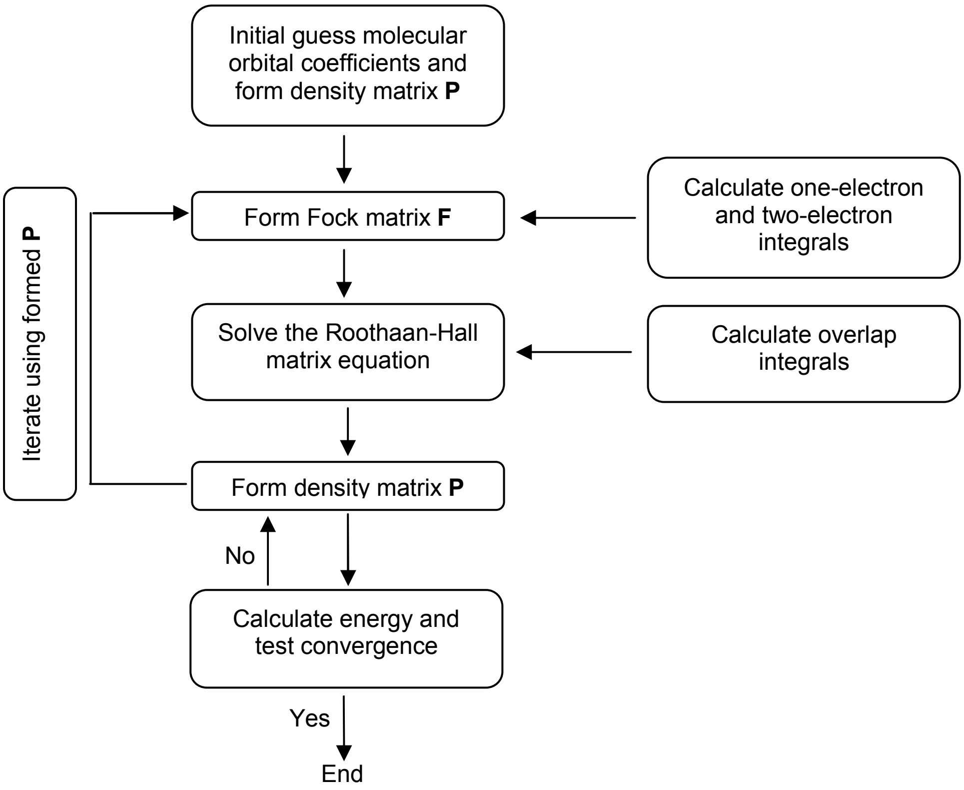

Scheme 2.2: The direct SCF method for the solution of the Roothaan-Hall equations for a closed-shell molecular system. The one-electron integrals need only to be evaluated once since they remain constant throughout the iterative calculation.

DFT is aimed at calculating the molecular ground-state electron (probability) density ρ_0 not the molecular wavefunction as in HF based methods. The Hohenberg-Kohn existence theorem [29] assures that the ground-state molecular energy and other ground-state properties can be uniquely determined from the ground-state electron density, which is a function of only three spatial variables, without the need to find the molecular wavefunction. The energy is then said to be a functional (i.e. a function of a function) of the electron density, that is

$$E_0 = E_0\left[\rho_0(\mathbf{r})\right]. \tag{2-35}$$

The individual components of the electronic energy are as well functionals of the electron density and hence

$$E_0\left[\rho_0\right]=T\left[\rho_0\right]+V_{ne}\left[\rho_0\right]+V_{ee}\left[\rho_0\right] \tag{2-36}$$

where V_{ne} is the expectation value of the $\hat{V}_{ne}$ operator (cf. Eq. 2-9) and is given by

$$V_{ne}\left[\rho_0\right]=\int \rho_0(\mathbf{r})\upsilon(\mathbf{r})\,d\mathbf{r} \tag{2-37}$$

where $\upsilon(\mathbf{r}_i)$ is the 'external' potential acting on electron i and is defined as

$$\upsilon(\mathbf{r}_i)=-\sum_{I=1}^{N}\frac{Z_I}{r_{iI}}\,. \tag{2-38}$$

The first and the third functionals in Eq. 2-36 are universal functionals completely independent of the system whereas the middle functional is system dependant. The Hohenberg-Kohn variational theorem [29] proves that the exact ground-state electron density minimizes the energy functional and any trial electron density cannot give a lower ground-state energy than the exact ground-state electron density. However, the universal functionals are unknown and the Hohenberg-Kohn theorems lack any information on how to find the electron density without finding the wavefunction.

The Kohn and Sham (KS) approach [30] to DFT calculations is to reintroduce orbitals, which in fact increases the complexity from 3 to 3n variables, and is thus analogous to the HF method. The Kohn-Sham DFT electronic energy of a molecule can be expressed as

$$E_0\left[\rho_0\right]=T_r\left[\rho_0\right]+V_{ne}\left[\rho_0\right]+J\left[\rho_0\right]+E_{xc}\left[\rho_0\right] \tag{2-39}$$

where T_r is the electronic kinetic energy of a reference system of non-interacting electrons given by

$$T_r[\rho_0] = \sum_{i=1}^{n} \int \psi_i^*(\mathbf{r}_1)\left[-\frac{1}{2}\nabla_1^2\right]\psi_i(\mathbf{r}_1)\,d\mathbf{r}_1, \tag{2-40}$$

J is the classical Coulombic electron-electron repulsion energy defined as

$$J[\rho_0] = \frac{1}{2}\iint \frac{\rho_0(\mathbf{r}_1)\rho_0(\mathbf{r}_2)}{r_{12}}\,d\mathbf{r}_1 d\mathbf{r}_2, \tag{2-41}$$

and E_{xc} is the exchange-correlation energy which is the sum of the kinetic energy deviation from the reference system and the electron-electron repulsion energy deviation from the classical system, that is,

$$E_{xc}[\rho_0] = \left(T[\rho_0] - T_r[\rho_0]\right) + \left(V_{ee}[\rho_0] - J[\rho_0]\right). \tag{2-42}$$

In Eq. 2-40, the ψ_i's are the KS spatial orbitals of the reference system analogous to the HF spatial orbitals and the KS wavefunction of the reference system can be represented by a Slater determinant similar to that of Eq. 2-16. Using the electron density of the reference system

$$\rho_r = \sum_{i=1}^{n} \left|\psi_i(\mathbf{r}_1)\right|^2 = \rho_0 \tag{2-43}$$

in Eq. 2-39 and applying the variational principle to minimize E_0 with respect to KS orbitals lead to the Kohn-Sham equations

$$\hat{F}^{\mathrm{KS}}(\mathbf{r}_1)\psi_i(\mathbf{r}_1) = \varepsilon_i \psi_i(\mathbf{r}_1) \tag{2-44}$$

where the Kohn-Sham one-electron operator $\hat{F}^{\mathrm{KS}}$ is defined as

$$\hat{F}^{\mathrm{KS}} = -\frac{1}{2}\nabla_1^2 - \sum_{I=1}^{N} \frac{Z_I}{r_{1I}} + \int \frac{\rho(\mathbf{r}_2)}{r_{12}}\,d\mathbf{r}_2 + V_{xc}(\mathbf{r}_1) \tag{2-45}$$

and

$$V_{xc}(\mathbf{r}) \equiv \frac{\delta E_{xc}[\rho(\mathbf{r})]}{\delta \rho(\mathbf{r})} \tag{2-46}$$

is the exchange-correlation potential (the functional derivative of the exchange-correlation energy E_{xc} with respect to the electron density function).

In analogy to the Roothaan-Hall procedure for solving the Hartree-Fock equations, the Kohn-Sham equations (2-44) can be represented in the matrix form

$$\mathbf{F}^{\mathrm{KS}}\mathbf{C} = \mathbf{S}\mathbf{C}\boldsymbol{\varepsilon} \tag{2-47}$$

where $\boldsymbol{\varepsilon}$ is a $b \times b$ diagonal matrix of orbital energies with each of its elements ε_i representing the one-electron orbital energy of KS spatial orbital ψ_i, $\mathbf{C}$ is the $b \times b$ matrix of the spatial orbital expansion coefficients c_{ri}, $\mathbf{S}$ is the $b \times b$ overlap matrix indicating the overlap between basis functions the elements of which are given by Eq. 2-28, and $\mathbf{F}^{\mathrm{KS}}$ is a $b \times b$ matrix called the Kohn-Sham matrix whose elements are given by

$$F_{rs}^{KS} = H_{rs}^{core} + J_{rs} + V_{rs}^{xc} \tag{2-48}$$

where H_{rs}^{core} and J_{rs} are given by Eqs. 2-30 and 2-31, respectively, and V_{rs}^{xc} is given by

$$V_{rs}^{xc} = \int \varphi_r(\mathbf{r}_1) V_{xc}(\mathbf{r}_1) \varphi_s(\mathbf{r}_1) \, d\mathbf{r}_1 . \tag{2-49}$$

The energy of a closed-shell molecule can be written in terms of the density matrix elements as

$$U_{\mathrm{KS}} = \frac{1}{2} \sum_{r=1}^{b} \sum_{s=1}^{b} P_{rs} \left(H_{rs}^{core} + F_{rs}^{KS} \right) + V_{nn} . \tag{2-50}$$

Eq. 2-47 is solved iteratively by the self-consistent field (SCF) method analogous to that depicted in Scheme 2.2 for the Hartree-Fock method.

In Eq. 2-39, the exact exchange-correlation energy functional E_{xc} is unknown and actual DFT calculations use approximate functionals and are hence not variational (i.e., they can give an energy lower than the exact energy). The approximate exchange-correlation energy functional includes the non-classical part of the electron-electron interaction (i.e. the exchange energy and the Coulombic correlation energy), the correction to the electron self-interaction that arises from the classical electrostatic repulsion (Eq. 2-41), and the kinetic correlation energy (i.e., the kinetic energy not covered by the non-interacting reference system). The types of approximate exchange-correlation functionals exist are: (1) local (spin) density approximation (L(S)DA), (2) generalized gradient approximation (GGA), (3) meta-GGA, (4) hybrid-GGA, and (5) hybrid meta-GGA. Scheme 2.3 illustrates the physical ingredients included in these functionals.

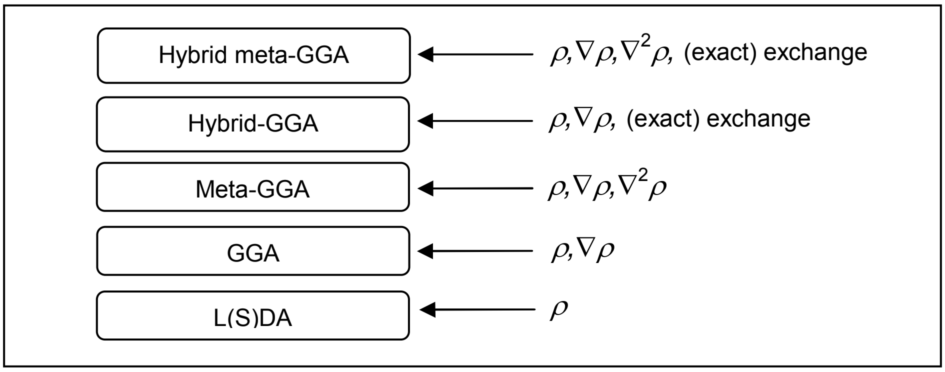

Scheme 2.3: DFT exchange-correlation energy functionals with their corresponding physical ingredients.

The most popular DFT functional used in electronic structure calculations on organic molecules is the B3LYP functional (Becke 3 parameter exchange functional and Lee-Yang-Parr correlation functional) [31-34], which is a hybrid-GGA functional defined as

$$E_{xc}^{B3LYP} = (1-a)E_x^{LSDA} + aE_x^{HF} + b\Delta E_x^{B88} + (1-c)E_c^{VWN3} + cE_c^{LYP} \qquad (2\text{-}51)$$

where the parameters a, b, and c have the values of 0.20, 0.72, and 0.81, respectively, and were determined by fitting to experimental data. The first three terms are the exchange energy functionals, namely, the local (spin) density approximation (E_x^{LSDA}), Becke's 1988 gradient correction (to the LSDA) for exchange (ΔE_x^{B88}) [31], and the exact exchange as defined in the Hartree-Fock method (E_x^{HF}). The last two terms are the local spin density correlation functional of

Vosko, Wilk and Nusair (E_c^{VWN3}) [32] and the Lee, Yang and Parr correlation functional (E_c^{LYP}) [33] that includes both local and gradient terms.

The exchange-correlation part (Eq. 2-49) of the Kohn-Sham matrix comprises integrals over complicated mathematical forms of the exchange-correlation potential V_{xc} that cannot be solved analytically. The practical procedure to evaluate such integrals is to employ numerical techniques where the integral is approximated by summing the integrand in steps determined by a grid [35]. Hence, the finer the grid the more accurate will be the DFT results.

2.2.5 Geometry optimization and vibrational frequencies

The molecular energy U (the molecular electronic energy including nucleus-nucleus repulsion) described thus far is for a point on the Born-Oppenheimer potential energy surface (single point energy). The equilibrium and transition structures that are of interest in chemistry correspond to stationary points on the PES (i.e. points where the first partial derivatives of the energy (the gradient) with respect to nuclear coordinates are zero) (cf. Figure 2.4). A geometry optimization of the molecule is therefore necessary to locate the desired stationary point on the PES. However, the energy of the molecule at a stationary point on the PES is not the true ground-state energy since it does not include the zero-point vibrational energy (ZPVE) due to molecular vibrations. The ZPVE is always positive even at temperatures close to absolute zero and the lowest energy a molecule can possess corresponds to the energy of the lowest vibrational state. Hence, the calculation of molecular vibrations is as well of importance.

Generally, in a geometry optimization, a starting geometry of the molecule is chosen and the energy is calculated as described in Sections 2.2.2 – 2.2.4. The energy is then differentiated with respect to nuclear coordinates to yield the forces acting on the nuclei (the negative of the gradient). The positions of the nuclei are then systematically displaced to get a new molecular geometry and the above steps repeated until the forces are essentially zero (below a preset value) and the displacement for the next step is very small.

Geometry optimization algorithms [36-42] for finding minima fall into non-derivative and derivative methods where the latter can be further categorized into first-order (the first partial derivative of the energy is used) and second-order (the first and second partial derivatives of the energy are used) techniques. The first-order methods include the steepest descents and conjugate gradient methods. The second order optimization algorithms include the Newton-Raphson and quasi-Newton methods. In quasi-Newton methods, estimates of the second partial derivatives of the energy (the Hessian) are used. Quasi-Newton methods are considered one of the best approaches to optimizing molecular geometries.

Locating transition structures on the PES is often more difficult than minima. The algorithms used can be generally grouped into two categories; methods based on interpolation between two minima and methods that use only local information [36-41]. Common interpolation methods include linear synchronous transit (LST) method, quadratic synchronous transit (QST) method, and nudged elastic band (NEB) method. Methods based on the updated Hessian Newton-Raphson approach are the most popular local methods.

At both the minimum equilibrium structure and transition structure the first partial derivates of the energy with respect to nuclear coordinates are all zero. The number of negative eigenvalues (imaginary frequencies) in the Hessian matrix is thus used to distinguish the structure of being a minimum (no negative eigenvalues) or a transition structure (one and only one negative eigenvalue).

The characterization of the complete PES is difficult and it is adequate for most chemical applications to obtain the energies and molecular properties at stationary points on the PES (Figure 2.4). The molecule energy U can be expanded in a Taylor series about a stationary structure as

$$\begin{aligned} U &= U_0 + \sum_{\alpha=1}^{3N} q_\alpha \left(\frac{\partial U}{\partial q_\alpha} \right)_0 + \frac{1}{2!} \sum_{\alpha=1}^{3N} \sum_{\beta=1}^{3N} q_\alpha q_\beta \left(\frac{\partial^2 U}{\partial q_\alpha \partial q_\beta} \right)_0 \\ &\quad + \frac{1}{3!} \sum_{\alpha=1}^{3N} \sum_{\beta=1}^{3N} \sum_{\gamma=1}^{3N} q_\alpha q_\beta q_\gamma \left(\frac{\partial^3 U}{\partial q_\alpha \partial q_\beta \partial q_\gamma} \right)_0 + \cdots \qquad (2\text{-}52) \\ &= \frac{1}{2} \sum_{\alpha=1}^{3N} \sum_{\beta=1}^{3N} q_\alpha q_\beta \left(\frac{\partial^2 U}{\partial q_\alpha \partial q_\beta} \right)_0 \end{aligned}$$

where U_0 is set equal to zero, q_α's are the mass-weighted Cartesian displacement coordinates of the nuclei ($\left(\sqrt{m_1}\,\Delta x_1, \sqrt{m_1}\,\Delta y_1, \sqrt{m_1}\,\Delta z_1, \ldots, \sqrt{m_N}\,\Delta z_N\right)$), the first derivates are all zero for the stationary structure, and the third and higher derivatives (the anharmonic components of the energy) are neglected for small displacements (i.e. harmonic oscillator approximation to the energy).

Using the mass-weighted Cartesian coordinates in addition to the introduction of a normal coordinate Q_γ that is defined as a linear combination of q_α's transform the 3N-dimensional nuclear Schrödinger equation (2-8) into a sum of 3N one-dimensional independent equations of the form

$$\left[-\frac{1}{2} \frac{\partial^2}{\partial Q_\gamma{}^2} + \frac{1}{2} \lambda_\gamma Q_\gamma^2 \right] \psi_\gamma(Q_\gamma) = E_\gamma \psi_\gamma(Q_\gamma) \qquad \gamma = 1, 2, \ldots, 3N \qquad (2\text{-}53)$$

where λ_γ (the mass-weighted force constant) is given by

$$\lambda_\gamma = \left(\frac{\partial^2 U}{\partial Q_\gamma^2} \right)_0 . \qquad (2\text{-}54)$$

Six (five for linear molecules) of the λ_γ values are (close to) zero and correspond to the translation and rotation modes [43-46]. The remaining $3N-6$ (5) values are nonzero and correspond to the normal modes of vibration. The total energy of the ground vibrational state is given by

$$E_{vib} = \frac{1}{2}\sum_{\gamma=1}^{3N-6} \omega_\gamma = ZPVE \tag{2-55}$$

where ω_γ is the harmonic oscillator natural frequency defined as

$$\omega_\gamma = \sqrt{\lambda_\gamma} \, . \tag{2-56}$$

The harmonic vibrational frequency (wavenumber) of the γ^{th} normal mode is given by

$$\bar{\nu}_\gamma = \frac{1}{2\pi c}\sqrt{\lambda_\gamma} \, . \tag{2-57}$$

Vibrational analysis must be carried out on stationary points where the first derivatives of the energy are all essentially zero (below a preset value). Moreover, the quantum mechanical method and basis set used for vibrational frequency calculation must be the same as those used for geometry optimization. The frequencies and ZPVE obtained from the harmonic oscillator approximation are systematically higher than the corresponding fundamental frequencies and thus need to be scaled. For the B3LYP method using the 6-31G(d) basis set the scaling factors of 0.9613 and 0.9804 are used for the frequencies and ZPVE, respectively. The total internal energy of the molecule is then given by

$$E_0 = U + ZPVE \, . \tag{2-58}$$

The analytical computation of energy derivatives [41,47-59] has the advantages of being more computationally efficient and more numerically accurate than numerical procedures. For DFT, the analytic first partial derivative of the energy with respect to a nuclear displacement coordinate x_α is given by

$$\begin{aligned}\frac{\partial U}{\partial x_\alpha} = {} & \sum_{r=1}^{b}\sum_{s=1}^{b} P_{rs}\frac{\partial H_{rs}^{core}}{\partial x_\alpha} + \frac{1}{2}\sum_{r=1}^{b}\sum_{s=1}^{b}\sum_{t=1}^{b}\sum_{u=1}^{b} P_{rs}P_{tu}\frac{\partial\left(rs\,|\,tu\right)}{\partial x_\alpha} \\ & -\sum_{r=1}^{b}\sum_{s=1}^{b} W_{rs}\frac{\partial S_{rs}}{\partial x_\alpha} + \frac{1}{2}\sum_{r=1}^{b}\sum_{s=1}^{b} P_{rs}\frac{\partial V_{rs}^{xc}}{\partial x_\alpha} + \frac{\partial V_{nn}}{\partial x_\alpha}\end{aligned} \qquad (2\text{-}59)$$

where W_{rs}'s are the elements of the energy-weighted density matrix **W** given by

$$W_{rs} = 2\sum_{i=1}^{n/2} \varepsilon_i c_{ri} c_{si} \,. \qquad (2\text{-}60)$$

The analytic second partial derivative is given by

$$\begin{aligned}\frac{\partial^2 U}{\partial x_\alpha \partial x_\beta} = {} & \sum_{r=1}^{b}\sum_{s=1}^{b} P_{rs}\frac{\partial^2 H_{rs}^{core}}{\partial x_\alpha \partial x_\beta} + \frac{1}{2}\sum_{r=1}^{b}\sum_{s=1}^{b}\sum_{t=1}^{b}\sum_{u=1}^{b} P_{rs}P_{tu}\frac{\partial^2\left(rs\,|\,tu\right)}{\partial x_\alpha \partial x_\beta} \\ & -\sum_{r=1}^{b}\sum_{s=1}^{b} W_{rs}\frac{\partial^2 S_{rs}}{\partial x_\alpha \partial x_\beta} + \frac{1}{2}\sum_{r=1}^{b}\sum_{s=1}^{b} P_{rs}\frac{\partial^2 V_{rs}^{xc}}{\partial x_\alpha \partial x_\beta} + \frac{\partial^2 V_{nn}}{\partial x_\alpha \partial x_\beta} \\ & +\sum_{r=1}^{b}\sum_{s=1}^{b}\frac{\partial P_{rs}}{\partial x_\beta}\frac{\partial H_{rs}^{core}}{\partial x_\alpha} + \sum_{r=1}^{b}\sum_{s=1}^{b}\sum_{t=1}^{b}\sum_{u=1}^{b}\frac{\partial P_{rs}}{\partial x_\beta}P_{tu}\frac{\partial\left(rs\,|\,tu\right)}{\partial x_\alpha} \\ & -\sum_{r=1}^{b}\sum_{s=1}^{b}\frac{\partial W_{rs}}{\partial x_\beta}\frac{\partial S_{rs}}{\partial x_\alpha} + \frac{1}{2}\sum_{r=1}^{b}\sum_{s=1}^{b}\frac{\partial P_{rs}}{\partial x_\beta}\frac{\partial V_{rs}^{xc}}{\partial x_\alpha}.\end{aligned} \qquad (2\text{-}61)$$

The first partial derivatives of the molecular orbital coefficients in the last four terms of Eq. 2-61 are required and can be computed by solving the coupled perturbed Kohn-Sham (CPKS) equations [41,53,60-64].

2.2.6 Thermochemical quantities

Of importance to the study of relating structure and reactivity are the thermochemical quantities of the reaction. Relative Gibbs free energies (ΔG) are often more meaningful with respect to the experiment than are relative energies at zero Kelvin (ΔE_0) (cf. Eq. 2-58). Hence, the results reported in this thesis are in terms of Gibbs free energies.

For the study of a chemical reaction at a given temperature, a thermal energy correction must be added to the energy defined by Eq. 2-58. The thermal correction includes the effects of molecular translation, rotation and vibration at the specified temperature and pressure [65-67].

The total internal thermal energy of the molecule is then given by

$$E_{298} = E_0 + E_{elect} + E_V + E_r + E_t \tag{2-62}$$

where 298 denotes that the thermal correction to the internal energy E_0 (Eq. 2-58) is at 298.15 K and the last four terms constitute the thermal correction as follows:

(1) E_{elect} describes the contribution of electronically excited states to the internal thermal energy. In Gaussian, the first and higher excited states are assumed to be inaccessible at any temperature and hence there is no contribution to the internal thermal energy from this term.

(2) E_v is the contribution to the internal thermal energy resulting from molecular vibration with the ZPVE being the largest contributor to this term. The occupation of higher vibrational states comprises the remainder. It should be pointed out that the ZPVE contribution is either included in E_0 or E_v depending on where the zero of energy is set (the bottom of the internuclear potential energy well or the first vibrational level).

(3) E_r and E_t are the contributions to the internal thermal energy due to rotation and translation, respectively.

The enthalpy is given by

$$H_{298} = E_{298} + RT \tag{2-63}$$

where R is the gas constant and T is the temperature in Kelvin (298.15 in this example). The Gibbs free energy is given by

$$G_{298} = H_{298} - TS_{298} \tag{2-64}$$

where S_{298} is the molar entropy of the molecule at 298.15 K, which includes the effects of molecular translation, rotation and vibration at the specified temperature and pressure. The above equations, in addition to the assumption that the first and higher electronic states are totally inaccessible, assume non-interacting molecules (ideal gas assumption).

Relative energies and thermochemical quantities are often reported rather than absolute quantities which are difficult to measure accurately. This is illustrated in Figure 2.6.

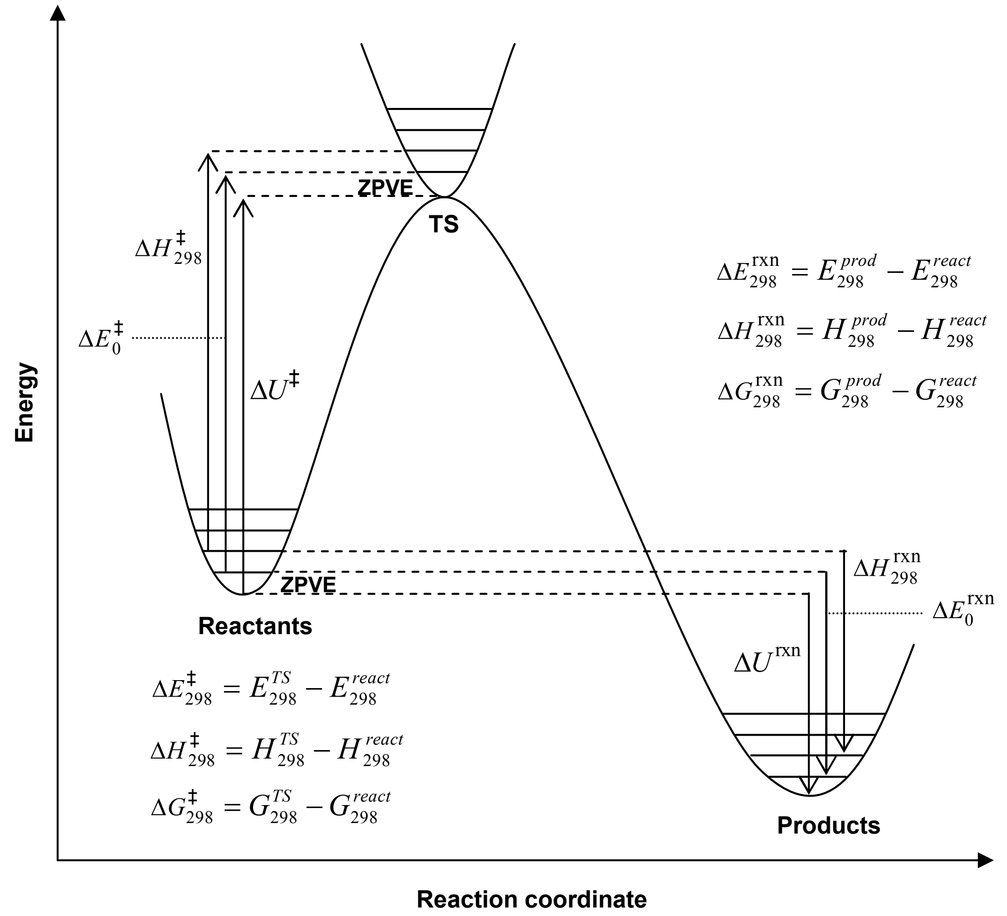

Figure 2.6: Relationship between computed energies and thermochemical quantities along a reaction path at 298.15 K and 1 atm pressure. U, E_0, E_{298}, H_{298}, and G_{298} are given by Eqs. 2-50, 2-58, 2-62, 2-63, and 2-64, respectively. TS = transition state. Note: the "transition state" term is used to denote a Boltzmann average on the Gibbs free energy surface while the "transition structure" term is used to describe the first-order saddle point on the potential energy surface.

In chemical reactions yielding more than one product, the products ratio (selectivity) is controlled either kinetically or thermodynamically or both. The Curtin-Hammett principle states that in stereoselective reactions starting from a substrate and giving rise to two or more stereoisomers, the favored reaction is not related to the more stable stereoisomer of the substrate. The favored reaction path is the one that proceeds through the lowest energy transition state even when the transition state is not derived from the more stable stereoisomer of the substrate. The extent of stereoselectivity results from the competition between the favored and the disfavored reaction paths and it solely depends on the Gibbs free energy difference between the competing stereoisomeric transition states [1,6,68,69]. The Curtin-Hammett principle hence applies to kinetically controlled reactions.

In most organic reactions, the activation barriers of the selectivity-determining steps are greater than the barriers connecting different isomers of the substrate [68,69]. Hence, the Curtin-Hammett principle can be applied to these reactions and the relative transition state Gibbs free energies correspond to the stereoselectivity of such reactions. Indeed, the Curtin-Hammett principle has also been shown applicable to (catalyzed) enantioselective Diels-Alder reactions [70,71].

According to Boltzmann statistics, the fraction X of a molecule M having a specific geometry at temperature T can be given by

$$X_M = \frac{e^{-G_M/RT}}{\sum_m e^{-G_m/RT}} \tag{2-65}$$

where m runs over all possible states (geometries). In this thesis, Eq. 2-65 is used to compute the fraction of an optimized *endo* or *exo* transition state structure with respect to all optimized *endo* or *exo* transition state structures. The average Gibbs free energy of the *endo* transition state structures is calculated by Eq. 2-66 with the calculation for the *exo* transition state structures being the same.

$$G_{endo} = \sum_{m}^{all\,endo} X_m G_m \tag{2-66}$$

The *endo* fraction is then computed by Eq. 2-67 with analogous formula being used for the *exo* fraction.

$$X_{endo} = \frac{1}{1 + e^{(G_{endo} - G_{exo})/RT}} \tag{2-67}$$

The percent enantiomeric excess (% *ee*) is calculated by

$$\%\,ee = \left| X_{endo} - X_{exo} \right| \times 100\,. \tag{2-68}$$

No attempt to calculate the absolute rate constants of the studied reactions was carried out. However, relative reaction rates derived from transition state theory [72-74] are reported and given by

$$k_{endo:exo} = e^{\left(\Delta G^{\ddagger}_{exo} - \Delta G^{\ddagger}_{endo}\right)/RT}\,. \tag{2-69}$$

The percent enantiomeric excess (%*ee*) and the relative reaction rate as functions of the difference in transition state Gibbs free energies are illustrated by Figure 2.7.

2.2.7 Molecular mechanics

Quantum mechanics is typically employed for modeling molecular systems with limited number of atoms and treating large molecular systems quantum mechanically is out of the question. Albeit less accurate than quantum mechanics, molecular mechanics is the choice for modeling large molecules where the solution of the electronic Schrödinger equation is avoided. In molecular mechanics, atoms are the building blocks of the system rather than electrons and nuclei used in quantum mechanics. Hence, in molecular mechanics, the bonding in the molecule must be defined explicitly.

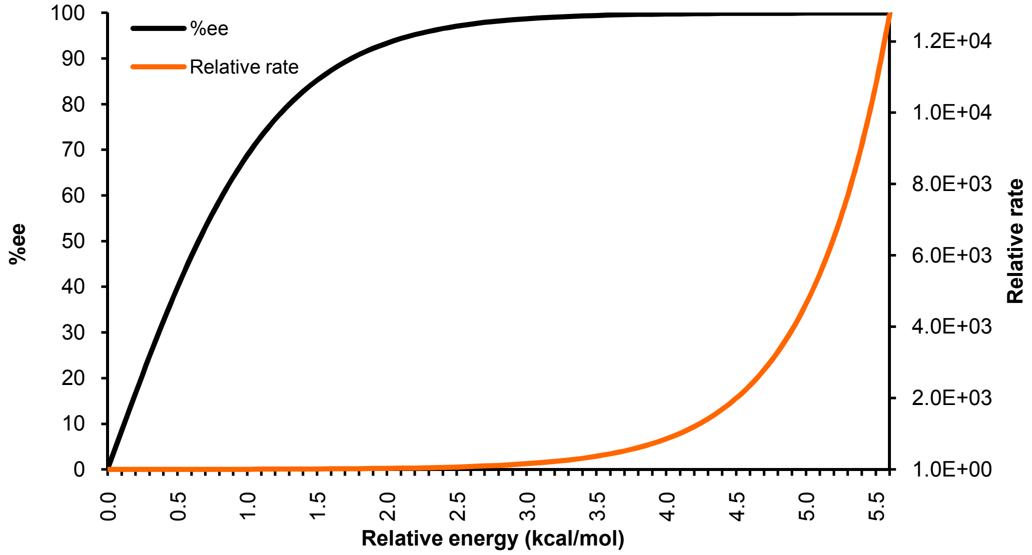

Figure 2.7: The relationship between percent enantiomeric excess, relative reaction rate and relative energy at 298.15 K.

Molecular mechanics is based on classical (Newtonian) mechanics and electrostatics [75,76]. Under the Born-Oppenheimer approximation, the set of classically formulated equations that are used to describe the potential energy surface of a molecule is called a force field [75]. The parameters in these equations are determined either by experiment or by quantum mechanical calculations [75]. A force field parameterized using a representative ‘training set’ of a specific class of molecules is expected to produce reliable results for only that class [41,77-79]. In addition, force fields make use of atom types where, for example, the parameters used to describe an sp^3 carbon are different from those used for an sp^2 carbon [41,77-79]. This allows the transferability of parameters. Widely used force fields include AMBER, CHARMM, and UFF.

The force field total energy (U_{total}) [41,76] is typically defined as

$$U_{\text{total}} = U_{\text{bond}} + U_{\text{bend}} + U_{\text{tors}} + U_{\text{vdw}} + U_{\text{elec}} + U_{\text{cross}} \tag{2-70}$$

where U_{bond}, U_{bend}, U_{tors}, U_{vdw}, U_{elec} and U_{cross} are the energy functions describing bonds stretching, angles bending, torsional rotations, van der Waals interactions, electrostatic interactions, and coupling interactions, respectively. The mathematical form of these energy functions and the parameters associated with them are force field dependent [41]. The U_{vdw} and U_{elec} terms are often called nonbonded interactions.

2.2.8 Classical molecular dynamics

The two main computer simulation techniques for understanding the properties of ensembles of molecules are Monte Carlo and molecular dynamics. In classical molecular dynamics [80-85], Newton's second equation ($\mathbf{F} = m\mathbf{a}$) is solved by step-by-step numerical integration. For an atom k in a molecule consisting of M atoms, Newton's second equation can be written as

$$-\frac{\partial U(\mathbf{r})}{\partial \mathbf{r}_k} = m_k \frac{d^2\mathbf{r}_k}{dt^2} \qquad k = 1,2,\ldots,M \tag{2-71}$$

where the left hand side is the force acting on atom k and $\mathbf{r}$ is the vector containing the $3M$ spatial Cartesian coordinates of all the atoms (i.e. $\mathbf{r} \equiv (\mathbf{r}_1, \mathbf{r}_2, \ldots, \mathbf{r}_M)$).

The set of second-order differential equations (Eq. 2-71) is numerically solved by several different integration algorithms [41,80-85] including the Verlet algorithm, the leap-frog algorithm and the velocity Verlet algorithm. The latter algorithm combines the advantages of the Verlet and leap-frog algorithms [41,82,85]. In the velocity Verlet algorithm, the equations for propagating an atom k read as follows

$$\mathbf{r}_k(t+\Delta t) = \mathbf{r}_k(t) + \mathbf{v}_k(t)\Delta t + \frac{1}{2}\mathbf{a}_k(t)\Delta t^2 \qquad \text{(2-72a)}$$

$$\mathbf{v}_k(t+\Delta t) = \mathbf{v}_k(t) + \frac{1}{2}\left[\mathbf{a}_k(t) + \mathbf{a}_k(t+\Delta t)\right]\Delta t \qquad \text{(2-72b)}$$

where $\mathbf{v}$, $\mathbf{a}$, t and Δt are the velocity, the acceleration, the current time and the time step, respectively. Hence, the solution of Eq. 2-71 provides the positions and velocities of all the atoms at every time step over a total time interval (i.e. a trajectory). The time step is typically a femtosecond. The desired total simulation time depends on the complexity of the force field used, the size of the molecule and the computing power available. However, the simulation time should be long enough to represent the physical or chemical phenomena being studied.

Typically, performing molecular dynamics simulation starts by defining the force field, the integration algorithm (the velocity Verlet algorithm in this example), and the thermodynamic ensemble to be used. The initial ($t=0$) positions and velocities of the atoms are then chosen. Next, the integration time step (Δt) and the number of integration steps (total simulation time) are defined. The forces at $t=0$ are then calculated from the energy expression (the left hand side of Eq. 2-71) to determine the acceleration of the atoms. At each subsequent integration step, the positions of the atoms are computed using Eq. 2-72a, the forces are calculated (and hence the accelerations), and the velocities of the atoms are obtained from Eq. 2-72b.

In a thermodynamic ensemble, quantities such as temperature (T), pressure (P), volume (V), number of moles (N), and energy (E) are controlled. The most important thermodynamic ensembles are: (1) the microcanonical (NVE) ensemble where N, V, and E are constant, (2) the canonical (NVT) ensemble in which N, V, and T are constant, and (3) the isothermal–isobaric (NPT) ensemble where N, P, and T are constant. Three of the most widely used methods for controlling the temperature are the Andersen thermostat [83,85,86], the Nosé-Hoover thermostat [83,85], and the Berendsen thermostat [85,87]. For controlling the pressure, the Andersen barostat [86], the Berendsen barostat [87], and the Parrinello–Rahman [88] barostat are commonly used.

2.2.9 Periodic boundary conditions

Simulating condensed phases that are macroscopic in nature necessitates the use of large number of atoms (or molecules) in order to be able to resemble the behavior of the real chemical system. However, computational resources impose a constraint on the size of the system to be simulated. Periodic boundary conditions (PBC) are used to alleviate this problem by making the chemical system under investigation appear as though it is infinite (Figure 2.8).

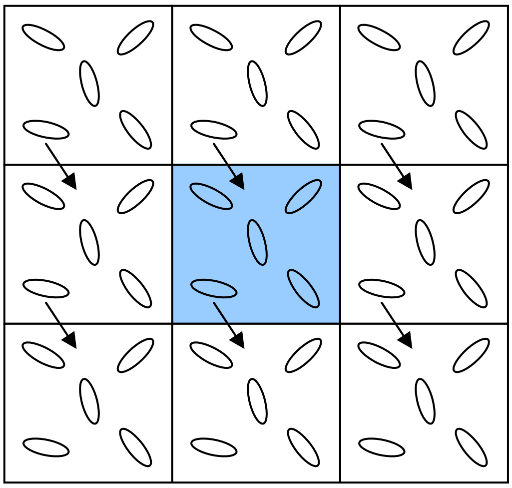

Figure 2.8: Periodic boundary conditions in two dimensions. The simulation box (in blue) is surrounded by eight periodic images. Arrows indicate that if during the simulation an atom (or a molecule) steps outside the boundary of the box, its image simultaneously enters the box.

To avoid double calculating the interatomic nonbonded interactions, a cutoff distance is employed during the simulation. The cutoff distance must be less than half the length of the shortest dimension of the simulation box [42,85]. However, long-range electrostatic interactions are often significant at distances larger than half the box length [42]. Ideally, the dimensions of the simulation box should exceed the range of any significant nonbonded interactions. However, this requires the use of a large simulation box which is computationally impractical. Several alternative methods to the use of a cutoff distance have been devised to handle long-range electrostatic interactions. These include the Ewald summation method [41,42,82-85,89] and the fast multipole moment (FMM) method [41,83-85,89].

2.2.10 Hybrid quantum mechanics/molecular mechanics (QM/MM) methods

In order to make large molecular systems amenable to electronic structure calculations, great advances have been made in developing hybrid QM/MM methods [90-93]. Hybrid QM/MM methods are related to the idea of dividing the molecular system under investigation into two parts where one part is treated by a high level theory (the QM part) and the other is treated by a low level theory (the MM part).

Unlike QM/MM, the ONIOM (our own n-layered integrated molecular orbital molecular mechanics) method is a flexible hybrid method where, in principle, any number and any level of theories can be combined (e.g., QM with QM, QM with MM, etc…) (Figure 2.9) [94-98]. The ONIOM method has been applied to investigate numerous different chemical processes that involve large systems. These include heterogeneous catalysts [99-105] and biomolecular systems [106-110].

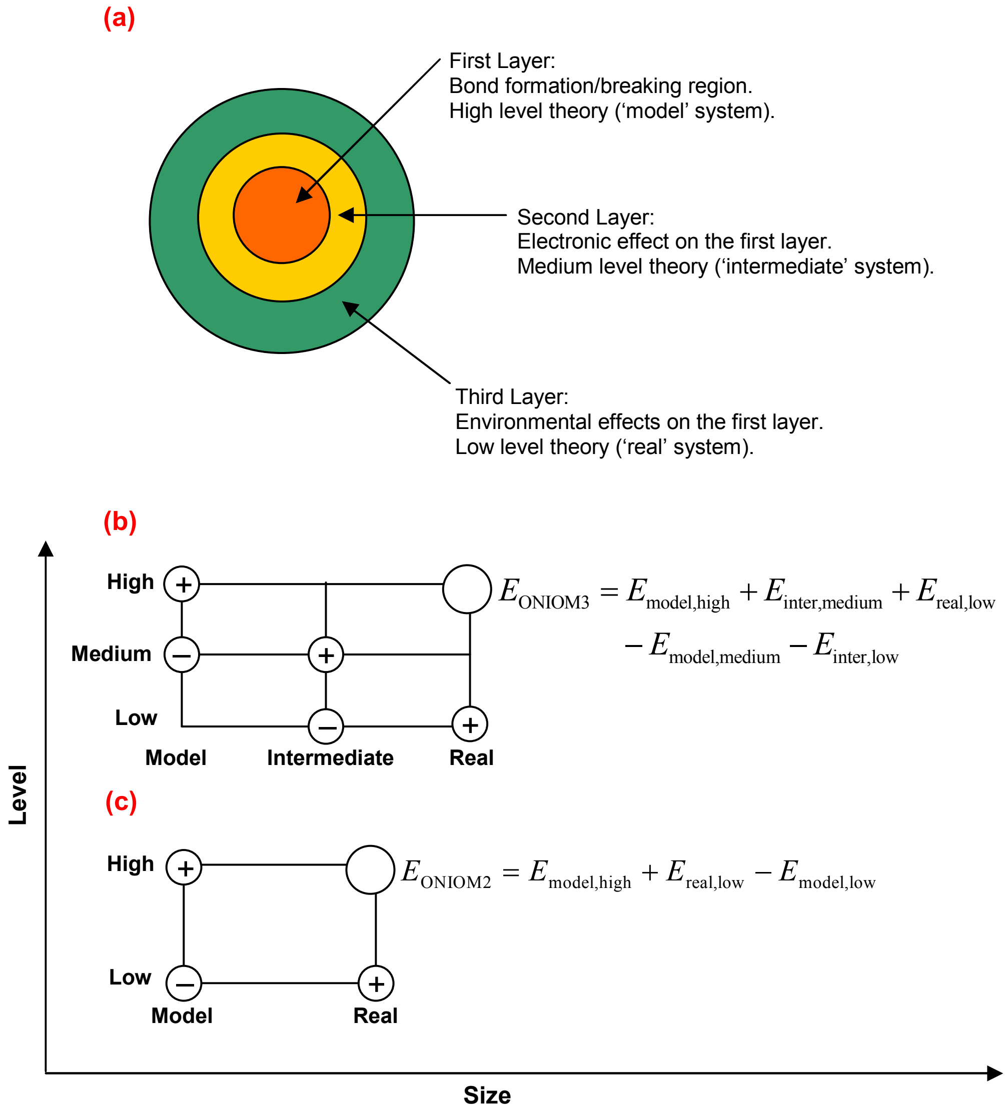

Figure 2.9: The ONIOM layers and models. (a) ONIOM layers, (b) three-layer ONIOM model, and (c) two-layer ONIOM model. Redrawn with modifications from reference 94.

For a two-layer system, the ONIOM energy is obtained by extrapolation and is given by

$$E_{\text{ONIOM}} = E_{\text{model,high}} + E_{\text{real,low}} - E_{\text{model,low}} \qquad \text{(2-73a)}$$

$$E_{\text{ONIOM}} = E_{\text{model,QM}} + E_{\text{real,MM}} - E_{\text{model,MM}} \qquad \text{(2-73b)}$$

where 'model' and 'real' refer to the part of the system that will be treated with the high level computational method and to the full system, respectively, 'high' denotes a high level computational method, and 'low' refers to a lower level method. Hence, for a two-layer system, three energy computations are carried out for an ONIOM single point calculation. Eq. 2-73b is a special case of Eq. 2-73a where the ‘model’ system is treated quantum mechanically and the ‘real’ system is treated by molecular mechanics. ONIOM can also be applied to more than two layers (cf. Figure 2.9). The ONIOM method attempts to reproduce the relative energies at the high level of theory rather than the absolute energies (i.e. $\Delta E_{\text{ONIOM}} \approx \Delta E_{\text{real,high}}$).

In ONIOM method, the dangling bonds that result from dividing the full system into regions are saturated by link atoms (usually hydrogens) and incorporated into the ‘model’ system [95].

As can be seen from Eq. 2-73b, the interaction between the layers is included at the MM level and ONIOM method, therefore, defaults to the mechanical embedding (ME) scheme [95,96]. In the ME scheme, the electrostatic interaction between the ‘model’ and ‘real’ systems is either performed at the MM level or omitted. In an electronic embedding (EE) scheme [95,96], the QM region is polarized by the partial charges of the MM region. The QM Hamiltonian (cf. Eq. 2-9) now includes the partial charges of the MM region. The electrostatic interaction operator is defined as

$$\hat{V}_{\text{elec}} = -\sum_{i=1}^{n} \sum_{k=1}^{\substack{MM \\ atoms}} \frac{q_k}{r_{ik}} + \sum_{I=1}^{N} \sum_{k=1}^{\substack{MM \\ atoms}} \frac{Z_I q_k}{R_{Ik}} . \tag{2-74}$$

A third embedding scheme, which is not implemented in the ONIOM method, is the polarized embedding [41,91]. In this embedding scheme, the MM region is polarized by the charges of the QM atoms.

2.3 References

1. E.V. Anslyn, D.A. Dougherty, Modern Physical Organic Chemistry, University Science Books, Herndon, VA, 2006.
2. M.B. Smith, J. March, March’s Advanced Organic Chemistry: Reactions, Mechanisms, and Structure, John Wiley & Sons, Inc., Hoboken, NJ, 2007.

3. E. Juaristi, Introduction to Stereochemistry and Conformational Analysis, John Wiley & Sons, Inc., New York, NY, 1991.
4. I.N. Levine, Quantum Chemistry, Prentice-Hall, Inc., Upper Saddle River, NJ, 2000.
5. J. McMurry, Organic Chemistry, Brooks/Cole Publishing Company, Pacific Grove, CA, 1992.
6. M. Nógrádi, Stereoselective Synthesis: A Practical Approach, VCH Publishers, Inc., New York, NY, 1995.
7. R.A. Aitken, Chirality. In: Asymmetric Synthesis (R.A. Aitken, S.N. Kilényi, editors), Blackie Academic & Professional, Glasgow, UK, 1995.
8. S.N. Kilényi, First- and Second-Generation Methods: Chiral Starting Materials and Auxiliaries. In: Asymmetric Synthesis (R.A. Aitken, S.N. Kilényi, editors), Blackie Academic & Professional, Glasgow, UK, 1995.
9. S.N. Kilényi, R.A. Aitken, Third- and Fourth-Generation Methods: Asymmetric Reagents and Catalysts. In: Asymmetric Synthesis (R.A. Aitken, S.N. Kilényi, editors), Blackie Academic & Professional, Glasgow, UK, 1995.
10. A. Berkessel, H. Gröger, Asymmetric Organocatalysis – From Biomimetic Concepts to Applications in Asymmetric Synthesis, WILEY-VCH, Weinheim, Germany, 2005, and references cited therein.
11. H. Pellissier, Asymmetric organocatalysis, Tetrahedron 63 (2007) 9267-9331.
12. P.I. Dalko, Asymmetric Organocatalysis: A New Stream in Organic Synthesis. In: Enantioselective Organocatalysis: Reactions and Experimental Procedures (P.I. Dalko, editor), WILEY-VCH, Weinheim, Germany, 2007.
13. S.C. Pan, B. List, New Concepts for Organocatalysis. In: Ernst Schering Foundation Symposium Proceedings: Organocatalysis (M.T. Reetz, B. List, S. Jaroch, H. Weinmann, editors), Springer-Verlag, Berlin, Germany, 2008.
14. E.J. Corey, Catalytic enantioselective Diels-Alder reactions: Methods, mechanistic fundamentals, pathways, and applications, Angewandte Chemie International Edition 41 (2002) 1650-1667.
15. Q-Y. Hu, G. Zhou, E.J. Corey, Application of chiral cationic catalysts to several classical syntheses of racemic natural products transforms them into highly enantioselective pathways, Journal of the American Chemical Society 126 (2004) 13708-13713.
16. E.J. Corey, Enantioselective catalysis based on cationic oxazaborolidines, Angewandte Chemie International Edition 48 (2009) 2100-2117.
17. E.J. Corey, T. Shibata, T.W. Lee, Asymmetric Diels-Alder reactions catalyzed by a triflic acid activated chiral oxazaborolidine, Journal of the American Chemical Society 124 (2002) 3808-3809.
18. D.H. Ryu, T.W. Lee, E.J. Corey, Broad-spectrum enantioselective Diels-Alder catalysis by chiral, cationic oxazaborolidines, Journal of the American Chemical Society 124 (2002) 9992-9993.
19. D.H. Ryu, E.J. Corey, Triflimide activation of a chiral oxazaborolidine leads to a more general catalytic system for enantioselective Diels-Alder addition, Journal of the American Chemical Society 125 (2003) 6388-6390.
20. G. Zhou, Q-Y. Hu, E.J. Corey, Useful enantioselective bicyclization reactions using an N-protonated chiral oxazaborolidine as catalyst, Organic Letters 5 (2003) 3979-3982.
21. D.H. Ryu, G. Zhou, E.J. Corey, Enantioselective and structure-selective Diels-Alder reactions of unsymmetrical quinones catalyzed by a chiral

oxazaborolidinium cation. Predictive selection rules, Journal of the American Chemical Society 126 (2004) 4800-4802.

22. D.H. Ryu, E.J. Corey, Enantioselective cyanosilylation of ketones catalyzed by a chiral oxazaborolidinium ion, Journal of the American Chemical Society 127 (2005) 5384-5387.
23. D.H. Ryu, G. Zhou, E.J. Corey, Nonparallelism between reaction rate and dienophile-catalyst affinity in catalytic enantioselective Diels-Alder reactions, Organic Letters 7 (2005) 1633-1636.
24. D. Liu, E. Canales, E.J. Corey, Chiral oxazaborolidine-aluminum bromide complexes are usually powerful and effective catalysts for enantioselective Diels-Alder reactions, Journal of the American Chemical Society 129 (2007) 1498-1499.
25. H.B. Schlegel, Exploring potential energy surfaces for chemical reactions: An overview of some practical methods, Journal of Computational Chemistry 24 (2003) 1514-1527.
26. H.B. Schlegel, Spin Contamination. In: Encyclopedia of Computational Chemistry, Vol. 4 (P.v.R. Schleyer, editor-in-chief), John Wiley & Sons Ltd., Chichester, UK, 1998.
27. C.C.J. Roothaan, New developments in molecular orbital theory, Reviews of Modern Physics 23 (1951) 69-89.
28. H.B. Schlegel, M.J. Frisch, Transformation between Cartesian and pure spherical harmonic Gaussians, International Journal of Quantum Chemistry 54 (1995) 83-87.
29. P. Hohenberg, W. Kohn, Inhomogeneous electron gas, Physical Review 136 (1964) B864-867.
30. W. Kohn, L.J. Sham, Self-consistent equations including exchange and correlation effects, Physical Review 140 (1965) A1133-1138.
31. A.D. Becke, Density-functional thermochemistry. III. The role of exact exchange, Journal of Chemical Physics 98 (1993) 5648-5652.
32. S.H. Vosko, L. Wilk, M. Nusair, Accurate spin-dependent electron liquid correlation energies for local spin density calculations: A critical analysis, Canadian Journal of Physics 58 (1980) 1200-1211.
33. C. Lee, W. Yang, R.G. Parr, Development of the Colle-Salvetti correlation-energy formula into a functional of the electron density, Physical Review B37 (1988) 785-789.
34. P.J. Stephens, F.J. Devlin, C.F. Chabalowski, M.J. Frisch, Ab initio calculation of vibrational absorption and circular dichroism spectra using density functional force fields, Journal of Physical Chemistry 98 (1994) 11623-11627.
35. W. Koch, M. Holthausen, A Chemist's Guide to Density Functional Theory, Wiley-VCH Verlag, Weinheim, Germany, 2001.
36. H.B. Schlegel, Optimization of Equilibrium Geometries and Transition Structures. In: *Ab Initio* Methods in Quantum Chemistry – I (K.P. Lawley, editor), John Wiley & Sons Ltd., Chichester, UK, 1987.
37. H.B. Schlegel, Some Practical Suggestions for Optimizing Geometries and Locating Transition States. In: New Theoretical Concepts for Understanding Organic Reactions (J. Bertrán, I.G. Csizmadia, editors), Kluwer Academic Publishers, Dordrecht, the Netherland, 1989.
38. H.B. Schlegel, Geometry Optimization on Potential Energy Surfaces. In: Advanced Series in Physical Chemistry – Vol. 2: Modern Electronic Structure

Theory – Part I (D.R. Yarkony, editor), World Scientific Publishing Co. Pte. Ltd., Singapore, 1995.

39. H.B. Schlegel, Geometry Optimization: 1. In: Encyclopedia of Computational Chemistry, Vol. 2 (P.v.R. Schleyer, editor-in-chief), John Wiley & Sons Ltd., Chichester, UK, 1998.
40. H.P. Hratchian, H.B. Schlegel, Finding Minima, Transition States, and Following Reaction Pathways on *Ab Initio* Potential Energy Surfaces. In: Theory and Applications of Computational Chemistry: The First Forty Years (C. Dykstra, G. Frenking, K.S. Kim, G.E. Scuseria, editors), Elsevier B.V., Amsterdam, the Netherlands, 2005.
41. F. Jensen, Introduction to Computational Chemistry, John Wiley & Sons Ltd, Chichester, England, 2007.
42. A. R. Leach, Molecular Modelling: Principles and Applications, Pearson Education Limited, Essex, England, 2001.
43. M.A. Ratner, G.C. Schatz, Introduction to Quantum Mechanics in Chemistry, Prentice-Hall, Inc., Upper Saddle River, NJ, 2001.
44. E.B. Wilson, J.C. Decius, P.C. Cross, Molecular Vibrations: The Theory of Infrared and Raman Vibrational Spectra, Dover Publications, Inc., Mineola, NY, 1980.
45. I.N. Levine, Molecular Spectroscopy, John Wiley & Sons, Inc., New York, NY, 1975.
46. J.W. Ochterski, Vibrational analysis in Gaussian, 1999. http://www.gaussian.-com/g_whitepap/vib.htm.
47. J.A. Pople, R. Krishnan, H.B. Schlegel, J.S. Binkley, Derivative studies in Hartree-Fock and Møller-Plesset theories, International Journal of Quantum Chemistry: Quantum Chemistry Symposium 13 (1979) 225-241.
48. H.B. Schlegel, J.S. Binkley, J.A. Pople, First and second derivatives of two electron integrals over Cartesian Gaussians using Rys polynomials, Journal of Chemical Physics 80 (1984) 1976-1981.
49. W.J. Hehre, L. Radom, P.v.R. Schleyer, J.A. Pople, *Ab Initio* Molecular Orbital Theory, John Wiley & Sons, Inc., New York, NY, 1986.
50. H.B. Schlegel, Analytical second derivatives of two electron integrals over *s* and *p* Cartesian Gaussians, Journal of Chemical Physics 90 (1989) 5630-5634.
51. P. Pulay, Analytical Derivative Techniques and the Calculation of Vibrational Spectra. In: Advanced Series in Physical Chemistry – Vol. 2: Modern Electronic Structure Theory – Part II (D.R. Yarkony, editor), World Scientific Publishing Co. Pte. Ltd., Singapore, 1995.
52. A. Szabo, N.S. Ostlund, Modern Quantum Chemistry: Introduction to Advanced Electronic Structure Theory, Dover Publications, Inc., Mineola, NY, 1996.
53. J. Gauss, Molecular Properties. In: NIC Series – Vol. 3: Modern Methods and Algorithms of Quantum Chemistry (J. Grotendorst, editor), John von Neumann Institute for Computing, Jülich, 2000. http://www.fz-juelich.de/nic-series/Volume3/Volume3.html.
54. R. Fournier, Second and third derivatives of the linear combination of Gaussian type orbitals-local spin density energy, Journal of Chemical Physics 92 (1990) 5422-5429.
55. B.I. Dunlap, J. Andzelm, Second derivatives of the local-density-functional total energy when the local potential is fitted, Physical Review A 45 (1992) 81-87.

56. A. Komornicki, G. Fitzgerald, Molecular gradients and hessians implemented in density functional theory, Journal of Chemical Physics 98 (1993) 1398-1421.
57. B.G. Johnson, M.J. Frisch, Analytic second derivatives of the gradient-corrected density functional energy. Effect of quadrature weight derivatives, Chemical Physics Letters 216 (1993) 133-140.
58. H. Jacobsen, A. Bérces, D.P. Swerhone, T. Ziegler, Analytic second derivatives of molecular energies: a density functional implementation, Computer Physics Communications 100 (1997) 263-276.
59. D. Egli, S.R. Billeter, Analytic second variational derivative of the exchange-correlation functional, Physical Review B 69 (2004) 115106 1-14.
60. J. Gerratt, I.M. Mills, Force constants and dipole-moment derivatives of molecules from perturbed Hartree-Fock calculations. I, The Journal of Chemical Physics 49 (1968) 1719-1739.
61. T.C. Caves, M. Karplus, Perturbed Hartree-Fock Theory. I. Diagrammatic double-perturbation analysis, The Journal of Chemical Physics 50 (1969) 3649-3661.
62. S.M. Colwell, C.W. Murray, N.C. Handy, R.D. Amos, The determination of hyperpolarisabilities using density functional theory, Chemical Physics Letters 210 (1993) 261-268.
63. A.M. Lee, S.M. Colwell, The determination of hyperpolarisabilities using density functional theory with nonlocal functionals, Journal of Chemical Physics 101 (1994) 9704-9709.
64. A. Bérces, R.M. Dickson, L. Fan, H. Jacobsen, D. Swerhone, T. Ziegler, An implementation of the coupled perturbed Kohn-Sham equations: perturbation due to nuclear displacements, Computer Physics Communications 100 (1997) 247-262.
65. J. B. Foresman, Æleen Frisch, Exploring Chemistry with Electronic Structure Methods, Gaussian, Inc., Pittsburgh, PA, 1996.
66. J.W. Ochterski, Thermochemistry in Gaussian, 2000. http://www.gaussian.-com/g_whitepap/thermo.htm.
67. O. Wiest, D.C. Montiel, K.N. Houk, Quantum mechanical methods and the interpretation and prediction of pericyclic reaction mechanisms, Journal of Physical Chemistry A 101 (1997) 8378-8388.
68. R. Bruckner, Advanced Organic Chemistry: Reaction Mechanisms, Harcourt/Academic Press, Burlington, MA, 2002.
69. F.A. Carey, R.J. Sundberg, Advanced Organic Chemistry: Part A: Structure and Mechanisms, Springer Science Business Media, LLC, 2007.
70. D. Suárez, J.A. Sordo, On the origin of the *endo*/*exo* selectivity in Diels-Alder reactions, Chemical Communications (1998) 385-386.
71. M.N. Paddon-Row, L.C. H. Kwan, A.C. Willis, M.S. Sherburn, Enantioselective oxazaborolidinium-catalyzed Diels-Alder reactions without CH···O hydrogen bonding, Angewandte Chemie International Edition 47 (2008) 7013-7017.
72. H. Eyring, The activated complex in chemical reactions, Journal of Chemical Physics 3 (1935) 107-115.
73. K.J. Laidler, M.C. King, Development of transition-state theory, Journal of Physical Chemistry 87 (1983) 2657–2664.
74. S.K. Upadhyay, Chemical Kinetics and Reaction Dynamics, Anamaya Publishers, New Delhi, India, 2006.

75. N.L. Allinger, Force Fields: A Brief Introduction. In: Encyclopedia of Computational Chemistry, Vol. 2 (P.v.R. Schleyer, editor-in-chief), John Wiley & Sons Ltd., Chichester, UK, 1998.
76. J.R. Maple, Force Fields: A General Discussion. In: Encyclopedia of Computational Chemistry, Vol. 2 (P.v.R. Schleyer, editor-in-chief), John Wiley & Sons Ltd., Chichester, UK, 1998.
77. D.C. Young, Computational Chemistry: A Practical Guide for Applying Techniques to Real-World Problems, John Wiley & Sons, Inc., New York, NY, 2001.
78. C.J. Cramer, Essentials of Computational Chemistry: Theories and Models, John Wiley & Sons Ltd, Chichester, England, 2004.
79. E. Lewars, Computational Chemistry: Introduction to the Theory and Applications of Molecular and Quantum Mechanics, Kluwer Academic Publishers, Dordrecht, the Netherland, 2004.
80. G. Sutmann, Classical Molecular Dynamics. In: NIC Series – Vol. 10: Quantum Simulations of Complex Many-Body Systems: From Theory to Algorithms (J. Grotendorst, D. Marx, A. Muramatsu, editors), John von Neumann Institute for Computing, Jülich, 2002. http://www.fz-juelich.de/nic-series/volume10/.
81. M.P. Allen, Introduction to Molecular Dynamics Simulation. In: NIC Series – Vol. 23: Computational Soft Matter: From Synthetic Polymers to Proteins (N. Attig, K. Binder, H. Grubmüller, K. Kremer, editors), John von Neumann Institute for Computing, Jülich, 2004. http://www.fz-juelich.de/nic-series/volume23/volume23.html.
82. M.P. Allen, D.J. Tildesley, Computer Simulation of Liquids, Oxford University Press, Oxford, UK, 1987.
83. D. Frenkel, B. Smit, Understanding Molecular Simulation: From Algorithms to Applications, Academic Press, London, UK, 2002.
84. D.C. Rapaport, The Art of Molecular Dynamics Simulation, Cambridge University Press, Cambridge, UK, 2004.
85. M.J. Field, A Practical Introduction to the Simulation of Molecular Systems, Cambridge University Press, Cambridge, UK, 2007.
86. H.C. Andersen, Molecular dynamics simulations at constant pressure and/or temperature, Journal of Chemical Physics 72 (1980) 2384-2393.
87. H.J.C. Berendsen, J.P.M. Postma, W.F. van Gunsteren, A. DiNola, J.R. Haak, Molecular dynamics with coupling to an external bath, Journal of Chemical Physics 81 (1984) 3684-3690.
88. M. Parrinello, A. Rahman, Polymorphic transitions in single crystals: A new molecular dynamics method, Journal of Applied Physics 52 (1981) 7182-7190.
89. P.Gibbon, G. Sutmann, Long-Range Interactions in Many-Particle Simulation. In: NIC Series – Vol. 10: Quantum Simulations of Complex Many-Body Systems: From Theory to Algorithms (J. Grotendorst, D. Marx, A. Muramatsu, editors), John von Neumann Institute for Computing, Jülich, 2002. http://www.fz-juelich.de/nic-series/volume10/.
90. J. Gao, Hybrid Quantum Mechanical/Molecular Mechanical (QM/MM) Methods. In: Encyclopedia of Computational Chemistry, Vol. 2 (P.v.R. Schleyer, editor-in-chief), John Wiley & Sons Ltd., Chichester, UK, 1998.
91. P. Sherwood, Hybrid Quantum Mechanics/Molecular Mechanics Approaches. In: NIC Series – Vol. 3: Modern Methods and Algorithms of Quantum

Chemistry (J. Grotendorst, editor), John von Neumann Institute for Computing, Jülich, 2000. http://www.fz-juelich.de/nic-series/Volume3/.

92. H. Lin, D.G. Truhlar, QM/MM: What have we learned, where are we, and where do we go from here? Theoretical Chemistry Accounts 117 (2007) 185-199.
93. A.L. Tchougréeff, Hybrid Methods of Molecular Modeling. Progress in Theoretical Chemistry and Physics – Vol. 17, Springer Science, Berlin, Germany, 2008.
94. K. Morokuma, ONIOM and its applications to material chemistry and catalyses, Bulletin of the Korean Chemical Society 24 (2003) 797-801.
95. T. Vreven, K. Morokuma, Hybrid Methods: ONIOM (QM:MM) and QM/MM. In: Annual Reports in Computational Chemistry – Vol. 2 (T.D.Crawford, editor), Elsevier B.V., Amsterdam, The Netherlands, 2006.
96. T. Vreven, K.S. Byun, I. Komáromi, S. Dapprich, J.A. Montgomery, Jr., K. Morokuma, M.J. Frisch, Combining quantum mechanics methods with molecular mechanics methods in ONIOM, Journal of Chemical Theory and Computation 2 (2006) 815-826.
97. T. Vreven, K. Morokuma, Ö. Farkas, H.B. Schlegel, M.J. Frisch, Geometry optimization with QM/MM, ONIOM, and other combined methods. I. Microiterations and constraints, Journal of Computational Chemistry 24 (2003) 760-769.
98. H.P. Hratchian, P.V. Parandekar, K. Raghavachari, M.J. Frisch, T. Vreven, QM:QM electronic embedding using Mulliken atomic charges: Energies and analytic gradients in an ONIOM framework, The Journal of Chemical Physics 128 (2008) 034107-1-11.
99. Y.V. Joshi, K.T. Thomson, Embedded cluster (QM/MM) investigation of C6 diene cyclization in HZSM-5, Journal of Catalysis 230 (2005) 440-463.
100. A. Rattanasumrit, V. Ruangpornvisuti, Theoretical study of conversion reactions of ketone to hydroxyalkylene in cluster models of zeolite H-ZSM-5, Journal of Molecular Catalysis A: Chemical 239 (2005) 68-75.
101. S. Namuangruk, P. Pantu, J. Limtrakul, Investigation of ethylene dimerization over faujasite zeolite by the ONIOM method, ChemPhysChem 6 (2005) 1333-1339.
102. J. Lomratsiri, M. Probst, J. Limtrakul, Structure and adsorption of a basic probe molecule on H-ZSM-5 nanostructured zeolite: An embedded ONIOM study, Journal of Molecular Graphics and Modelling 25 (2006) 219-225.
103. S. Yuan, J. Wang, Y.-B. Duan, Y.-W. Li, H. Jiao, An ONIOM2 study on pyridine adsorption in the main channels of Li- and Na-MOR, Journal of Molecular Catalysis A: Chemical 256 (2006) 130-137.
104. P. Pantu, B. Boekfa, J. Limtrakul, The adsorption of saturated and unsaturated hydrocarbons on nanostructured zeolites (H-MOR and H-FAU): An ONIOM study, Journal of Molecular Catalysis A: Chemical 277 (2007) 171-179.
105. J. Sirijaraensre, J. Limtrakul, Effect of the acidic strength on the vapor phase Beckmann rearrangement of cyclohexanone oxime over the MFI zeolite: An embedded ONIOM study, Physical Chemistry Chemical Physics 11 (2009) 578-585.
106. T. Vreven, K. Morokuma, Investigation of the $S_0 \rightarrow S_1$ excitation in bacteriorhodopsin with the ONIOM (MO:MM) hybrid method, Theoretical Chemistry Accounts 109 (2003) 125-132.

107. W. Deng, T. Vreven, M.J. Frisch, K.B. Wiberg, Application of the ONIOM method to enantioselective deprotonation in the presence of spartein, Journal of Molecular Structure: THEOCHEM 775 (2006) 93-99.
108. E.M. Sproviero, K. Shinopoulos, J.A. Gascón, J.P. McEvoy, G.W. Brudvig, V.S. Batista, QM/MM computational studies of substrate water binding to the oxygen-evolving centre of photosystem II, Philosophical Transactions of the Royal Society B 363 (2008) 1149-1156.
109. M. Lundberg, T. Kawatsu, T. Vreven, M.J. Frisch, K. Morokuma, Transition states in a protein environment – ONIOM QM:MM modeling of isopenicillin N synthesis, Journal of Chemical Theory and Computation 5 (2009) 222-234.
110. P. Banáš, P. Jurečka, N.G. Walter, J. Šponer, M. Otyepka, Theoretical studies of RNA catalysis: Hybrid QM/MM methods and their comparison with MD and QM, Methods 49 (2009) 202-216.
111. J.P. Lowe, K.A. Peterson, Quantum Chemistry, Elsevier Academic Press, Burlington, MA, 2006.
112. D.A. McQuarrie, Quantum Chemistry, University Science Books, Sausalito, CA, 2007.
113. D.B. Cook, Handbook of Computational Chemistry, Oxford University Press, Oxford, UK, 1998.
114. T. Helgaker, P. Jørgensen, J. Olsen, Molecular Electronic-Structure Theory, John Wiley & Sons Ltd, Chichester, England, 2000.
115. P.W. Atkins, R.S. Friedman, Molecular Quantum Mechanics, Oxford University Press, Oxford, UK, 2004.
116. M. Springborg, Methods of Electronic Structure Calculations: From Molecules to Solids, John Wiley & Sons Ltd, Chichester, England, 2000.
117. J. Kohanoff, Electronic Structure Calculations for Solids and Molecules: Theory and Computational Methods, Cambridge University Press, Cambridge, UK, 2006.
118. S.M. Bachrach, Computational Organic Chemistry, John Wiley & Sons, Inc., Hoboken, NJ, 2007.
119. C. Trindle, D. Shillady, Electronic Structure Modeling: Connections between Theory and Software, CRC Press, Boca Raton, FL, 2008.
120. A. Hinchliffe, Modelling Molecular Structures, John Wiley & Sons Ltd, Chichester, England, 2000.
121. R.G. Parr, W. Yang, Density Functional Theory of Atoms and Molecules, Oxford University Press, Oxford, UK, 1989.
122. J.M. Seminario, P. Politzer (editors), Modern Density Functional Theory: A Tool for Chemistry, Elsevier Science B.V., Amsterdam, The Netherlands, 1995.
123. D.S. Sholl, J.A. Steckel, Density Functional Theory: A Practical Introduction, John Wiley & Sons, Inc., Hoboken, NJ, 2009.
124. H.B. Schlegel, J.J.W. McDouall, Do You Have SCF Stability and Convergence Problems? In: Computational Advances in Organic Chemistry: Molecular Structure and Reactivity (C. Ögretir, I.G. Csizmadia, editors), Kluwer Academic Publishers, Dordrecht, the Netherland, 1991.

3 Enantioselective Organocatalytic Diels-Alder Reactions: A Density Functional Theory and Kinetic Isotope Effects Study

The quantum mechanical analysis of the energetics and electronic structures of molecules at equilibrium and transition states provides an important tool for understanding chemical reactions. Density functional methods are increasingly being used in investigating a variety of chemical reactions and providing a cost-effective yet accurate way of including the electron correlation effects. The B3LYP functional is one of the most popular functionals for the calculations on organic molecules. In this chapter, the application of density functional theory at the B3LYP/6-31G(d) level to the enantioselective Diels-Alder reaction is explored. The outcomes of the current study are presented with emphasis on relating them to theory and experiment.

3.1 Introduction

The Diels-Alder cycloaddition reaction is one of the most powerful reactions for the construction of six-membered rings with several stereogenic centers in a regio- and stereo-controlled way. In addition, this reaction is seen as the key step in the synthesis of many important compounds such as reserpine, cortisone and myrocin C.

The development of enantioselective Diels-Alder reactions involving the use of chiral organocatalysts has been the subject of numerous studies [1-11]. For example, the chiral oxazaborolidinium cation **13** has been shown to be a very useful and versatile catalyst for the synthesis of many biologically complex molecules such as estrone, the oral contraceptive desogestrel, and the antiflu drug oseltamivir [3].

In the Diels-Alder reaction, a molecule with a conjugated system of four π electrons (the diene) reacts with another molecule with two π electrons (the dienophile) to produce a molecule with a six-membered ring by the formation of two new σ bonds. The nature of the formation of these new σ bonds has been the subject of long debate [12-16]. Two mechanisms are possible; a concerted mechanism involving a partial formation of the two new σ bonds in a single transition structure, and a stepwise mechanism having a biradical or zwitterionic intermediate with one of the σ bonds formed. In the concerted mechanism, if the two σ bonds are formed to the same extent, then the reaction is synchronous. Otherwise, it is asynchronous. Although an agreement has been reached in favor of the concerted mechanism, the presence of external influences such as a catalyst may change the mechanism from concerted to stepwise [17-19]. Furthermore, the existence of both concerted and stepwise trajectories has been suggested by femtosecond dynamics investigations of the Diels-Alder reaction [20,21].

With the use of electronic structure calculations it is possible to gain insights into the details of chemical reactions and molecular structures and properties that are difficult to achieve experimentally. In addition, electronic structure calculations help elucidate experimental results and make predictions that can then be tested experimentally. In such calculations, appropriate stationary points on the potential energy surface corresponding to equilibrium and transition structures are often located and characterized, and a reaction mechanism(s) is then proposed.

Density functional methods often yield energies within the desired chemical accuracy (errors less than 2 kcal/mol) despite their inability to systematically improve such accuracy [22]. The inclusion of electron correlation in DFT as well as DFT's high computational efficiency have allowed the computation of many chemically interesting systems without imposing serious constraints on the system size. Numerous examples of the application of DFT to the Diels-Alder reaction are found in the chemical literature. The B3LYP/6-31G(d) has been the method of choice for such application and has proven to produce energies and thermochemical quantities comparable with experiment in addition to high quality equilibrium and transition structures [19,23-42].

The work described in this chapter explores the application of density functional theory for better understanding of the Diels-Alder reactions involving chiral oxazaborolidinium cation as an organocatalyst. The rules affecting the site selectivity and enantioselectivity are computationally investigated, and the mechanistic aspects of the Diels-Alder reactions in the presence of the oxazaborolidinium cation are described. The understanding of the role of the catalyst is of importance in order to improve the catalyst itself or to help design other enantioselective syntheses.

3.2 Computational Details

Single-point energy calculations, geometry optimizations, and vibrational frequencies of the reactants, transition structures and products were carried out *in vacuo* using density functional theory with the B3LYP functional and the 6-31G(d) basis set as implemented in the Gaussian 03 program [43].

Prior to B3LYP/6-31G(d) calculations, all equilibrium and transition structures were optimized and characterized using the AM1 semiempirical method followed by B3LYP/3-21G calculations. This often allows reaching better structures and reduces the total number of steps required at the higher level of theory.

The default SCF algorithm in the Gaussian 03 program is a combination of two direct inversion in the iterative subspace (DIIS) [44,45] extrapolation methods, namely, EDIIS [46] and CDIIS [47]. In the event of convergence problem, in particular for transition structures, the keyword “`scf=(maxconventionalcycles=20,xqc)`” was used. Using this keyword, the default algorithm is applied for the first 20 cycles then the quadratically convergent (QC) SCF algorithm [48] is used. This algorithm ensures convergence though it is slower than the default procedure.

Geometry optimizations to local minima and transition structures were accomplished with the Berny algorithm [49] in redundant internal coordinates [50] without any symmetry restriction. The Berny algorithm is a quasi-Newton algorithm that uses an estimate of the Hessian constructed from a simple valence force field. The estimated Hessian is then updated at each geometry optimization step using the computed gradient. For transition structure optimization, the Hessian is computed at the first step using the current quantum mechanical method and then improved in subsequent steps using the computed gradient. The redundant internal coordinates are built from all bonds, all valence angles between bonded atoms, and all dihedral angles between bonded atoms. The use of such coordinates significantly reduces the number of steps required for geometry optimization as compared to Cartesian coordinates or nonredundant internal coordinates (*Z*-matrix coordinates).

Vibrational frequency calculations were performed at the optimized geometries to verify whether the obtained structures are minima or transition structures as well as to determine zero-point vibrational energies and thermochemical quantities (enthalpies, entropies, and Gibbs free energies). In Gaussian, an extra geometry optimization step is routinely performed after each frequency calculation using the accurately computed Hessian in order to confirm that the structure is a stationary point. If all the optimization convergence criteria are met then the program will print “`-- Stationary point found`”. In case that the structure was not a stationary point, an additional geometry optimization was carried out reading the accurate Hessian from the frequency calculation. This was done by including the keywords "`Opt=ReadFC Geom=Check Guess=Read`" in the input file. The obtained structure was then reconfirmed by a frequency calculation. The vibration associated with the imaginary frequency was ensured to correspond to a displacement in the direction of the reaction coordinate. This was achieved with the graphical user interface for Gaussian program (GaussView). The zero-point vibrational energies and thermochemical quantities were calculated using frequencies scaled by 0.9804. Thermochemical quantities were calculated at both 298.15 K and 178.15 K and at 1.0 atm pressure.

The ISOEFF07 program [51] was used for kinetic isotope effects calculations at 298.15 K.

3.3 Results and Discussion

3.3.1 Description of the studied reactions and stereochemical nomenclature

The Diels-Alder reaction of quinones is highly useful in the synthesis of many complex natural products. An example of an enantioselective reaction utilizing the chiral oxazaborolidinium cation catalyst **13** in a Diels-Alder reaction has been shown by Corey in a reaction between 2-methyl-1,3-butadiene (isoprene) **14** and 2,3-dimethyl-1,4-benzoquinone **15** [3,6] and is illustrated in Figure 3.1.

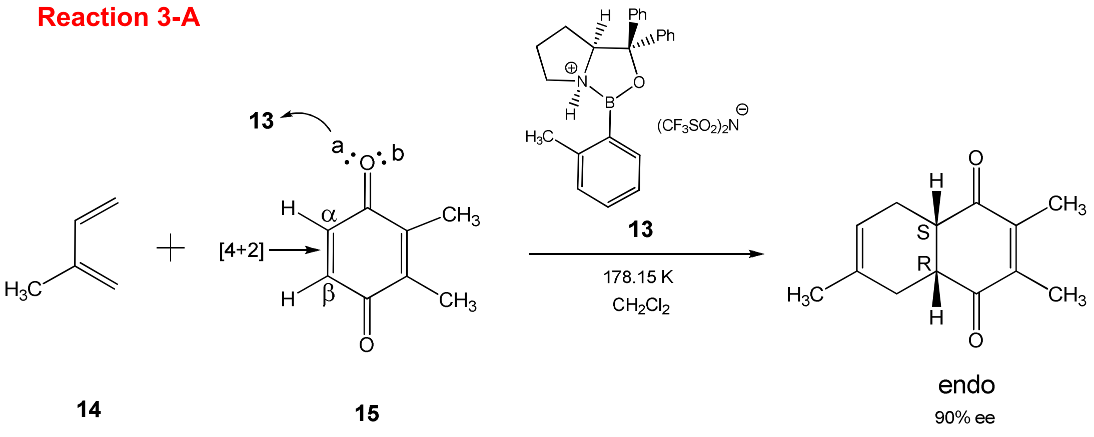

Figure 3.1: Corey's enantioselective Diels-Alder reaction of benzoquinone using chiral oxazaborolidinium catalyst (reference 6).

The structure and stereochemical configuration of the major product from this reaction can be predicted using the experimentally derived Corey's predictive selection rules and mechanistic model [2,3,8]. These can be summarized as follows:

(1) At the transition state, the bonding of the diene to carbon β to the carbonyl group that coordinates with the catalyst is stronger than bonding to carbon α (i.e. a concerted asynchronous reaction pathway) (Figure 3.2).

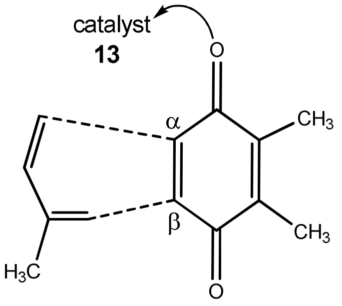

Figure 3.2: Asynchronous bond formation at the transition state.

(2) The double bond of the benzoquinone bearing two hydrogens is more reactive than that bearing substituents (site selectivity).

(3) The predominant product will result from coordination of the catalyst to the oxygen lone pair from the *a* side (i.e. *syn* to the HC═CH subunit that undergoes the [4 + 2]-cycloaddition) rather than the *b* side (i.e. *anti* to the HC═CH subunit that undergoes the [4 + 2]-cycloaddition) since *a* is sterically more accessible than *b* (Figure 3.1). The primary interaction in this coordination complex is between the carbonyl oxygen and the boron of the catalyst. The secondary interaction is between the C_{α}–H hydrogen and the catalyst oxygen (i.e. a nonconventional hydrogen bond [52,53]).

(4) The preferred catalyst coordination is at the more basic of the two benzoquinone oxygens. In addition, the coordination of the catalyst to the carbonyl persists not only in the transition state but even in the Diels-Alder cycloadduct.

(5) The preferred addition of the diene is to the front face of the α,β double bond (i.e. away from the phenyl groups of the catalyst). The other route of addition is to the rear face of the α,β double bond.

(6) The favored 3-dimensional transition state corresponds to the *endo* arrangement of the diene and the catalyst-coordinated benzoquinone (i.e. the reactants lie directly on top of one another so that the two hydrogens attached to the α and β carbon atoms end up *syn* to the two-carbon unsaturated bond in the product). If the two hydrogens end up *anti* to the two-carbon unsaturated bond in the product, then the transition state corresponds to the *exo* arrangement.

(7) The *s-cis* diene is more reactive than the *s-trans* rotamer.

In the Diels-Alder Reaction 3-A (Figure 3.1), there is a pair of possible enantiomers of the catalyst **13**, either the *S* or the *R* stereoisomer. In addition, there are two rotamers for each configuration resulting from the rotation about the B–*o*-tolyl bond. Besides, the diene can adapt the *s-cis* or the *s-trans* conformation and there are two possible sites (double bonds) on the benzoquinone that the diene can attack approaching from either the front or the rear face. Moreover, the catalyst coordination to the benzoquinone can be *syn* or *anti* to the HC═CH subunit that undergoes the [4 + 2]-cycloaddition. Since there are two stereogenic carbons in the products, there will be up to four diastereomeric transition states ((*S*,*R*), (*R*,*S*), (*R*,*R*), and (*S*,*S*)). Fortunately, in this reaction, there is no issue of regioselectivity since 2,3-

dimethyl-1,4-benzoquinone is C_2 symmetric. Also, since the two benzoquinone oxygens are equally available for catalyst coordination, Corey's predictive rule number 4 does not apply here. Thus, there would be numerous possible pathways for this reaction to proceed.

To simplify matters, the model catalyst **16** is used throughout this investigation. This catalyst eliminates the need for the rotamers mentioned above to be considered and reduces the computational cost as it requires smaller number of basis functions compared to the catalyst **13**. The (*S*)-enantiomer of the catalyst **16** is used since it is the more commonly used enantiomer in experimental studies [4-11,54].

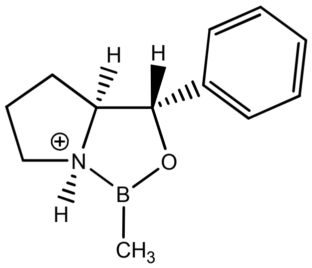

16

As for the possible diastereomeric products, only the enantiomeric pair (*S*,*R*) and (*R*,*S*) is considered in the current work since the (*S*,*R*)-enantiomer is the major product observed experimentally (Figure 3.1) [3,6].

To investigate the site selectivity, only the uncatalyzed reaction pathways are considered. These are depicted in Figures 3.3 and 3.4. Only the addition of the diene to the less substituted double bond of the benzoquinone in the presence of catalyst **16** as illustrated in Figures 3.5 and 3.6 is studied here (cf. Section 3.3.2).

Reaction 3-B

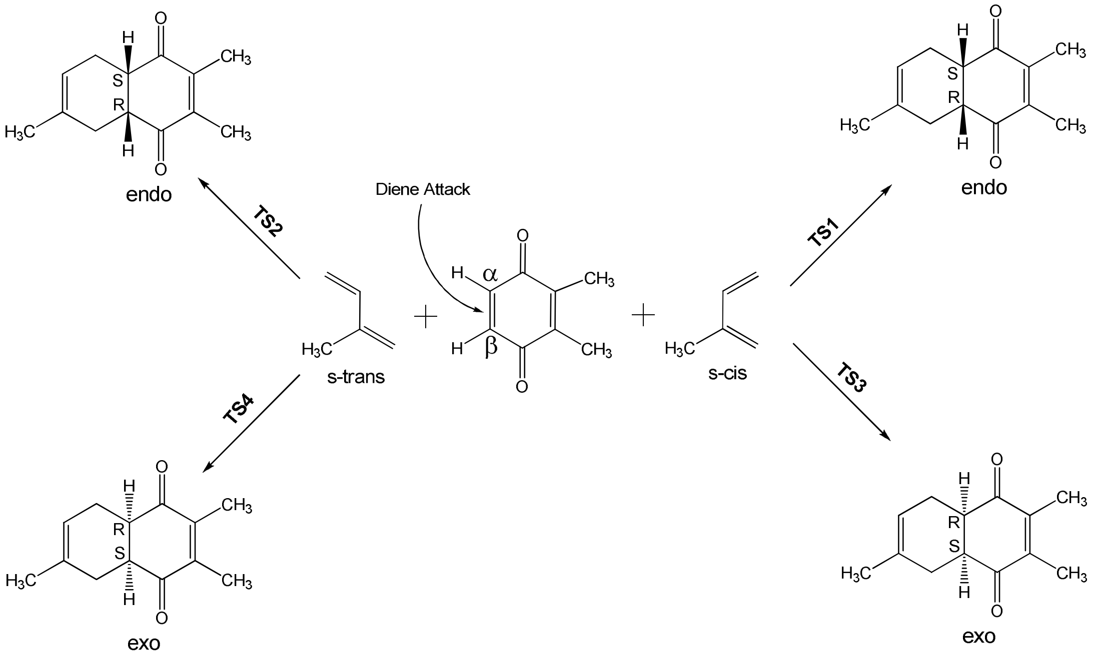

Figure 3.3: Uncatalyzed Diels-Alder reaction with four possible reaction pathways. Diene addition to the less substituted double bond. Transition states are as shown in Figure 3.10.

Reaction 3-C

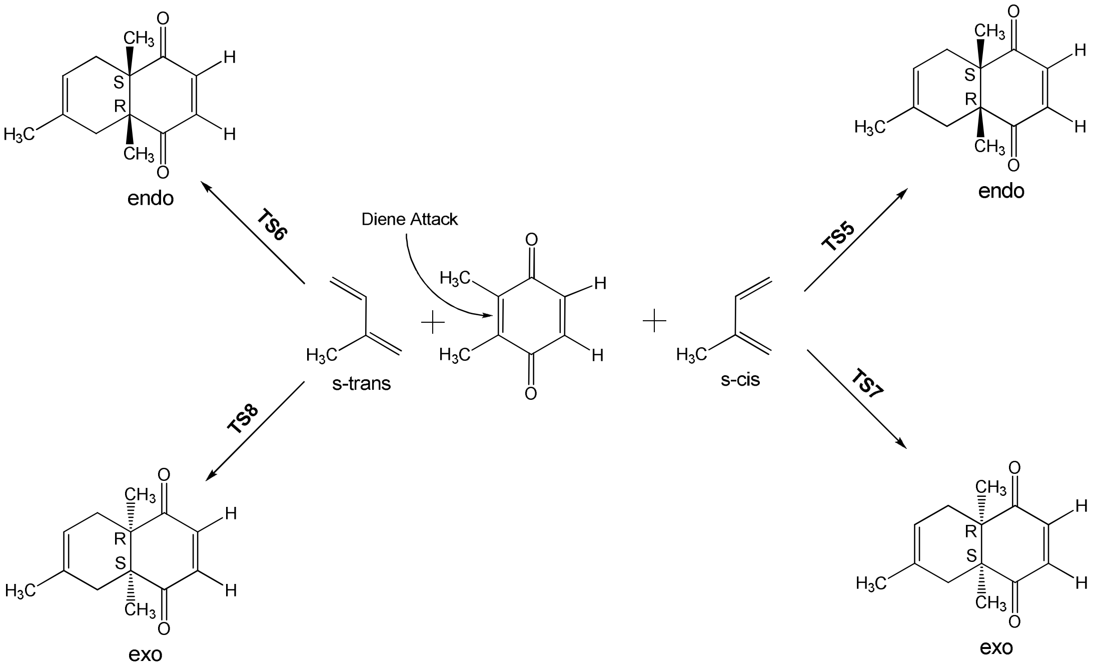

Figure 3.4: Uncatalyzed Diels-Alder reaction with four possible reaction pathways. Diene addition to the methyl substituted double bond. Transition states are as shown in Figure 3.11.

Reaction 3-D

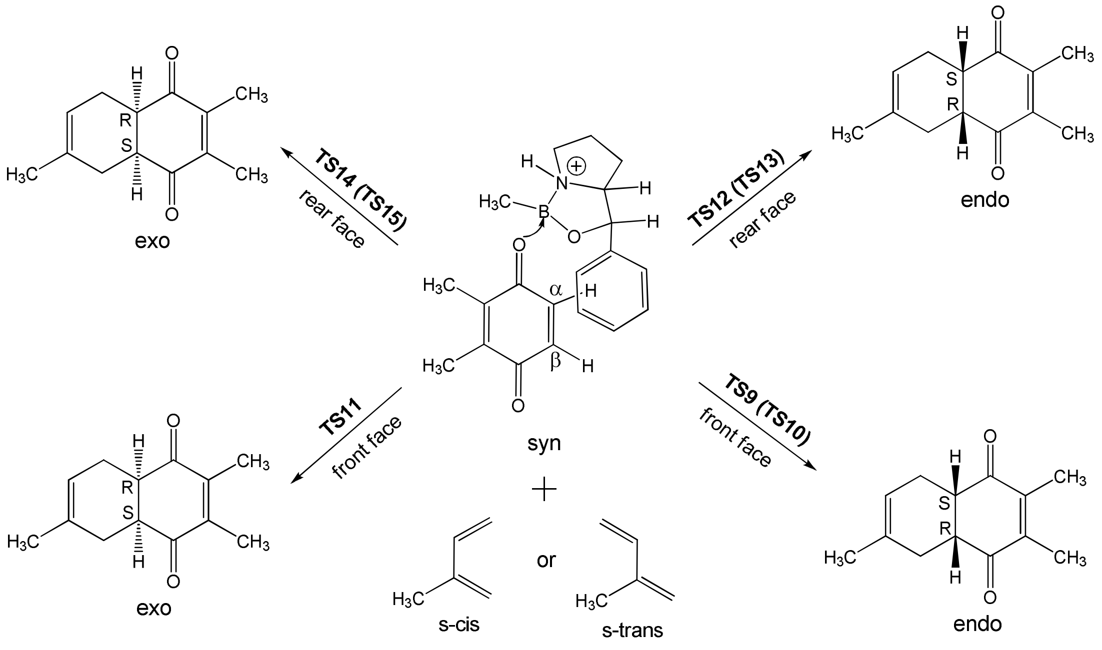

Figure 3.5: Catalyzed Diels-Alder reaction with eight possible reaction pathways. The catalyst is coordinated syn to the HC═CH double bond that undergoes the [4+2]-cycloaddition. Transition states are as shown in Figure 3.13. In brackets are the transition states involving the s-trans diene.

Reaction 3-E

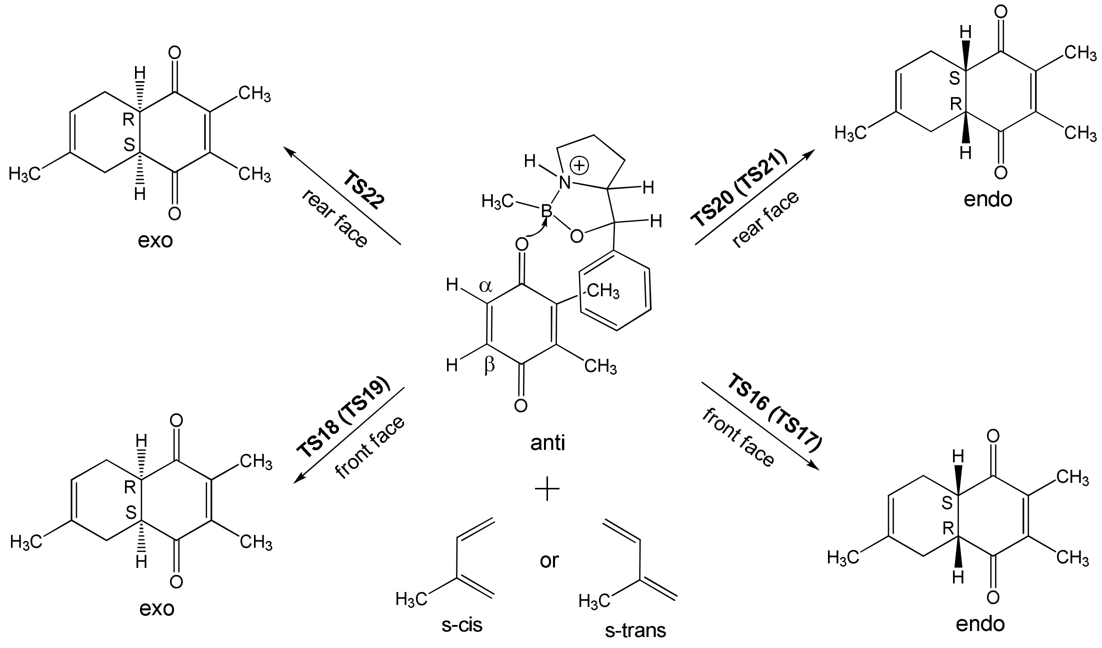

Figure 3.6: Catalyzed Diels-Alder reaction with eight possible reaction pathways. The catalyst is coordinated anti to the HC═CH double bond that undergoes the [4+2]-cycloaddition. Transition states are as shown in Figure 3.14. In brackets are the transition states involving the s-trans diene.

3.3.2 Geometries and energetics of stationary points

The B3LYP/6-31G(d) optimized structures of the reactants are shown in Figure 3.7. The *s-cis* diene **R1** is less stable than the *s-trans* diene **R2** by 2.7 kcal/mol and represents only 0.05% of the Boltzmann population at 178.15 K.

The *syn* **R5** and *anti* **R6** coordination complexes between benzoquinone **R3** and catalyst **R4** are also shown in Figure 3.7. A stronger coordination is observed for the *syn* complex having a B–O bond length shorter by 0.06 Å than that of the *anti* complex. Besides, the *syn* complex exhibits a nonconventional hydrogen bond between the C_α–H hydrogen and the catalyst oxygen with 2.27 Å bond length. The stronger coordination in addition to the presence of hydrogen bonding in the *syn* complex led to a 7.0 kcal/mol stabilization for the *syn* complex as compared to the *anti* complex. This corresponds to almost a 100% of the Boltzmann population being represented by the *syn* complex. Furthermore, the Gibbs free energies for the *syn* and *anti* coordination complexes are lower than those of the separated reactants (**R3** + **R4**) by 9.8 and 2.8 kcal/mol at 178.15 K, respectively (Figure 3.8). At 298.15 K, however, the *anti* coordination is unfavored since the complex free energy is 2.7 kcal/mol higher than the separated reactants (Figure 3.8). The *syn* coordination is still favored but with a stabilization of only 4.4 kcal/mol (Figure 3.8).

The B3LYP/6-31G(d) optimized structures of the products are displayed in Figure 3.9. **P1** (*endo*) and **P2** (*exo*) are the products of Reactions 3-B, 3-D, and 3-E whereas **P3** (*endo*) and **P4** (*exo*) are the products of Reaction 3-C. From the relative free energies given in Figure 3.9, it is obvious that the diene addition to the double bond bearing two hydrogens leads to more stable products (> 11 kcal/mol) than the diene addition to the double bond bearing the methyl groups.

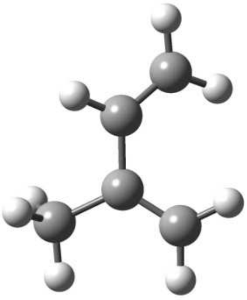

R1

ΔG_{rel}=+2.7 (2.6)

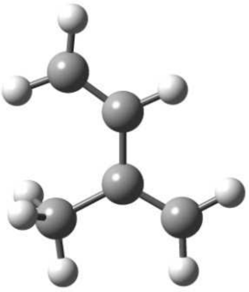

R2

ΔG_{rel}=0.0

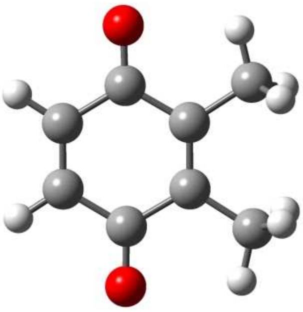

R3

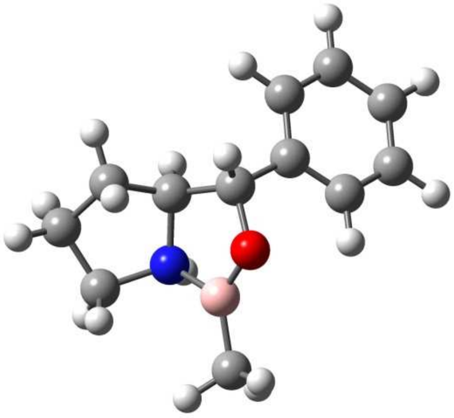

R4

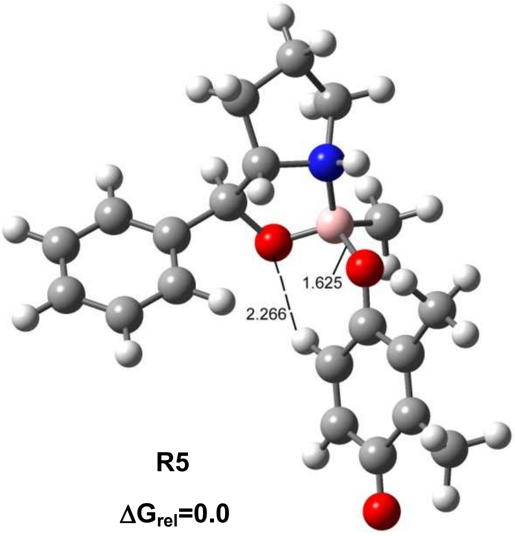

R5

ΔG_{rel}=0.0

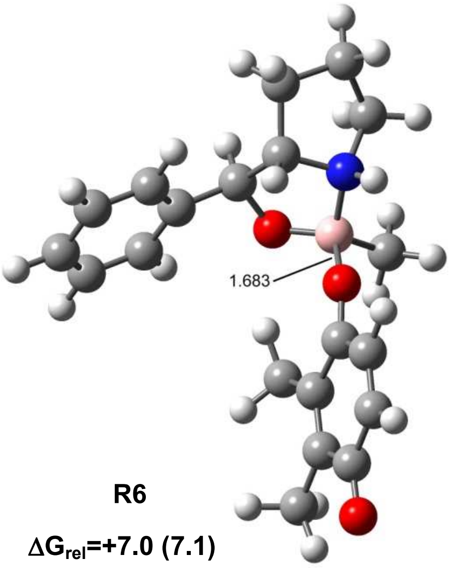

R6

ΔG_{rel}=+7.0 (7.1)

Figure 3.7: Reactants B3LYP/6-31G(d) optimized structures. Relative free energies are in kcal/mol at 178.15 K with relative free energies at 298.15 K given in brackets. Distances are in angstroms. For names see text. Color code: carbon in grey, hydrogen in white, oxygen in red, nitrogen in blue, and boron in pink.

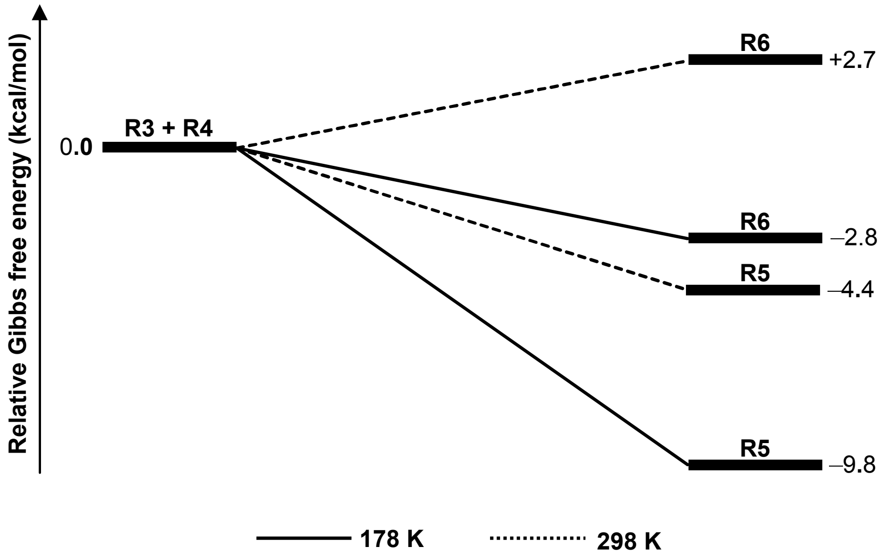

*Figure 3.8: Relative Gibbs free energies for the coordination between **R3** and catalyst **R4** at 178.15 K and 298.15 K.*

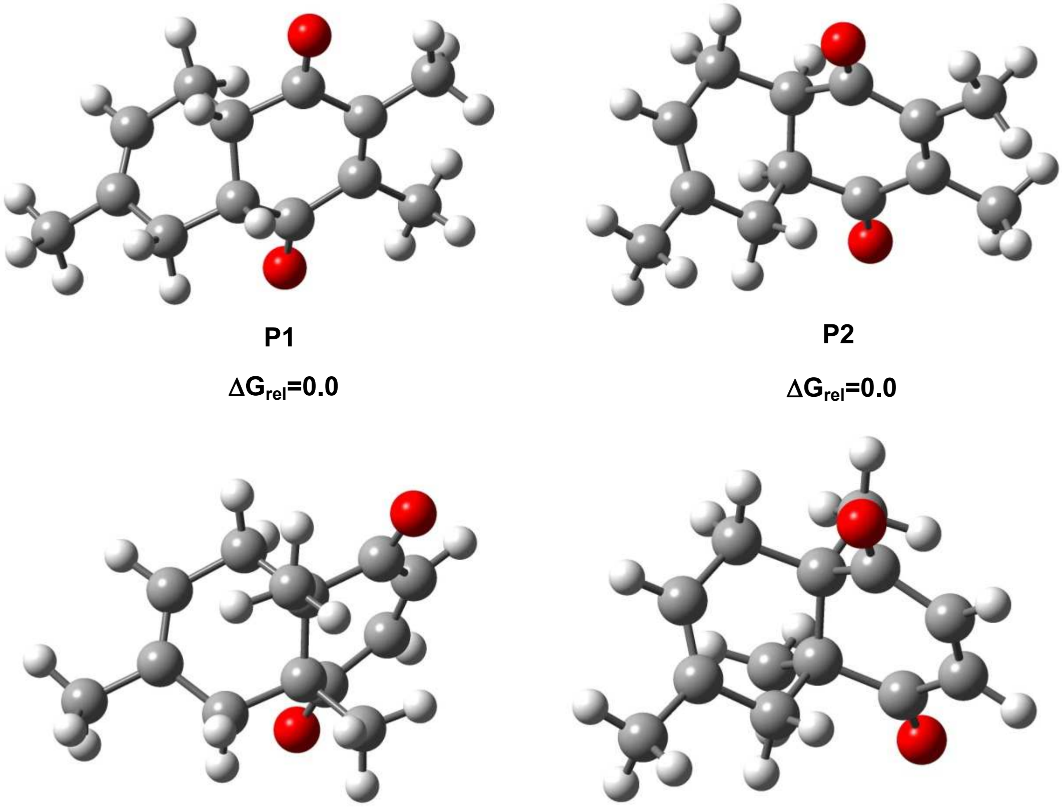

P1

ΔG_{rel}=0.0

P2

ΔG_{rel}=0.0

P3

ΔG_{rel}=+11.6 (12.4)

P4

ΔG_{rel}=+11.6 (12.4)

Figure 3.9: Products B3LYP/6-31G(d) optimized structures. Relative free energies are in kcal/mol at 178.15 K with relative free energies at 298.15 K given in brackets. For names see text.

The optimized transition structures at the B3LYP/6-31G(d) level of theory for the uncatalyzed Reactions 3-B and 3-C are given in Figures 3.10 and 3.11, respectively. As is shown in the figures, the transition structures involving the attack of the diene at the less substituted double bond of the benzoquinone are more stable by 7.2 – 13.4 kcal/mol at 178.15 K. This is in agreement with Corey’s predictive rule number 2 discussed earlier (Section 3.3.1).

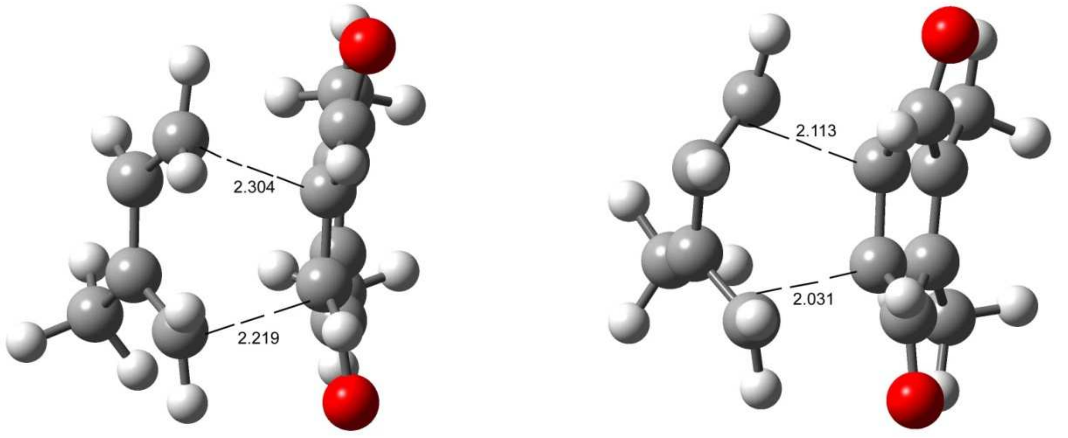

TS1

ΔG_{rel}=0.0

TS2

ΔG_{rel}=+19.8 (19.8)

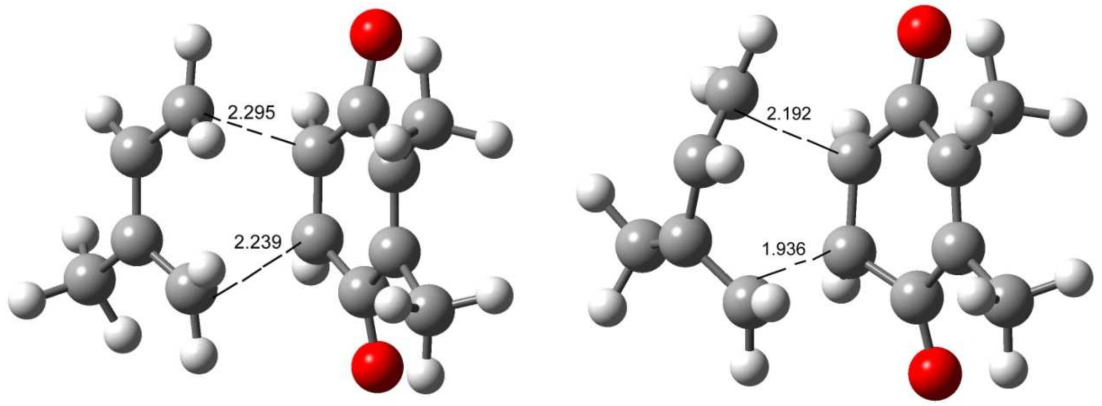

TS3

ΔG_{rel}=+0.9 (0.7)

TS4

ΔG_{rel}=+19.0 (19.0)

Figure 3.10: B3LYP/6-31G(d) optimized transition structures for the uncatalyzed Reaction 3-B. Relative free energies are in kcal/mol at 178.15 K with relative free energies at 298.15 K given in brackets. Distances are in angstroms. ***TS1*** *= endo transition state involving the s-cis diene,* ***TS2*** *= endo transition state involving the s-trans diene,* ***TS3*** *= exo transition state involving the s-cis diene, and* ***TS4*** *= exo transition state involving the s-trans diene.*

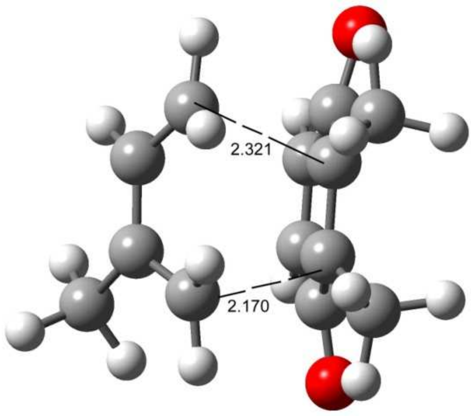

TS5

ΔG_{rel}=+7.2 (7.8)

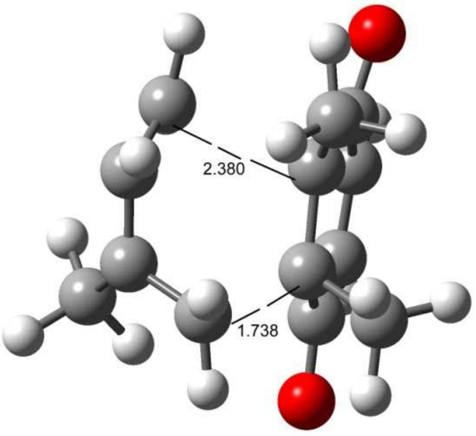

TS6

ΔG_{rel}=+30.4 (31.4)

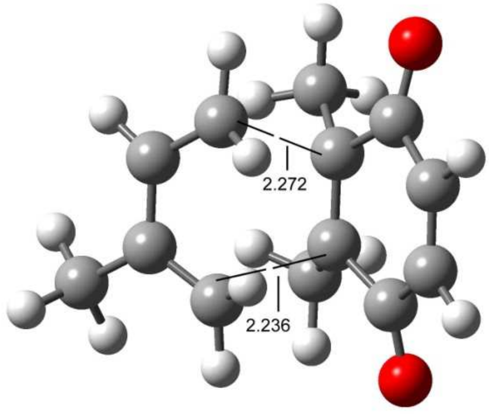

TS7

ΔG_{rel}=+9.2 (9.8)

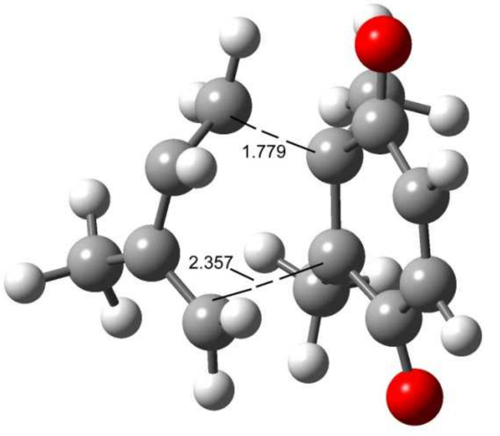

TS8

ΔG_{rel}=+32.4 (33.4)

Figure 3.11: B3LYP/6-31G(d) optimized transition structures for the uncatalyzed Reaction 3-C. Relative free energies are in kcal/mol at 178.15 K with relative free energies at 298.15 K given in brackets. These energies are relative to ***TS1****. Distances are in angstroms.* ***TS5*** *= endo transition state involving the s-cis diene,* ***TS6*** *= endo transition state involving the s-trans diene,* ***TS7*** *= exo transition state involving the s-cis diene, and* ***TS8*** *= exo transition state involving the s-trans diene.*

The *s-cis* diene **R1** is more reactive than the *s-trans* diene **R2** and transition structures involving the *s-cis* diene are lower by > 18 kcal/mol than those having the *s-trans* diene (Figure 3.10). This is in accord with Corey's predictive rule number 7 mentioned earlier (Section 3.3.1). The reaction energy diagram for the uncatalyzed Reaction 3-B is shown in Figure 3.12. At 178.15 K, the conversion rate to the *endo* product is 12 times faster than the rate at which the *exo* product is formed. However, this rate is reduced by 4 times at 298.15 K. The *endo*/*exo* selectivity is calculated to be 84.7% and 52.1% at 178.15 K and 298.15 K, respectively.

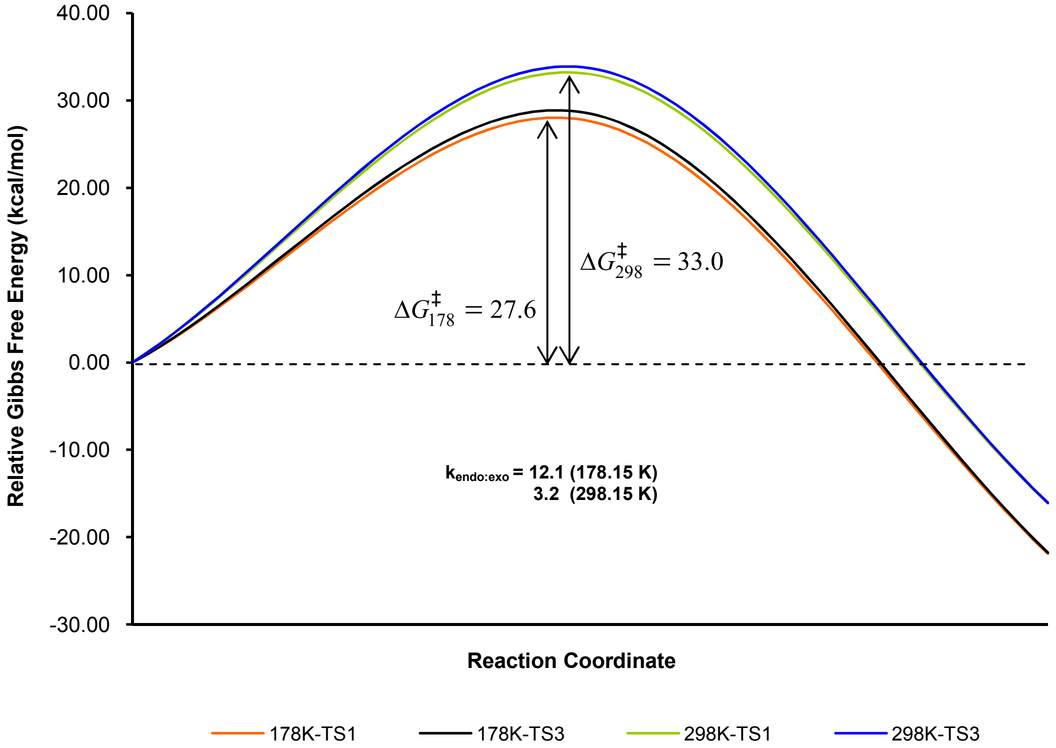

Figure 3.12: Reaction energy diagram for the uncatalyzed Reaction 3-B at 178.15 K and 298.15 K showing activation free energies and relative rates. Free energies are in kcal/mol. ***TS1*** *and* ***TS3*** *are as shown in Figure 3.10.*

The degree of asynchronicity for transition structures are found to be in the range of 0.06 – 0.26 Å (Figure 3.10) and all these transition structures, therefore, correspond to concerted asynchronous reaction pathways. This asynchronicity can be rationalized by the frontier molecular orbital (FMO) theory [23,55]. For example, in **TS1**, the slight asynchronicity of 0.09 Å is due to the LUMO having slightly larger coefficient on the β carbon of the benzoquinone rendering it more electrophilic than the α carbon (the β carbon contributes 4.7% of the LUMO while the α carbon contributes 4.2% of the LUMO). As a result, a slightly larger overlap between the β carbon and the diene HOMO leads to a slightly stronger and shorter bond at the transition structure.

Shown in Figures 3.13 and 3.14 are the B3LYP/6-31G(d) computed transition structures for the catalyzed Reactions 3-D and 3-E, respectively. Consistent with the results of the uncatalyzed reactions, the transition structures involving the *s-cis* diene are 18 – 23 kcal/mol lower in energy than those having the *s-trans* diene. This is again in accord with Corey's predictive rule number 7 discussed in Section 3.3.1.

The *syn* transition structures (Figure 3.13) are more stable than their *anti* counterparts (Figure 3.14) by about 3.2 to 9.8 kcal/mol. For both *syn* and *anti* transition structures, the B–O bond length is shorter (on average) than that of the reactant by 0.08 Å and 0.11 Å, respectively indicating stronger complexation at the transition state. A relatively stronger coordination is observed for the *syn* transition structures with B–O bond lengths shorter by about 0.01 to 0.04 Å than those of the *anti* transition structures. As in the case of the reactants, the *syn* transition structures possess a nonconventional hydrogen bond between the C_α–H hydrogen and the catalyst oxygen with bond lengths in the range of 2.28 – 2.53 Å. On these grounds, Corey's predictive rule number 3 of Section 3.3.1 holds valid for the studied reactions.

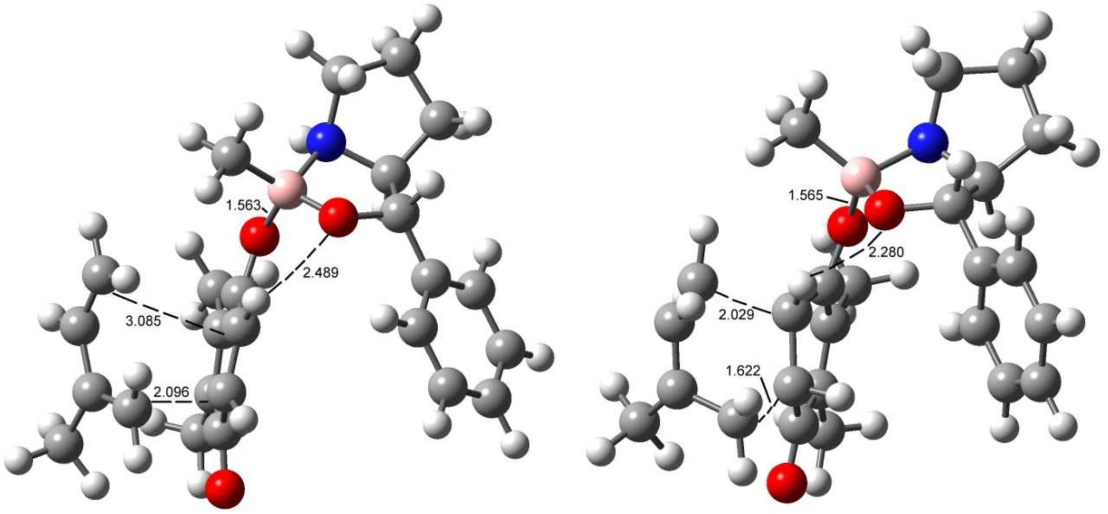

TS9

ΔG_{rel}=0.0

TS10

ΔG_{rel}=+19.1 (19.6)

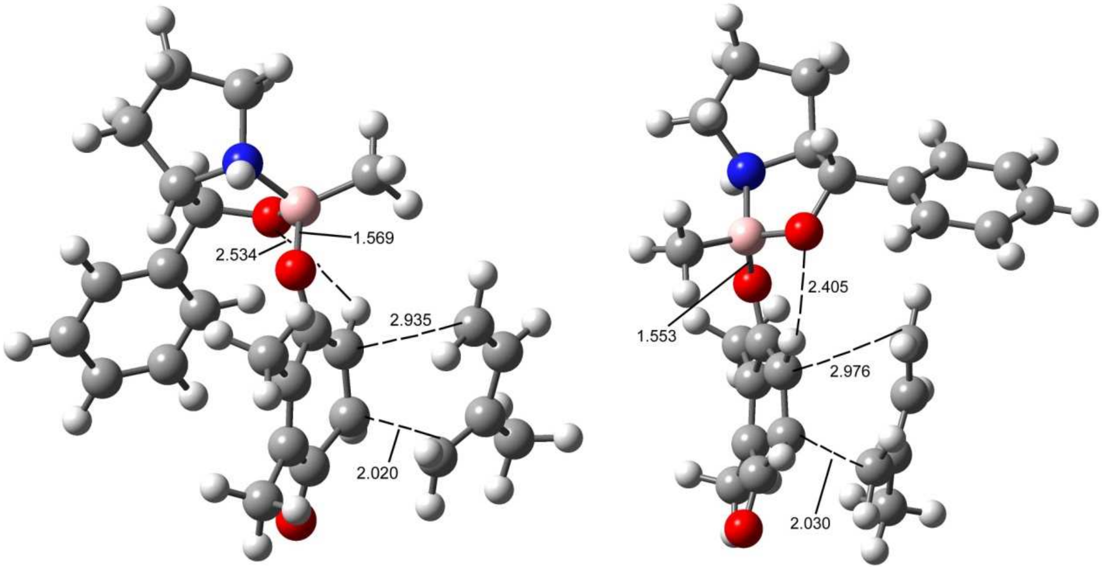

TS11

ΔG_{rel}=+4.8 (4.3)

TS12

ΔG_{rel}=+1.3 (1.3)

Figure 3.13: B3LYP/6-31G(d) optimized transition structures for the catalyzed Reaction 3-D. Relative free energies are in kcal/mol at 178.15 K with relative free energies at 298.15 K given in brackets. Distances are in angstroms. ***TS9*** *= endo transition state involving the s-cis diene attack to the front face,* ***TS10*** *= endo transition state involving the s-trans diene attack to the front face,* ***TS11*** *= exo transition state involving the s-cis diene attack to the front face, and* ***TS12*** *= endo transition state involving the s-cis diene attack to the rear face. The exo transition state involving the s-trans diene attack to the front face could not be located.*

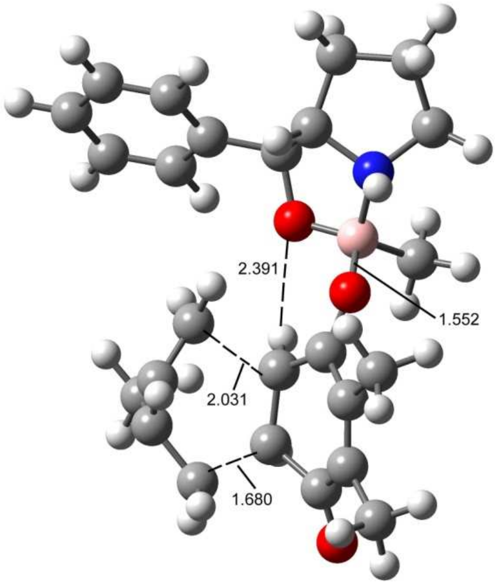

TS13

ΔG_{rel}=+24.4 (24.3)

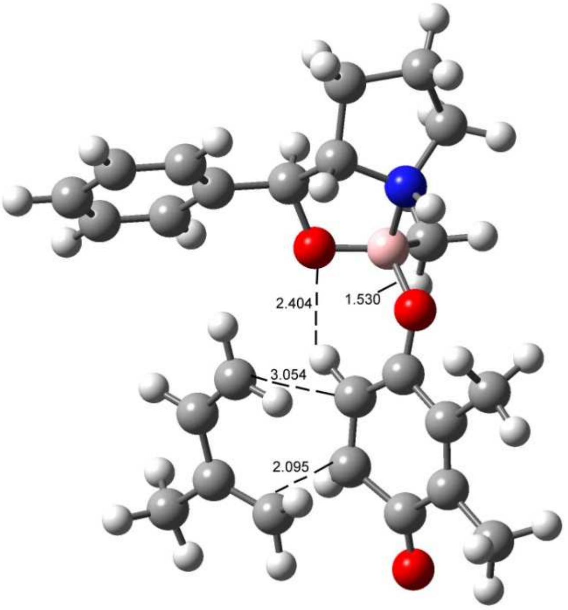

TS14

ΔG_{rel}=+1.7 (1.4)

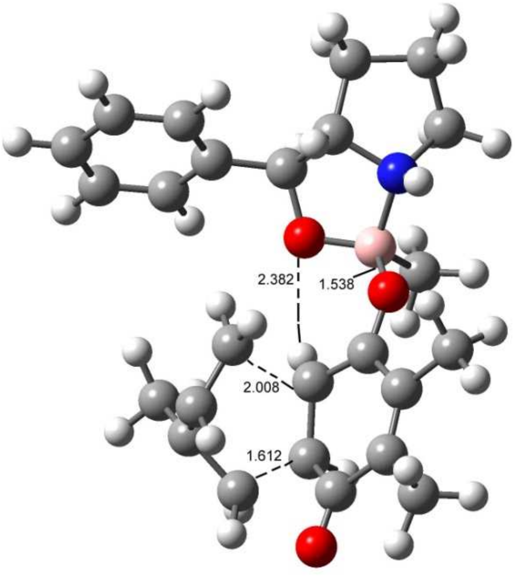

TS15

ΔG_{rel}=+20.6 (21.0)

*Figure 3.13 (Continued): **TS13** = endo transition state involving the s-trans diene attack to the rear face, **TS14** = exo transition state involving the s-cis diene attack to the rear face, and **TS15** = exo transition state involving the s-trans diene attack to the rear face.*

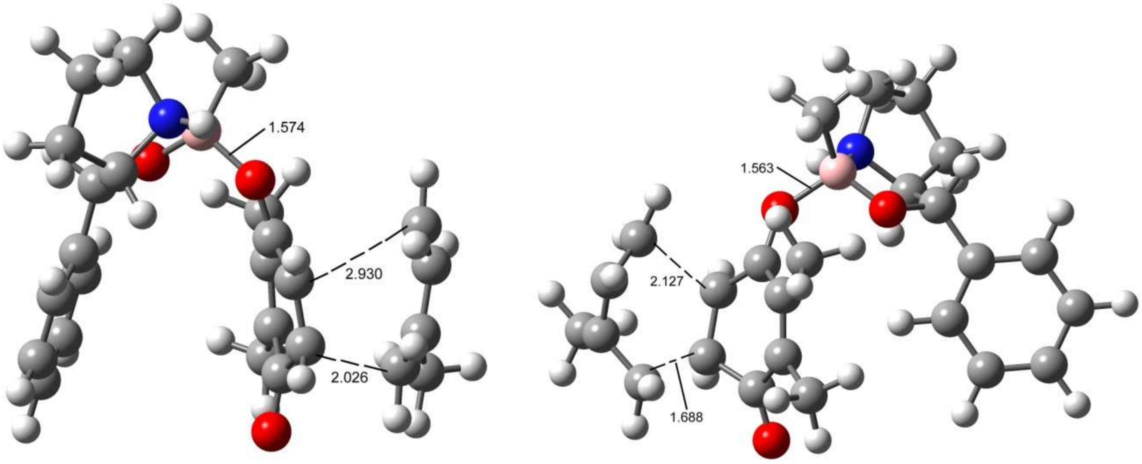

TS16

ΔG_{rel}=+7.9 (7.8)

TS17

ΔG_{rel}=+28.1 (28.3)

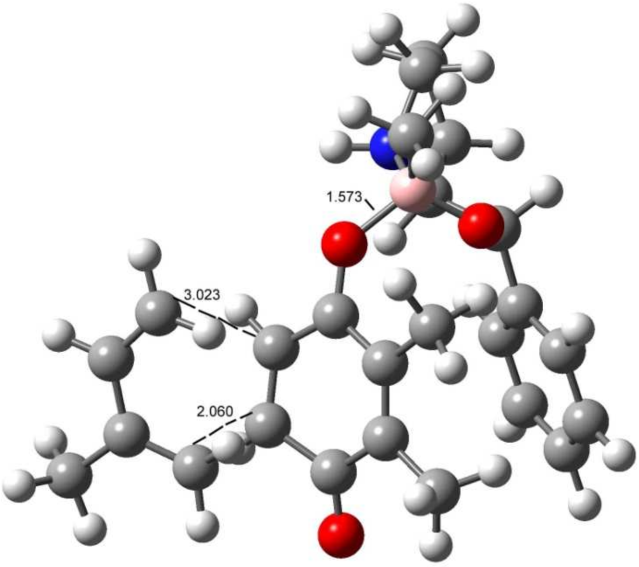

TS18

ΔG_{rel}=+8.3 (7.9)

Figure 3.14: B3LYP/6-31G(d) optimized transition structures for the catalyzed Reaction 3-E. Relative free energies are in kcal/mol at 178.15 K with relative free energies at 298.15 K given in brackets. These energies are relative to ***TS9****. Distances are in angstroms.* ***TS16*** *= endo transition state involving the s-cis diene attack to the front face,* ***TS17*** *= endo transition state involving the s-trans diene attack to the front face, and* ***TS18*** *= exo transition state involving the s-cis diene attack to the front face. The exo transition state involving the s-trans diene attack to the rear face could not be located.*

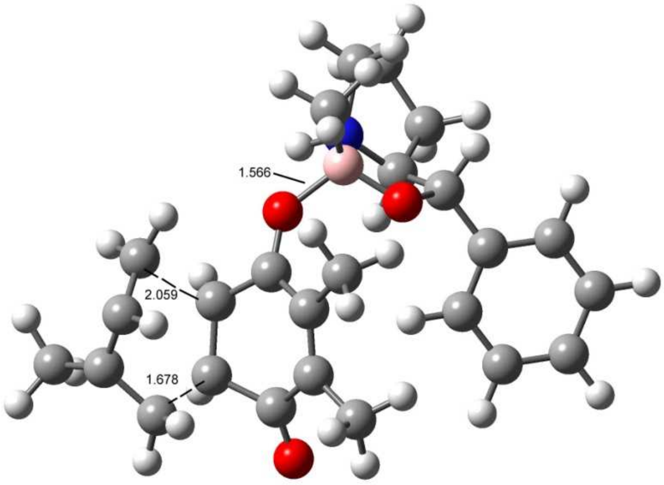

TS19

ΔG_{rel}=+25.7 (25.9)

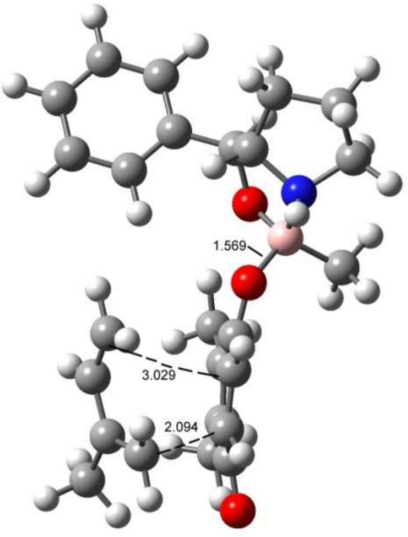

TS20

ΔG_{rel}=+4.7 (4.6)

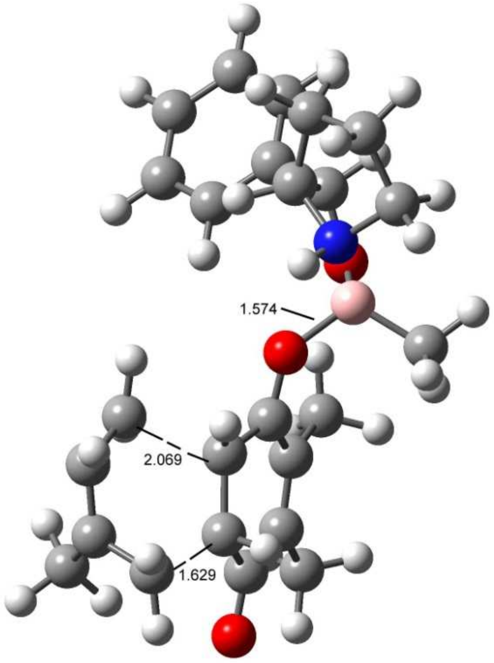

TS21

ΔG_{rel}=+24.5 (25.0)

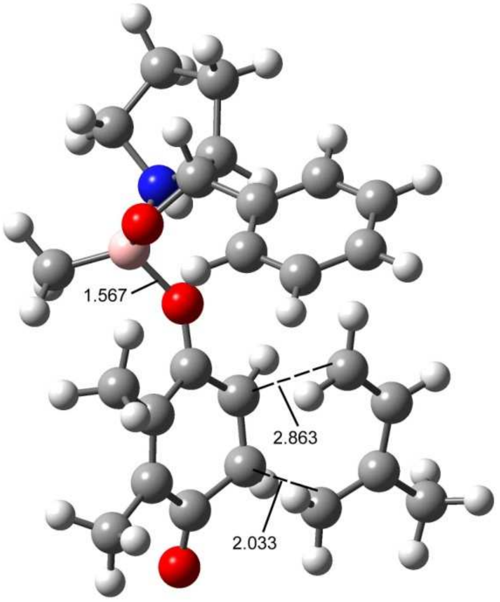

TS22

ΔG_{rel}=+11.1 (11.3)

*Figure 3.14 (Continued): **TS19** = exo transition state involving the s-trans diene attack to the front face, **TS20** = endo transition state involving the s-cis diene attack to the rear face, **TS21** = endo transition state involving the s-trans diene attack to the rear face, and **TS22** = exo transition state involving the s-cis diene attack to the rear face.*

For the *endo* transition states at 178.15 K, the lowest energy transition state is **TS9** representing ~ 97.55% of the Boltzmann population of the *endo* transition states. This transition state involves an *s-cis* diene addition to the front face of the α,β double bond of the benzoquinone and the catalyst is coordinated *syn* to this bond. This result supports Corey's predictive rules 3 and 5 mentioned in Section 3.3.1. The next lowest transition state **TS12** has ~ 2.45% of the Boltzmann population of the *endo* transition states. It is similar to **TS9** but the diene addition is to the rear face of the α,β double bond of the benzoquinone. At 298.15 K, **TS9** and **TS12** contribute ~ 90.02% and ~ 9.94% of the Boltzmann population, respectively. The remaining 0.04% is due to **TS20**, which is similar to **TS12** but with the catalyst coordinated *anti* to the α,β double bond that undergoes the cycloaddition.

As for the *exo* transition states at 178.15 K, **TS14** represents the most stable transition state with ~ 99.98% of the Boltzmann population of the *exo* transition states. It is similar to **TS12** except that the arrangement is *exo*. The remaining 0.02% is for **TS11**, which is similar to **TS14** but with the diene addition to the front face of the α,β double bond of the benzoquinone. The percentages at 298.15 K are ~ 99.18% and 0.82% for **TS14** and **TS11**, respectively.

The reaction energy diagram for the catalyzed Reaction 3-D is illustrated in Figure 3.15. At 178.15 K, the *endo* pathway is 116 times faster than the *exo* route but it is reduced by ~ 12 times at 298.15 K. In addition, as compared to the uncatalyzed reaction (Figure 3.12), the reaction rate is markedly enhanced in the presence of the catalyst through lowering the activation free energy barriers by more than 13 kcal/mol. The catalyst also leads to an enhanced enantioselectivity and the percent enantiomeric excess (%*ee*) is calculated to be 98.3% and 80.5% at 178.15 K and

298.15 K, respectively. This is in agreement with Corey's predictive rule number 6 that the preferred transition state has an *endo* arrangement (Section 3.3.1).

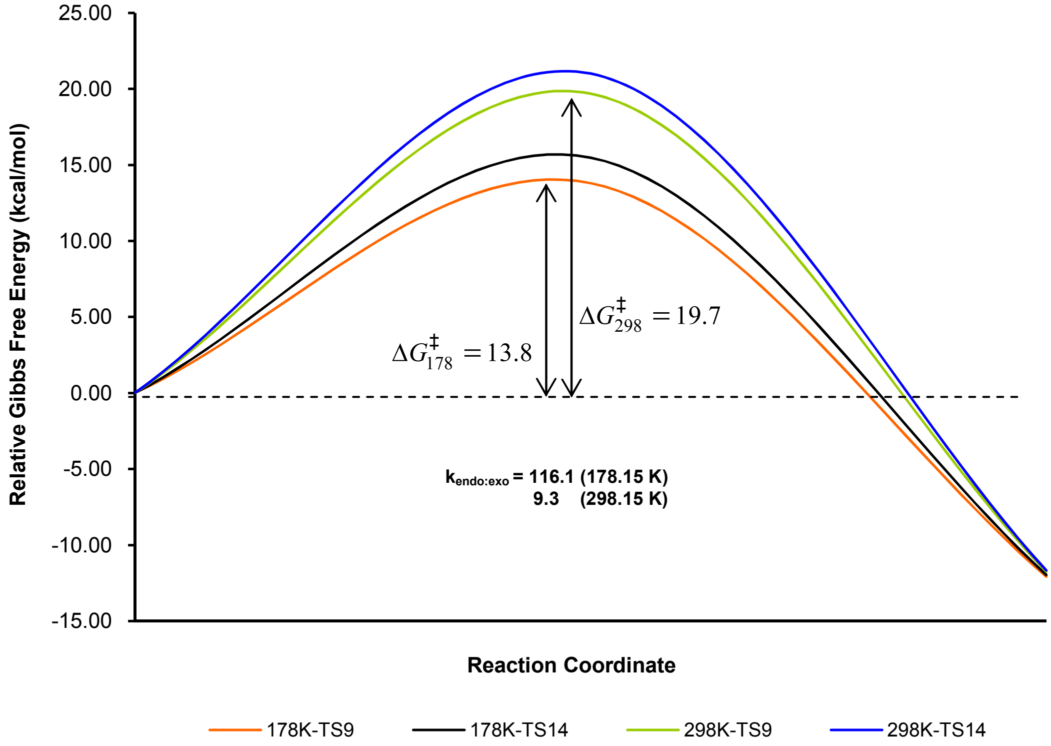

Figure 3.15: Reaction energy diagram for the catalyzed Reaction 3-D at 178.15 K and 298.15 K showing activation free energies and relative rates. Free energies are in kcal/mol. ***TS9*** *and* ***TS14*** *are as shown in Figure 3.13.*

The enantiomeric excess of the product observed experimentally is 90% (Figure 3.1). This discrepancy between the experimental and calculated enantioselectivities can be attributed to computational errors such as simplification of the catalyst, and approximations and inaccuracies associated with the DFT/B3LYP method. In addition, reaction conditions are presumably more complex and different from those of computation. Moreover, the solvent effects were not included in this study. The use of the polarizable continuum model with the integral equation formalism (IEFPCM), the self-consistent isodensity polarizable continuum model (SCIPCM), and the conductor-like polarizable continuum model (CPCM), together with different topological models/atomic radii that define the solute cavity (UAHF, UAKS, and Bondi) [56] failed to meet the default geometry optimization convergence thresholds.

The average degree of asynchronicity for the transition structures involving the *s-cis* diene is calculated to be 0.93 Å (Figures 3.13 and 3.14). Thus, these transition structures point to concerted but highly asynchronous reaction pathways where the bond between the diene and carbon β of the dienophile is being formed in a larger extent than the bond between the diene and carbon α of the dienophile. This result reinforces Corey's predictive rule number 1 discussed in Section 3.3.1. Similar to the uncatalyzed case, the asynchronicity can be explained by the frontier molecular orbital (FMO) theory [23,55]. For instance, the high degree of asynchronicity (0.99 Å) found in the transition structure **TS9** is due to the LUMO having much larger coefficient on the β carbon of the benzoquinone causing it to be much more electrophilic than the α carbon (the β carbon possesses 12.9% of the LUMO while the α carbon has only 2.0% of the LUMO). This results in a much larger overlap between the β carbon and the diene HOMO leading to a much stronger and shorter bond at the transition structure.

As depicted in Figures 3.13 and 3.14, the bond between the *s-trans* diene and carbon β of the dienophile is in the range of 1.61 – 1.69 Å indicating an almost formed C–C bond. Attempts to locate earlier transition structures on the potential energy surface were not successful implying that the formation of this bond is barrierless (or having a very low activation barrier). Hence, the formation of the second C–C bond is presumed to be the rate determining step for the *s-trans* pathway. In all cases however, the transition structures with the *s-trans* diene are 18

– 23 kcal/mol higher in energy than those having the *s-cis* diene rendering reaction pathways with *s-trans* diene less likely to happen.

3.3.3 Kinetic isotope effects

Equilibrium isotope effects (EIEs) are the result of bonding and non-bonding interactions at minimum stationary points. On the other hand, kinetic isotope effects (KIEs) yield information about transition structures and result from isotopic substitution that has an effect on the rate of the reaction [57,58]. Comparison of experimental KIEs with theoretically calculated ones is useful in elucidating organic reaction mechanisms. KIEs can also provide information on the transition structures such as the extent of bond formation [14-16,59-64].

Isotopic substitution does not alter the electronic energy and structure but changes the vibration associated with the isotopically substituted bond which in turn influences the zero-point vibrational energy (ZPVE). Often, isotopic substitution involves replacing hydrogen by deuterium (or tritium) since hydrogen isotopes have the largest relative mass differences [57,58].

Primary kinetic isotope effects result from isotopic substitution of a hydrogen atom directly involved in the reaction while secondary kinetic isotope effects (2º-KIEs) result from isotopic substitution of a hydrogen atom not directly involved in the reaction [65]. 2º-KIEs can be normal ($k_{\mathrm{H}}/k_{\mathrm{D}} > 1$) or inverse ($k_{\mathrm{H}}/k_{\mathrm{D}} < 1$), where k_{H} and k_{D} are the reaction rate constants for hydrogen and deuterium, respectively. In Diels-Alder reactions, the hybridized state of termini carbons of the diene and dienophile change from sp^2 to sp^3 resulting in an increase of the corresponding C–H out-of-plane bending frequency [58,66]. Hence, an inverse 2º-KIE is expected for the Diels-Alder reaction. In addition, KIEs for the stepwise mechanism are all normal whereas for the concerted mechanism are all inverse [66].

In the ISOEFF07 program, the requirements for the theoretical calculation of KIEs are the isotopic frequencies for the reactant and the transition state. Based on the transition state theory, the KIE can be computed from the frequencies of the normal modes of vibration by [51]

$$\frac{k_{\mathrm{L}}}{k_{\mathrm{H}}}=\frac{\nu_{\mathrm{L}}^{\ddagger}}{\nu_{\mathrm{H}}^{\ddagger}}\prod_{i}^{3N^{\mathrm{R}}-6}\frac{u_{i\mathrm{H}}^{\mathrm{R}}\,.\,\sinh\left(u_{i\mathrm{L}}^{\mathrm{R}}/2\right)}{u_{i\mathrm{L}}^{\mathrm{R}}\,.\,\sinh\left(u_{i\mathrm{H}}^{\mathrm{R}}/2\right)}\prod_{i}^{3N^{\ddagger}-7}\frac{u_{i\mathrm{L}}^{\ddagger}\,.\,\sinh\left(u_{i\mathrm{H}}^{\ddagger}/2\right)}{u_{i\mathrm{H}}^{\ddagger}\,.\,\sinh\left(u_{i\mathrm{L}}^{\ddagger}/2\right)} \tag{3-1}$$

where L and H represent the light and heavy isotopes, respectively, R and ‡ denote the reactant and transition state, respectively, and ν is the isotopic frequency. $u = h\nu / k_B T$ where *h* and k_B are Planck's and Boltzmann constants and *T* is the temperature.

The KIEs can be calculated accurately as long as the vibrational frequencies are computed accurately. In this work, the frequencies calculated by the Gaussian program at the B3LYP/6-31G(d) level of theory were used as the input for the ISOEFF07 KIEs calculations. To account for the anharmonicity of molecular vibrations, the frequencies were scaled by 0.9613 during the ISOEFF07 KIEs calculations.

Figures 3.16 and 3.17 show the experimental values for the KIEs for analogous uncatalyzed and catalyzed Diels-Alder reactions reported in the literature. Figure 3.18 shows the theoretically calculated KIEs obtained in this study for **TS1**, **TS3**, **TS9** and **TS14**.

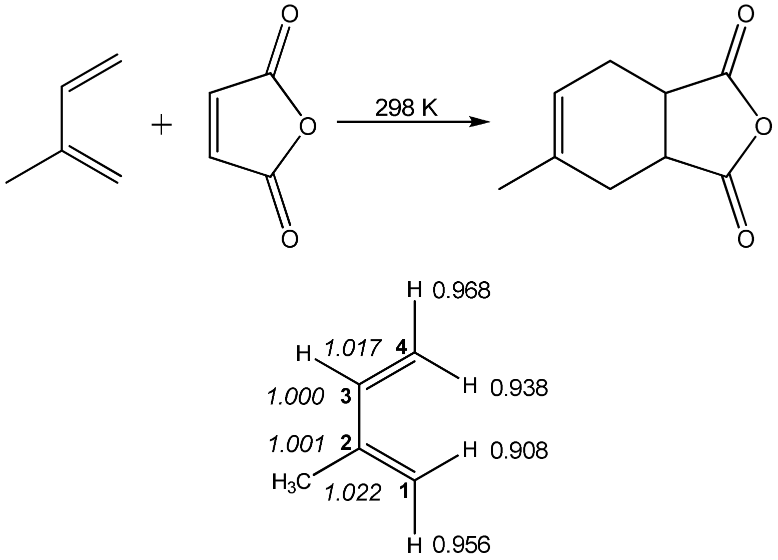

Figure 3.16: Experimental ^{2}H and ^{13}C (italicized numbers) KIEs at 298 K for the uncatalyzed Diels-Alder reaction between isoprene and maleic anhydride (reference 59).

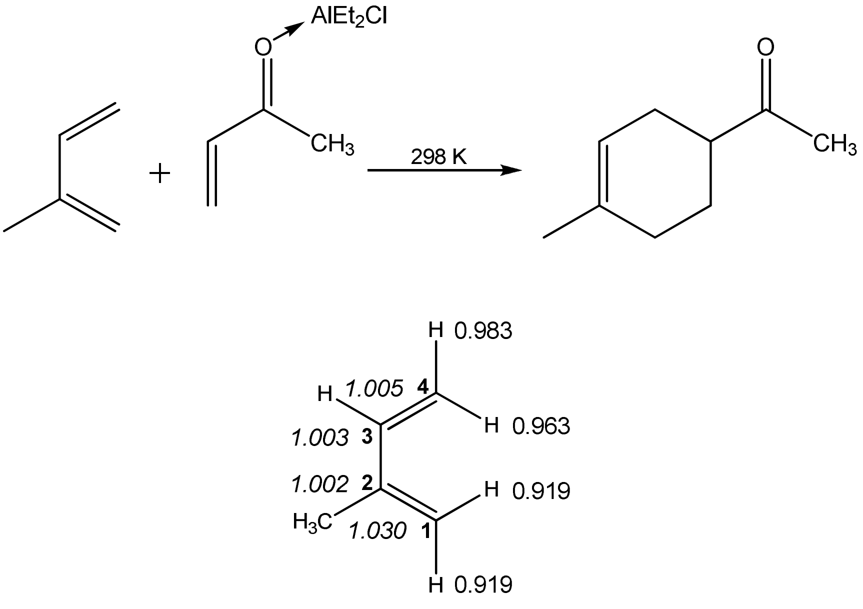

Figure 3.17: Experimental ^{2}H and ^{13}C (italicized numbers) KIEs at 298 K for the Lewis acid catalyzed Diels-Alder reaction of isoprene and methyl vinyl ketone (reference 61).

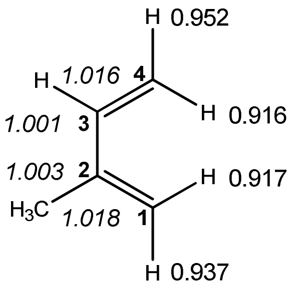

TS1

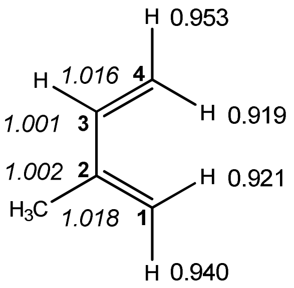

TS3

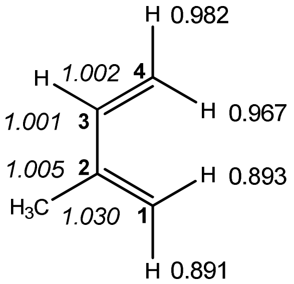

TS9

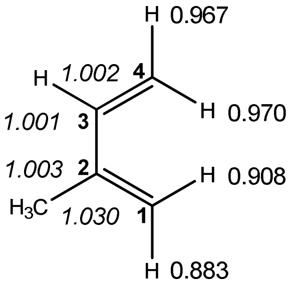

TS14

*Figure 3.18: B3LYP/6-31G(d) computed ^{2}H and ^{13}C (italicized numbers) KIEs at 298 K for the uncatalyzed Reaction 3-B (**TS1** and **TS3**) and the catalyzed Reaction 3-D (**TS9** and **TS14**).*

From the figures, there is a good agreement between the calculated and experimental KIEs. In Figure 3.18, the different ^{2}H 2º-KIEs at C-1 over C-4 point to asynchronicity in bond formation to C-1 versus C-4 at the transition structure [59] with the asynchronicity being more pronounced for the catalyzed reaction. In addition, for **TS1** and **TS3**, the small difference of ^{13}C KIEs at C-1 and C-4 suggest a slightly asynchronous mechanism. For **TS9** and **TS14**, the large ^{13}C KIE at C-1 and small ^{13}C KIEs at the other carbons could indicate both stepwise mechanism and highly asynchronous concerted mechanism [61]. The ^{2}H 2º-KIEs, however, clearly show a concerted mechanism. The large inverse ^{2}H 2º-KIEs at C-4 are indicative of bond formation to C-4 at the transition structure [61]. Such inverse ^{2}H 2º-KIEs are not characteristic of a stepwise mechanism [61]. Hence, the studied catalyzed reaction is presumed to proceed through a concerted but highly asynchronous mechanism.

3.3.4 Preliminary data and further investigations

The Danishefsky's diene (*trans*-1-methoxy-3-trimethylsilyloxy-1,3-butadiene) is a useful diene in the Diels-Alder reaction and has been employed in the synthesis of many compounds [67,68]. It is an electron-rich diene and thus shows a high reactivity towards dienophiles. The presence of the methoxy group renders the Diels-Alder reaction regiospecific by connecting the electrophilic carbon attached to the methoxy group with the most nucleophilic atom of the dienophile.

As mentioned in Section 3.1, understanding the role of the catalyst can help in the design of other enantioselective syntheses. Hence, in this part of the work, the application of the model catalyst **16** to a Diels-Alder reaction involving Danishefsky diene is explored. The studied reaction pathways are depicted in Figures 3.19 and 3.20. The following simplifications are made in the studied reaction: (1) the model (*S*)-catalyst **16** is used, (2) the same dienophile as in Corey's reaction (Figure 3.1) is used considering only the diene addition to the less substituted double bond of the dienophile (Section 3.3.2), (3) only the *s-cis* Danishefsky diene is considered and a simpler structure for this diene is used by replacing the trimethylsilyloxy group by a methoxy group, (4) the use of the Danishefsky diene introduces one more stereogenic center into the product and hence there are 8 possible diastereomeric products of which only 4 are considered, and (5) since there is no experimental data, the reaction is studied at only 298.15 K.

Reaction 3-F

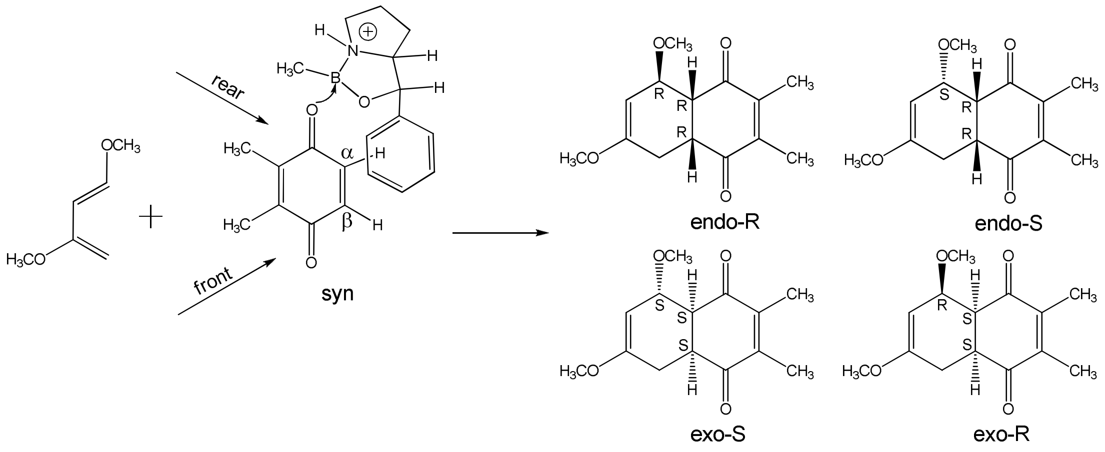

Figure 3.19: Catalyzed Diels-Alder reaction with eight possible reaction pathways. The catalyst is coordinated syn to the $HC{=}CH$ double bond that undergoes the [4+2]-cycloaddition.

Reaction 3-G

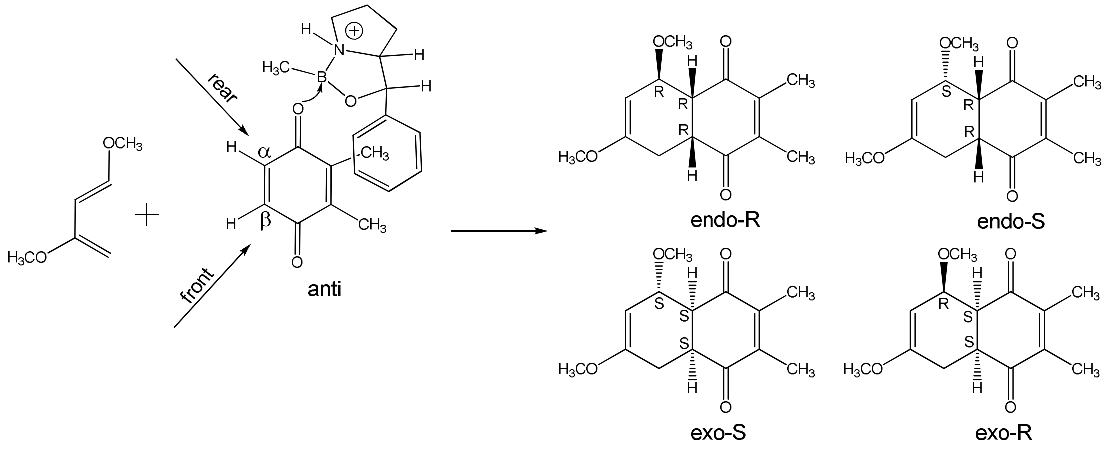

Figure 3.20: Catalyzed Diels-Alder reaction with eight possible reaction pathways. The catalyst is coordinated anti to the $HC{=}CH$ double bond that undergoes the [4+2]-cycloaddition.

Only four transition structures could be located on the potential energy surface for this reaction. These transition structures lead to the two diastereomers *endo-R* and *exo-R*. The B3LYP/6-31G(d) optimized structures for the model Danishefsky diene **R7** and the two diastereomers *endo-R* **P5** and *exo-R* **P6** are shown in Figure 3.21. The four transition structures are given in Figure 3.22.

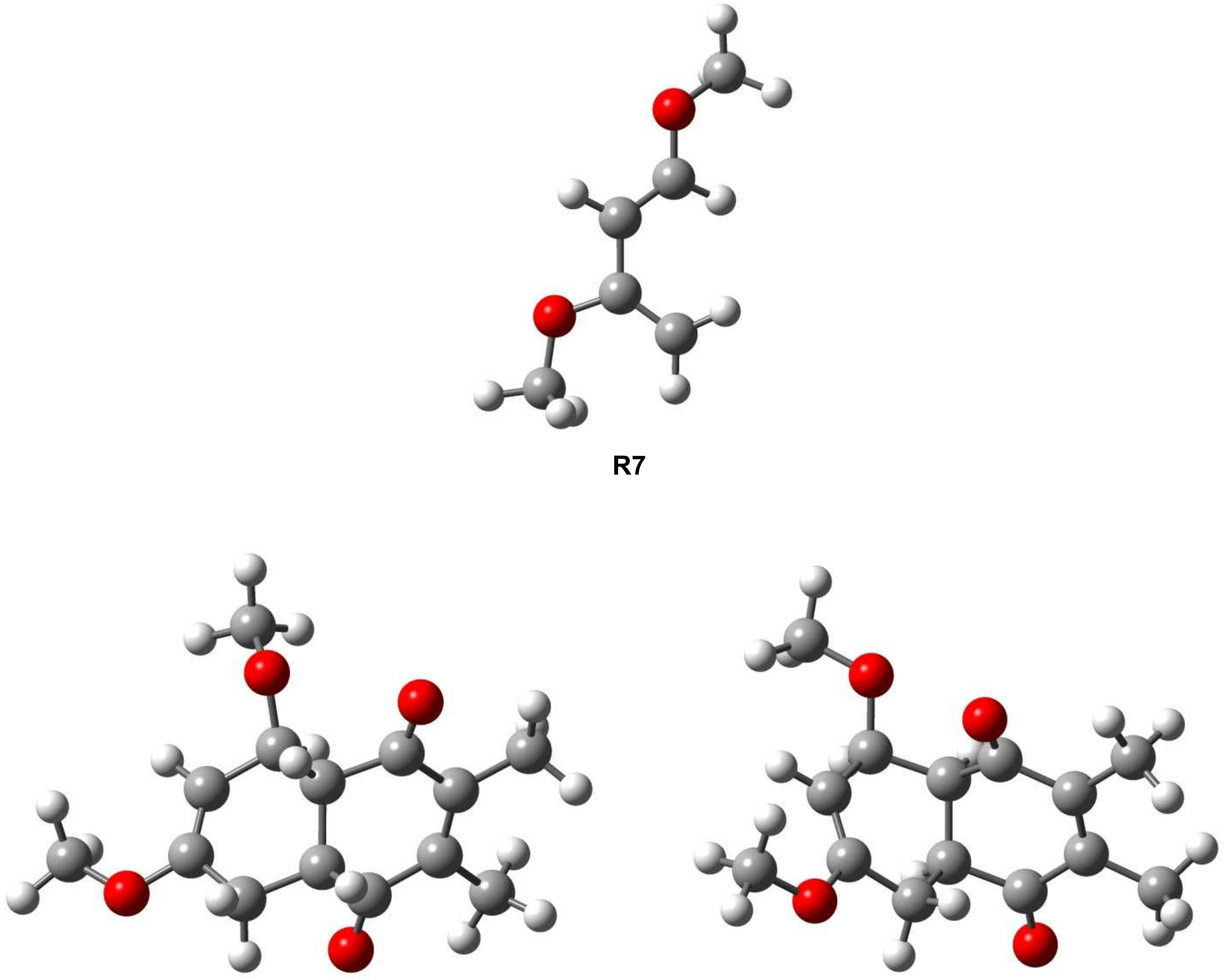

R7

P5

ΔG_{rel}=0.0

P6

ΔG_{rel}=+4.3

Figure 3.21: B3LYP/6-31G(d) optimized structures for Danishefsky diene and products. Relative free energies are in kcal/mol at 298.15 K. For names see text.

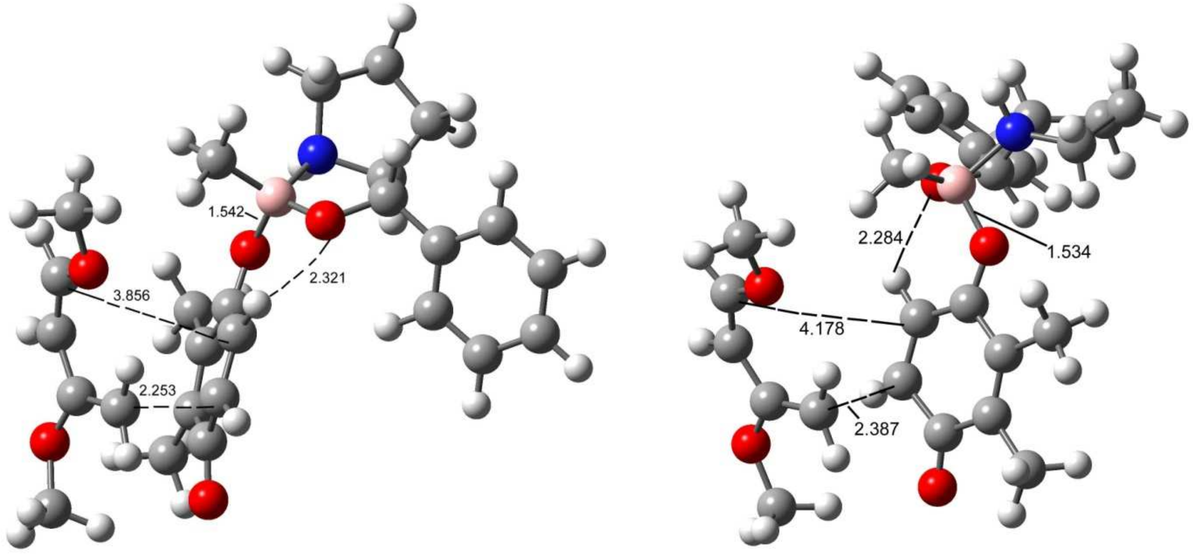

TS23

ΔG_{rel}=+1.5

TS24

ΔG_{rel}=0.0

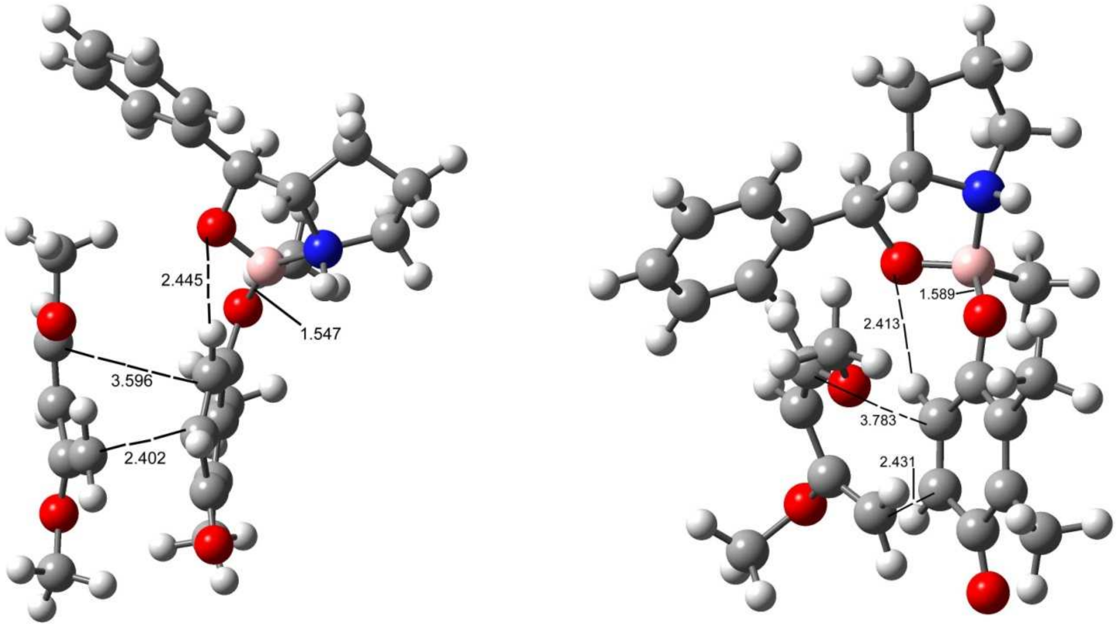

TS25

ΔG_{rel}=+2.4

TS26

ΔG_{rel}=+10.1

Figure 3.22: B3LYP/6-31G(d) optimized transition structures for the catalyzed Reaction 3-F. Relative free energies are in kcal/mol at 298.15 K. Distances are in angstroms. ***TS23*** *= endo transition state involving the s-cis diene attack to the front face,* ***TS24*** *= exo transition state involving the s-cis diene attack to the front face,* ***TS25*** *= endo transition state involving the s-cis diene attack to the rear face, and* ***TS26*** *= exo transition state involving the s-cis diene attack to the rear face. For all transition structures, the carbon atom attached to the OMe group has the R configuration.*

The *exo* transition state **TS24** represents the most stable transition state with an almost 100% of the Boltzmann population of the *exo* transition states. It involves the *s-cis* Danishefsky diene addition to the front face of the α,β double bond of the dienophile and the catalyst is coordinated *syn* to this bond. The carbon atom connected to the methoxy group possesses the *R* configuration. The next lowest *exo* transition state is **TS26**. It is similar to **TS24** except that the diene addition is to the rear face of the α,β double bond of the benzoquinone.

The lowest energy *endo* transition state is **TS23** representing ~ 81.28% of the Boltzmann population of the *endo* transition states. It is similar to **TS24** but the transition state arrangement is *endo*. The next lowest *endo* transition state is **TS25** having ~ 18.72% of the Boltzmann population of the *endo* transition states. It is similar to **TS23** but with the diene addition to the rear face of the α,β double bond of the dienophile.

The energy diagram for Reaction 3-F is illustrated in Figure 3.23. In contrast to Reaction 3-D (Figure 3.15), the *exo* pathway is 12 times faster than the *endo* channel. However, the *endo-R* product is 4.3 kcal/mol more stable than the *exo-R* product. Thus, Reaction 3-F can be controlled both kinetically and thermodynamically with the *exo* product being the kinetically favored product and the *endo* product being the thermodynamically favored product. In addition, there is a substantial lowering (> 14 kcal/mol) of the free energy of activation upon the use of the more reactive Danishefsky diene as compared to isoprene (Figure 3.23 vs. Figure 3.15). Moreover, in the presence of the Danishefsky diene, the stereoselectivity of the reaction is fairly enhanced. The percent diastereomeric excess (%*de*) is calculated to be 88.2%. Therefore, based on these preliminary data, the use of catalyst **16** is recommended for reactions such as Reaction 3-F.

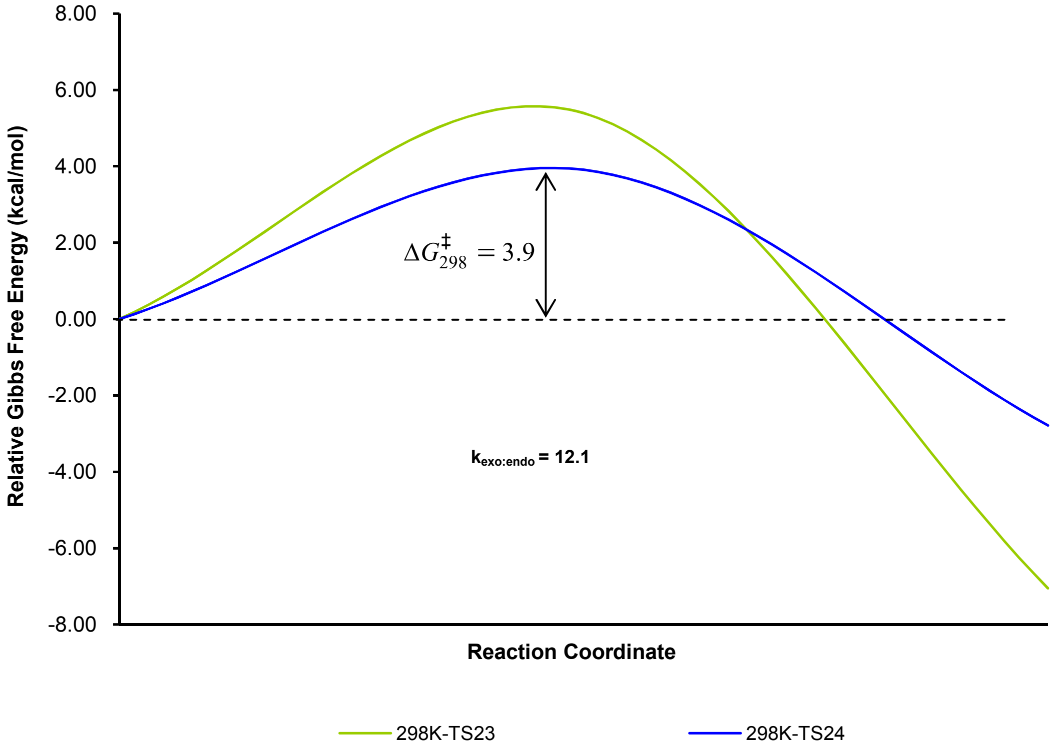

Figure 3.23: Reaction energy diagram for the catalyzed Reaction 3-F at 298.15 K showing activation free energy (kcal/mol) and relative rate. ***TS23*** *and* ***TS24*** *are as shown in Figure 3.22.*

The average degree of asynchronicity for the transition structures is found to be 1.49 Å (Figure 3.22). Thus, the Diels-Alder reaction involving the Danishefsky diene is more asynchronous than that involving isoprene (1.49 Å vs. 0.93 Å). To further elucidate the mechanism, KIEs are calculated for Reaction 3-F and are given in Figure 3.24. At the transition states, the average distance between C-1 of the Danishefsky diene and carbon α of the benzoquinone is calculated to be 3.85 Å (Figure 3.22). This distance is larger than the van der Waals contact distance (3.40 Å) of the two carbons and hence there is no hint of bonding between the two carbons at these transition states. Despite this fact, the theoretically calculated KIEs (Figure 3.24) indicate a concerted but highly asynchronous reaction mechanism instead of a stepwise mechanism.

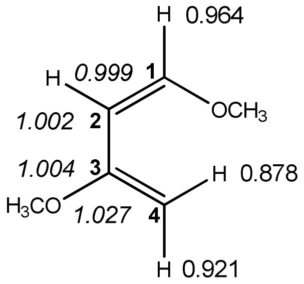

TS23

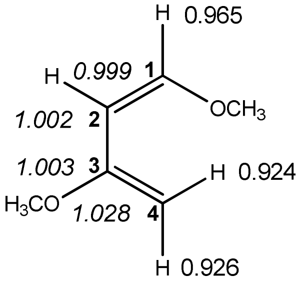

TS24

*Figure 3.24: B3LYP/6-31G(d) computed ^{2}H and ^{13}C (italicized numbers) KIEs at 298 K for Reaction 3-F (**TS23** and **TS24**).*

It should be pointed out that the complete description of a chemical reaction mechanism requires more than just locating stationary points along a reaction path. The time-evolution of the chemical process (i.e. molecular dynamics) is of importance for distinguishing between concerted and stepwise mechanisms. As stated in Section 3.1, femtosecond dynamics studies have suggested the presence of both concerted and stepwise trajectories for the Diels-Alder reaction [20,21]. *Ab initio* molecular dynamics (AIMD) calculations employing the atom-centered density matrix propagation (ADMP) method [69-71] have been used to study important chemical reactions such as the Staudinger reaction [72-75]. Compared to other AIMD methods, the ADMP method has the fundamental advantage of linear scaling of computational time with system size [69-71]. The study of organocatalytic Diels-Alder reaction using the ADMP method for gaining further insights into the mechanism of this vital reaction is thus recommended.

3.4 Conclusion

The enantioselectivity and mechanism of the Diels-Alder reaction between isoprene **14** and 2,3-dimethyl-1,4-benzoquinone **15** in the presence of the model chiral cationic oxazaborolidinium catalyst **16** have been studied by density functional theory using the B3LYP functional together with the 6-31G(d) basis set. Both uncatalyzed and catalyzed reactions were investigated to explore the effect of the catalyst on this reaction in terms of energetics, selectivity, and mechanism. The free energy of activation was significantly lowered (> 13 kcal/mol) in the presence of the catalyst. In addition, the catalyzed reaction showed an improved *endo*/*exo* selectivity of greater than 13 percentage points. Moreover, both uncatalyzed and catalyzed reactions showed concerted asynchronous reaction mechanism with the degree of asynchronicity being more evident in the presence of the catalyst.

Two different types of dienes were considered in the current work, namely, isoprene and Danishefsky diene. In the presence of the catalyst, both dienes showed comparable stereoselectivity. The Diels-Alder reaction in the presence of isoprene is most likely to go through the *endo* channel while in the presence of Danishefsky diene, the *exo* route is favored. In both cases, the preferred catalyst coordination is *syn* to the HC═CH double bond of the dienophile that undergoes the [4 + 2]-cycloaddition and the diene addition is to the front face of this double bond. Based on the optimized transition structures and theoretical kinetic isotope effects calculations, the Diels-Alder reactions involving both dienes are predicted to proceed through concerted but highly asynchronous mechanism. The degree of asynchronicity is more pronounced in the presence of Danishefsky diene. The theoretical outcome of the current study is in excellent agreement with Corey's experimentally derived predictive selection rules [8].

3.5 References

1. A. Berkessel, H. Gröger, Asymmetric Organocatalysis – From Biomimetic Concepts to Applications in Asymmetric Synthesis, WILEY-VCH, Weinheim, Germany, 2005, and references cited therein.
2. E.J. Corey, Catalytic enantioselective Diels-Alder reactions: Methods, mechanistic fundamentals, pathways, and applications, Angewandte Chemie International Edition 41 (2002) 1650-1667.
3. E.J. Corey, Enantioselective catalysis based on cationic oxazaborolidines, Angewandte Chemie International Edition 48 (2009) 2100-2117.
4. E.J. Corey, T. Shibata, T.W. Lee, Asymmetric Diels-Alder reactions catalyzed by a triflic acid activated chiral oxazaborolidine, Journal of the American Chemical Society 124 (2002) 3808-3809.
5. D.H. Ryu, T.W. Lee, E.J. Corey, Broad-spectrum enantioselective Diels-Alder catalysis by chiral, cationic oxazaborolidines, Journal of the American Chemical Society 124 (2002) 9992-9993.
6. D.H. Ryu, E.J. Corey, Triflimide activation of a chiral oxazaborolidine leads to a more general catalytic system for enantioselective Diels-Alder addition, Journal of the American Chemical Society 125 (2003) 6388-6390.
7. G. Zhou, Q-Y. Hu, E.J. Corey, Useful enantioselective bicyclization reactions using an N-protonated chiral oxazaborolidine as catalyst, Organic Letters 5 (2003) 3979-3982.
8. D.H. Ryu, G. Zhou, E.J. Corey, Enantioselective and structure-selective Diels-Alder reactions of unsymmetrical quinones catalyzed by a chiral oxazaborolidinium cation. Predictive selection rules, Journal of the American Chemical Society 126 (2004) 4800-4802.
9. D.H. Ryu, E.J. Corey, Enantioselective cyanosilylation of ketones catalyzed by a chiral oxazaborolidinium ion, Journal of the American Chemical Society 127 (2005) 5384-5387.
10. D.H. Ryu, G. Zhou, E.J. Corey, Nonparallelism between reaction rate and dienophile-catalyst affinity in catalytic enantioselective Diels-Alder reactions, Organic Letters 7 (2005) 1633-1636.
11. D.Liu, E. Canales, E.J. Corey, Chiral oxazaborolidine-aluminum bromide complexes are usually powerful and effective catalysts for enantioselective Diels-Alder reactions, Journal of the American Chemical Society 129 (2007) 1498-1499.
12. J. Sauer, R. Sustmann, Mechanistic aspects of Diels-Alder reactions: A critical survey, Angewandte Chemie International Edition 19 (1980) 779-807.
13. K.N. Houk, J. Gonzalez, Y. Li, Pericyclic reaction transition states: Passion and punctilios, 1935-1995, Accounts of Chemical Research 28 (1995) 81-90.
14. E. Goldstein, B. Beno, K.N. Houk, Density functional theory prediction of the relative energies and isotope effects for the concerted and stepwise mechanisms of the Diels-Alder reaction of butadiene and ethylene, Journal of the American Chemical Society 118 (1996) 6036-6043.
15. K.N. Houk, B.R. Beno, M. Nendel, K. Black, H.Y. Yoo, S. Wilsey, J.K. Lee, Exploration of pericyclic reaction transition structures by quantum mechanical methods: Competing concerted and stepwise mechanisms, Journal of Molecular Structure (Theochem) 398-399 (1997) 169-179.
16. D.A. Singleton, S.R. Merrigan, A.A. Thomas, Stereochemical labeling at natural abundance. Stereochemistry, isotope effects, and mechanism of the

Diels-Alder reaction of hexachlorocyclopentadiene with ethyl vinyl ether, Tetrahedron Letters 40 (1999) 639-642.

17. J. Tanaka, S. Kanemasa, Ab initio study of Lewis acid catalyzed nitrone cycloaddition to electron deficient alkenes. Does a Lewis acid catalyst change the reaction mechanism? Tetrahedron 57 (2001) 899-905.
18. Y-S. Fu, S-C. Tsai, C-H. Huang, S-Y. Yen, W-P. Hu, S. J. Yu, Kinetics study and theoretical modeling of the Diels-Alder reactions of cyclopentadiene and cyclohexadiene with methyl vinyl ketone. The effects of a novel organotungsten catalyst, Journal of Organic Chemistry 68 (2003) 3068-3077.
19. Z. Pi, S. Li, Theoretical study on the Diels-Alder reaction between 2-methylacrolein and cyclopentadiene catalyzed by a cationic oxazaborolidine Lewis acid, Journal of Physical Chemistry A 110 (2006) 9225-9230.
20. B.A. Horn, J.L. Herek, A.H. Zewail, Retro-Diels-Alder femtosecond reaction dynamics, Journal of the American Chemical Society 118 (1996) 8755–8756.
21. E.W.-G. Diau, S.D. Feyter, A.H. Zewail, Femtosecond dynamics of retro Diels-Alder reactions: The concept of concertedness, Chemical Physics Letters 304 (1999) 134-144.
22. W. Koch, M. Holthausen, A Chemist's Guide to Density Functional Theory, Wiley-VCH Verlag, Weinheim, Germany, 2001.
23. S. Kong, J.D. Evanseck, Density functional theory study of aqueous-phase rate acceleration and *endo*/*exo* selectivity of the butadiene and acrolein Diels-Alder reaction, Journal of the American Chemical Society 122 (2000) 10418-10427.
24. M.J. Lilly, M.N. Paddon-Row, M.S. Sherburn, C.I. Turner, New insights into the *endo–exo* stereoselectivity of the intramolecular Diels-Alder reaction of 1,3,8-nonatrienes, Chemical Communications (2000) 2213-2214.
25. C.D. Valentin, M. Freccero, M. Sarzi-Amadè, R. Zanaletti, Reactivity and *endo–exo* selectivity in Diels-Alder reaction of *o*-quinodimethanes. An experimental and DFT computational study, Tetrahedron 56 (2000) 2547-2559.
26. M. Avalos, R. Babiano, J.L. Bravo, P. Cintas, J.L. Jiménez, J.C. Palacios, M.A. Silva, Computational studies on the BF_3-catalyzed cycloaddition of furan with methyl vinyl ketone: A new look at Lewis acid catalysis, Journal of Organic Chemistry 65 (2000) 6613-6619.
27. R. Robiette, J. Marchand-Brynaert, D. Peeters, Influence of diene substitution on transition state stabilization in Diels-Alder reaction, Journal of Organic Chemistry 67 (2002) 6823-6826.
28. A.G. Leach, K.N. Houk, Diels-Alder and ene reactions of singlet oxygen, nitroso compounds and triazolinediones: Transition states and mechanisms from contemporary theory, Chemical Communications (2002) 1243-1255.
29. R. Robiette, J. Marchand-Brynaert, D. Peeters, Theoretical study of the influence of phosphonate substituents on Diels-Alder reactions, Journal of Molecular Structure (Theochem) 587 (2002) 159-169.
30. R. Vijaya, T.C. Dinadayalane, G.N. Sastry, Diels-Alder reactions between cyclic five-membered dienes and acetylene, Journal of Molecular Structure (Theochem) 589-590 (2002) 291-299.
31. Z. Zdravkovski, Theoretical study of the Diels-Alder reactions of benzene with fluorinated dienophiles, Journal of Molecular Structure (Theochem) 684 (2004) 99-102.
32. S. Sakai, T. Okumura, Theoretical studies on the substituent effects for concerted and stepwise mechanisms of the Diels-Alder reaction between

butadiene and ethylene, Journal of Molecular Structure (Theochem) 685 (2004) 89-95.

33. C.N. Alves, F.F. Camilo, J. Gruber, A.B.F. da Silva, A density functional theory study on the molecular mechanism of the cycloaddition between (*E*)-methyl cinnamate and cyclopentadiene, Chemical Physics 306 (2004) 35-41.
34. M. Pasikowska, P. Fiedorow, H. Koroniak, Theoretical studies of the Diels-Alder reaction of 1-fluoroethylene with some model dienes, Journal of Molecular Structure: THEOCHEM 713 (2005) 193-199.
35. M.-L. Boulanger, T. Leyssens, R. Robiette, D. Peeters, Theoretical approach of steric effects in the Diels-Alder reaction, Journal of Molecular Structure: THEOCHEM 731 (2005) 101-106.
36. J.E. Rodríguez-Borges, X. García-Mera, F. Fernández, V.H.C. Lopes, A.L. Magalhães, M.N.D.S. Cordeiro, Experimental and DFT study of the aza-Diels-Alder reaction between cyclopentadiene and protonated benzylimine derivated from glyoxylates, Tetrahedron 61 (2005) 10951-10957.
37. C.N. Alves, A.S. Carneiro, J. Andrés, L.R. Domingo, A DFT study of the Diels-Alder reaction between methyl acrolein derivatives and cyclopentadiene. Understanding the effects of Lewis acids catalysts based on sulfur containing boron heterocycles, Tetrahedron 62 (2006) 5502-5509.
38. X. Zhang, H. Du, Z. Wang, Y.-D. Wu, K. Ding, Experimental and theoretical studies on the hydrogen-bond-promoted enantioselective hetero-Diels-Alder reaction of Danishefsky's diene with benzaldehyde, Journal of Organic Chemistry 71 (2006) 2862-2869.
39. R. Gordillo, T. Dudding, C.D. Anderson, K.N. Houk, Hydrogen bonding catalysis operates by charge stabilization in highly polar Diels-Alder reactions, Organic Letters 9 (2007) 501-503.
40. H. Dirhoussi, A. Sbai, A computational theoretical study of the Diels-Alder reaction between β–ionone and maleic anhydride. Influence of Lewis acid catalyst, and inclusion of solvent effects, Internet Electronic Journal of Molecular Design 6 (2007) 36-46.
41. C.D. Anderson, T. Dudding, R. Gordillo, K.N. Houk, Origin of enantioselection in hetero-Diels-Alder reactions catalyzed by Naphthyl-TADDOL, Organic Letters 10 (2008) 2749-2752.
42. M.N. Paddon-Row, C.D. Anderson, K.N. Houk, Computational evaluation of enantioselective Diels-Alder reactions mediated by Corey's cationic oxazaborolidine catalysts, Journal of Organic Chemistry 74 (2009) 861-868.
43. Gaussian 03, Revision E.01, M. J. Frisch, G. W. Trucks, H. B. Schlegel, G. E. Scuseria, M. A. Robb, J. R. Cheeseman, J. A. Montgomery, Jr., T. Vreven, K. N. Kudin, J. C. Burant, J. M. Millam, S. S. Iyengar, J. Tomasi, V. Barone, B. Mennucci, M. Cossi, G. Scalmani, N. Rega, G. A. Petersson, H. Nakatsuji, M. Hada, M. Ehara, K. Toyota, R. Fukuda, J. Hasegawa, M. Ishida, T. Nakajima, Y. Honda, O. Kitao, H. Nakai, M. Klene, X. Li, J. E. Knox, H. P. Hratchian, J. B. Cross, V. Bakken, C. Adamo, J. Jaramillo, R. Gomperts, R. E. Stratmann, O. Yazyev, A. J. Austin, R. Cammi, C. Pomelli, J. W. Ochterski, P. Y. Ayala, K. Morokuma, G. A. Voth, P. Salvador, J. J. Dannenberg, V. G. Zakrzewski, S. Dapprich, A. D. Daniels, M. C. Strain, O. Farkas, D. K. Malick, A. D. Rabuck, K. Raghavachari, J. B. Foresman, J. V. Ortiz, Q. Cui, A. G. Baboul, S. Clifford, J. Cioslowski, B. B. Stefanov, G. Liu, A. Liashenko, P. Piskorz, I. Komaromi, R. L. Martin, D. J. Fox, T. Keith, M. A. Al-Laham, C. Y. Peng, A.

Nanayakkara, M. Challacombe, P. M. W. Gill, B. Johnson, W. Chen, M. W. Wong, C. Gonzalez, and J. A. Pople, Gaussian, Inc., Wallingford CT, 2004.
44. P. Pulay, Convergence acceleration of iterative sequences. The case of SCF iteration, Chemical Physics Letters 73 (1980) 393-398.
45. P. Pulay, Improved SCF convergence acceleration, Journal of Computational Chemistry 3 (1982) 556-560.
46. K.N. Kudin, G.E. Scuseria, E. Cancès, A black-box self-consistent field convergence algorithm: One step closer, Journal of Chemical Physics 116 (2002) 8255-8261.
47. http://www.gaussian.com/g_tech/g_ur/m_eff.htm.
48. G.B. Bacskay, A quadratically convergent Hartree-Fock (QC-SCF) method. Application to closed shell systems, Chemical Physics 61 (1981) 385-404.
49. H.B. Schlegel, Estimating the Hessian for gradient-type geometry optimizations, Theoretica Chimica Acta 66 (1984) 333-340.
50. C. Peng, P.Y. Ayala, H.B. Schlegel, M.J. Frisch, Using redundant internal coordinates to optimize equilibrium geometries and transition states, Journal of Computational Chemistry 17 (1996) 49-56.
51. V. Anisimov, P. Paneth, ISOEFF98. A program for studies of isotope effects using Hessian modifications, Journal of Mathematical Chemistry 26 (1999) 75-86. The program is available by request from Professor P. Paneth (paneth@p.lodz.pl).
52. E.J. Corey, T.W. Lee, The formyl C–H···O hydrogen bond as a critical factor in enantioselective Lewis-acid catalyzed reactions of aldehydes, Chemical Communications (2001) 1321-1329.
53. M.D. Mackey, J.M. Goodman, Conformational preferences of $R^1R^2C{=}O{\bullet}H_2BF$ complexes, Chemical Communications (1997) 2383-2384.
54. Q-Y. Hu, G. Zhou, E.J. Corey, Application of chiral cationic catalysts to several classical syntheses of racemic natural products transforms them into highly enantioselective pathways, Journal of the American Chemical Society 126 (2004) 13708-13713.
55. D.M. Birney, K.N. Houk, Transition structures of the Lewis acid-catalyzed Diels-Alder reaction of butadiene with acrolein. The origins of selectivity, Journal of the American Chemical Society 112 (1990) 4127–4133.
56. http://www.gaussian.com/g_tech/g_ur/k_scrf.htm, and references cited therein.
57. F.A. Carey, R.J. Sundberg, Advanced Organic Chemistry: Part A: Structure and Mechanisms, Springer Science Business Media, LLC, 2007.
58. T.H. Lowry, K.S. Richardson, Mechanism and Theory in Organic Chemistry, Harper Collins Publishers, New York, NY, 1987.
59. D.A. Singleton, A.A. Thomas, High-precision simultaneous determination of multiple small kinetic isotope effects at natural abundance, Journal of the American Chemical Society 117 (1995) 9357-9358.
60. B.R. Beno, K.N. Houk, D.A. Singleton, Synchronous or asynchronous? An "experimental" transition state from a direct comparison of experimental and theoretical kinetic isotope effects for a Diels-Alder reaction, Journal of the American Chemical Society 118 (1996) 9984-9985.
61. D.A. Singleton, S.R. Merrigan, B.R. Beno, K.N. Houk, Isotope effects for Lewis acid catalyzed Diels-Alder reactions. The experimental transition state, Tetrahedron Letters 40 (1999) 5817-5821.
62. A.G. Leach, K.N. Houk, Transition states and mechanisms of the hetero-Diels-Alder reactions of hyponitrous acid, nitrosoalkanes, nitrosoarenes, and

nitrosocarbonyl compounds, Journal of Organic Chemistry 66 (2001) 5192-5200.

63. N.J. Saettel, O. Wiest, D.A. Singleton, M.P. Meyer, Isotope effects and the mechanism of an electron-transfer-catalyzed Diels-Alder reaction, Journal of the American Chemical Society 124 (2002) 11552-11559.
64. O. Acevedo, J.D. Evanseck, The effect of solvent on a Lewis acid catalyzed Diels-Alder reaction, using computed and experimental kinetic isotope effects, Organic Letters 5 (2003) 649-652.
65. R. Bruckner, Advanced Organic Chemistry: Reaction Mechanisms, Harcourt/Academic Press, Burlington, MA, 2002.
66. S.M. Bachrach, Computational Organic Chemistry, John Wiley & Sons, Inc., Hoboken, NJ, 2007.
67. S. Danishefsky, T. Kitahara, Useful diene for the Diels-Alder reaction, Journal of the American Chemical Society 96 (1974) 7807–7808.
68. S. Danishefsky, Siloxy dienes in total synthesis, Accounts of Chemical Research 14 (1981) 400-406.
69. H.B. Schlegel, J.M. Millam, S.S. Iyengar, G.A. Voth, A.D. Daniels, G.E. Scuseria, M.J. Frisch, *Ab initio* molecular dynamics: Propagating the density matrix with Gaussian orbitals, Journal of Chemical Physics 114 (2001) 9758-9763.
70. S.S. Iyengar, H.B. Schlegel, J.M. Millam, G.A. Voth, G.E. Scuseria, M.J. Frisch, *Ab initio* molecular dynamics: Propagating the density matrix with Gaussian orbitals. II. Generalizations based on mass-weighting, idempotency, energy conservation, and choice of initial conditions, Journal of Chemical Physics 115 (2001) 10291-10302.
71. H.B. Schlegel, S.S. Iyengar, X. Li, J.M. Millam, G.A. Voth, G.E. Scuseria, M.J. Frisch, *Ab initio* molecular dynamics: Propagating the density matrix with Gaussian orbitals. III. Comparison with Born-Oppenheimer dynamics, Journal of Chemical Physics 117 (2002) 8694-8704.
72. L. Joubert, C. Adamo, Static and dynamic descriptions of bond breaking/formation: A complementary view? The Journal of Chemical Physics 123 (2005) 211103-1-4.
73. W.Q. Tian, Y.A. Wang, Dynamics of the Staudinger reaction, Journal of Chemical Theory and Computation 1 (2005) 353-362.
74. L. Joubert, M. Pavone, V. Barone, C. Adamo, Comparative static and dynamic study of a prototype S_N2 reaction, Journal of Chemical Theory and Computation 2 (2006) 1220-1227.
75. A.N. Jay, K.A. Daniel, E.V. Patterson, Atom-centered density matrix propagation calculations on the methyl transfer from CH_3Cl to NH_3: Gas-phase and continuum-solvated trajectories, Journal of Chemical Theory and Computation 3 (2007) 336-343.

4

Density Functional Theory Investigation of the Enantioselectivity and Mechanism of an Organocatalytic Diels-Alder Reaction

To provide further information in addition to the energetics and electronic structures of the molecules involved in a chemical reaction, the work of the present chapter deals with various aspects of density functional theory as applied to the study of the selectivity and the mechanism of the Diels-Alder reaction. The theoretical methods used include the reaction force profiles, the topological analysis of the electron density and the global reactivity descriptors. Theoretical backgrounds of these approaches are also introduced.

4.1 Introduction

As in wavefunction based methods, density functional theory (DFT) calculations generate numbers that often need to be translated into a language that reveals their chemical relevance. As stated by Robert G. Parr [1] "Accurate calculation is not synonymous with useful interpretation. To calculate a molecule is not to understand it".

Conceptual density functional theory provides a means for the prediction and interpretation of the chemical reactivity on the basis of the response of the system's energy and of the system's electron density to changes in the external potential and/or the number of electrons [2-4]. This corresponds to conceptually simple and chemically meaningful quantities. For example, the electronegativity has been identified as the negative of the electronic chemical potential, which is the first partial derivative of the total electronic energy of the molecule with respect to its number of electrons at constant external potential [5].

The Diels-Alder reaction, in terms of the nature of the interaction between the diene and the dienophile as well as the selectivity, mechanism, and progress of the reaction, has been studied through various theoretical approaches. These include: (1) frontier molecular orbital (FMO) analysis [6-11], (2) bond order analysis, natural bond orbital (NBO) methods, and topological analysis of the electron localization function (ELF) [6-8,12-19], (3) global and local reactivity descriptors [20-24], (4) reaction path and reaction forces [25], and (5) aromaticity [26,27].

The objective of the present chapter is to examine the applicability of some of the abovementioned theoretical approaches to rationalize the mechanism and enantioselectivity of the Diels-Alder reaction. The reaction studied is between 2-methyl-1,3-butadiene **14** and 2,3-dimethyl-1,4-benzoquinone **15** in the presence of catalyst **16** (cf. Figures 3.1 and 3.5). Only the most energetically favorable transition states for the *endo* (**TS9**) and the *exo* (**TS14**) channels are considered. It is hopeful that the outcome of the current work will aid in deeper understanding of the mechanism and enantioselectivity of organocatalytic Diels-Alder reactions.

4.2 Computational Details

All DFT calculations were carried out *in vacuo* at the B3LYP/6-31G(d) level of theory as implemented in the Gaussian 03 program [28] (for details cf. Section 3.2). All atomic charges were obtained from the natural population analysis (NPA) [29-31] at the same level of theory using the NBO program (version 3.1) integrated into Gaussian 03. The reaction forces were obtained by tracing the intrinsic reaction coordinate (IRC) [32-36] as implemented in Gaussian 03 using the same calculation level. The initial force constants for the IRC calculation were taken from the corresponding previous frequency run used to confirm the transition structure. A total of 40 points were examined along the reaction path (both the forward and the backward directions) with a default step size of 0.1 amu$^{1/2}$ Bohr.

Electron localization function (ELF) [17,37-42] calculations were performed for the reactants, products, transition structures and critical points along the IRC path using the DGrid program [43]. The DGrid program requires only the Gaussian formatted checkpoint file and converts it to a special formatted file that contains all the necessary information for it to run.

The Mayer bond orders [44-47] were calculated for the reactants, products, transition structures and critical points along the IRC path using the EFF-AO program [48]. This was achieved by performing single-point HF/STO-3G calculations at the B3LYP/6-31G(d) optimized structures using the Gaussian 03 program. The Gaussian formatted checkpoint file is then used by the EFF-AO program for bond order analysis. The use of the minimal STO-3G basis set is recommended for bond order and valence indices analysis and gives the most reliable values [49-51].

Global reactivity indices including electronic chemical potential (μ), chemical hardness (η), and electrophilicity (ω) are calculated as follows [52,53]:

$$\mu \approx \frac{1}{2}\left(\varepsilon_{\mathrm{H}} + \varepsilon_{\mathrm{L}}\right) \tag{4-1}$$

$$\eta \approx \varepsilon_{\mathrm{L}} - \varepsilon_{\mathrm{H}} \tag{4-2}$$

$$\omega = \frac{\mu^2}{2\eta} \tag{4-3}$$

where ε_{H} and ε_{L} are the one-electron energies of the HOMO and the LUMO, respectively.

4.3 Results and Discussion

4.3.1 Reaction force analysis along the intrinsic reaction coordinate

The path on the potential energy surface connecting the reactants and the products through the transition structure is termed the reaction path [35]. The steepest descent reaction path from the transition structure to the reactants and to the products is called the minimum energy path (MEP) (depicted by red lines in Figure 2.4) [35]. If the reaction path is described in terms of mass-weighted coordinates, the MEP is referred to as the intrinsic reaction coordinate (IRC) [32].

Several reaction path following algorithms have been devised [35,36] with the one developed by Gonzalez and Schlegel [33,34] being the most widely used. The Gonzalez-Schlegel (GS) algorithm is shown in Figure 4.1. In the GS algorithm, the gradient at point $\mathbf{q}_i$ is first calculated and a step of size ½ s is taken along the direction of this gradient in order to find point $\mathbf{q}$\`. On the surface of a hypersphere of radius ½ s and centered at $\mathbf{q}$\`, a constrained minimization is then performed in order to locate the next point $\mathbf{q}_{i+1}$[33-36]. The points $\mathbf{q}_i$, $\mathbf{q}$\` and $\mathbf{q}_{i+1}$ form an isosceles triangle. Hence, the path between $\mathbf{q}_i$ and $\mathbf{q}_{i+1}$ represents an arc of a circle and the gradients at these points are tangent to this path [33-36]. The GS algorithm requires only first derivatives at points along the path and second derivatives are only needed at the transition state.

During a chemical reaction, the changes in the physical and chemical properties of the reaction complex (i.e. the reacting molecules) along the IRC can be investigated to gain insights into the reaction mechanism. The motion of the reaction complex across the IRC is a direct result of the forces exerted on its atoms. These forces can be associated with particular internal coordinates and regions of repulsive (forces > 0) and attractive (forces < 0) interatomic forces can be distinguished [25,54-57].

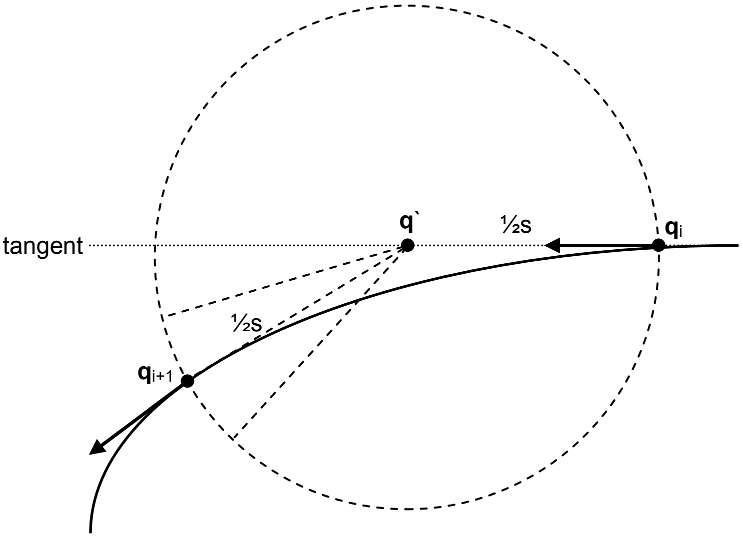

Figure 4.1: Second-order Gonzalez-Schlegel reaction path following algorithm.

The reaction force (**F**) is defined as the first partial derivative of the potential energy (*U*) with respect to nuclear coordinates (**R**), that is

$$\mathbf{F}(\mathbf{R}) = -\frac{\partial U(\mathbf{R})}{\partial \mathbf{R}}. \tag{4-4}$$

The IRC for the Diels-Alder reaction between diene **14** and dienophile **15** in the presence of catalyst **16** for both the *endo* and *exo* routes is shown in Figure 4.2. As observed in the figure, the *endo* path is more energetically favored over the *exo* route throughout the course of the reaction. For both *endo* and *exo* channels, the IRC behavior is characterized by a moderate increase in energy towards the transition state and a steeper decrease in energy towards the products. This behavior reflects the asynchronous nature of the reaction.

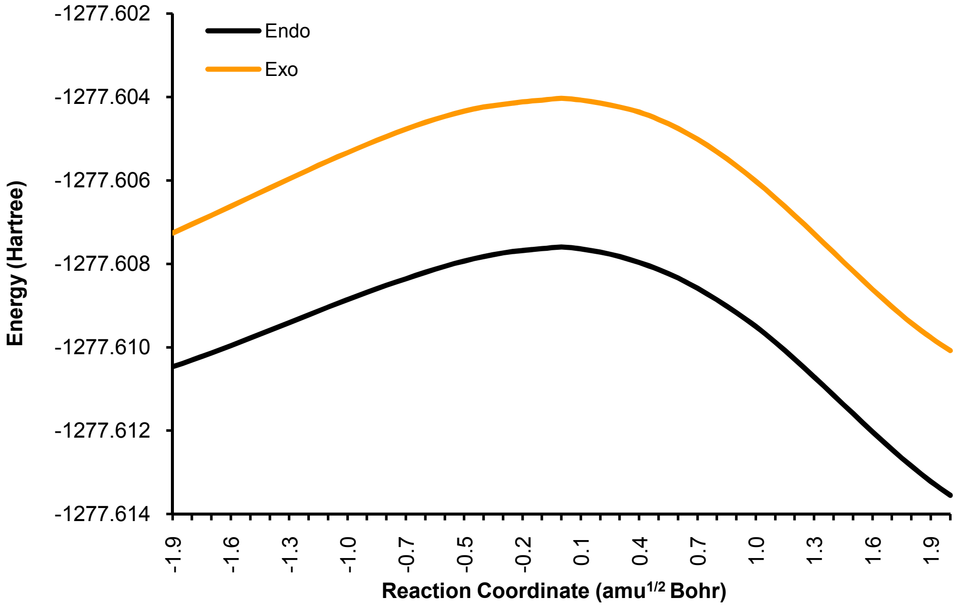

Figure 4.2: B3LYP/6-31G(d) IRC for the endo (starting from ***TS9****) and the exo (starting from* ***TS14****) channels of the Diels-Alder reaction between* ***14*** *and* ***15*** *in the presence of catalyst* ***16*** *(cf. Reaction 3-D, Chapter 3).*

The reaction forces associated with the internal coordinate R1 (i.e. the coordinate that corresponds to the forming carbon-carbon bond) along the IRC are illustrated in Figure 4.3 for both *endo* and *exo* routes. The total reaction forces along the IRC for both *endo* and *exo* channels are represented in Figure 4.4.

As can be seen from Figures 4.3 and 4.4, the reaction force profile possesses three key points along the IRC, namely, α, TS and β [55-57]. Initially, the reaction is described by an increasing repulsive force that reaches its peak at point α. At this point, the repulsive force starts to diminish smoothly due to the presence of an attractive force until the point where the repulsive and attractive forces are the same (**F**(**R**) = 0) is reached. This point corresponds to the transition state (TS). After the TS, the attractive force becomes predominant and increases sharply until point β is reached. At this point, the attractive force begins to decrease until it reaches zero for the product.

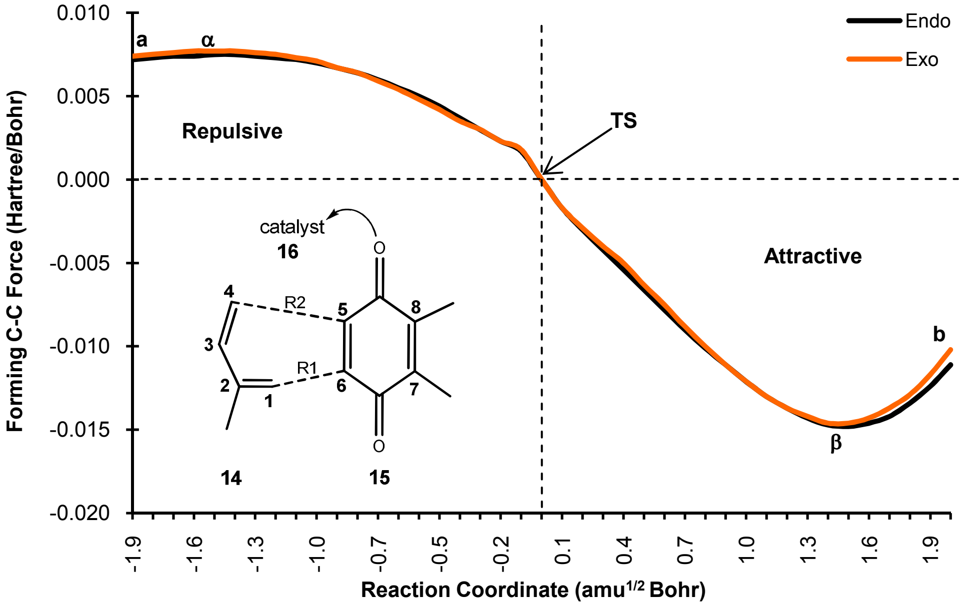

Figure 4.3: Reaction force profiles associated with the internal coordinate R1 for the endo and the exo channels of the Diels-Alder reaction between ***14*** *and* ***15*** *in the presence of catalyst* ***16*** *(cf. Reaction 3-D, Chapter 3). Points a, α, TS, β and b are described in the text.*

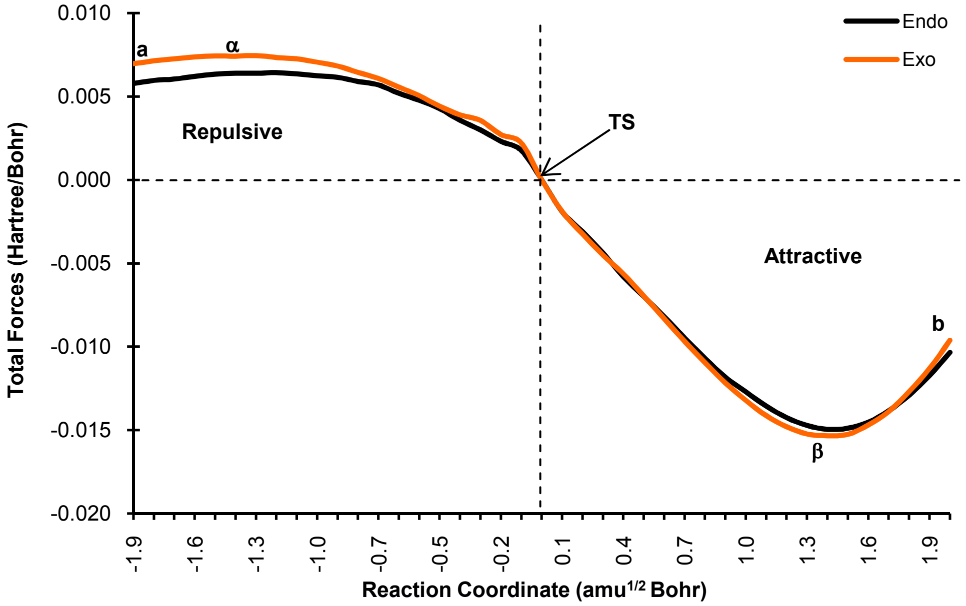

Figure 4.4: Reaction force profiles associated with all Cartesian coordinates for the endo and the exo channels of the Diels-Alder reaction between ***14*** *and* ***15*** *in the presence of catalyst* ***16*** *(cf. Reaction 3-D, Chapter 3). Points a, α, TS, β and b are described in the text.*

For both *endo* and *exo* channels, monitoring the internal coordinate R1 along the IRC shows that the repulsive force starts to diminish at point α where the R1 value is 2.38 Å. At this distance, the overlap between π-orbitals is ~ 0.02 Å [25] which marks the start of the attractive force. The attractive force persists until point β where the R1 value is 1.82 Å. At this point, the final stage for the formation of the carbon-carbon single bond begins.

Both Figures 4.3 and 4.4 show the *endo* route to have less repulsive forces than the *exo* path. This leads to a lowering of the reaction barrier (i.e. the activation energy) for the *endo* channel rendering it the kinetically preferred path for this reaction. In addition, after point β towards the products, the attractive forces due to carbon-carbon single bond formation become more evident for the *endo* path. Again, this reflects that the formation of the *endo* product is favored over the *exo* one.

4.3.2 Natural population analysis (NPA)

The wavefunction of a particle has no physical meaning but the square of the wavefunction gives the probability of finding this particle in a given volume in space. In molecular orbital theory, the electron density for a given molecular orbital is defined as

$$\rho_i(\mathbf{r}) = \left|\psi_i(\mathbf{r})\right|^2 . \tag{4-5}$$

The electron density of a closed-shell molecule is then given by

$$\rho(\mathbf{r}) = 2\sum_{i}^{n/2} \rho_i(\mathbf{r}) . \tag{4-6}$$

The integration of the molecule electron density gives the total number of electrons in the molecule, that is

$$\int \rho(\mathbf{r})\, d\mathbf{r} = n . \tag{4-7}$$

The electron density by itself does not directly reveal chemically meaningful concepts. However, population analysis aims at analyzing the electron density and assigning electrons to a particular atom or orbital. Population analysis methods can be classified into three groups [58,59]: (1) orbital-based methods such as Mulliken population analysis (MPA) and natural population analysis (NPA), (2) methods based on the molecular electrostatic potential such as the CHELPG scheme, and (3) methods based on the topological analysis of the electron density such as the atoms-in-molecules (AIM) method and the electron localization function (ELF) model.

The natural bond orbital (NBO) analysis includes NPA and is aimed at describing the *n*-electron wavefunction in terms of localized orbitals that closely resemble the chemist's view of the chemical bond.

For closed-shell single-determinant (HF or DFT) wavefunction, the first-order density matrix (also called the one-electron density matrix) can be written in terms of the canonical molecular orbital coefficients and is identical to the density matrix defined by Eq. 2-33 [59-65]. This matrix holds essential information of chemical significance such as electron distribution and chemical bonding. The eigenvectors and the eigenvalues that result from the diagonalization of the density matrix are called 'natural orbitals' and 'occupation numbers', respectively [58-62,65-67]. These natural orbitals are unsuitable for chemical analysis since they are delocalized over all atoms (i.e. they are similar to canonical molecular orbitals) [31,66]. Hence, the one-electron density matrix is partitioned into atomic sub-blocks [59,68-70] according to

$$\mathbf{P} = \begin{pmatrix} \mathbf{P}_{\mathrm{AA}} & \mathbf{P}_{\mathrm{AB}} & \mathbf{P}_{\mathrm{AC}} & \cdots \\ \mathbf{P}_{\mathrm{BA}} & \mathbf{P}_{\mathrm{BB}} & \mathbf{P}_{\mathrm{BC}} & \cdots \\ \mathbf{P}_{\mathrm{CA}} & \mathbf{P}_{\mathrm{CB}} & \mathbf{P}_{\mathrm{CC}} & \cdots \\ \vdots & \vdots & \vdots & \ddots \end{pmatrix} \tag{4-8}$$

where each block on the main diagonal corresponds to basis functions associated with a particular atom and every off-diagonal block is related to basis functions belonging to a pair of atoms. Independently diagonalizing (with respect to the associated overlap matrix) each block on the main diagonal gives orbitals that are termed 'pre-natural atomic orbitals' (pre-NAOs) [58,59]. These pre-NAOs are generally non-orthogonal and need to be orthogonalized (i.e. the interatomic overlap between pre-NAOs is removed) so as the sum of their occupation numbers gives the total number of electrons [31,58,59,70]. The resultant final orbitals are called NAOs. The nuclear charge minus the sum of all occupancies of the NAOs that belong to a particular atom gives the natural atomic charge. Core orbitals are defined as those NAOs that have high occupation numbers (> 1.999), while lone pairs as those NAOs with occupation numbers of > 1.90. The core and lone pair contributions to the density matrix are then removed and the 2×2 sub-blocks of the density matrix concerning each pair of atoms are diagonalized [58,59,69,70]. The resulting eigenvectors with high occupation numbers (> 1.90) are called 'natural bond orbitals' (NBOs) and describe the chemical bonds between atoms in a localized fashion [59,70]. As compared to MPA, NPA derived atomic charges are less dependent on the basis set used [31]. In addition NPA occupation numbers satisfy the Pauli Exclusion Principle (i.e. they fall in the range of 0 to 2 for spatial orbitals) [31].

Contrary to the energy, which is an overall quantity integrated over the entire molecule, chemical bonds are local in nature [71]. Therefore, the investigation of the chemical bond formation during a chemical reaction provides information that cannot be described by the energy alone. The natural population analysis offers a tool for evaluating the charge transfer (CT) along the reaction path. In normal electron demand Diels-Alder reaction, the donor (i.e. the diene) highest occupied molecular orbital (HOMO) loses electrons in two different ways. A portion of the charge density is directly transferred from the HOMO of the diene to the lowest unoccupied molecular orbital (LUMO) of the dienophile and another portion is utilized to form the intermolecular bonds by the overlapping between these molecular orbitals [71].

The charge transferred from diene **14** to dienophile **15** along the IRC is given in Table 4.1.

Table 4.1: Natural population analysis of the charge (e) transferred from **14** to **15** along the IRC. Points are as illustrated in Figures 4.3 and 4.4.

	CT
Endo Path	
Point (a)	0.293
Point (α)	0.293
TS	0.294
Point (β)	0.294
Point (b)	0.295
Exo Path	
Point (a)	0.154
Point (α)	0.189
TS	0.220
Point (β)	0.268
Point (b)	0.278

As can be deduced from the table, the charge transfer associated with the more favorable *endo* path is larger than that associated with the *exo* route. This larger charge transfer leads to a lower exchange (or Pauli) repulsion (smaller repulsive forces (cf. Figures 4.3 and 4.4)) and hence is responsible for the lower activation energy of the *endo* channel [25].

The progress of the charge transfer along the IRC is also much faster for the *endo* channel than that of the *exo* route, and is almost completed at the transition state (Table 4.1). This leads to a lower barrier and more stabilization for the *endo* route.

For both the *endo* and *exo* paths, point b on the IRC marks the end of charge transfer. At this point, the total amount of charge transferred from diene **14** to dienophile **15** is 0.30 e and 0.28 e for the *endo* and the *exo* channels, respectively (Table 4.1), indicating a more polar character for the *endo* route.

4.3.3 Topological analysis of the electron localization function

As in the case of NBO analysis, the electron localization function (ELF) aids in understanding the concept of electron pair localization (core, lone pair and bonding electrons) that corresponds to Lewis structures, which in turn helps in the rationalization and understanding of the molecular structure, bonding, chemical reactivity, and reaction mechanism [13-16,72-77]. The ELF is different from NBO methods in that it is based on the electron density rather than the wavefunction.

The mathematical form of the ELF [17,37,39-41] for a closed-shell system is given by

$$\mathrm{ELF}(\mathbf{r}) = \left(1 + \left(\frac{D}{D_0}\right)^2\right)^{-1} \tag{4-9}$$

where D (Eq. 4-10) and D_0 (Eq. 4-11) represent the curvature of the electron pair density of identical spin electrons for the real system and a uniform electron gas with the same density, respectively.

$$D = \frac{1}{2}\sum_{i=1}^{n/2} \left|\nabla \psi_i(\mathbf{r})\right|^2 - \frac{1}{8}\frac{\left|\nabla \rho(\mathbf{r})\right|^2}{\rho(\mathbf{r})} \tag{4-10}$$

$$D_0 = \frac{3}{10}\left(3\pi^2\right)^{2/3} \rho(\mathbf{r})^{5/3}. \tag{4-11}$$

The first term on the right hand side of Eq. 4-10 is the kinetic energy density of the non-interacting system while the second term is the von Weizsäcker kinetic energy density. The function *D* measures the local excess of kinetic energy density due to Pauli repulsion [17]. For regions of space occupied by unlike spin electron pair, the Pauli repulsion is negligible, the first and second terms of Eq. 4-10 are almost identical, the value of the function *D* is near zero, and the value of the ELF is close to one [17,37]. On the other extreme, an ELF value close to zero represents a completely delocalized situation. The ELF shows only little dependence on the theoretical level used to obtain the electron density and the molecular orbitals [17,41].

The topological analysis of the ELF gradient field (∇ ELF($\mathbf{r}$)) allows partitioning of the molecular space into basins of attractors (maxima) that correspond to the bonds and lone pairs in the Lewis structure model [17,40]. There are two types of basins [17,40]: a core basin (C) that contains a nucleus (except a proton) and a valence basin (V) that lacks nucleus and is always connected with one or more core basins. A monosynaptic basin is connected with only one core basin and corresponds to a lone pair. A disynaptic basin is connected with two core basins and represents a two-center covalent bond. Higher synaptic orders are also possible. Integrating the electron density over the basin volume produces the basin population.

The topology of the ELF of the reacting complex (the diene **14**, the dienophile **15**, and the catalyst **16**) is analyzed in order to gain insights into the electron density evolution along the IRC. This corresponds to the breaking and formation of the carbon-carbon double bonds along the IRC. The ELF method differentiates between the carbon-carbon single and double bonds in accordance with the Lewis model.

Double bonds are characterized by two disynaptic basins whilst single bonds are represented by only one disynaptic basin.

The electron populations of the more relevant valence basins are listed in Table 4.2. In the case of carbon-carbon double bonds, the electron population is given as the sum of the two individual electron populations associated with the two disynaptic basins used to describe the double bond.

Table 4.2: Electron populations for the valence ELF basins of the reacting complex (**14-15-16**) along the IRC. Points and carbon numbers are as illustrated in Figure 4.3.

	$V_{1+2}(C_1,C_2)$	$V_1(C_2,C_3)$	$V_{1+2}(C_3,C_4)$	$V_{1+2}(C_5,C_6)$	$V_1(C_1,C_6)$
Endo Path					
Point (a)	3.64	1.89	3.55	3.66	-
Point (α)	3.63	1.89	3.55	3.66	-
TS	3.58	1.89	3.55	3.63	-
Point (β)	*1.86*	1.90	3.54	*1.80*	*1.73*
Point (b)	*1.86*	1.90	3.55	*1.81*	*1.77*
Exo Path					
Point (a)	3.64	1.90	3.56	3.66	-
Point (α)	3.63	1.90	3.55	3.65	-
TS	3.59	1.90	3.56	3.64	-
Point (β)	*1.86*	1.89	3.57	*1.79*	*1.74*
Point (b)	*1.86*	1.89	3.58	*1.80*	*1.78*

For both *endo* and *exo* channels, the most noticeable changes in the electron population along the IRC are observed at point β (Table 4.2). At this point, the two disynaptic basins $V_{i=1,2}(C_1,C_2)$ found at the preceding points are merged into one disynaptic basin $V_1(C_1,C_2)$ with an electron population of 1.86 e. This indicates the transformation of $C_1{=}C_2$ double bond of the diene into C_1—C_2 single bond. Similarly, the two disynaptic basins $V_{i=1,2}(C_5,C_6)$ found at the preceding points are fused into one disynaptic basin $V_1(C_5,C_6)$ with an electron population of 1.80 e pointing out to the transformation of $C_5{=}C_6$ double bond of the dienophile into C_5—C_6 single bond. In addition, one new disynaptic basin $V_1(C_1,C_6)$ with an electron population of 1.73 e is created which indicates that the formation of C_1—C_6 single bond is in its final stage (the electron population of the disynaptic basin $V_1(C_1,C_6)$ is 1.82 e for the products). The flow of the electron density to the newly created basin is continued and the formation of $C_1—C_6$ single bond is complete after point b.

The topological analysis of the ELF, however, did not provide any sign regarding the formation of $C_4—C_5$ single bond and the formation of $C_2═C_3$ double bond. This might be due to the high asynchronous nature of the studied reaction.

As observed in Table 4.2, both *endo* and *exo* channels show the same trend with almost identical basin populations. Hence, it was not possible to investigate the *endo*/*exo* selectivity based on the topological analysis of the ELF.

4.3.4 Bond order analysis

Changes in chemical bonds during a chemical reaction influence the energy of the system. The extent of changes in bonding between the atoms of the system can be measured by the bond order. The bond order and valence indices obtained from quantum chemical calculations possess excellent interpretive power and are useful in systematically comparing the results attained for related molecules. One of the methods for calculating the bond order and valence indices is that developed by Mayer [44-47]. For closed-shell systems, the Mayer bond order (BO) between atoms A and B is defined as

$$BO_{A-B} = \sum_{r\in A}\sum_{s\in B}\left(\mathbf{PS}\right)_{rs}\left(\mathbf{PS}\right)_{sr} \tag{4-12}$$

where **P** and **S** are the density and overlap matrices whose elements are similar to those defined by Eqs. 2-33 and 2-28, respectively. And the valence of the atom is the sum of its bond orders, that is

$$V_A = \sum_{B\neq A} BO_{A-B}\ . \tag{4-13}$$

The diatomic interaction energy can be partitioned into individual components that are of different physical origins and are chemically meaningful such as electrostatic (or Coulomb) energy and exchange (or Pauli) repulsion energy [78-82]. The electrostatic contribution to the diatomic interaction energy in the energy decomposition scheme proposed by Mayer [45,47,80] provides a link between the bond order and the diatomic energy. In a point-charge approximation, the electrostatic interaction energy is given by [45,47,80]

$$E_{A-B}^{\text{point}} = \frac{1}{R_{A-B}}\left(q_A q_B - \frac{1}{2} BO_{A-B} \right) \tag{4-14}$$

where $R_{\mathrm{A-B}}$ is the distance between atoms A and B, and q is the Mulliken atomic charge. In addition to the classical electrostatic interaction, Eq. 4-14 includes a non-classical exchange repulsion energy contribution that is related to the bond order [45,47,80].

The extent of the bond breaking/forming along the IRC for both *endo* and *exo* channels as assessed by the use of Mayer bond order is given in Table 4.3. The associated bond lengths are also provided in the table. As is displayed in Table 4.3, the transformation of $C_1{=}C_2$ and $C_5{=}C_6$ double bonds into the corresponding single bonds is more evident and is more advanced than the transformation of $C_3{=}C_4$ double bond consistent with the results obtained from the topological analysis of the ELF (Section 4.3.3). Moreover, the bond order analysis shows that the formation of $C_2{=}C_3$ double bond is progressing despite at a slower rate than the break of the $C_1{=}C_2$ and $C_5{=}C_6$ double bonds.

The formation of C_1—C_6 single bond is observed to progress faster than the formation of C_4—C_5 single bond indicating a highly asynchronous bond formation. This is consistent with the topological analysis of the ELF (Section 4.3.3). Besides, at point b on the IRC, the bond order analysis revealed the formation of C_1—C_6 single bond to be at a very advanced stage.

Table 4.3: Computed Mayer bond orders, BO, for the reacting complex (**14-15-16**) along the IRC. The corresponding bond lengths (Å) are given in brackets. Points and carbon numbers are as illustrated in Figure 4.3.

	BO_{1-2}	BO_{2-3}	BO_{3-4}	BO_{4-5}	BO_{5-6}	BO_{1-6}
Endo Path						
Point (a)	1.787	1.079	1.887	0.012	1.701	0.073
	[1.368]	[1.456]	[1.350]	[3.210]	[1.365]	[2.449]
Point (α)	1.734	1.093	1.870	0.018	1.645	0.118
	[1.375]	[1.451]	[1.351]	[3.165]	[1.373]	[2.334]
TS	1.535	1.149	1.807	0.040	1.446	0.309
	[1.399]	[1.437]	[1.357]	[3.085]	[1.399]	[2.096]
Point (β)	1.222	1.265	1.683	0.074	1.169	0.663
	[1.443]	[1.418]	[1.366]	[3.010]	[1.442]	[1.820]
Point (b)	1.138	1.311	1.635	0.087	1.103	0.770
	[1.462]	[1.411]	[1.370]	[2.960]	[1.459]	[1.714]
Exo Path						
Point (a)	1.790	1.076	1.893	0.014	1.683	0.076
	[1.366]	[1.456]	[1.349]	[3.164]	[1.369]	[2.455]
Point (α)	1.740	1.089	1.878	0.019	1.628	0.119
	[1.372]	[1.451]	[1.350]	[3.127]	[1.377]	[2.347]
TS	1.528	1.146	1.812	0.040	1.414	0.324
	[1.395]	[1.437]	[1.356]	[3.054]	[1.404]	[2.095]
Point (β)	1.217	1.261	1.688	0.065	1.147	0.674
	[1.437]	[1.418]	[1.366]	[2.980]	[1.448]	[1.812]
Point (b)	1.136	1.307	1.639	0.074	1.087	0.778
	[1.454]	[1.410]	[1.371]	[2.930]	[1.465]	[1.704]

To investigate the influence of the bond breaking/forming on the diatomic energy in terms of the electrostatic and exchange interactions, Eq. 4-14 is applied for each atomic pair involved in the reaction. The results are tabulated in Table 4.4. The Mulliken atomic charges used for these calculations are those obtained at the same level of theory (HF/STO-3G) used to calculate the bond orders. The relative energy in units of kcal/mol for each point along the IRC is also listed in the table.

From Table 4.4, in terms of the electrostatic and exchange interactions, the break of $C_1{=}C_2$, $C_3{=}C_4$, and $C_5{=}C_6$ double bonds is repulsive and destabilizing while the formation of C_1—C_6 and C_4—C_5 single bonds, and $C_2{=}C_3$ double bond is attractive and stabilizing. Based on the total energy of these interactions, the *endo* channel is more stable than the *exo* path at points α, TS, and β with the stabilization in the energy being more evident at point α and at the transition state (2.13 and 1.11 kcal/mol, respectively, Table 4.4). These results describe, in part, the preference of the *endo* channel over the *exo* route in the studied reaction. However, it should be pointed out that the *exo* route is slightly more stable than the *endo* path at points a and b (Table 4.4).

Table 4.4: Computed electrostatic (and exchange) interaction energies (eV) for atomic pairs involved in the reaction between diene **14** and dienophile **15** in the presence of catalyst **16** along the IRC. Points and carbon numbers are as illustrated in Figure 4.3.

	C_1-C_2	C_2-C_3	C_3-C_4	C_4-C_5	C_5-C_6	C_1-C_6	Total Energy (eV)	E_{rel} E_{exo}–E_{endo} (kcal/mol)
Endo Path								
Point (a)	–9.43	–5.35	–9.97	0.03	–8.98	–0.22	–33.92	–0.19
Point (α)	–9.12	–5.44	–9.95	–0.03	–8.64	–0.37	–33.56	2.13
TS	–8.01	–5.81	–9.52	–0.04	–7.45	–1.07	–31.89	1.11
Point (β)	–6.30	–6.55	–8.85	–0.16	–5.80	–2.60	–30.25	0.26
Point (b)	–5.82	–6.84	–8.58	–0.21	–5.39	–3.19	–30.03	–0.41
Exo Path								
Point (a)	–9.49	–5.34	–10.02	0.02	–8.86	–0.24	–33.93	
Point (α)	–9.20	–5.43	–9.94	0.01	–8.53	–0.38	–33.47	
TS	–8.03	–5.81	–9.56	–0.05	–7.27	–1.13	–31.84	
Point (β)	–6.33	–6.54	–8.89	–0.15	–5.67	–2.66	–30.24	
Point (b)	–5.87	–6.83	–8.62	–0.19	–5.29	–3.25	–30.05	

The Hammond postulate [83] relates the rate of the chemical reaction to the geometrical parameters of the transition state structure as compared to those of the reactants and the products. The transition state structure resembles either the reactants or the products depending on which of these are closer to it in energy [84-86].

The reaction studied in the present work is an exergonic reaction (cf. Figure 3.15) and the transition state structure is, therefore, similar to the reactants. In addition, based on the Hammond postulate, the *endo* transition state structure should resemble the reactants more than the *exo* transition state structure since it possesses the lower activation energy. To examine the applicability of the Hammond postulate to the studied reaction, the deviation of some of the structural parameters of the transition state structure from those of the reactants are calculated and are given in Table 4.5.

Table 4.5: Calculated deviations in bond lengths, B, (Å) and dihedral angle, D, (degrees) from the reactants for the *endo* and *exo* transition state structures of the reaction between diene **14** and dienophile **15** in the presence of catalyst **16**. Carbon numbers are as illustrated in Figure 4.3.

	$B_{1\text{-}2}$	$B_{2\text{-}3}$	$B_{3\text{-}4}$	$B_{5\text{-}6}$	D_{1234}
Endo Path					
TS	0.057	0.042	0.019	0.055	38.096
Exo Path					
TS	0.053	0.042	0.018	0.060	38.272

The net deviation in bond lengths is identical for both *endo* and *exo* channels (Table 4.5). The deviation in the dihedral angle, however, is slightly more (~ 0.2°, Table 4.5) for the *exo* transition state structure as compared to the *endo* transition state structure. In addition, the use of bond orders as a measure of the Hammond postulate has been suggested [87]. Despite being a rather crude measure, its application to similar reactions for the qualitative evaluation of the chemical reactivity has been proven useful [6-8,88]. In terms of bond order, the Hammond postulate states that the transition state structure with the smallest bond order for the forming bond should have the lowest activation energy [6]. For the *endo* transition state structure, the bond order values of the forming bonds C_1—C_6 and C_4—C_5 are 0.309 and 0.040, respectively (Table 4.3). The corresponding *exo* transition state structure bond order values are 0.324 and 0.040, respectively (Table 4.3). Thus, the bond order of the forming C_4—C_5 is identical for both transition state structures whereas the bond order of the forming C_1—C_6 is slightly smaller for the *endo* transition state structure. This indicates that it is a slightly earlier transition state structure and hence has lower activation energy. Therefore, the applicability of the Hammond postulate is fairly suitable for the studied reaction.

The final issue regarding the structural parameters to comment about is the boron-oxygen bond length along the IRC. It is observed that the length of this bond is not only shortened in going from the reactants to the transition state structure (from 1.63 Å to 1.56 Å) but also from the transition state structure to the final point examined on the IRC (i.e. point b) (from 1.56 Å to 1.55 Å). This is in line with Corey's prediction (cf. Section 3.3.1) who stated [89], "It is important to note in this context that the coordination of catalyst to the carbonyl persists not only in the transition state but even in the Diels–Alder adduct".

4.3.5 Analysis of the global and local reactivity indices

The chemical reactivity indices obtained by differentiation of the energy or the electron density with respect to the number of electrons and/or the external potential are often classified based on the dependence on position [3,90]. Global reactivity indices have the same value everywhere in the molecule and provide general information about its reactivity. These include electronegativity, electrophilicity, and chemical potential, hardness and softness. Local reactivity indices such as Fukui function, electron density, and local hardness and softness change throughout the molecule and offer information on site- and regioselectivities [3,90].

The reactivity indices provide useful tools to examine the polar character of the Diels-Alder reaction [18-24]. In this section, the role of the chiral oxazaborolidinium cation catalyst **16** is investigated using the static global and local reactivity indices, namely, the electronic chemical potential (μ), the chemical hardness (η), the global electrophilicity (ω), and the local electrophilicity (ω_k). The calculated values for these indices for diene **14**, dienophile **15** and the coordination complex **15-16** (the *syn* coordination) are given in Table 4.6.

Table 4.6: Computed electronic chemical potential, μ, chemical hardness, η, global electrophilicity, ω, and local electrophilicity, ω_k, for **14**, **15**, and complex **15-16**. All values are in eV. Local electrophilicities are calculated for only **15** and complex **15-16**. Carbon numbers are as illustrated in Figure 4.3.

	μ	η	ω	ω_k			
				C_5	C_6	C_7	C_8
System							
14	–3.30	5.77	0.94				
15	–5.21	3.84	3.53	0.13	0.13	0.09	0.09
15-16 (*syn*)	–8.28	2.02	17.01	0.57	0.85	0.64	0.08

The electron transfer is derived from the chemical potential difference between the reactants and electrons tend to flow from molecules of high chemical potential (low electronegativity) to molecules of low chemical potential (high electronegativity) [90]. The electronic chemical potential of diene **14** is higher than that of dienophile **15** (Table 4.6) indicating that the charge is transferred from the diene to the dienophile along the studied Diels-Alder reaction. In addition, the electronic chemical potential difference is increased upon the coordination between dienophile **15** and catalyst **16** from 1.91 eV in the reaction between **14** and **15** to 4.98 eV in the reaction between **14** and complex **15-16**. Moreover, the chemical hardness is lowered for the coordination complex **15-16** (Table 4.6) (i.e. complex **15-16** is less resistant to charge transfer than dienophile **15**). Hence, the charge transfer is enhanced for the catalyzed reaction. The flow of charge from the diene to the dienophile is in agreement with the charge transfer analysis carried out at the transition state structures (Section 4.3.2).

The use of Parr-Pearson static charge transfer equation (Eq. 4-15) [90,91] estimates the amount of charge transferred (Δn) from the diene to the dienophile. The associated energy stabilization (ΔE) is defined by Eq. 4-16 [90,91].

$$\Delta n = \frac{\mu_{diene} - \mu_{dienophile}}{\eta_{diene} + \eta_{dienophile}} \tag{4-15}$$

$$\Delta E = \frac{-\left(\mu_{diene} - \mu_{dienophile}\right)^2}{2\left(\eta_{diene} + \eta_{dienophile}\right)}\,. \tag{4-16}$$

Applying these equations, the amount of charge transferred from diene **14** to dienophile **15** is 0.20 e while that from diene **14** to complex **15-16** is 0.64 e. The associated energy stabilization is 4.9 kcal/mol for the reaction between **14** and **15** and is 24.7 kcal/mol for the reaction between **14** and complex **15-16**. For the catalyzed reaction, the amount of charge transferred is larger than that obtained from the charge transfer analysis discussed in Section 4.3.2 (0.64 e vs. 0.29 e). This discrepancy might be attributed to the use of static global quantities to define the charge transfer in Eq. 4-15. These global quantities are for the isolated reactants. The larger charge transfer is also accompanied by an overstabilization of the energy (19.8 kcal/mol (i.e. 24.7 – 4.9 kcal/mol) vs. 14.6 kcal/mol (calculated as the difference between the activation energies of the catalyzed and uncatalyzed reactions using the electronic energy)). However, in charge transfer analysis using different theoretical models, the emphasis is usually on trends that are consistent with chemical intuition rather than absolute values [92-94]. Both results obtained are in qualitative agreement and the role of the catalyst in enhancing the charge transfer from the diene to the dienophile which in turn leads to stabilization in energy is reproduced in both approaches.

As observed in Table 4.6, the coordination of catalyst **16** to dienophile **15** increases the electrophilicity from 3.53 eV to 17.01 eV rendering the coordination complex **15-16** a much stronger electrophile than dienophile **15**. The large increase in electrophilicity also indicates that the catalyzed Diels-Alder reaction possesses a more polar character than the uncatalyzed reaction. This is consistent with the results obtained for charge transfer using Eq. 4-15.

Local reactivity descriptors are important in order to better understand the site- and regioselectivities of chemical reactions. One of the most commonly used local reactivity index is the Fukui function ($f(\mathbf{r})$) [95-97]. The Fukui function is defined as the first partial derivative of the electron density ($\rho(\mathbf{r})$) with respect to the number of electrons at constant external potential. It is important to condense the values of the Fukui function to the atoms of the molecule to describe the site- and regioselectivities. The local electrophilicity index (ω_k) describes the electrophilic character of a reactive atom (k) in a molecule and is defined as [53,98]

$$\omega_k = \omega f_k^+ \tag{4-17}$$

where ω is the global electrophilicity index and f_k^+ is the condensed Fukui function for nucleophilic attack given by

$$f_k^+ = Q_k^{n+1} - Q_k^n \tag{4-18}$$

where Q_k is Mulliken's gross atomic population associated with atom k (or alternatively, gross atomic population from any population analysis scheme) for molecules with $n+1$ and n number of electrons. The Mulliken's gross atomic population for the $n+1$ molecule was obtained by running single point calculations (B3LYP/6-31G(d)) at the geometries optimized at the B3LYP/6-31G(d) level of theory and adding an extra electron.

Analysis of the local electrophilicity indices (Table 4.6) shows that for dienophile **15**, the site bearing two hydrogens (C_5 and C_6) is more electrophilic than the site bearing the two methyl groups (C_7 and C_8) which is consistent with the results obtained in Section 3.3.2. The coordination of dienophile **15** to catalyst **16** increases the electrophilic character of the carbon atoms with C_6 being the most electrophilic position of the molecule. This is in line with the findings based on the frontier molecular orbital (FMO) analysis discussed in Section 3.3.2.

For the catalyzed reaction, the electrophilicity for C_6 is higher than that for C_5 and the high asynchronicity of the catalyzed reaction can be described on the basis of the local electrophilicity values. By the same argument used to explain the asynchronicity in terms of the FMO theory (Section 3.3.2), the high degree of asynchronicity for the catalyzed reaction can be attributed to the larger overlap between the diene and the dienophile at C_6 which leads to a stronger and shorter bond.

4.4 Conclusion

The mechanism and enantioselectivity of the Diels-Alder reaction between 2-methyl-1,3-butadiene **14** and 2,3-dimethyl-1,4-benzoquinone **15** in the presence of organocatalyst **16** have been studied using the DFT method at the B3LYP/6-31G(d) level of theory. The focus of this study is mainly on the rationalization of the mechanism and the enantioselectivity of the Diels-Alder reaction using various DFT based theoretical models. These included the reaction force analysis, the natural population analysis of the charge transfer, the topological analysis of the electron localization function (ELF), the bond order analysis, and analysis based on the global and local reactivity descriptors.

The reaction force analysis and natural population analysis of the charge transfer pointed out to the preference of the *endo* channel to the *exo* route for the studied Diels-Alder reaction since the former exhibited a larger charge transfer at the transition state structure which led to smaller repulsive forces that eventually resulted in activation energy lowering.

The topological analysis of the electron localization function (ELF) did not allow the differentiation between the *endo* and the *exo* routes. However, it provided a way for describing the breaking and formation of the bonds along the intrinsic reaction coordinate (IRC). These could be described by the disappearance and appearance of basins of attractors along the IRC. Moreover, the analysis of these basins along the IRC indicated a highly asynchronous nature of the studied Diels-Alder reaction.

The bond order and bond length analyses along the IRC also provided a tool to study the mechanism of the Diels-Alder reaction and, in agreement with the topological analysis of the ELF, indicated a highly asynchronous mechanism.

The influence of the bond breaking/forming on the diatomic energy in terms of the electrostatic and exchange interactions was also investigated. At the transition state structures, these interactions led to a more energetically stable *endo* transition state structure as compared to the *exo* transition state structure which partly described the *endo* selectivity of the studied reaction. Subsequently, the applicability of the bond order as a measure of the Hammond postulate was examined and the findings fairly suggested a preference of the *endo* transition state structure to the *exo* transition state structure since the former showed a smaller bond order for one of the two forming bonds.

Based on the analysis of the global reactivity indices, the catalyzed Diels-Alder reaction possessed a more polar character than the uncatalyzed reaction owing to the increase in the electronic chemical potential difference between diene **14** and coordination complex **15-16** and the decrease in the chemical hardness of the coordination complex **15-16**. The electrophilicity of dienophile **15** was as well enhanced upon the coordination with catalyst **16**.

The analysis of the local electrophilicity index offered a tool to rationalize the site selectivity and proved the less substituted double bond of dienophile **15** to be the most preferred site for diene **14** nucleophilic attack. Moreover, the local electrophilicity index helped to explain the high asynchronicity encountered in the catalyzed reaction and attributed it to the relatively large difference between the electrophilicity of the dienophile carbons involved in the cycloaddition reaction. The extent of the overlap between the termini carbons of the diene and the carbons of the dienophile is therefore unequal and the bond formation is asynchronous.

4.5 References

1. R.G. Parr, Density Functional Theory in Chemistry. In: Density Functional Methods in Physics (R. M. Dreizler, J. da Providencia, editors), Plenum Press, New York, NY, 1985.
2. P. Geerlings, F. De Proft, Chemical reactivity as described by quantum chemical methods, International Journal of Molecular Sciences 3 (2002) 276-309.
3. A. Cedillo, Density Functional Theory Models of Reactivity Based on an Energetic Criterion. In: Theoretical Aspects of Chemical Reactivity (A. Toro-Labbé, editor), Elsevier B.V., Amsterdam, The Netherlands, 2007.
4. J.L. Gázquez, Chemical Reactivity Concepts in Density Functional Theory. In: Chemical Reactivity Theory: A Density Functional View (P.K. Chattaraj, editor), CRC Press, Boca Raton, FL, 2009.
5. R.G. Parr, R.A. Donnelly, M. Levy, W.E. Palke, Electronegativity: The density functional viewpoint, Journal of Chemical Physics 68 (1978) 3801-3807.
6. B.S. Jursic, 1,3,4-oxadiazoles as dienes in Diels-Alder reactions studied with AM1 semiempirical and hybrid density functional methods. Are 1,3,4-oxadiazoles practical synthones for the preparation of valuable organic materials? Journal of Molecular Structure (Theochem) 452 (1998) 153-168.
7. B.S. Jursic, Suitability of furan, pyrrole, and thiophene as dienes for Diels-Alder reactions viewed through their stability and reaction barriers for reactions with acetylene, ethylene, and cyclopropene. An AM1 semiempirical and B3LYP hybrid density functional theory study, Journal of Molecular Structure (Theochem) 454 (1998) 105-116.
8. B.S. Jursic, Theoretical investigation of suitability of pyrrole as diene for Diels-Alder reaction, Journal of Molecular Structure (Theochem) 454 (1998) 277-286.
9. A. Ogawa, H. Fujimoto, Reexamination of orbital interactions in Diels-Alder reactions, Tetrahedron Letters 43 (2002) 2055-2057.
10. T. Lipińska, Experimental and theoretical FMO interaction studies of the Diels-Alder reaction of 5-acetyl-3-methythio-1,2,4-triazine with cyclic enamines, Tetrahedron 61 (2005) 8148-8158.

11. R.K. Bansal, N. Gupta, S.K. Kumawat, Origin of the stereo- and regioselectivities in the Diels-Alder reactions of azaphospholes: A DFT investigation, Tetrahedron 62 (2006) 1548-1556.
12. B.S. Jursic, A comparison of 3,3-dimethyl-1-phosphabutyne and 3,3-dimethylbutyne as dienophiles for Diels-Alder reaction. An AM1 semiempirical study, Journal of Molecular Structure (Theochem) 342 (1995) 121-129.
13. S. Berski, J. Andrés, B. Silvi, L.R. Domingo, The joint use of catastrophe theory and electron localization function to characterize molecular mechanisms. A density functional study of the Diels-Alder reaction between ethylene and 1,3-butadiene, Journal of Physical Chemistry A 107 (2003) 6014-6024.
14. V. Polo, L.R. Domingo, J. Andrés, Toward an understanding of the catalytic role of hydrogen-bond donor solvents in the hetero-Diels-Alder reaction between acetone and butadiene derivative, Journal of Physical Chemistry A 109 (2005) 10438-10444.
15. L.R. Domingo, M.T. Picher, P. Arroyo, Towards an understanding of the polar Diels-Alder reactions of nitrosoalkenes with enamines: A theoretical study, European Journal of Organic Chemistry (2006) 2570-2580.
16. E. Chamorro, R. Notario, J.C. Santos, P. Pérez, A theoretical scale for pericyclic and pseudopericyclic reactions, Chemical Physics Letters 443 (2007) 136-140.
17. P. Fuentealba, E. Chamorro, J.C. Santos, Understanding and Using the Electron Localization Function. In: Theoretical Aspects of Chemical Reactivity (A. Toro-Labbé, editor), Elsevier B.V., Amsterdam, The Netherlands, 2007.
18. J. Soto-Delgado, L.R. Domingo, R. Araya-Maturana, R. Contreras, Understanding the stereo- and regioselectivities of the polar Diels-Alder reactions between 2-acetyl-1,4-benzoquinone and methyl substituted 1,3-butadienes: a DFT study, Journal of Physical Organic Chemistry 22 (2009) 578-584.
19. F. Teixeira, J.E. Rodríguez-Borges, A. Melo, M.N.D.S. Cordeiro, Stereoselectivity of the aza-Diels-Alder reaction between cyclopentadiene and protonated phenylethylimine derived from glyoxylates. A density functional theory study, Chemical Physics Letters 477 (2009) 60-64.
20. S.M. Mekelleche, R. Benhabib, Elucidation of the regioselectivity in Diels-Alder reactions by means of theoretical approaches, Journal of Molecular Structure (Theochem) 709 (2004) 31-34.
21. S. Noorizadeh, H. Maihami, A theoretical study on the regioselectivity of Diels-Alder reactions using electrophilicity index, Journal of Molecular Structure: THEOCHEM 763 (2006) 133-144.
22. A. Benmeddah, S.M. Mekelleche, W. Benchouk, B. Mostefa-Kara, D. Villemin, Prediction of the reactivity of 2(5H)-furanones as potential dienophiles in Diels-Alder reactions using philicity indexes, Journal of Molecular Structure: THEOCHEM 821 (2007) 42-46.
23. L.R. Domingo, M.J. Aurell, M.N. Kneeteman, P.M. Mancini, Mechanistic details of the domino reaction of nitronaphthalenes with the electron-rich dienes. A DFT study, Journal of Molecular Structure: THEOCHEM 853 (2008) 68-76.
24. J. Soto-Delgado, L.R. Domingo, R. Contreras, Understanding the influence of Lewis acids in the regioselectivity of the Diels-Alder reactions of 2-methoxy-5-

methyl-1,4-benzoquinone: A DFT study, Journal of Molecular Structure: THEOCHEM 902 (2009) 103-108.

25. E. Kraka, A. Wu, D. Cremer, Mechanism of the Diels-Alder reaction studied with the united reaction valley approach: Mechanistic differences between symmetry-allowed and symmetry-forbidden reactions, Journal of Physical Chemistry A 107 (2003) 9008-9021.
26. H. Jiao, P.v.R. Schleyer, Aromaticity of pericyclic reaction transition structures: Magnetic evidence, Journal of Physical Organic Chemistry 11 (1998) 655-662.
27. M-F. Cheng, W-K. Li, A computational study of the Diels-Alder reactions involving acenes: Reactivity and aromaticity, Chemical Physics Letters 368 (2003) 630-638.
28. Gaussian 03, Revision E.01, M. J. Frisch, G. W. Trucks, H. B. Schlegel, G. E. Scuseria, M. A. Robb, J. R. Cheeseman, J. A. Montgomery, Jr., T. Vreven, K. N. Kudin, J. C. Burant, J. M. Millam, S. S. Iyengar, J. Tomasi, V. Barone, B. Mennucci, M. Cossi, G. Scalmani, N. Rega, G. A. Petersson, H. Nakatsuji, M. Hada, M. Ehara, K. Toyota, R. Fukuda, J. Hasegawa, M. Ishida, T. Nakajima, Y. Honda, O. Kitao, H. Nakai, M. Klene, X. Li, J. E. Knox, H. P. Hratchian, J. B. Cross, V. Bakken, C. Adamo, J. Jaramillo, R. Gomperts, R. E. Stratmann, O. Yazyev, A. J. Austin, R. Cammi, C. Pomelli, J. W. Ochterski, P. Y. Ayala, K. Morokuma, G. A. Voth, P. Salvador, J. J. Dannenberg, V. G. Zakrzewski, S. Dapprich, A. D. Daniels, M. C. Strain, O. Farkas, D. K. Malick, A. D. Rabuck, K. Raghavachari, J. B. Foresman, J. V. Ortiz, Q. Cui, A. G. Baboul, S. Clifford, J. Cioslowski, B. B. Stefanov, G. Liu, A. Liashenko, P. Piskorz, I. Komaromi, R. L. Martin, D. J. Fox, T. Keith, M. A. Al-Laham, C. Y. Peng, A. Nanayakkara, M. Challacombe, P. M. W. Gill, B. Johnson, W. Chen, M. W. Wong, C. Gonzalez, and J. A. Pople, Gaussian, Inc., Wallingford CT, 2004.
29. A. Reed, R.B. Weinstock, F. Weinhold, Natural population analysis, Journal of Chemical Physics 83 (1985) 735-746.
30. A. Reed, L.A. Curtiss, F. Weinhold, Intermolecular interactions from a natural bond orbital, donor-acceptor viewpoint, Chemical Reviews 88 (1988) 899-926.
31. F. Weinhold, Natural Bond Orbital Methods. In: Encyclopedia of Computational Chemistry, Vol. 3 (P.v.R. Schleyer, editor-in-chief), John Wiley & Sons Ltd., Chichester, UK, 1998.
32. K. Fukui, The path of chemical reactions - the IRC approach, Accounts of Chemical Research 14 (1981) 363-368.
33. C. Gonzalez, H.B. Schlegel, An improved algorithm for reaction path following, Journal of Chemical Physics 90 (1989) 2154-2161.
34. C. Gonzalez, H.B. Schlegel, Reaction path following in mass-weighted internal coordinates, Journal of Physical Chemistry 94 (1990) 5523-5527.
35. H.B. Schlegel, Reaction Path Following. In: Encyclopedia of Computational Chemistry, Vol. 4 (P.v.R. Schleyer, editor-in-chief), John Wiley & Sons Ltd., Chichester, UK, 1998.
36. H.P. Hratchian, H.B. Schlegel, Finding Minima, Transition States, and Following Reaction Pathways on *Ab Initio* Potential Energy Surfaces. In: Theory and Applications of Computational Chemistry: The First Forty Years (C. Dykstra, G. Frenking, K.S. Kim, G.E. Scuseria, editors), Elsevier B.V., Amsterdam, the Netherlands, 2005.

37. P. Fuentealba, D. Guerra, A. Savin, An Introduction to the Electron Localization Function. In: Chemical Reactivity Theory: A Density Functional View (P.K. Chattaraj, editor), CRC Press, Boca Raton, FL, 2009.
38. A.D. Becke, K.E. Edgecombe, A simple measure of electron localization in atomic and molecular systems, Journal of Chemical Physics 92 (1990) 5397-5403.
39. M. Kohout, A. Savin, Atomic shell structure and electron numbers, International Journal of Quantum Chemistry 60 (1996) 875-882.
40. A. Savin, B. Silvi, F. Colonna, Topological analysis of the electron localization function applied to delocalized bonds, Canadian Journal of Chemistry 74 (1996) 1088-1096.
41. A. Savin, The electron localization function (ELF) and its relatives: interpretations and difficulties, Journal of Molecular Structure: THEOCHEM 727 (2005) 127-131.
42. E. Matito, B. Silvi, M. Duran, M. Solà, Electron localization function at the correlated level, The Journal of Chemical Physics 125 (2006) 024301-1 – 024301-9.
43. M. Kohout, DGrid, version 4.5, Radebeul, 2009. The program is available by request from Dr. M. Kohout (kohout@cpfs.mpg.de).
44. I. Mayer, Charge, bond order and valence in the *ab initio* SCF theory, Chemical Physics Letters 97 (1983) 270-274; Addendum: Chemical Physics Letters 117 (1985) 396.
45. I. Mayer, On bond orders and valences in the *ab initio* quantum chemical theory, International Journal of Quantum Chemistry 29 (1986) 73-84.
46. I. Mayer, Bond orders and valences from *ab initio* wave functions, International Journal of Quantum Chemistry 29 (1986) 477-483.
47. I. Mayer, Bond order and valence indices: A personal account, Journal of Computational Chemistry 28 (2007) 204-221.
48. I. Mayer, Program "EFF-AO", Version 1.0, Chemical Research Center, Hungarian Academy of Sciences, Budapest, 2008. The program is available at http://occam.chemres.hu/programs/index.html.
49. G. Lendvay, Characterization of the progress of chemical reactions by ab initio bond orders, Journal of Physical Chemistry 98 (1994) 6098–6104.
50. G. Lendvay, On the correlation of bond order and bond length, Journal of Molecular Structure (Theochem) 501-502 (2000) 389-393.
51. G. Lendvay, Characterization of Changes in Chemical Reactions by Bond Order and Valence Indices. In: Chemical Reactivity Theory: A Density Functional View (P.K. Chattaraj, editor), CRC Press, Boca Raton, FL, 2009.
52. R.G. Parr, L.v. Szentpály, S. Liu, Electrophilicity index, Journal of the American Chemical Society 121 (1999) 1922–1924.
53. P. Pérez, L.R. Domingo, A. Aizman, R. Contreras, The Electrophilicity Index in Organic Chemistry. In: Theoretical Aspects of Chemical Reactivity (A. Toro-Labbé, editor), Elsevier B.V., Amsterdam, The Netherlands, 2007.
54. E. Kraka, Reaction Path Hamiltonian and its Use for Investigating Reaction Mechanisms. In: Encyclopedia of Computational Chemistry, Vol. 4 (P.v.R. Schleyer, editor-in-chief), John Wiley & Sons Ltd., Chichester, UK, 1998.
55. P. Politzer, A. Toro-Labbé, S. Gutiérrez-Oliva, B. Herrera, P. Jaque, M.C. Concha, J.S. Murray, The reaction force: Three key points along an intrinsic reaction coordinate, Journal of Chemical Sciences 117 (2005) 467-472.

56. A. Toro-Labbé, S. Gutiérrez-Oliva, P. Politzer, J.S. Murray, Reaction Force: A Rigorously Defined Approach to Analyzing Chemical and Physical Processes. In: Chemical Reactivity Theory: A Density Functional View (P.K. Chattaraj, editor), CRC Press, Boca Raton, FL, 2009.
57. A. Toro-Labbé, S. Gutiérrez-Oliva, J.S. Murray, P. Politzer, The reaction force and the transition region of a reaction, Journal of Molecular Modeling 15 (2009) 707-710.
58. S.M. Bachrach, Population Analysis and Electron Densities from Quantum Mechanics. In: Reviews in Computational Chemistry – Vol. 5 (K.B. Lipkowitz, D.B. Boyd, editors), VCH Publishers, Inc., New York, NY, 1994.
59. F. Jensen, Introduction to Computational Chemistry, John Wiley & Sons Ltd, Chichester, England, 2007.
60. P.-O. Löwdin, Quantum theory of many-particle systems. I. Physical interpretations by means of density matrices, natural spin-orbitals, and convergence problems in the method of configurational interaction, Physical Review 97 (1955) 1474-1489.
61. P.-O. Löwdin, Quantum theory of many-particle systems. II. Study of the ordinary Hartree-Fock approximation, Physical Review 97 (1955) 1490-1508.
62. P.-O. Löwdin, Quantum theory of many-particle systems. III. Extension of the Hartree-Fock scheme to include degenerate systems and correlation effects, Physical Review 97 (1955) 1509-1520.
63. E.R. Davidson, Natural Orbitals. In: Advances in Quantum Chemistry – Vol. 6 (P.-O. Löwdin, editor), Academic Press, Inc., New York, NY, 1972.
64. W.J. Hehre, L. Radom, P.v.R. Schleyer, J.A. Pople, *Ab Initio* Molecular Orbital Theory, John Wiley & Sons, Inc., New York, NY, 1986.
65. K. Jug, M.S. Gopinathan, Valence in Molecular Orbital Theory. In: Theoretical Models of Chemical Bonding – Part 2: The Concept of the Chemical Bond (Z.B. Maksić, editor), Springer-Verlag, Berlin, Germany, 1990.
66. R. McWeeny, Some recent advances in density matrix theory, Reviews of Modern Physics 32 (1960) 335-369.
67. E.R. Davidson, Natural Orbitals. In: Encyclopedia of Computational Chemistry, Vol. 3 (P.v.R. Schleyer, editor-in-chief), John Wiley & Sons Ltd., Chichester, UK, 1998.
68. D. Caldwell, P. Redington, H. Eyring, Density matrix method for orbital localization, Proceedings of the National Academy of Sciences of the USA 76 (1979) 3042-3045.
69. J.P. Foster, F. Weinhold, Natural hybrid orbitals, Journal of the American Chemical Society 102 (1980) 7211-7218.
70. J.-M. André, D.H. Mosley, M.-C. André, B. Champagne, E. Clementi, J.G. Fripiat, L. Leherte, L. Pisani, D.P. Vercauteren, M. Vracko, Exploring Aspects of Computational Chemistry: Concepts, Presses Universitaires de Namur, Namur, Belgium, 1997.
71. H. Fujimoto, S. Inagaki, K. Fukui, On the Donor-Acceptor Relationship in Cyclic Additions. In: Frontier Orbitals and Reaction Paths: Selected Papers of Kenichi Fukui (K. Fukui, H. Fujimoto, editors), World Scientific Publishing, Singapore, 1977.
72. M. Oliva, V.S. Safont, J. Andrés, O. Tapia, Electronic mechanistic pattern for C-C bond-breaking from transition structures in Rubisco’s chemistry, Chemical Physics Letters 340 (2001) 391-399.

73. J. Santos, V. Polo, J. Andrés, An electron localization function study of the trimerization of acetylene: Reaction mechanism and development of aromaticity, Chemical Physics Letters 406 (2005) 393-397.
74. E. Rincón, A. Toro-Labbé, Reaction force and electron localization function analysis of the metal chelation process in Mg(II)–thymine complex, Chemical Physics Letters 438 (2007) 93-98.
75. G. Gopakumar, V.S. Nguyen, M.T. Nguyen, Molecular mechanism of hydrogen release reactions: Topological analysis using the electron localization function, Journal of Molecular Structure: THEOCHEM 811 (2007) 77-89.
76. O. Donoso-Tauda, A. Aizman, C.A. Escobar, J.C. Santos, Substituent effects in the mechanism of mono-substituted acetylene trimerization: A topological analysis of the electron localization function, Chemical Physics Letters 469 (2009) 219-223.
77. W. Benchouk, S.M. Mekelleche, M.J. Aurell, L.R. Domingo, Understanding the regio- and chemoselective polar [3+2] cycloaddition of the Padwa carbonyl ylides with α-methylene ketones. A DFT study, Tetrahedron 65 (2009) 4644-4651.
78. K. Morokuma, Molecular orbital studies of hydrogen bonds. III. $C=O\cdots H–O$ hydrogen bond in $H_2CO\cdots H_2O$ and $H_2CO\cdots 2H_2O$, Journal of Chemical Physics 55 (1971) 1236-1244.
79. K. Kitaura, K. Morokuma, A new energy decomposition scheme for molecular interactions within the Hartree-Fock approximation, International Journal of Quantum Chemistry 10 (1976) 325-340.
80. I. Mayer, Towards a “chemical” Hamiltonian, International Journal of Quantum Chemistry 23 (1983) 341-363.
81. F.M. Bickelhaupt, E.J. Baerends, Kohn-Sham Density Functional Theory: Predicting and Understanding Chemistry. In: Reviews in Computational Chemistry – Vol. 15 (K.B. Lipkowitz, D.B. Boyd, editors), Wiley-VCH, Inc., New York, NY, 2000.
82. I. Mayer, A. Hamza, Interatomic exchange energy components, International Journal of Quantum Chemistry 92 (2003) 174-180.
83. G.S. Hammond, A correlation of reaction rates, Journal of the American Chemical Society 77 (1955) 334–338.
84. R. Bruckner, Advanced Organic Chemistry: Reaction Mechanisms, Harcourt/Academic Press, Burlington, MA, 2002.
85. F.A. Carey, R.J. Sundberg, Advanced Organic Chemistry: Part A: Structure and Mechanisms, Springer Science Business Media, LLC, 2007.
86. M.B. Smith, J. March, March’s Advanced Organic Chemistry: Reactions, Mechanisms, and Structure, John Wiley & Sons, Inc., Hoboken, NJ, 2007.
87. K.A. Connors, Chemical Kinetics: The Study of Reaction Rates in Solution, VCH Publishers, Inc., New York, NY, 1990.
88. B.S. Jursic, Exploring Reaction Outcomes Through the Reactivity-Selectivity Principle Estimated by Density Functional Theory Studies. In: Theoretical Organic Chemistry (C. Párkányi, editor), Elsevier Science B.V., Amsterdam, The Netherlands, 1998.
89. D.H. Ryu, G. Zhou, E.J. Corey, Enantioselective and structure-selective Diels-Alder reactions of unsymmetrical quinones catalyzed by a chiral oxazaborolidinium cation. Predictive selection rules, Journal of the American Chemical Society 126 (2004) 4800-4802.

90. R.G. Parr, W. Yang, Density Functional Theory of Atoms and Molecules, Oxford University Press, Oxford, UK, 1989.
91. R.G. Parr, R.G. Pearson, Absolute hardness: Companion parameter to absolute electronegativity, Journal of the American Chemical Society 105 (1983) 7512–7516.
92. K.C. Gross, P.G. Seybold, C.M. Hadad, Comparison of different atomic charge schemes for predicting pKa variations in substituted anilines and phenols, International Journal of Quantum Chemistry 90 (2002) 445-458.
93. C.J. Cramer, Essentials of Computational Chemistry: Theories and Models, John Wiley & Sons Ltd, Chichester, England, 2004.
94. A.A. Oliferenko, S.A. Pisarev, V.A. Palyulin, N.S. Zefirov, Atomic Charges *via* Electronegativity Equalization: Generalizations and Perspectives. In: Advances in Quantum Chemistry – Vol. 51 (J.R. Sabin, E. Brandas, editors), Academic Press, Burlington, MA, 2006.
95. A.K. Chandra, M.T. Nguyen, Fukui Function and Local Softness as Reactivity Descriptors. In: Chemical Reactivity Theory: A Density Functional View (P.K. Chattaraj, editor), CRC Press, Boca Raton, FL, 2009.
96. P.W. Ayers, W. Yang, L.J. Bartolotti, Fukui Function. In: Chemical Reactivity Theory: A Density Functional View (P.K. Chattaraj, editor), CRC Press, Boca Raton, FL, 2009.
97. P. Thanikaivelan, J. Padmanabhan, V. Subramaniam, T. Ramasami, Chemical reactivity and selectivity using Fukui functions: Basis set and population scheme dependence in the framework of B3LYP theory, Theoretical Chemistry Accounts 107 (2002) 326-335.
98. S. Liu, Electrophilicity. In: Chemical Reactivity Theory: A Density Functional View (P.K. Chattaraj, editor), CRC Press, Boca Raton, FL, 2009.

5

An ONIOM Study on the Enantioselectivity of Diels-Alder Reaction Catalyzed by SiO_2–Immobilized Chiral Oxazaborolidinium Cation

Heterogeneous catalysis is essential in various fields of chemistry. Anchoring a homogeneous catalyst to a solid support is a strategy that combines the advantages of both homogeneous and heterogeneous catalyses. Modeling large molecular systems accurately and reliably by quantum mechanical methods is a challenge that entails the use of hybrid quantum mechanics/molecular mechanics (QM/MM) methods. In the current chapter, the hybrid method 'ONIOM' is applied to examine the mechanism and enantioselectivity of Diels-Alder reaction in the presence of a silica-supported organocatalyst.

5.1 Introduction

Organic synthesis on solid-phase has been receiving an increasing attention in the community of synthetic organic chemists as a method for carrying out chemical reactions with high regio- and/or stereoselectivity under environmentally benign, solvent-free conditions. The solid-phase approach to enantioselective synthesis has proven suitable for a number of enantioselective reactions [1]. Various support materials have been used for solid-phase organic synthesis including polystyrene, polysaccharides, and silica [2].

Heterogeneous catalysis is important in many industrial processes for fine chemicals synthesis [3]. Heterogenization by immobilizing a homogeneous catalyst on a solid support is a strategy that attempts to combine the advantages of homogeneous catalysis (e.g., high enantioselectivity) with the advantages of heterogeneous catalysis such as the ease of separation of the catalyst from the product, the reusability of the catalyst and the reduction in cost [3-5]. Catalyst immobilization methods [3,5-10] can be classified mainly into two groups, namely, covalent and non-covalent immobilization. Solid supports used include organic polymeric materials (e.g., polystyrene resins) and inorganic solids such as silica and zeolites.

Silica- and organic polymer-immobilized catalysts such as transition-metal complexes with chiral ligands and chiral organocatalysts are now commonplace in enantioselective organic synthesis involving numerous types of organic reactions [11-35]. The enantioselective Diels-Alder reaction is a versatile tool for the synthesis of pharmaceutical and natural products. An important class of heterogeneous catalysts for enantioselective Diels-Alder reaction is concerned with chiral Lewis acids (both organic and inorganic) anchored to organic polymeric or inorganic solid materials [11-20].

Oxazaborolidines attached to polystyrene resin [26,27,29] and to silica [34,36] are among numerous chiral organocatalysts that have been used in enantioselective heterogeneous catalysis. Their main use was the enantioselective reduction of ketones. However, the use of solid-supported oxazaborolidine catalysts for the Diels-Alder reaction has not been reported.

In the current chapter, the Diels-Alder reaction between 2-methyl-1,3-butadiene **14** and 2,3-dimethyl-1,4-benzoquinone **15** in the presence of amino silica-immobilized catalyst **16** is computationally investigated. The emphasis is mainly to gain an understanding of the enantioselectivity and mechanism of this reaction which can be later tested experimentally.

5.2 Methods and Computational Details

5.2.1 Preparation of amorphous silica bulk and surface

Classical molecular dynamics simulations were carried out using the SageMD2 software package [37]. The model of bulk amorphous silica was generated by classical molecular dynamics using the well-established melt-quench method (see below) [38-55]. The building of amorphous silica bulk and surface is illustrated in Figure 5.1.

All simulations were carried out using the velocity Verlet integration algorithm with an integration time step of 1.6 fs and employing periodic boundary conditions. The Berendsen thermostat and barostat were used for controlling the temperature and the pressure. The potential used for these simulations is a two-body interatomic potential [44-46] of the form

$$U(r) = \frac{q_k q_l}{r} + U_0\left[e^{-2\alpha(r-r_0)} - 2e^{-\alpha(r-r_0)}\right] \qquad (5\text{-}1)$$

where q_k and q_l are the charges on atoms k and l; r is the distance between atoms k and l; and U_0 (the potential well depth), α (the potential width control parameter) and r_0 (the equilibrium interatomic distance) are the adjustable Morse potential parameters. These parameters were taken from the literature [44-46] and are listed in Table 5.1. Cutoff distances for Morse interactions were set to 9 Å. Electrostatic interactions were calculated by Ewald summation method with a real space cutoff distance of 7 Å. The charges used are +1.30 and –0.65 for the Si and O atoms, respectively [45,46].

Table 5.1: Morse potential parameters for silica.

	U_0 (eV)	α (1/Å)	r_0 (Å)
Si–Si	0.007695	2.0446	3.7598
Si–O	1.99597	2.6518	1.6280
O–O	0.023272	1.3731	3.791

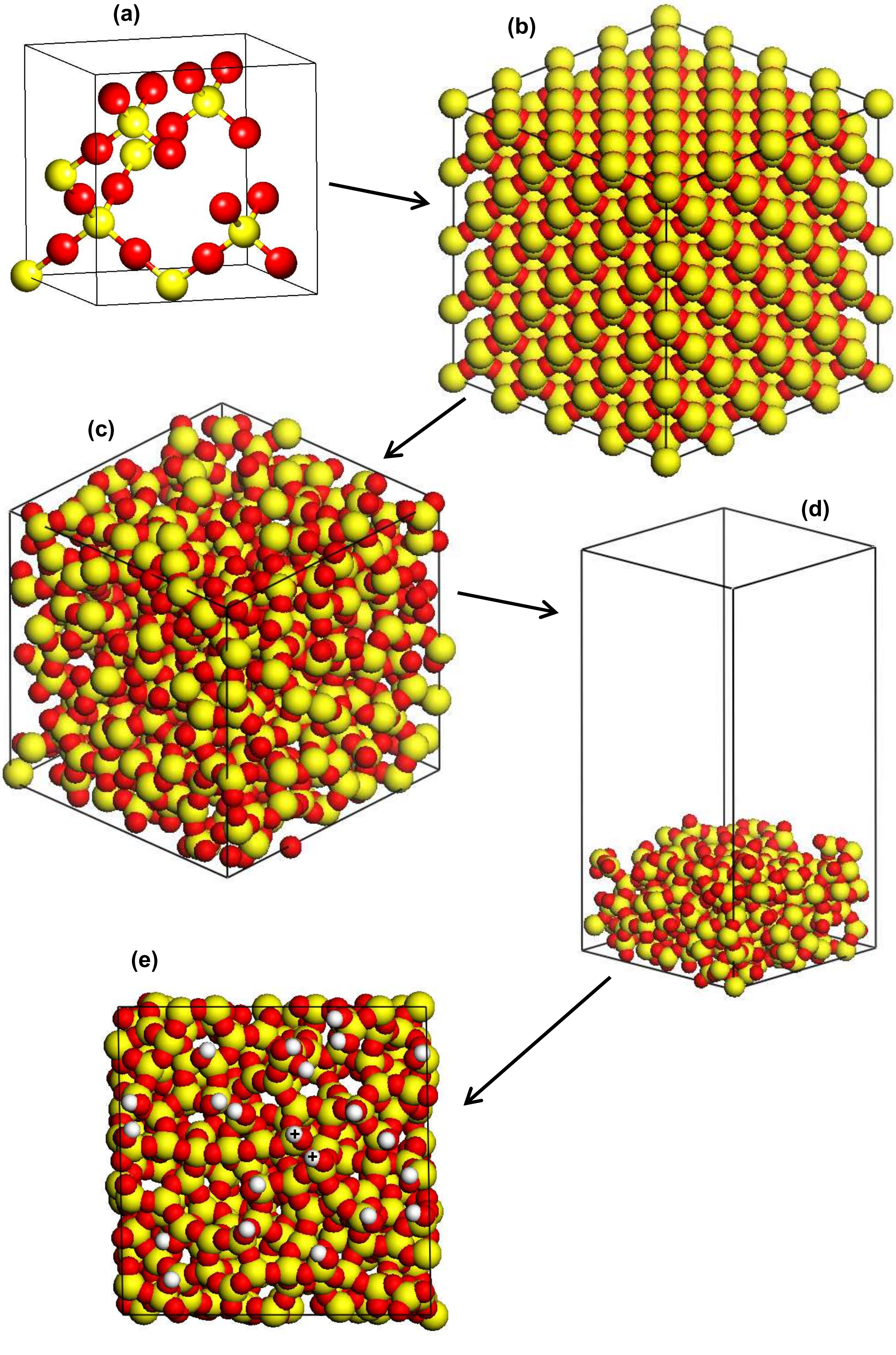

Figure 5.1: Building amorphous silica bulk and surface. (a) β-Cristobalite unit cell, (b) β-cristobalite supercell, (c) created bulk amorphous silica, (d) final amorphous silica surface, and (e) final amorphous silica surface with silanol groups (top view). The two hydrogen atoms with the '+' sign indicate where the functionalization of the surface will take place. Silicon, oxygen and hydrogen atoms are displayed in yellow, red and white, respectively.

To construct bulk amorphous silica, a β-cristobalite unit cell (Si_8O_{16}) was replicated 4 × 4 × 4 times to produce a cubic supercell (28.6 Å × 28.6 Å × 28.6 Å) of 1536 atoms ($Si_{512}O_{1024}$). The cooling cycle 1-I suggested by Huff et al. [43] was then followed. It started with an NVT simulation at 8000 K for 20 ps to remove any memory of the initial atomic configuration followed by NVT simulations at 4000 K, 2000 K and 1000 K. At each temperature step, the simulation was run for 20 ps. A 10 ps of NVT dynamics at 300 K and then a 30 ps of NPT simulation at 300 K and 1 atm pressure completed the cycle.

To create the amorphous silica surface, the bulk amorphous silica was cleaved in the middle along the *Y*-direction. The resultant slab (~ 14 Å in thickness) was taken to produce the amorphous silica surface. A few atoms were taken out from the system to keep its electroneutrality and the final slab consisted of 246 SiO_2 units. The system was made periodic in three dimensions by placing a vacuum of 42 Å (i.e. ~ 3 times the slab thickness) on top of the silica surface. This enables the use of Ewald summation method and the long vacuum gap usually reduces the unwanted interactions between the silica surface and the periodic images. Atoms situated within 3 Å from the bottom of the slab in the *Y*-direction were fixed during the simulation. The slab was then annealed using the same potential used for creating the bulk amorphous silica. A 10 ps NVT dynamics at 1500 K followed by an NVT simulation at 300 K for 10 ps resulted in the desired amorphous silica surface.

It should be pointed out that the choice of the initial temperature and the thickness of the immobilized atoms influence the final amorphous silica surface in terms of the surface defects (undercoordinated or overcoordinated atoms) [38,41]. The higher the temperature and the thinner the layer of fixed atoms usually result in a lower surface defects. A key for choosing the temperature would be the glass transition temperature below which all structural changes in silica are arrested [53]. In simulations, this temperature is different from experimental and depends on the potential used. Using the same potential employed in the current work, Takada et al. [45] estimated the glass transition temperature to be 1400 K. Hence, in the present work, the initial temperature of 1500 K was selected and yielded the desired amorphous silica surface (Section 5.3.1). As for the simulation time, it has been shown that the surface defect density becomes stable with little or no changes after 10 ps [42]. In another study, a simulation time of ~1 ps was reported adequate to produce the surface defects [55].

5.2.2 ONIOM models and details of the calculations

Modeling heterogeneous catalytic systems is typically performed using one of three different representations of the catalyst: clusters, embedded clusters or slabs [56]. In the present work, the slab model was used. 3-Aminopropyltrimethoxysilane (a commonly used grafting molecule) was attached to the generated amorphous silica surface (Figure 5.1e) to produce an aminopropyl-functionalized silica surface (Figure 5.2). The chiral oxazaborolidinium cation catalyst **16** was then covalently immobilized on the amino silica surface (Figure 5.3).

All ONIOM (QM:MM) calculations were performed *in vacuo* using the Gaussian 03 program [58]. Density functional theory with the B3LYP functional and the 6-31G(d) basis set was chosen as the QM method while the ‘universal force field’ (UFF) [59] was selected as the MM method. The UFF atom types for the Si and O atoms that are part of the silica slab were specified explicitly with Si3 for Si and O_3_z for O. For the remaining atoms in the system, the UFF atom types automatically assigned by the Gaussian 03 program were accepted. The molecular connectivity was also explicitly specified (keyword “`geom=connectivity`”).

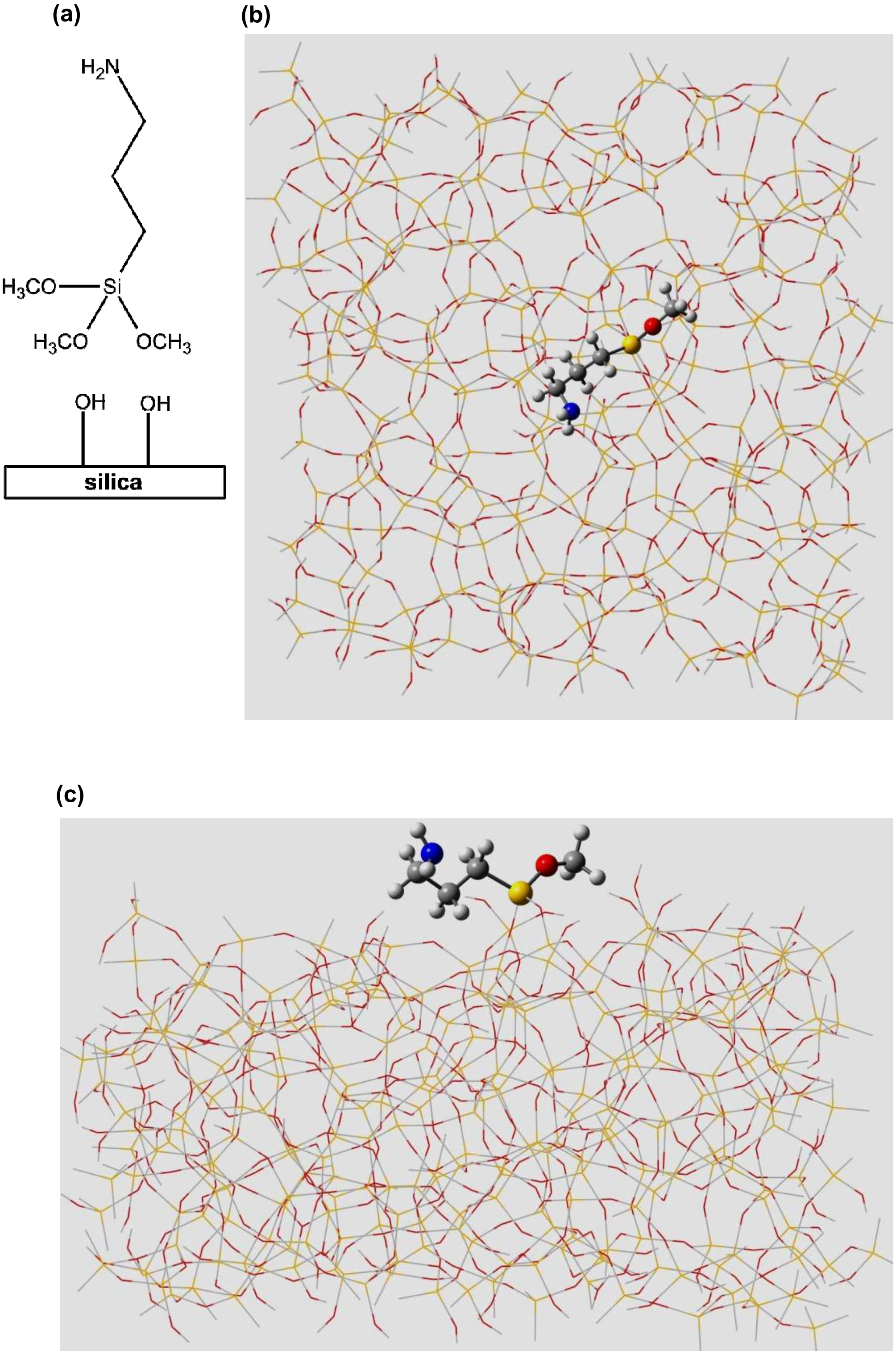

Figure 5.2: Amino silica surface. (a) 3-Aminopropyltrimethoxysilane to be attached to the silica surface, (b) UFF optimized amino silica surface (top view), and (c) UFF optimized amino silica surface (side view). Hydrogens were used to fill out the valence that resulted from removing the periodic boundary conditions. Hydrogens were added using the HyperChem program [57].

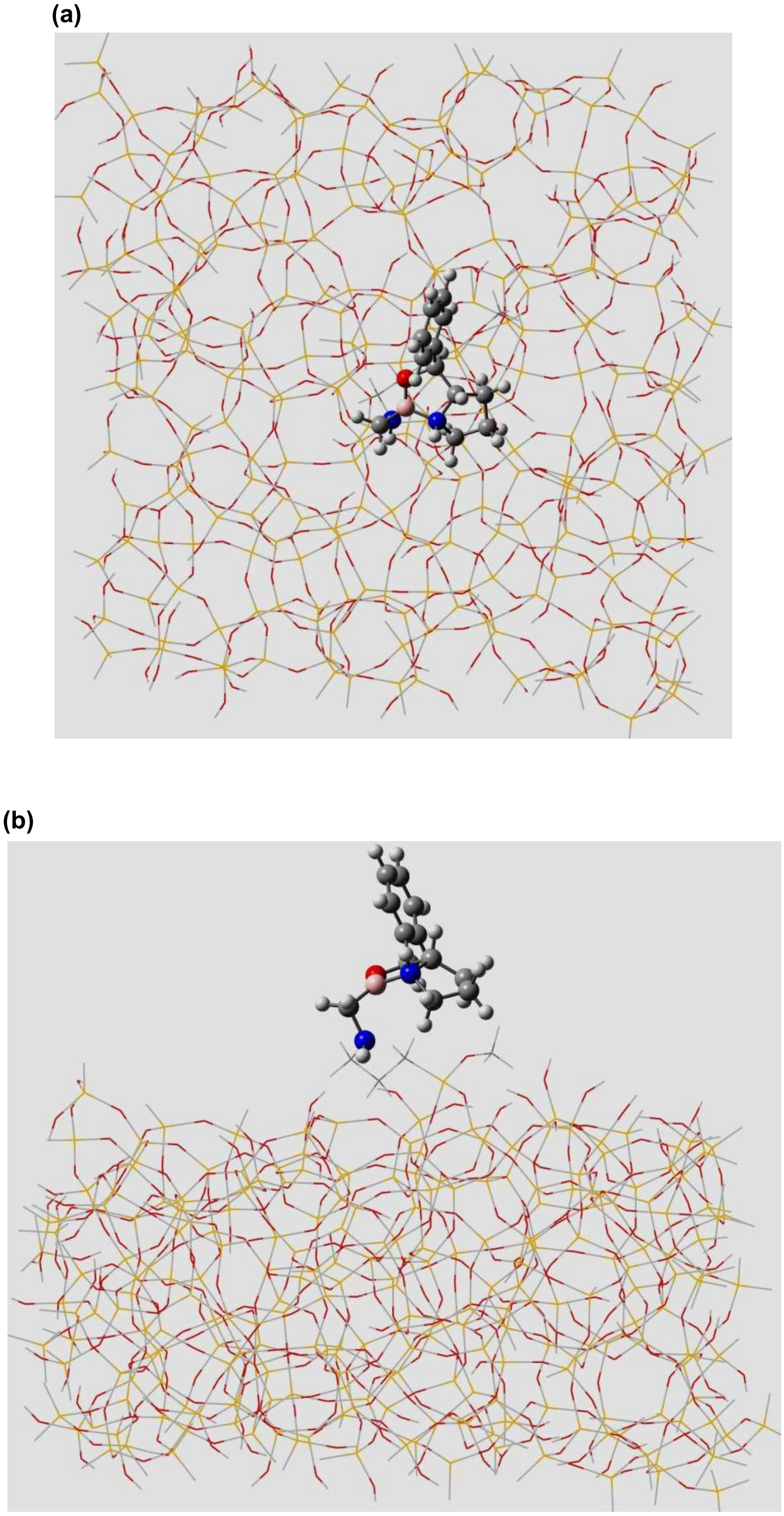

Figure 5.3: ONIOM(B3LYP/6-31G(d):UFF) optimized amino silica-immobilized catalyst ***16****. (a) Top view and (b) side view. The QM layer is in the ball-and-stick representation and the MM layer is in the wireframe representation.*

No charges were assigned to the MM atoms and the electrostatic interactions at both the MM and QM levels are, thus, ignored in the current study. The UFF does not include default values for partial charges. For determining the partial charges, the use of the charge equilibration procedure (QEq) might be suitable [60]. In this procedure, the computed charges are allowed to adjust to geometrical changes. However, it has been shown that the performance of the UFF without charges is better than the UFF combined with QEq [61]. In addition, in the Gaussian program, the QEq partial charges are calculated only at the initial geometry and are not updated during the course of geometry optimization [62]. Since charges depend on structural parameters, the electrostatic interactions will not be calculated accurately using charges derived from the initial structure. In an embedded cluster ONIOM(QM:MM) study on the cyclization of C6 diene in zeolites, Joshi and Thomson [63] concluded that the MM partial charges caused nearly constant shifts in the energetics, and not necessarily in a stabilizing manner. Furthermore, since the ONIOM method neglects the polarization of the MM region, the effect of the MM charges will be overestimated [64]. The ONIOM-ME method is therefore used for all calculations.

In the Gaussian 03 program, the default algorithm used for ONIOM(QM:MM) geometry optimization to a minimum is different than the algorithm used for optimization to a transition structure. In the geometry optimization to a minimum, ONIOM(QM:MM) takes advantage of the microiterations procedure [65] that allows the use of a fast MM optimizer so that the entire MM layer is fully minimized at each geometry optimization step of the QM layer. This is a computationally efficient procedure that allows faster geometry optimization than the ‘normal’ procedure which includes all atoms in the geometry optimization similar to a regular non-

ONIOM calculation. In the Gaussian 03 program, the ‘normal’ procedure is the only procedure available for optimization to a transition structure. Therefore, ONIOM(QM:MM) transition structure searches are computationally demanding.

Vibrational frequency calculations were carried out at the optimized geometries to verify whether the obtained structures are minima or transition structures as well as to determine zero-point vibrational energies and thermodynamic quantities. The vibration associated with the imaginary frequency was ensured to correspond to a displacement in the direction of the reaction coordinate. The zero-point vibrational energies and thermodynamic quantities were computed using frequencies scaled by 0.9804. Thermodynamic quantities were calculated at 298.15 K and at 1.0 atm pressure.

5.3 Results and Discussion

5.3.1 Characterization of the amorphous silica bulk and surface

In this section, the amorphous silica bulk and surface are characterized. The characterization approach followed is simple rather than exhaustive. The density of the bulk amorphous silica obtained in this study is 2.25 g/cm^3, a value close to the experimental density of 2.20 g/cm^3 [66,67].

On the silica surface (Figure 5.1d), the non-bridging oxygens (i.e. oxygen atoms bonded to less than two silicon atoms) density is 1.9/nm^2. The tricoordinated silicon atoms density is 0.9/nm^2. To obtain a hydroxylated surface, hydrogens were added to non-bridging oxygens and hydroxyl groups to tricoordinated silicons. This resulted in a surface (Figure 5.1e) having a silanol number (i.e. the number of hydroxyl groups per square nanometer) of 2.8 OH/nm^2. This silanol number is close to the silanol number obtained for thermally treated silica at 673 K (~ 3 OH/nm^2) [66-68].

Silica calcined at 673 K has been used as a solid support for organometallic catalysts [17,20].

The surface chemistry of silica is dominated by the surface silanol groups that participate in adsorption of molecules (e.g., water) as well as chemical modification of silica surfaces [68]. Types of silanol groups on the surface of silica include isolated, geminal and vicinal (or H-bonded) silanols (Figure 5.4). At low temperatures, vicinal silanols almost entirely cover the surface [69]. Dehydroxylation of the silica surface begins at temperatures above 473 K and the silanol number decreases with increasing temperature. Vicinal silanols may remain on the silica surface up to ~ 723 K, geminal silanols up to ~ 1073 K, and isolated silanols up to ~ 1273 K [66]. The ratio of the isolated silanols to geminal silanol groups on the silica surface is estimated to be ~ 85/15 at temperatures in the range of 723 K to 1073 K [66]. In the current work, the percentages of isolated, geminal and vicinal silanols are found to be 73%, 18% and 9%, respectively. This indicates that the simulated silica obtained in the present work corresponds to silica obtained by thermal treatment at temperatures close to 723 K, in line with the conclusion reached by using the silanol number.

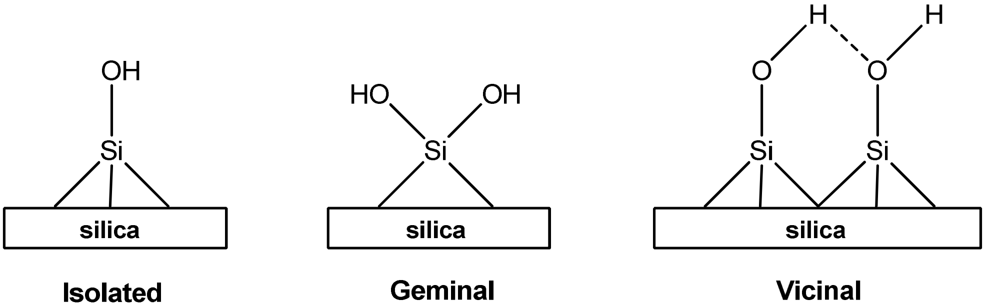

Figure 5.4: Silanol groups on the surface of silica.

In their experiment regarding the enantioselectivity of Diels-Alder reactions on SiO_2-immobilized Cu-bis(oxazoline) catalyst, Tanaka et al. [17] recommended that the loading of the catalyst is controlled to be at 0.1 molecule/nm^2. This would allow the organofunctionalization of the silica surface surrounding the catalyst. As mentioned in Section 5.2.2, one molecule of catalyst **16** was covalently attached to the amino silica surface (Figure 5.3). The loading of catalyst **16** on the silica surface is therefore 0.12 molecule/nm^2. Furthermore, as stated in the 'specification sheet' for 3-aminopropyl-functionalized silica [70], 9% of the surface active groups are functionalized. This corresponds to two silanol groups for the silica surface obtained in this study. Hence, only one molecule of 3-aminopropyltrimethoxysilane was attached to the silica surface and the silica surface obtained in the current work is considered to be a good representative model and attachment of additional molecules of catalyst **16** to the silica surface was not necessary.

5.3.2 Diels-Alder reaction on the silica surface

The Diels-Alder reaction studied on the silica surface is between isoprene **14** and 2,3-dimethyl-1,4-benzoquinone **15** in the presence of amino silica-supported catalyst **16** as shown in Figure 5.5. Since optimization to a transition structure in ONIOM(QM:MM) is computationally demanding, only the *syn* transition structures are considered in this study. This choice is based on the results obtained in Chapter 3 (Section 3.3.2, Figure 3.13 vs. Figure 3.14) which indicated the *syn* transition structures to be more stable than the *anti* transition structures. In addition, the *syn* coordination between benzoquinone **15** and amino silica-immobilized catalyst **16** is stronger than the *anti* coordination and the B–O bond length for the *syn* coordination complex is shorter by 0.03 Å than that of the *anti* complex. The *syn* complex also has a nonconventional hydrogen bond between the C_α–H hydrogen and the oxygen of the catalyst with 2.66 Å bond length. This stronger coordination combined with the presence of hydrogen bonding in the *syn* coordination complex resulted in an 11.6 kcal/mol stabilization for the *syn* complex as compared to the *anti* complex which corresponds to a 100% of the Boltzmann population being represented by the *syn* complex. Furthermore, the *anti* coordination is unfavored since the complex Gibbs free energy is 6.2 kcal/mol higher than that of the separated reactants. On the other hand, the free energy for the *syn* coordination complex is lower than that of the separated reactants by 5.4 kcal/mol and is therefore strongly favored over the *anti* coordination complex.

Reaction 5-A

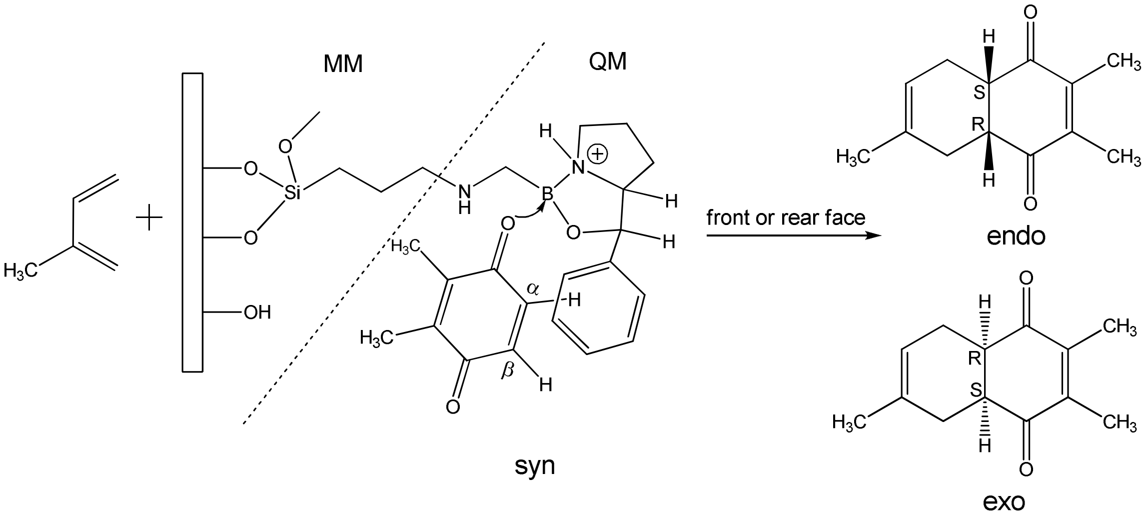

Figure 5.5: Catalyzed Diels-Alder reaction with catalyst immobilized on amino SiO_2 surface having four possible reaction pathways. The catalyst is coordinated syn to the HC═CH double bond that undergoes the [4+2]-cycloaddition. The dotted line indicates the partitioning into MM and QM regions.

The ONIOM(B3LYP/6-31G(d):UFF) optimized transition structures are shown in Figure 5.6. The B–O bond length (on average) at the transition structures is shorter than that of the reactant by 0.02 Å indicating a slightly stronger complexation at the transition state. Similar to the reactant, the transition structures possess a nonconventional hydrogen bond between the C_α–H hydrogen and the oxygen of the catalyst with bond lengths ranging from 2.15 Å to 2.61 Å.

TS28 possesses the lowest free energy representing almost a 100% of the Boltzmann population of the *endo* transition states. This transition state corresponds to an *s-cis* diene addition to the rear face of the α,β double bond of the benzoquinone. For the *exo* transition states, **TS29** is the most stable transition state and represents 99.92% of the Boltzmann population of the *exo* transition states. The *endo* path is preferred to the *exo* route and the percent enantiomeric excess (%*ee*) is calculated to be 86.5%. The results are in agreement with those obtained for the homogeneous catalyst (Chapter 3) with the exception that the *endo* transition structure has a preference for the rear face addition and the *exo* transition structure favors the front face addition.

The average degree of asynchronicity for the transition structures is found to be 0.99 Å (Figure 5.6) pointing out to concerted but highly asynchronous reaction pathways where the bond between the diene and carbon β of the dienophile is being formed in a greater extent than the bond between the diene and carbon α of the dienophile.

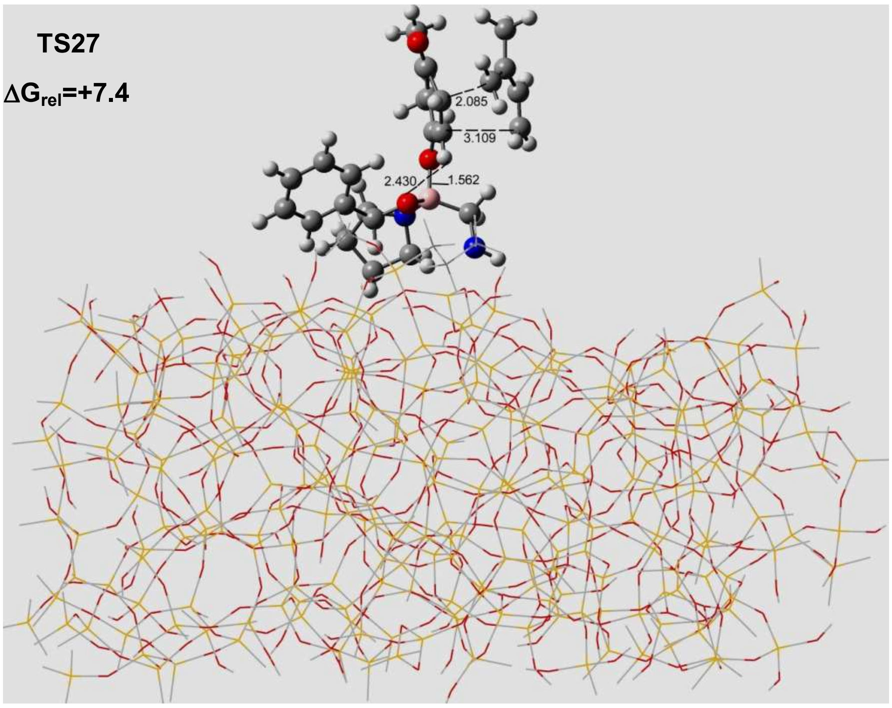

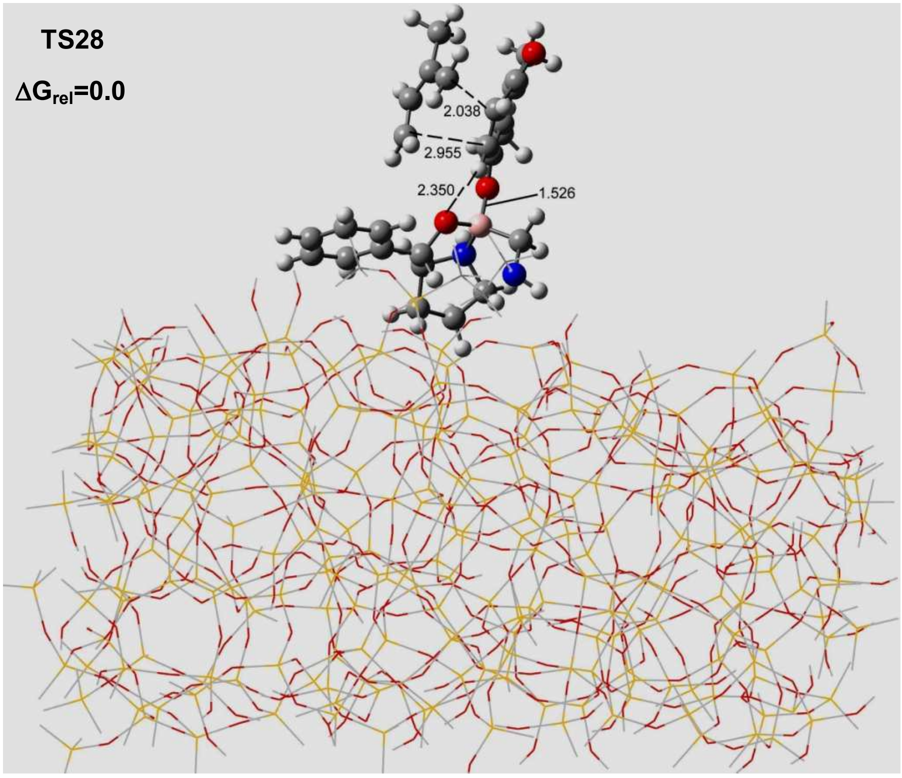

Figure 5.6: ONIOM(B3LYP/6-31G(d):UFF) optimized transition structures for the catalyzed Reaction 5-A. Relative free energies are in kcal/mol and distances are in angstroms. ***TS27*** *= endo transition state involving the s-cis diene attack to the front face and* ***TS28*** *= endo transition state involving the s-cis diene attack to the rear face.*

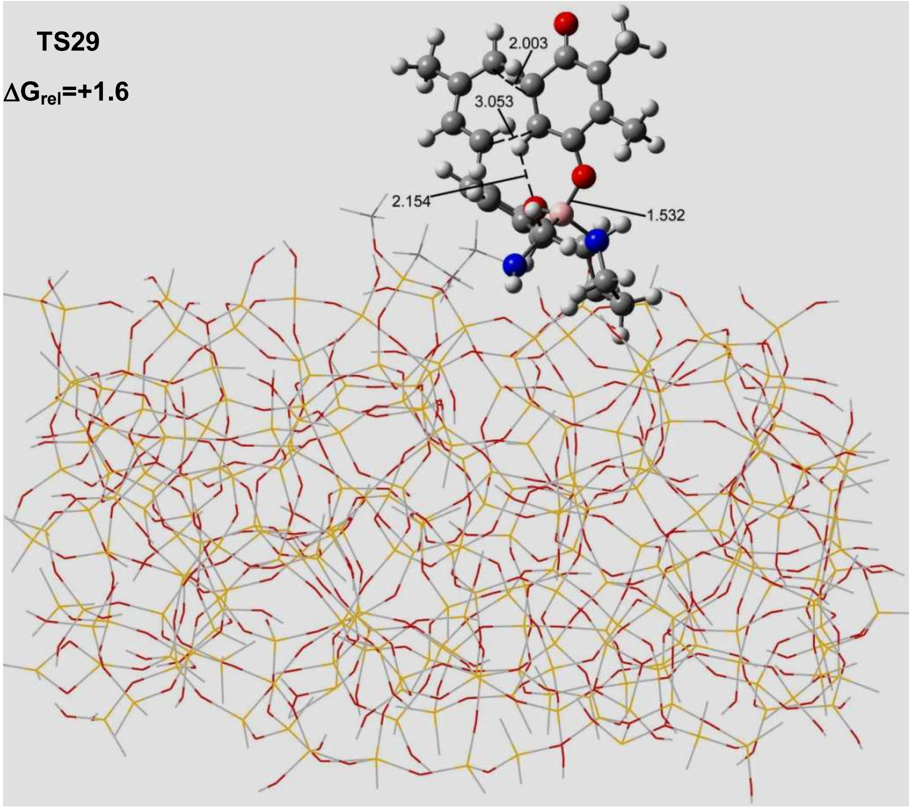

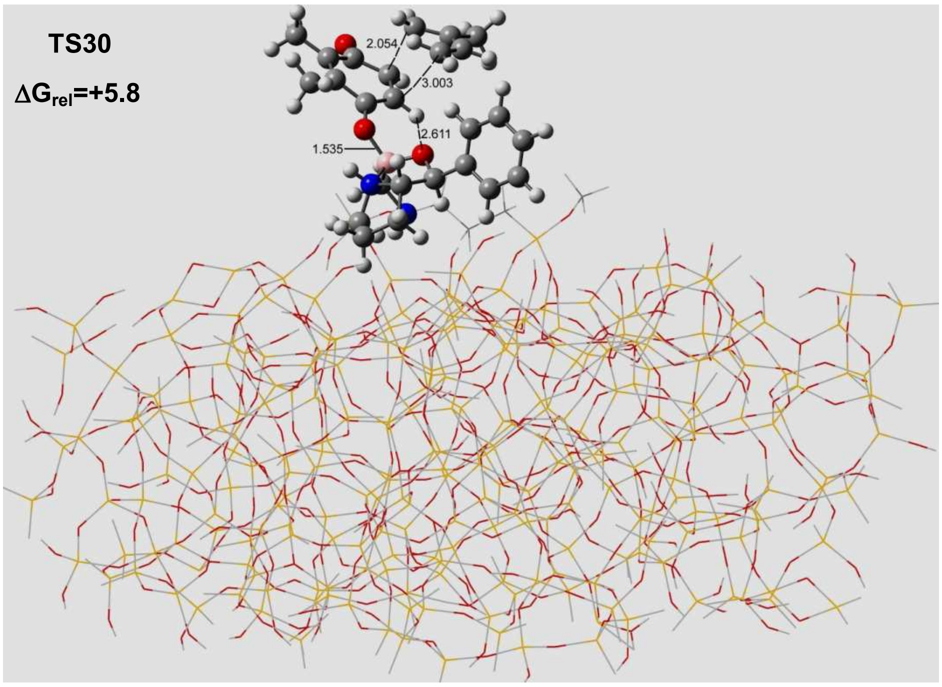

*Figure 5.6 (Continued): **TS29** = exo transition state involving the s-cis diene attack to the front face and **TS30** = exo transition state involving the s-cis diene attack to the rear face.*

5.3.3 Limitations of the study and future recommendations

The ONIOM method as implemented in the Gaussian 03 program does not work in combination with the periodic boundary conditions, the polarizable continuum solvation models, and the intrinsic reaction coordinate calculation. The current work therefore did not utilize any of these methods.

As mentioned in Section 5.2.2, ONIOM(QM:MM) transition structure searches as implemented in the Gaussian 03 program are computationally demanding. This imposed a constraint on the number of investigations that could be performed. For example, it was not possible to test the transition state structures with the ONIOM-EE method. In addition, the silica surface functionalization around the catalyst can influence the outcome of the reaction [16,17,20]. This was also not tested. In the Gaussian 09 program, however, ONIOM(QM:MM) optimization to a transition structure makes use of the microiterations procedure which makes optimizations to transition structures much more efficient. The comparison between ONIOM-ME and ONIOM-EE methods as well as the study of the effect of the surface nature surrounding the catalyst with these two methods are suggested.

As discussed above, ONIOM(QM:MM)-ME lacks the description of the electrostatic interactions between the QM and MM layers at the high level of theory. Since QM/MM methods including ONIOM(QM:MM) neglect the polarization of the MM region by the QM region, the effect of the MM charges is overestimated in ONIOM-EE. In the Gaussian program, these charges are also derived from the initial input structure and are not updated during the course of geometry optimization. In addition, the appropriateness of using MM charges in constructing the QM Hamiltonian has been questioned [71].

A method which could not be carried out in this work due to technical difficulties is ONIOM(QM:QM) in combination with periodic boundary conditions. The QM theory for treating the reaction site may be chosen to be B3LYP/6-31G(d) whereas the QM method for treating the silica slab can be any suitable DFT functional (e.g., PBE96) with plane wave basis set and pseudopotentials. Such a combination can be achieved by using the PSPW (pseudopotential plane wave) module implemented in the NWChem program. This method is expected to provide more accurate and reliable results than ONIOM(QM:MM).

5.4 Conclusion

The Diels-Alder reaction between diene **14** and dienophile **15** in the presence of SiO_2-immobilized catalyst **16** has been studied by the hybrid ONIOM(B3LYP/6-31G(d):UFF) method within the mechanical embedding scheme. The amorphous silica surface was obtained by classical molecular dynamics using the melt-quench method. The silica surface was characterized and found to closely resemble silicas calcined at 673 K. The model chiral cationic oxazaborolidinium catalyst **16** was immobilized on the aminopropyl-functionalized silica surface to act as a heterogeneous catalyst for the Diels-Alder reaction. The preferred SiO_2-supported catalyst **16** coordination to dienophile **15** was observed to be *syn* to the HC═CH double bond of the dienophile that undergoes the [4 + 2]-cycloaddition. The favored reaction path was through an *endo* transition state and the calculated enantioselectivity was 86.5%. The reaction was observed to proceed via a concerted but highly asynchronous reaction mechanism. The enantioselectivity and the mechanism of the Diels-Alder reaction on silica surface are generally comparable to those observed for the homogeneous catalyst (cf. Chapter 3).

5.5 References

1. T. Leßmann, H. Waldmann, Enantioselective synthesis on the solid phase, Chemical Communications (2006) 3380-3389.
2. F.Z. Dörwald, Organic Synthesis on Solid Phase: Supports, Linkers, Reactions, Wiley-VCH, Weinheim, Germany, 2000.
3. G.V. Smith, F. Notheisz, Heterogeneous Catalysis in Organic Chemistry, Academic Press, Burlington, MA, 1999.
4. J.A.M. Brandts, E.G.M. Kuijpers, P.H. Berben, Application of Immobilized Homogeneous Catalysts in Enantio- and Chemoselective Hydrogenation Reactions. In: Science and Technology in Catalysis 2002: Proceedings of the Fourth Tokyo Conference on Advanced Catalytic Science and Technology (M. Anpo, M. Onaka, H. Yamashita, editors), Kodansha Ltd., Tokyo, Japan, 2003.
5. T. Maschmeyer, L. van de Water, An Overview of Zeolite, Zeotype and Mesoporous Solids Chemistry: Design, Synthesis and Catalytic Properties. In: Catalysts for Fine Chemical Synthesis – Vol. 4: Microporous and Mesoporous Solid Catalysts (E.G. Derouane, editor), John Wiley & Sons, Ltd., Chichester, England, 2006.
6. C.E. Song, S-g. Lee, Supported chiral catalysts on inorganic materials, Chemical Reviews 102 (2002) 3495-3524.
7. C. Li, Chiral synthesis on catalysts immobilized in microporous and mesoporous materials, Catalysis Reviews: Science and Engineering 46 (2004) 419-492.
8. R. Haag, S. Roller, Polymeric supports for the immobilisation of catalysts, Topics in Current Chemistry 242 (2004) 1-42.
9. J. Horn, F. Michalek, C.C. Tzschucke, W. Bannwarth, Non-covalently solid-phase bound catalysts for organic synthesis, Topics in Current Chemistry 242 (2004) 43-75.
10. B.M.L. Dioos, I.F.J. Vankelecom, P.A. Jacobs, Aspects of immobilisation of catalysts on polymeric supports, Advanced Synthesis & Catalysis 348 (2006) 1413-1446.
11. G.J. Meuzelaar, R.A. Sheldon, Heterogeneous Catalysis of Diels-Alder Reactions. In: Solid Acid Catalysis: Miscellaneous. In: Fine Chemicals through Heterogeneous Catalysis (R.A. Sheldon, H. van Bekkum, editors), Wiley-VCH, Weinheim, Germany, 2001.
12. S. Itsuno, K. Watanabe, T. Koizumi, K. Ito, Asymmetric Diels-Alder reaction of cyclopentadiene with methacrolein using polymer-supported chiral catalysts, Reactive Polymers 24 (1995) 219-227.
13. J.D. Winkler, W. McCoull, Diels-Alder reaction on solid supports using polymer-bound oxazolidinones, Tetrahedron Letters 39 (1998) 4935-4936.
14. D. Rechavi, M. Lemaire, Heterogenization of a chiral bis(oxazoline) catalyst by grafting onto silica, Organic Letters 3 (2001) 2493-2496.
15. D. Rechavi, M. Lemaire, Enantioselective catalysis using heterogeneous bis(oxazoline) ligands: Which factors influence the enantioselectivity? Chemical Reviews 102 (2002) 3467-3494.
16. M. Tada, Y. Iwasawa, Advanced chemical design with supported metal complexes for selective catalysis, Chemical Communications (2006) 2833-2844.

17. S. Tanaka, M. Tada, Y. Iwasawa, Enantioselectivity promotion by achiral surface functionalization on SiO_2-supported Cu-bis(oxazoline) catalysts for asymmetric Diels-Alder reactions, Journal of Catalysis 245 (2007) 173-183.
18. J.M. Fraile, J.I. García, J.A. Mayoral, Recent advances in the immobilization of chiral catalysts containing bis(oxazolines) and related ligands, Coordination Chemistry Reviews 252 (2008) 624-646.
19. J.M. Fraile, J.I. García, C.I. Herrerías, J.A. Mayoral, E. Pires, L. Salvatella, Beyond reuse in chiral immobilized catalysis: The bis(oxazoline) case, Catalysis Today 140 (2009) 44-50.
20. K. Motokura, M. Tada, Y. Iwasawa, Organofunctionalized catalyst surfaces highly active and selective for carbon-carbon bond-forming reactions, Catalysis Today 147 (2009) 203-210.
21. M.I. Burguete, J.M. Fraile, J.I. García, E. García-Verdugo, C.I. Herrerías, S.V. Luis, J.A. Mayoral, Bis(oxazoline)copper complexes covalently bonded to insoluble support as catalysts in cyclopropanation reactions, The Journal of Organic Chemistry 66 (2001) 8893-8901.
22. A. Corma, H. García, A. Moussaif, M.J. Sabater, R. Zniber, A. Redouane, Chiral copper(II) bisoxazoline covalently anchored to silica and mesoporous MCM-41 as a heterogeneous catalyst for the enantioselective Friedel-Crafts hydroxyalkylation, Chemical Communications (2002) 1058-1059.
23. L.-N. Huang, X.-P. Hui, Z.-C. Chen, C. Yin, P.-F. Xu, X.-X. Yu, S.-Y. Cheng, Enantioselective addition of phenylacetylene to aldehydes catalyzed by silica-immobilized titanium(IV) complex of β-hydroxyamide, Journal of Molecular Catalysis A: Chemical 275 (2007) 9-13.
24. S. Doherty, P. Goodrich, C. Hardacre, V. Pârvulescu, C. Paun, Efficient heterogeneous asymmetric catalysis of the Mukaiyama aldol reaction by silica- and ionic liquid-supported Lewis acid copper(II) complexes of bis(oxazolines), Advanced Synthesis & Catalysis 350 (2008) 295-302.
25. C. McDonagh, P. O'Leary, Electrostatically immobilised BOX and PYBOX metal catalysts: Application to ene reactions, Tetrahedron Letters 50 (2009) 979-982.
26. C. Franot, G.B. Stone, P. Engeli, C. Spöndlin, E. Waldvogel, A polymer-bound oxazaborolidine catalyst: Enantioselective borane reductions of ketones, Tetrahedron Asymmetry 6 (1995) 2755-2766.
27. M.D. Price, J.K. Sui, M.J. Kurth, N.E. Schore, Oxazaborolidines as functional monomers: Ketone reduction using polymer-supported Corey, Bakshi, and Shibata catalysts, The Journal of Organic Chemistry 67 (2002) 8086-8089.
28. J.M. Fraile, J.A. Mayoral, J. Serrano, M.A. Pericàs, L. Solà, D. Castellnou, New silica-immobilized chiral amino alcohol for the enantioselective addition of diethylzinc to benzaldehyde, Organic Letters 5 (2003) 4333-4335.
29. S. Degni, C.-E. Wilén, A. Rosling, Highly catalytic enantioselective reduction of aromatic ketones using chiral polymer-supported Corey, Bakshi, and Shibata catalysts, Tetrahedron Asymmetry 15 (2004) 1495-1499.
30. D. Font, C. Jimeno, M.A. Pericàs, Polystyrene-supported hydroxyproline: An insoluble, recyclable organocatalyst for the asymmetric aldol reaction in water, Organic Letters 8 (2006) 4653-4655.
31. I. Hermans, J. van Deun, K. Houthoofd, J. Peeters, P.A. Jacobs, Silica-immobilized N-hydroxyphthalimide: An efficient heterogeneous autoxidation catalyst, Journal of catalysis 251 (2007) 204-212.

32. Y.-B. Zhao, L.-W. Zhang, L.-Y. Wu, X. Zhong, R. Li, J.-T. Ma, Silica-supported pyrrolidine–triazole, an insoluble, recyclable organocatalyst for the enantioselective Michael addition of ketones to nitroalkenes, Tetrahedron Asymmetry 19 (2008) 1352-1355.
33. T. Miao, L. Wang, Polystyrene-immobilized pyrrolidine as a highly stereoselective and recyclable organocatalyst for asymmetric Michael addition of cyclohexanone to nitroolefins, Tetrahedron Letters 49 (2008) 2173-2176.
34. J. Yune, K. Molvinger, F. Quignard, Efficient new supported catalyst for asymmetric reductions, Catalysis Today 138 (2008) 104-109.
35. K. Ding, Y. Uozumi (editors), Handbook of Asymmetric Heterogeneous Catalysis, Wiley-VCH, Weinheim, Germany, 2008.
36. U. Balakrishnan, N. Ananthi, S.T. Selvan, R.Pal, K. Ariga, S. Velmathi, A. Vinu, Preparation and characterization of chiral oxazaborolidine complex immobilized SBA-15 and its application in the asymmetric reduction of prochiral ketones, Chemistry - An Asian Journal (in press).
37. A.A. Selezenev, A.Y. Aleynikov, N.S. Gantchuk, P.V. Yermakov, J.K. Labanowski, A.A. Korkin, SAGE MD: Molecular-dynamic software package to study properties of materials with different models for interatomic interactions, Computational Materials Science 28 (2003) 107-124.
38. E.R. Cruz-Chu, A. Aksimentiev, K. Schulten, Water–silica force field for simulating nanodevices, Journal of Physical Chemistry B 110 (2006) 21497-21508.
39. X. Yang, Z. Xu, C. Zhang, Molecular dynamics simulation of dense carbon dioxide fluid on amorphous silica surfaces, Journal of Colloid and Interface Science 297 (2006) 38-44.
40. X. Yang, X. Yue, Adsorption and structure of Lennard–Jones model fluid in slit-like amorphous silica nanopores, Colloids and Surfaces A: Physicochemical and Engineering Aspects 301 (2007) 166-173.
41. F. Zipoli, D. Donadio, M. Bernasconi, Simulation of the grafting of organosilanes at the surface of dry amorphous silica, Journal of Physics: Condensed Matter 20 (2008) 224011.
42. Y. Qin, X. Yang, Y. Zhu, J. Ping, Molecular dynamics simulation of interaction between supercritical CO_2 fluid and modified silica surfaces, Journal of Physical Chemistry C 112 (2008) 12815-12824.
43. N.T. Huff, E. Demiralp, T. Çagin, W.A. Goddard III, Factors affecting molecular dynamics simulated vitreous silica structures, Journal of Non-Crystalline Solids 253 (1999) 133-142.
44. E. Demiralp, T. Çagin, W.A. Goddard III, Morse stretch potential charge equilibrium force field for ceramics: Application to the quartz-stishovite phase transition and to silica glass, Physical Review Letters 82 (1999) 1708-1711.
45. A. Takada, P. Richet, C.R.A. Catlow, G.D. Price, Molecular dynamics simulations of vitreous silica structures, Journal of Non-Crystalline Solids 345&346 (2004) 224-229.
46. V.V. Hoang, N.T. Hai, H. Zung, Tetrahedral ↔ octahedral network structure transition in simulated vitreous SiO_2, Physics Letters A 356 (2006) 246-250.
47. T. Yoshioka, A. Yasumoto, K. Kishi, T. Tsuru, MD simulation studies for effect of membrane structures and dynamics on gas permeation properties through microporous amorphous silica membranes, Desalination 233 (2008) 333-341.

48. B.W.H. van Beest, G.J. Kramer, R.A. van Santen, Force fields for silicas and aluminophosphates based on *ab initio* calculations, Physical Review Letters 64 (1990) 1955-1958.
49. K. Vollmayr, W. Kob, K. Binder, Cooling-rate effects in amorphous silica: A computer-simulation study, Physical Review B 54 (1996) 15808-15827.
50. J. Horbach, W. Kob, Static and dynamic properties of a viscous silica melt, Physical Review B 60 (1999) 3169-3181.
51. A. Carré, L. Berthier, J. Horbach, S. Ispas, W. Kob, Amorphous silica modeled with truncated and screened Coulomb interactions: A molecular dynamics simulation study, The Journal of Chemical Physics 127 (2007) 114512-1-9.
52. Y. Wang, X. Xu, L. Zheng, Molecular dynamics simulation of ultrafast laser ablation of fused silica film, Applied Physics A: Materials Science & Processing 92 (2008) 849-852.
53. V.A. Bakaev, Continuous random network at the silica surface, Physical Review B 60 (1999) 10723-10726.
54. S. von Alfthan, A. Kuronen, K. Kaski, Realistic models of amorphous silica: A comparative study of different potentials, Physical Review B 68 (2003) 073203-14.
55. E.A. Leed, C.G. Pantano, Computer modeling of water adsorption on silica and silicate glass fracture surfaces, Journal of Non-Crystalline Solids 325 (2003) 48-60.
56. L.J. Broadbelt, R.Q. Snurr, Applications of molecular modeling in heterogeneous catalysis research, Applied Catalysis A: General 200 (2000) 23-46.
57. HyperChem(TM), Hypercube, Inc., 1115 NW 4th Street, Gainesville, Florida 32601, USA.
58. Gaussian 03, Revision E.01, M. J. Frisch, G. W. Trucks, H. B. Schlegel, G. E. Scuseria, M. A. Robb, J. R. Cheeseman, J. A. Montgomery, Jr., T. Vreven, K. N. Kudin, J. C. Burant, J. M. Millam, S. S. Iyengar, J. Tomasi, V. Barone, B. Mennucci, M. Cossi, G. Scalmani, N. Rega, G. A. Petersson, H. Nakatsuji, M. Hada, M. Ehara, K. Toyota, R. Fukuda, J. Hasegawa, M. Ishida, T. Nakajima, Y. Honda, O. Kitao, H. Nakai, M. Klene, X. Li, J. E. Knox, H. P. Hratchian, J. B. Cross, V. Bakken, C. Adamo, J. Jaramillo, R. Gomperts, R. E. Stratmann, O. Yazyev, A. J. Austin, R. Cammi, C. Pomelli, J. W. Ochterski, P. Y. Ayala, K. Morokuma, G. A. Voth, P. Salvador, J. J. Dannenberg, V. G. Zakrzewski, S. Dapprich, A. D. Daniels, M. C. Strain, O. Farkas, D. K. Malick, A. D. Rabuck, K. Raghavachari, J. B. Foresman, J. V. Ortiz, Q. Cui, A. G. Baboul, S. Clifford, J. Cioslowski, B. B. Stefanov, G. Liu, A. Liashenko, P. Piskorz, I. Komaromi, R. L. Martin, D. J. Fox, T. Keith, M. A. Al-Laham, C. Y. Peng, A. Nanayakkara, M. Challacombe, P. M. W. Gill, B. Johnson, W. Chen, M. W. Wong, C. Gonzalez, and J. A. Pople, Gaussian, Inc., Wallingford CT, 2004.
59. A.K. Rappé, C.J. Casewit, K.S. Colwell, W.A. Goddard III, W.M. Skiff, UFF, a full periodic table force field for molecular mechanics and molecular dynamics simulations, Journal of the American Chemical Society 114 (1992) 10024-10035.
60. A.K. Rappe, W.A. Goddard III, Charge equilibration for molecular dynamics simulations, Journal of Physical Chemistry 95 (1991) 3358-3363.
61. K. Gundertofte, T. Liljefors, P.-o. Norrby, I. Pettersson, A comparison of conformational energies calculated by several molecular mechanics methods, Journal of Computational Chemistry 17 (1996) 429-449.

62. Molecular Mechanics Methods. http://www.gaussian.com/g_tech/g_ur/k_mm-.htm.
63. Y.V. Joshi, K.T. Thomson, Embedded cluster (QM/MM) investigation of C6 diene cyclization in HZSM-5, Journal of Catalysis 230 (2005) 440-463.
64. M. Lundberg, T. Kawatsu, T. Vreven, M.J. Frisch, K. Morokuma, Transition states in a protein environment – ONIOM QM:MM modeling of isopenicillin N synthesis, Journal of Chemical Theory and Computation 5 (2009) 222-234.
65. T. Vreven, K. Morokuma, Ö. Farkas, H.B. Schlegel, M.J. Frisch, Geometry optimization with QM/MM, ONIOM, and other combined methods. I. Microiterations and constraints, Journal of Computational Chemistry 24 (2003) 760-769.
66. H.E. Bergna, Colloid Chemistry of Silica: An Overview. In: Colloidal Silica: Fundamentals and Applications (H.E. Bergna, W.O. Roberts, editors), CRC Press, Boca Raton, FL, 2006.
67. Y. Iwasawa, Inorganic Oxide-Attached Metal Catalysts. In: Tailored Metal Catalysts (Y. Iwasawa, editor), D. Reidel Publishing Company, Dordrecht, Holland, 1986.
68. R.T. Yang, Adsorbents: Fundamentals and Applications, John Wiley & Sons, Inc., Hoboken, NJ, 2003.
69. M. Alkam, M. Dogan, Silica Gels: Surface Chemistry. In: Encyclopedia of Surface and Colloid Science (P. Somasundaran, editor), CRC Press, Boca Raton, 2006.
70. Sigma-Aldrich, Product Number: 364258, Product Name: 3-aminopropyl-functionalized silica gel. http://www.sigmaaldrich.com/catalog/Advanced-SearchPage.do.
71. H. Lin, D.G. Truhlar, QM/MM: What have we learned, where are we, and where do we go from here? Theoretical Chemistry Accounts 117 (2007) 185-199.

6

A DFT Investigation on the Enantioselective Cyanosilylation of Aldehydes Catalyzed by Chiral Oxazaborolidinium Cation

Catalytic enantioselective synthesis of cyanohydrins from aldehydes is essential since cyanohydrins can be transformed into a number of biologically important molecules. Various types of chiral catalysts have been developed in order to obtain good enantioselectivities. In the present chapter, the enantioselectivity and mechanism of the cyanosilylation of aldehydes using the chiral organocatalyst oxazaborolidinium ion are investigated by means of density functional theory with the popular B3LYP functional.

6.1 Introduction

The cyanosilylation of aldehydes and ketones is an essential reaction in organic synthesis for the production of cyanohydrins that are industrially key precursors in the synthesis of biologically important compounds such as α-hydroxy acids and their derivatives, and β-amino alcohols. The general synthetic route of cyanohydrins is the addition of the mild cyanating agent trimethylsilyl cyanide (TMSCN) to the carbonyl compounds in the presence of a catalyst. Lewis acids (e.g., [1,2]), Lewis bases (e.g., [3,4]) and bifunctional catalysts (e.g., [5,6]) have been employed as catalysts. A large number of chiral catalysts have been developed for the production of enantiomerically pure cyanohydrins with the majority consisting of transition-metal complexes with chiral ligands. However, efficient syntheses of cyanohydrins utilizing organocatalysts have been recently devised [7-17].

High enantioselectivities (> 90%) for the cyanosilylation of aldehydes catalyzed by chiral oxazaborolidinium cation catalyst **13** have been reported [8]. The stereochemical configuration of the cyanohydrins produced and a mechanistic model have been proposed [8]. The mechanistic model is as follows: (1) the formation of a coordination complex **17** between catalyst **13** and the aldehyde, (2) the nucleophilic attack on the formyl carbon is facilitated by the complexation and occurs at the front face since the rear face is shielded by the phenyl ring, (3) the rotation about the B–O bond is fixed due to the nonconventional C–H•••O hydrogen bond [18,19], (4) the isocyanide should be more reactive as a cyanosilylation reagent than the isomeric cyanide, and (5) the silylated (*R*)-cyanohydrin is produced preferentially.

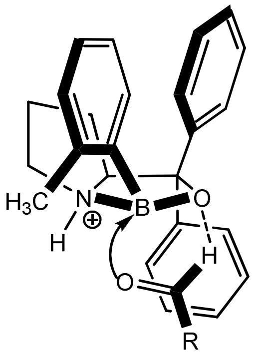

17

The objective of the current study is to theoretically investigate the enantioselectivity and mechanism of the cyanosilylation of aldehydes in the presence of chiral oxazaborolidinium cation catalyst.

6.2 Computational Details

Geometry optimizations and vibrational frequencies of the reactants, transition structures, intermediates and products were performed *in vacuo* using the hybrid density functional method B3LYP with the 6-31G(d) basis set as implemented in the Gaussian 03 program [20]. The default SCF algorithm (EDIIS/CDIIS) in the Gaussian 03 program was used unless in case of convergence problem, in particular for transition structures, where the keyword "`scf=(maxconventional-`

`cycles=20,xqc)`" was used. This keyword instructs the program to use the default SCF algorithm for the first 20 cycles then to use the quadratically convergent (QC) SCF algorithm in order to ensure convergence. Geometry optimizations to local minima and transition structures were accomplished with the Berny algorithm in redundant internal coordinates without any symmetry restriction. Vibrational frequency calculations were carried out at the optimized geometries to verify whether the obtained structures are minima or transition structures as well as to determine zero-point vibrational energies and thermochemical quantities. The vibration associated with the imaginary frequency was ensured to correspond to a displacement in the direction of the reaction coordinate. This was achieved with the graphical user interface for Gaussian program (GaussView). The zero-point vibrational energies and thermochemical quantities were computed using frequencies scaled by 0.9804. Thermochemical quantities were calculated at 273.15 K and at 1.0 atm pressure.

6.3 Results and Discussion

A typical example representing the enantioselective cyanosilylation of aldehydes in the presence of chiral oxazaborolidinium catalyst is depicted in Figure 6.1 (Reaction 6-A).

The studied simplified model of Reaction 6-A is illustrated in Figure 6.2 (Reaction 6-B). The simplifications are as follows: (1) the model (*S*)-catalyst **16** is used instead of catalyst **13**, (2) trimethylsilyl cyanide (TMSCN) and triphenylphosphine oxide (Ph_3PO) are represented by H_3SiCN and Me_3PO, respectively, and (3) only the coordination mode that allows the formation of the nonconventional hydrogen bond between the formyl hydrogen of benzaldehyde and the oxygen of catalyst **16** is considered.

Reaction 6-A

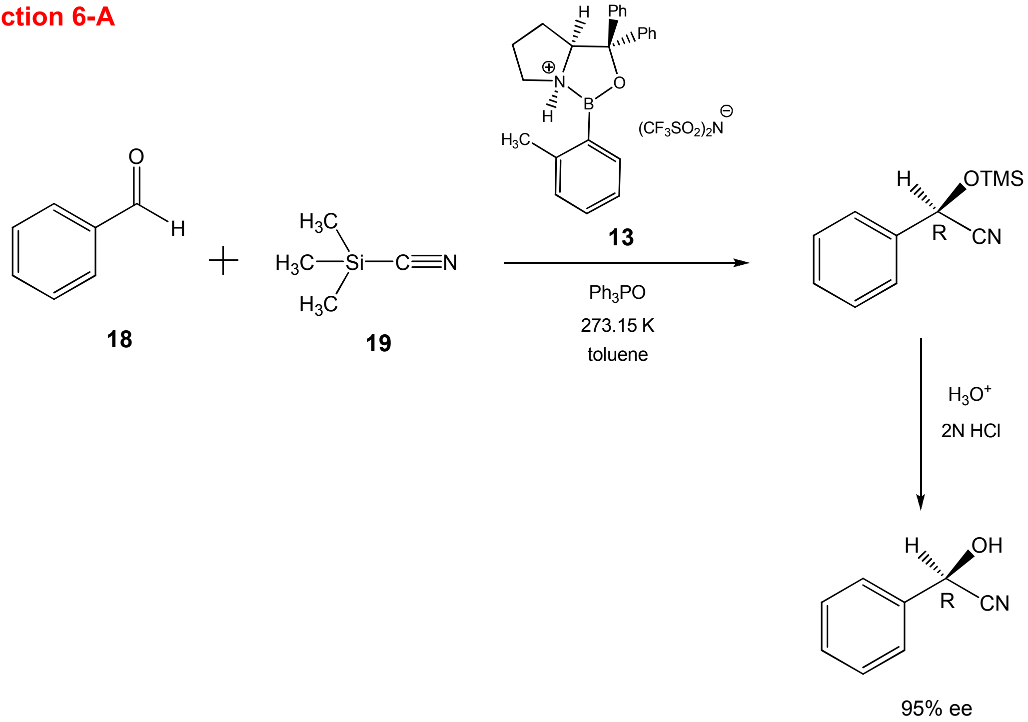

Figure 6.1: Corey's enantioselective cyanosilylation of benzaldehyde using chiral oxazaborolidinium catalyst (reference 8).

Reaction 6-B

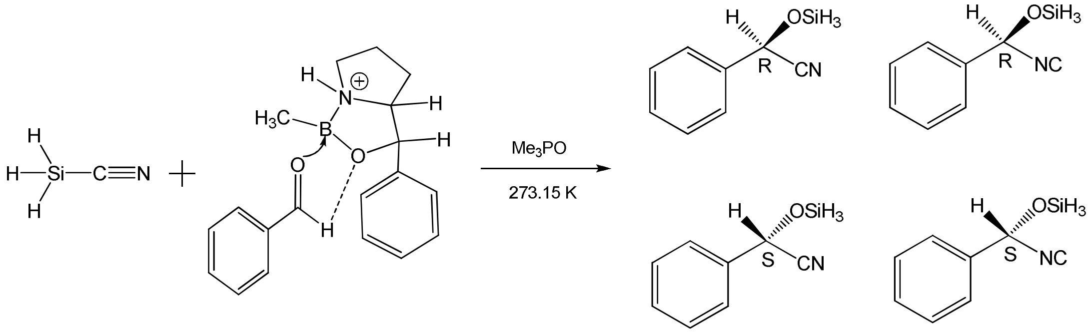

Figure 6.2: Modeled enantioselective cyanosilylation of benzaldehyde using chiral oxazaborolidinium catalyst ***16****.*

The Ph_3PO acts as an enantioselectivity promoter and is incorporated into the catalytic Lewis acid structures leading to the so called 'two-center catalysis' (i.e. Lewis acid – Lewis base bifunctional catalysis) [8,21]. NMR and IR experiments [8] have supported the idea that Ph_3PO reacts with TMSCN and suggested the possible formation of isocyanide $Ph_3P(OTMS)(NC)$ as a reactive intermediate. This isocyanide is expected to be a more reactive cyanosilylation reagent than the isomeric cyanide [8]. At the B3LYP/6-31G(d) level employed in the present work, the Gibbs free energy for isocyanide is 6.7 kcal/mol higher than that of cyanide. The isomerization takes place via the transition state structure depicted in Figure 6.3. The transition state possesses a three-membered ring structure and the free energy barrier for this isomerization step is found to be 30.9 kcal/mol.

Based on the isomerization from cyanide to isocyanide and on the stereochemical configuration of the transition state (*R* or *S*), there are eight possible transition states as shown in Figure 6.4. Four-membered ring or five-membered ring transition state structures are possible depending on whether the attack on the formyl carbon is initiated by the carbon atom or the nitrogen atom of the cyano group.

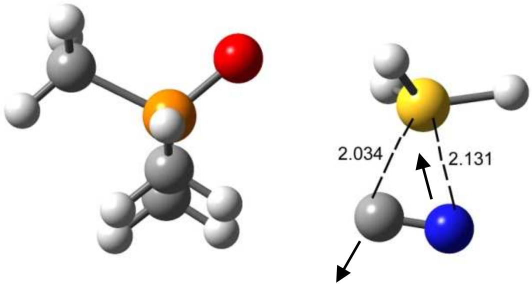

Figure 6.3: B3LYP/6-31G(d) optimized transition state structure for the isomerization from Me_3POH_3SiCN to Me_3POH_3SiNC. Color code: carbon in grey, hydrogen in white, oxygen in red, nitrogen in blue, silicon in yellow and phosphorus in orange. Arrows indicate displacement vectors. Distances are in angstroms.

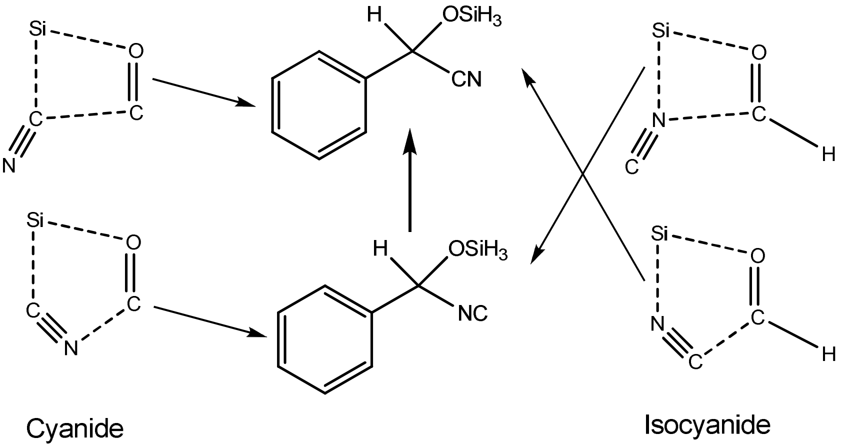

Figure 6.4: Possible transition states of the cyanosilylation of aldehydes. Products have either the R or the S configuration.

In the current study, the B3LYP/6-31G(d) calculations show that in the presence of model catalyst **16**, the cyanosilylation of benzaldehyde takes place by a stepwise mechanism. Starting the transition state searches with four-membered ring structures led to the same transition state structures obtained from five-membered ring structures. Hence, only five-membered-like transition state structures could be located. The B3LYP/6-31G(d) located transition state structures and intermediates are shown in Figures 6.5 – 6.10.

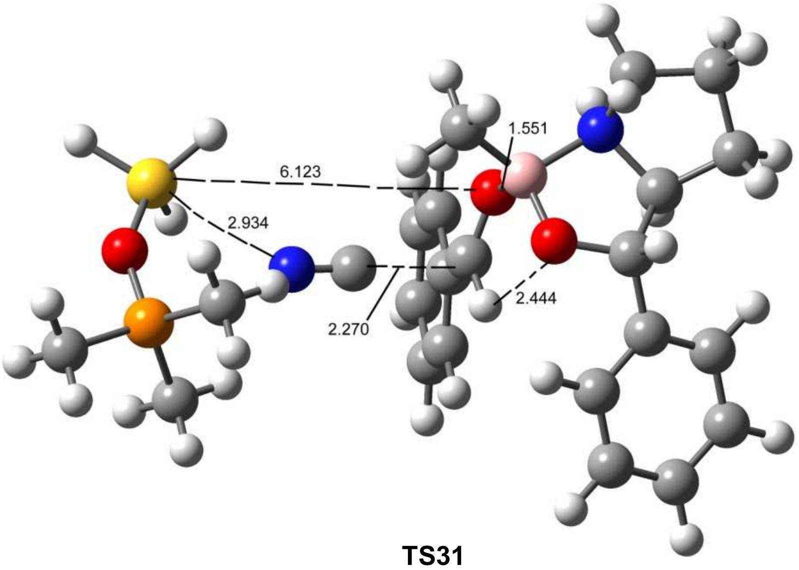

TS31

ΔG_{rel}=0.0

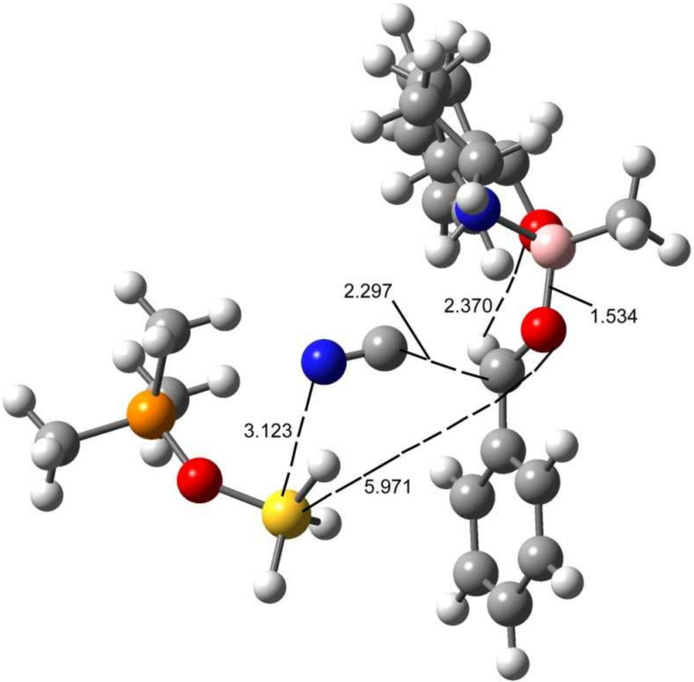

TS32

ΔG_{rel}=+2.6

Figure 6.5: B3LYP/6-31G(d) optimized first transition structures for Reaction 6-B (isocyanide path). Relative free energies are in kcal/mol at 273.15 K. Distances are in angstroms. ***TS31*** *= transition state having the R configuration and* ***TS32*** *= transition state having the S configuration. Color code: carbon in grey, hydrogen in white, oxygen in red, nitrogen in blue, silicon in yellow, boron in pink and phosphorus in orange.*

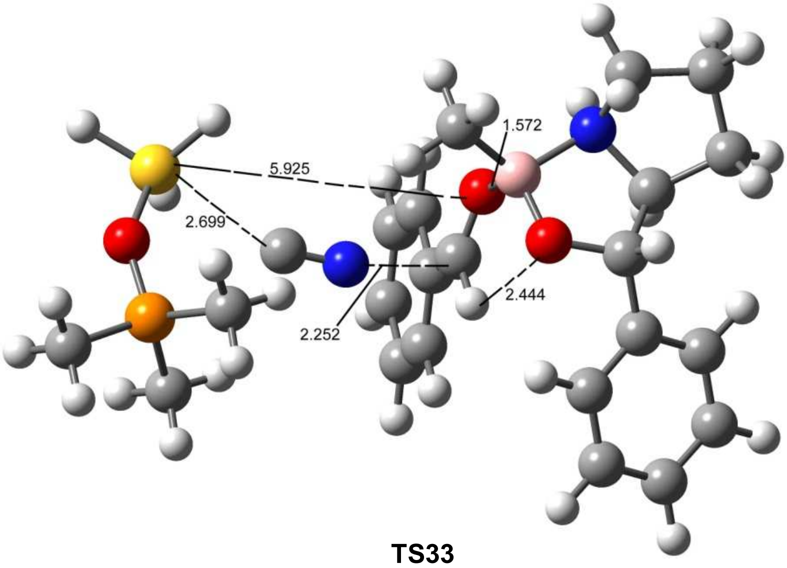

TS33

ΔG_{rel}=0.0

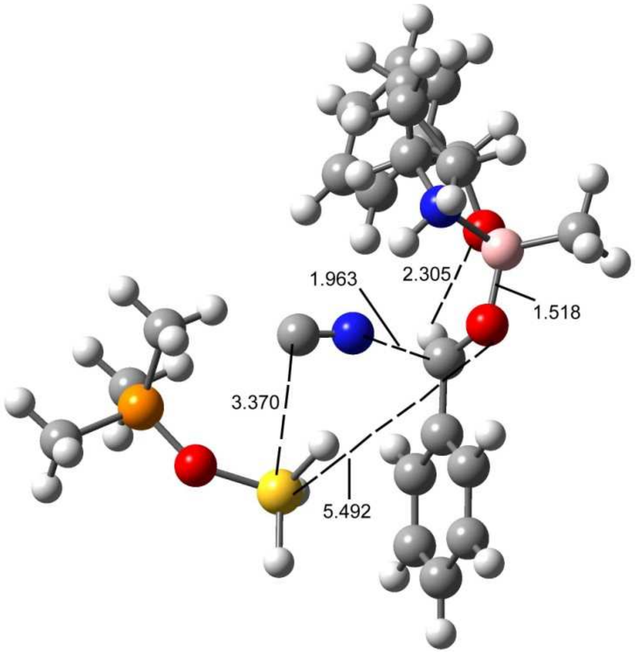

TS34

ΔG_{rel}=+2.5

Figure 6.6: B3LYP/6-31G(d) optimized first transition structures for Reaction 6-B (cyanide path). Relative free energies are in kcal/mol at 273.15 K. Distances are in angstroms. ***TS33*** *= transition state having the R configuration and* ***TS34*** *= transition state having the S configuration.*

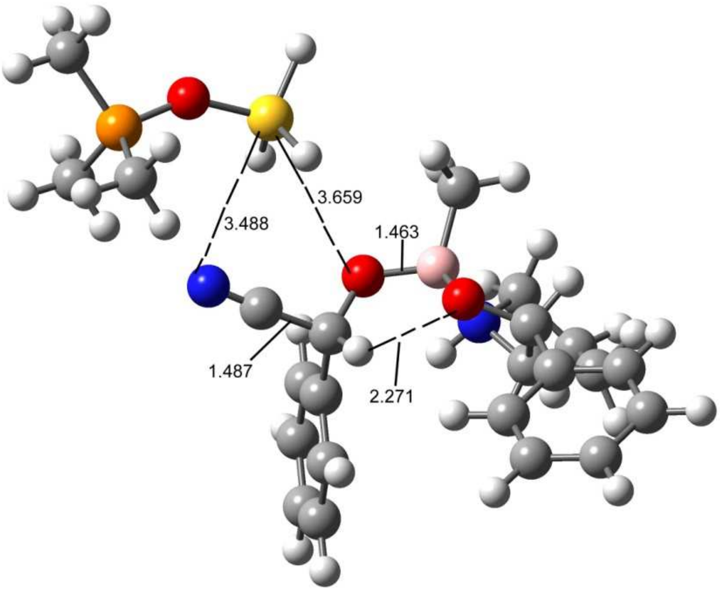

Int1

ΔG_{rel}=0.0

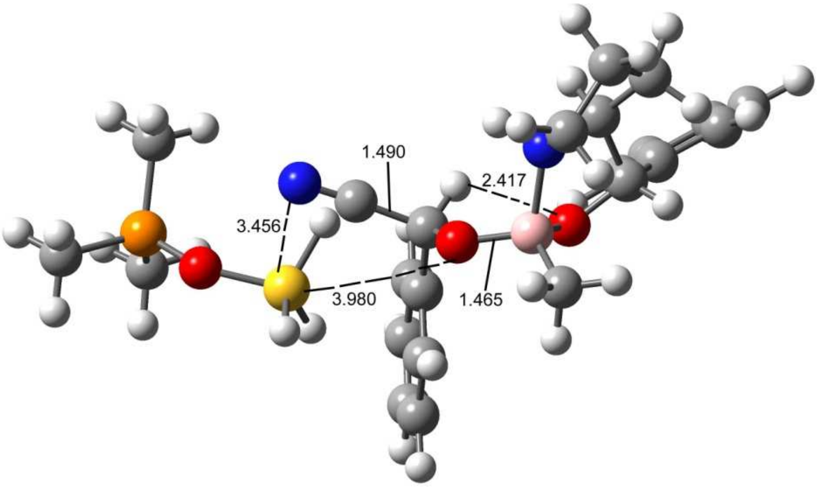

Int2

ΔG_{rel}=+4.0

Figure 6.7: B3LYP/6-31G(d) optimized intermediates for Reaction 6-B (isocyanide path). Relative free energies are in kcal/mol at 273.15 K. Distances are in angstroms. ***Int1*** *= intermediate having the R configuration and* ***Int2*** *= intermediate having the S configuration.*

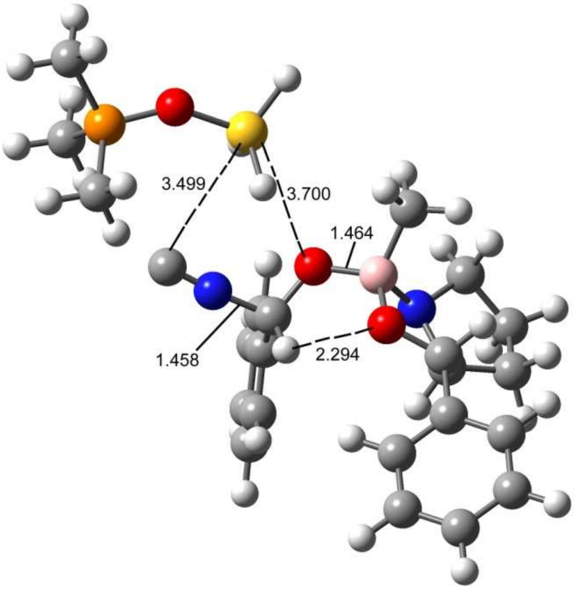

Int3

ΔG_{rel}=0.0

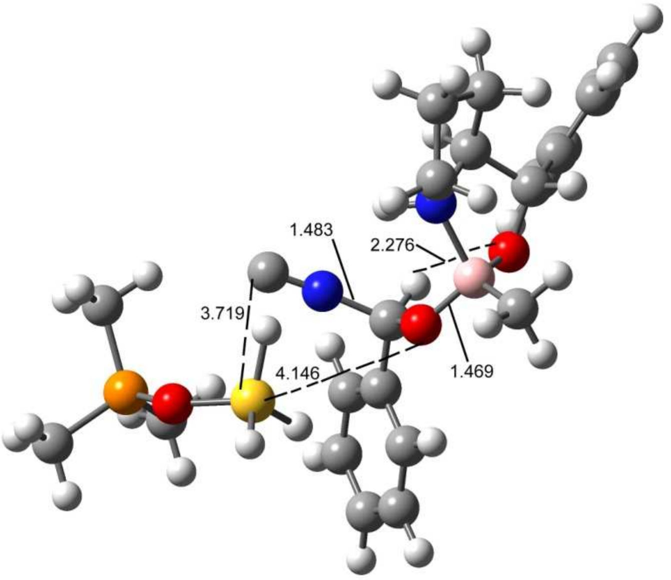

Int4

ΔG_{rel}=+3.7

Figure 6.8: B3LYP/6-31G(d) optimized intermediates for Reaction 6-B (cyanide path). Relative free energies are in kcal/mol at 273.15 K. Distances are in angstroms. ***Int3*** *= intermediate having the R configuration and* ***Int4*** *= intermediate having the S configuration.*

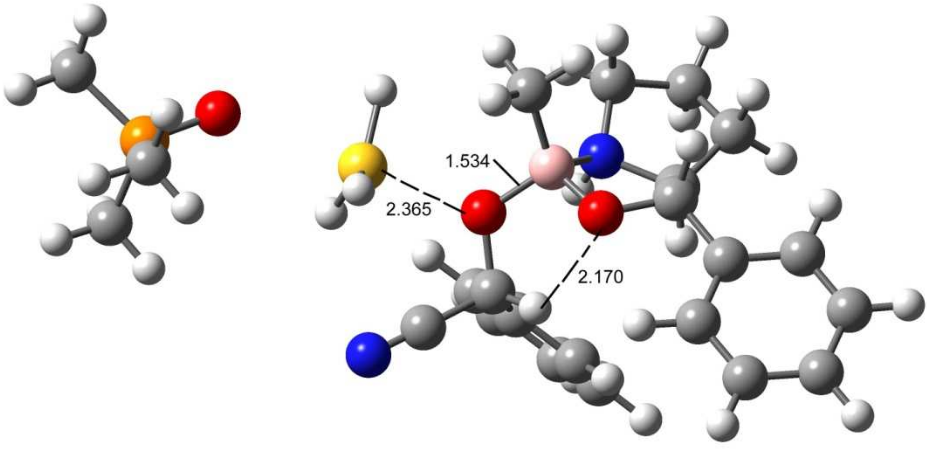

TS35

ΔG_{rel}=0.0

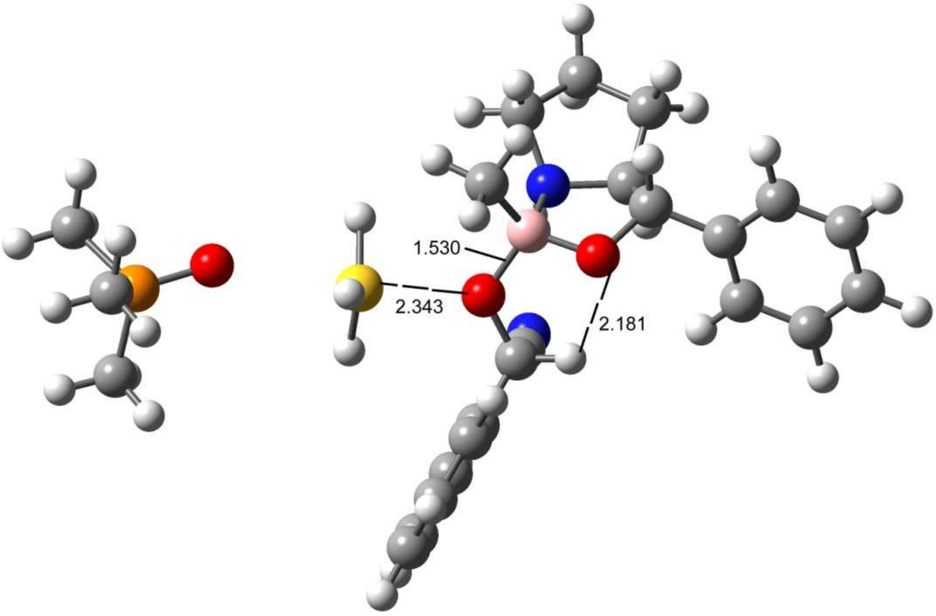

TS36

ΔG_{rel}=+2.9

Figure 6.9: B3LYP/6-31G(d) optimized second transition structures for Reaction 6-B (isocyanide path). Relative free energies are in kcal/mol at 273.15 K. Distances are in angstroms. ***TS35*** *= transition state having the R configuration and* ***TS36*** *= transition state having the S configuration.*

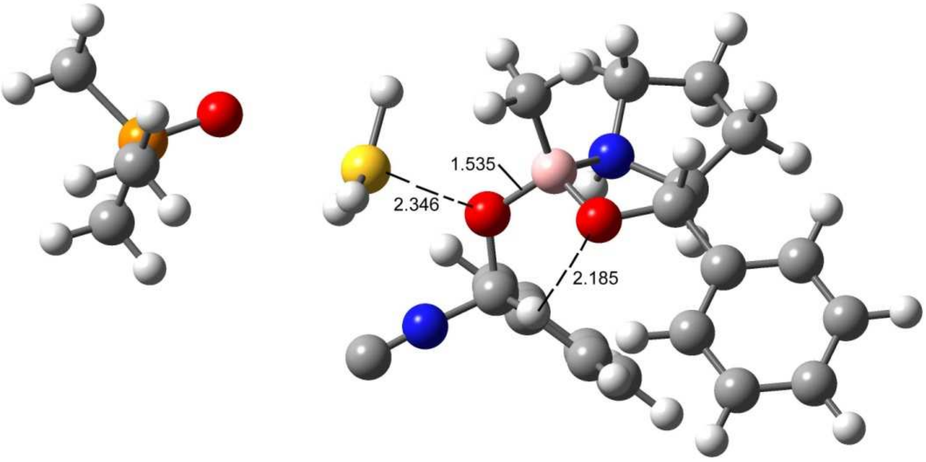

TS37

ΔG_{rel}=0.0

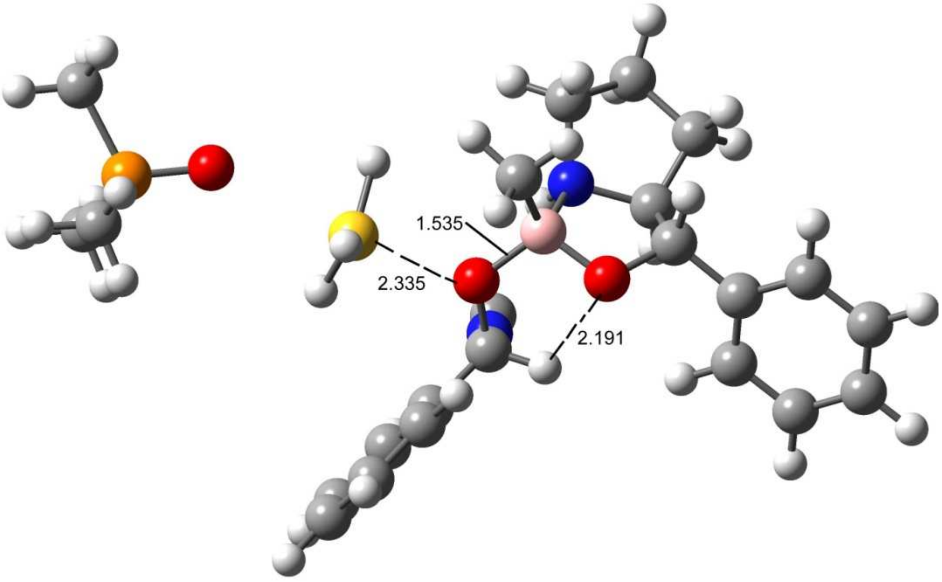

TS38

ΔG_{rel}=+3.4

Figure 6.10: B3LYP/6-31G(d) optimized second transition structures for Reaction 6-B (cyanide path). Relative free energies are in kcal/mol at 273.15 K. Distances are in angstroms. ***TS37*** *= transition state having the R configuration and* ***TS38*** *= transition state having the S configuration.*

Table 6.1 lists the B3LYP/6-31G(d) computed activation free energies for the four possible reaction pathways (isocyanide path with the *R* or *S* configuration and cyanide channel with the *R* or *S* configuration). As can be seen from the table, the present calculations show the isocyanide to be more reactive than the isomeric cyanide with a maximum difference in activation free energies of 11.7 kcal/mol (based on the first activation free energies). This result is in agreement with the prediction made by Ryu and Corey [8] that the isocyanide would be a more reactive cyanosilylation reagent than the isomeric cyanide.

Table 6.1: B3LYP/6-31G(d) calculated activation free energies (kcal/mol).

	$\Delta G_1^\ddagger$	$\Delta G_2^\ddagger$
Isocyanide – *R*	5.1	34.1
Isocyanide – *S*	7.7	32.9
Cyanide – *R*	16.8	32.2
Cyanide – *S*	19.2	31.9

The imaginary frequencies associated with the first transition state structures (Figures 6.5 and 6.6) correspond to a swing motion of the (iso)cyano group between the formyl carbon and the silicon atom. The direction of the displacement vector is towards the formyl carbon indicating the formation of the C–C or N–C bond and the breaking of the Si–N or Si–C bond. For the second transition state structures (Figures 6.9 and 6.10), the imaginary frequencies correspond to the formation of the Si–O(benzaldehyde) bond. Therefore, the major steps involved in the cyanosilylation of benzaldehyde catalyzed by **16** are the nucleophilic addition of the iso(cyano) group to the formyl carbon of the benzaldehyde to give an intermediate (Figures 6.7 and 6.8) followed by a nucleophilic substitution step where the Me_3PO is the leaving group. The activation free energy of this step is higher than that of the nucleophilic addition step (Table 6.1) rendering it the rate determining step of the cyanosilylation reaction.

Based on the rate determining step, the *R* transition structures are lower in free energy than the corresponding *S* transition structures (Figures 6.9 and 6.10). For both the cyanide and isocyanide paths, the percent enantiomeric excess (%*ee*) is found to be greater than 99% at 273.15 K favoring the *R* enantiomer.

6.4 Conclusion

The mechanism and enantioselectivity of the cyanosilylation of benzaldehyde **18** by the cyanosilylation reagent Me_3POH_3SiCN and its isomer Me_3POH_3SiNC in the presence of the model chiral oxazaborolidinium ion catalyst **16** have been investigated by density functional theory using the B3LYP functional with the 6-31G(d) basis set. Both cyanide and isocyanide paths showed stepwise reaction mechanism where the formation of N–C bond (cyanide path) or C–C bond (isocyanide path) is accomplished in the first step of the reaction. The formation of the Si–O bond takes place in a subsequent step and it is the rate determining step of the cyanosilylation reaction. The isocyanide exhibited higher reactivity than the isomeric cyanide. On the basis of the rate determining step, the preferred enantiomer was found to possess the *R* configuration and the calculated enantioselectivities for both cyanide and isocyanide routes were found to be > 99%.

6.5 References

1. K. Iwanami, M. Aoyagi, T. Oriyama, Iron(III) triflate-catalyzed one-pot synthesis of acetal-type protected cyanohydrins from carbonyl compounds, Tetrahedron Letters 47 (2006) 4741-4744.
2. L. Mei, S.W. Long, H.K. Liang, W.S. Xuan, Studies on cyanosilylation reaction catalyzed by Ln—N complexes, Applied Organometallic Chemistry 22 (2008) 181-186.
3. S.S. Kim, J.T. Lee, S.H. Lee, Mild and efficient silylcyanation of aldehydes catalyzed by alkali metal fluorides, Bulletin of the Korean Chemical Society 26 (2005) 993-994.

4. G.K.S. Prakash, H. Vaghoo, C. Panja, V. Surampudi, R. Kultyshev, T. Mathew, G.A. Olah, Effect of carbonates/phosphates as nucleophilic catalysts in dimethylformamide for efficient cyanosilylation of aldehydes and ketones, Proceedings of the National Academy of Sciences of the U.S.A. 104 (2007) 3026-3030.
5. M. Kanai, N. Katob, E. Ichikawab, M. Shibasaki, Power of cooperativity: Lewis acid-Lewis base bifunctional asymmetric catalysis, Synlett (2005) 1491-1508.
6. K. Shen, X. Liu, Q. Li, X. Feng, Highly enantioselective cyanosilylation of ketones catalyzed by a bifunctional Ti(IV) complex, Tetrahedron 64 (2008) 147-153.
7. J. Casas, C. Nájera, J.M. Sansano, J.M. Saá, BINOLAM, a recoverable chiral ligand for bifunctional enantioselective catalysis: The asymmetric synthesis of cyanohydrins, Organic Letters 4 (2002) 2589-2592.
8. D.H. Ryu, E.J. Corey, Highly enantioselective cyanosilylation of aldehydes catalyzed by a chiral oxazaborolidinium ion, Journal of the American Chemical Society 126 (2004) 8106-8107.
9. D.E. Fuerst, E.N. Jacobsen, Thiourea-catalyzed enantioselective cyanosilylation of ketones, Journal of the American Chemical Society 127 (2005) 8964-8965.
10. S.S. Kim, J.M. Kwak, G. Rajagopal, Asymmetric cyanosilylation of aldehydes by chiral Ti-TADDOL complex, Bulletin of the Korean Chemical Society 27 (2006) 1638-1640.
11. Y. Suzuki, M.D. Abu Bakar, K. Muramatsu, M. Sato, Cyanosilylation of aldehydes catalyzed by *N*-heterocyclic carbenes, Tetrahedron 62 (2006) 4227-4231.
12. X. Wang, S.-K. Tian, Catalytic cyanosilylation of ketones with simple phosphonium salt, Tetrahedron Letters 48 (2007) 6010–6013.
13. I.V.P. Raj, G. Suryavanshi, A. Sudalai, Organocatalytic activation of TMSCN by basic ammonium salts for efficient cyanation of aldehydes and imines, Tetrahedron Letters 48 (2007) 7211-7214.
14. M.G. Dekamin, S. Javanshir, M.R. Naimi-Jamal, R. Hekmatshoar, J. Mokhtari, Potassium phthalimide-N-oxyl: An efficient catalyst for cyanosilylation of carbonyl compounds under mild conditions, Journal of Molecular Catalysis A: Chemical 283 (2008) 29-32.
15. S.T. Kadam, S.S. Kim, N-Iodosuccinimide (NIS) a novel and effective catalyst for the cyanosilylation of aldehydes under mild reaction conditions, Catalysis Communications 9 (2008) 1342-1345.
16. M.G. Dekamin, J. Mokhtari, M.R. Naimi-Jamal, Organocatalytic cyanosilylation of carbonyl compounds by tetrabutylammonium phthalimide-N-oxyl, Catalysis Communications 10 (2009) 582-585.
17. M.G. Dekamin, S. Sagheb-Asl, M.R. Naimi-Jamal, An expeditious synthesis of cyanohydrin trimethylsilyl ethers using tetraethylammonium 2-(carbamoyl)benzoate as a bifunctional organocatalyst, Tetrahedron Letters 50 (2009) 4063-4066.
18. E.J. Corey, T.W. Lee, The formyl $C–H\cdots O$ hydrogen bond as a critical factor in enantioselective Lewis-acid catalyzed reactions of aldehydes, Chemical Communications (2001) 1321-1329.
19. M.D. Mackey, J.M. Goodman, Conformational preferences of $R^1R^2C{=}O{\cdot}H_2BF$ complexes, Chemical Communications (1997) 2383-2384.

20. Gaussian 03, Revision E.01, M. J. Frisch, G. W. Trucks, H. B. Schlegel, G. E. Scuseria, M. A. Robb, J. R. Cheeseman, J. A. Montgomery, Jr., T. Vreven, K. N. Kudin, J. C. Burant, J. M. Millam, S. S. Iyengar, J. Tomasi, V. Barone, B. Mennucci, M. Cossi, G. Scalmani, N. Rega, G. A. Petersson, H. Nakatsuji, M. Hada, M. Ehara, K. Toyota, R. Fukuda, J. Hasegawa, M. Ishida, T. Nakajima, Y. Honda, O. Kitao, H. Nakai, M. Klene, X. Li, J. E. Knox, H. P. Hratchian, J. B. Cross, V. Bakken, C. Adamo, J. Jaramillo, R. Gomperts, R. E. Stratmann, O. Yazyev, A. J. Austin, R. Cammi, C. Pomelli, J. W. Ochterski, P. Y. Ayala, K. Morokuma, G. A. Voth, P. Salvador, J. J. Dannenberg, V. G. Zakrzewski, S. Dapprich, A. D. Daniels, M. C. Strain, O. Farkas, D. K. Malick, A. D. Rabuck, K. Raghavachari, J. B. Foresman, J. V. Ortiz, Q. Cui, A. G. Baboul, S. Clifford, J. Cioslowski, B. B. Stefanov, G. Liu, A. Liashenko, P. Piskorz, I. Komaromi, R. L. Martin, D. J. Fox, T. Keith, M. A. Al-Laham, C. Y. Peng, A. Nanayakkara, M. Challacombe, P. M. W. Gill, B. Johnson, W. Chen, M. W. Wong, C. Gonzalez, and J. A. Pople, Gaussian, Inc., Wallingford CT, 2004.
21. M. Shibasaki, M. Kanai, K. Funabashi, Recent progress in asymmetric two-center catalysis, Chemical Communications (2002) 1989-1999.